Departamento de Física Atómica, Molecular y Nuclear
Universidad Complutense de Madrid

Tesis doctoral:

Simulaciones avanzadas aplicadas al diseño de escáneres y mejora de la calidad de imagen en tomografía por emisión de positrones

realizada por Samuel España Palomares
dirigida por José Manuel Udías Moinelo

2009

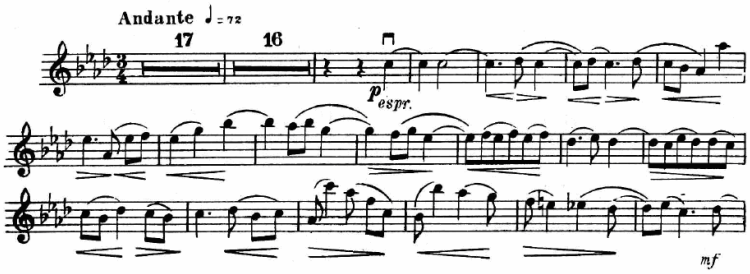

Passacaglia, Violin Concerto No. 1 in A minor, Opus 77.

Dmitri Shostakovich.

Contents

Preludio

Todo comenzó una mañana cuando aún me encontraba cursando asignaturas de cuarto curso allá por el año 2002, poco antes de los exámenes de Junio. Se anunciaba en los pasillos de la Facultad un seminario sobre un tema relacionado con la física médica. El tema a tratar era el PET y su ponente Juan José Vaquero. Yo por aquel entonces ya había decidido dedicarme a la física médica cuando terminara la licenciatura y para ello pensaba presentarme a las pruebas selectivas de Radiofísicos Hospitalarios. Aquel seminario me hizo pensar en la posibilidad remota, pensaba yo, de dedicarme a la investigación en Física Médica en lugar de a su aplicación.

Unos meses más tarde, ya en quinto curso, realicé las prácticas de la asignatura Física Nuclear y de Partículas. Controlando el laboratorio se encontraba el profesor José Manuel Udías, que me comentó la posibilidad de realizar, en el Departamento de Física Atómica, Molecular y Nuclear, trabajos de introducción a la investigación relacionados con la Física Médica. Unas semanas más tarde me enteré de que ese mismo profesor junto con otro del Departamento, José Luís Contreras, ofrecían un trabajo sobre PET. Con ellos dos comencé a trabajar en PET y el tema me apasionó por completo. A José Luís Contreras le agradezco su gran ayuda durante la realización del trabajo y el interés que ha mostrado siempre por lo que hago. Al finalizar el trabajo y con él la licenciatura, fue José Manuel Udías el que me propuso comenzar a trabajar con él en PET en colaboración con el Laboratorio de Imagen Médica del Hospital Gregorio Marañón (LIM-HGGM), en el cual trabajaba Juan José Vaquero. Ese día fui dando saltos de alegría a contárselo a mi familia, que por supuesto transmitió al resto de familia y amigos que iban a tener un premio Nobel en casa, lo que no estaba claro aún era si sería en Física o en Medicina.

Bromas aparte, tengo que agradecer a José Manuel la oportunidad que me brindó y la confianza que puso y sigue poniendo en mí. En aquel momento empecé a darme cuenta de su modo de trabajar. Me encerró en su despacho una tarde entera y me contó todos los proyectos que tenía en mente. Luego me dio un montón de artículos y tesis para leer, me instaló un ordenador (con Linux, por supuesto) y me dio un libro de programación en Fortran. Ya sólo necesitaba ponerme manos a la obra, aunque faltaba una sorpresa final. Todo ese trabajo no iba hacerlo yo sólo. Otro chico que también acababa de terminar la licenciatura, Joaquín López, trabajaría conmigo dentro del mismo proyecto. Y de este modo comenzamos los tres a trabajar juntos.

A José Manuel Udías tengo que agradecerle la paciencia que ha tenido y sigue teniendo para explicar y resolverme cualquier duda y por transmitirme parte de la pasión que pone en lo que hace. También tengo que agradecer su omnipresencia. Muchas veces no he sabido dónde estaba durantes días o incluso semanas, pero tampoco importaba mucho porque cualquier consulta que le hiciera por email me la respondía después de estudiárselo a conciencia a los pocos minutos o como máximo horas. Daban igual el día o la hora.

Con Joaquín López he compartido codo con codo todo el trabajo de estos años. Innumerables viajes, conversaciones y todo tipo de aventuras. De él he aprendido a no rendirme cuando me surge cualquier problema y a ser creativo, en el sentido de intentar siempre buscar más allá de lo conocido, lo cuál nos ha llevado muchas veces a reinventar la rueda (de ahí su frase "Si crees que has descubierto algo, es que no has leído lo suficiente").

También agradezco a Juan José Vaquero y Manuel Desco, del LIM-HGGM, todo el apoyo recibido y el haberme abierto las puertas de su laboratorio siempre que lo he necesitado, sin olvidar el soporte económico sin el cuál nada de esto habría sido posible.

De vuelta a la Facultad, el grupo comenzó a crecer pasados unos meses. Esther Vicente fue la primera y con ella he compartido no pocas peripecias y he disfrutado intentando resolverle dudas y problemas que me han hecho aprender a mí también cosas nuevas y afianzar lo que ya sabía. Catherine Murphy también empezó con ganas aunque finalmente nos ganó el pulso la empresa privada. Luego se incorporaron Elena Herranz y Jacobo Cal con los que también he compartido muchas horas de trabajo y que aportan la ilusión y frescura propia de los primerizos y no tan primerizos. Y porque no sólo de PET vive el hombre, también agradezco su apoyo a otros profesores y veteranos del grupo como Joaquín Retamosa, Elvira Moya, José María Gómez, Eduardo Faleiro, Javier Rodríguez, Armando Relaño, Laura Muñoz, Raquel Álvarez, y especialmente a César Fernández, Luis Mario Fraile y Cristina Martínez, con los que he tenido una relación más estrecha que me ha enseñado mucho. Pablo Corzo y Joaquín Escayo me han ayudado con la informática estos últimos años y Paloma Vaquero me ha facilitado enormemente las labores burocráticas, que no son pocas. Y no puedo olvidarme de Mihai Furnica, que ha puesto siempre su lado más abstracto. También tengo que agradecer a otros alumnos que han hecho el trabajo de investigación en nuestro grupo, con algunos de los cuales he participado como codirector. Con su ilusión y esfuerzo también he aprendido muchas cosas. Ellos son José Luís Izquierdo, Marta Larraona, Adriana Martín de Aguilera y Rosa Gantes.

En el Hospital Gregorio Marañón he tenido también muy buenos compañeros y colaboradores. Al principio recibí la ayuda de Antonio Molins que enseguida caminó por otros derroteros. Fue entonces cuando llegó Eduardo Lage, con el cuál he mantenido numerosas conversaciones donde nuestros conocimientos se complementaban y que me ha facilitado siempre toda la información que he necesitado para la colaboración con su grupo. A Gustavo Tapias tengo que agradecerle su cooperación y disponibilidad, sobre todo en el último año. Con otros como Javier Sánchez y Mónica Abella también mantuve una fructífera colaboración en los primeros años de doctorado. También agradezco la acogida del siempre creciente número de personas de este grupo, como son Trajana, Marisa, Marina, Javi Pascau, Verónica, Ángel, Alexia, Santi Redondo, Juan, Chema, Judit, Alex, José, Irina, Cris, Santiago Reig, Carlos y algunos más que seguro que me olvido. Algunos de ellos me han ayudado en mi trabajo y con casi todos he aprendido cosas nuevas que me han hecho tener una visión más amplia de la imagen médica.

A Jurgen Seidel le agradezco la paciencia que ha tenido siempre para responder a nuestras preguntas y su cooperación durante mi estancia en Baltimore, donde Benjamin Tsui y su grupo me acogieron como uno más de los suyos.

Con Antonio Sanz y Santiago García, de la Universidad Rey Juan Carlos, hemos mantenido una productiva colaboración y agradezco todo lo que me han enseñado sobre las GPUs.

También agradezco a Nerea por escuchar con paciencia las batallitas de los positrones y las ratas, a mis padres, hermanos, cuñados, abuela y resto de familia por darme siempre ánimos, a Juan Manuel por su gran interés y apoyo y a Miguel Ángel por su confianza.

En resumidas cuentas, que yo soy el principal autor de este trabajo pero que sólo ha sido posible gracias a la ayuda recibida de éstas y otras muchas personas.

Introduction, aims and document structure

Since the first PET scanner was developed in the 1970s, positron emission tomography has been established in oncology, cardiology and neurology. The extension of this technique to preclinical research has represented a great challenge in the last decade, during which very high resolution PET scanners for laboratory animals such as mice and rats have been developed. Nowadays, it is possible to obtain PET images with submillimetric resolution and some PET scanners have sensitivity in excess of 10%. This has been possible thanks to technological developments in the detection of gamma photons and electronic processing. Likewise, the advent of faster computers, improvement of the reconstruction algorithms and widespread use of Monte Carlo simulation methods have played an important role in recent PET developments.

PET research involves different areas of knowledge and requires multidisciplinary teams of biologists, physicians, pharmacists, engineers, technicians and physicists, among others. The basic principles of PET are governed by Nuclear Physics. The Nuclear Physics Group (GFN) of the Universidad Complutense de Madrid provided with a helpful and rich environment for the development of this work. The GFN has the theoretical and experimental Nuclear Physics knowledge needed to understand the PET technique in detail and to contribute to its development. The collaboration with the Laboratorio de Imagen Médica of the Hospital General Universitario Gregorio Marañón provided us their extensive experience in medical imaging and with access to many real data from several PET scanners.

Realistic simulation of PET scanners allows for improving all phases of the production of the image, from the design of the scanner and detectors to the computation of the system response matrix (SRM) that is employed during the reconstruction process, through data acquisition, data processing and data corrections. As a result, an overall improvement of the quality of the images can be obtained. That is, images with better spatial resolution and signal to noise ratio, and with more accurate and reproducible quantification results are produced. Faster computers and accurate Monte Carlo codes that are available today allow for simulations that incorporate the significant physics of emission, interactions, and electronics of PET scanners.

In this thesis we tried to improve the quality of PET images by intensive use of Monte Carlo simulations in order to tackle the processes that take place during the acquisition of PET data. We have focused this work in high resolution PET scanners for small animal studies. These scanners require advanced reconstruction methods in order to achieve spatial resolution of the order of 1 mm. Indeed, to achieve this resolution goal, the system response matrix employed by statistical reconstructions methods must be very accurate (Herraiz *et al.*, 2006).

The goals of this thesis can be summarized as follows:

- Development of a Monte Carlo application (PeneloPET) for its use in PET (chapter 4).
- Validation of PeneloPET in order to assess its reliability (chapter 5).
- Use of PeneloPET for the improvement of the quality of the images obtained with existing small animal PET scanners (chapters 6 and 7).
- Study of the applications of PeneloPET in the design of new small animal PET scanners (chapter 8).

The structure of this thesis can be summarized as follows:

- Theoretical framework.
  - Chapter 1. Introduction to physics principles involved in the PET technique, the operation of the different components of a PET scanner, and the description of the most relevant parameters of PET scanners.
  - Chapter 2. Basic introduction to image reconstruction.
  - Chapter 3. Introduction to Monte Carlo techniques and to several simulation packages.
- Development of PeneloPET.
  - Chapter 4. Description of PeneloPET, a Monte Carlo tool for PET simulations.
  - Chapter 5. Validation of PeneloPET. Comparison of simulated acquisitions to real measurements and to results of other simulation packages.
- Applications of PeneloPET.
  - Chapter 6. Determination of the SRM for 3D-OSEM reconstruction method.
  - Chapter 7. *A priori* estimation of the reliability of detected events in order to improve the quality of the images reconstructed.
  - Chapter 8. Considerations that must be taken into account during the design of a small animal PET scanner.

In the next paragraphs, a further explanation of the work presented in this thesis is given.

The first goal of this thesis has been the development of a Monte Carlo tool (PeneloPET (España *et al.*, 2009)) capable of realistic simulations of PET scanners. There are several packages for the simulation of the transport of radiation through the matter. We have chosen one of them (PENELOPE (Baró *et al.*, 1995)) as the core over which we built the tools necessary to reproduce all aspects of PET. PeneloPET is described in chapter 4 and validated in chapter 5. Further, the advantages of having an advanced simulation tool is exemplified by several applications presented in the remaining chapters of this thesis.

The second goal of this work has been to calculate in an optimal way, the system response matrix, removing redundancies and taking advantage of symmetries and quasi-symmetries, so that a system response matrix (SRM) enough small to keep inside RAM memory of ordinary industry-standard computers could be obtained. The SRM computed in this way has been applied to the reconstruction, using the 3D-OSEM method (Hudson and Larkin, 1994), of PET data acquired with small animal scanners (Herraiz *et al.*, 2006). We show this in chapter 6.

No detection device is perfect and no measured data is free from errors. We tried to analyze the errors and uncertainties in PET data measurement, and employ this to produce *a priori* information about the individual reliability of each event acquired. Indeed, we analyze the information obtained during PET acquisitions, such as energy deposited in the detectors, singles and coincidence rates, position of interaction, and so on. We use this event reliability analysis to reduce the impact of data uncertainties and errors in the images reconstructed. This is presented in chapter 7.

The design of modern scanners is nowadays paced with the development of Monte Carlo simulation tools, which will thus play an overly significant role in the definition of the next generation of PET scanners. In chapter 8 we use intensively the Monte Carlo simulations to determine the parameters of PET scanners that have the largest impact in performance.

1. Principles of PET

1.1. Introduction

Positron Emission Tomography (PET) (Cherry *et al.*, 2003) is a technique used in clinical medicine and biomedical (preclinical) research to create images that show how certain organs perform their physiological function. Radioactive nuclei are introduced into the patient to label tracer molecules that probe physiological processes. These radioactive nuclei emit positrons that annihilate with electrons from the tissue. An annihilation event usually results in two gamma photons being emitted at nearly 180 degrees and with an energy of 511 keV each (Figure 1.1). The gamma photons are detected in coincidence in a detector ring so that two gamma photons detected in coincidence define a *line of response* (LOR) along which the positron annihilation took place. The information recorded in every possible LOR is assembled and, with the aid of image processing tools, it is employed to produce an image of the activity and thereby of the functionality of the organism.

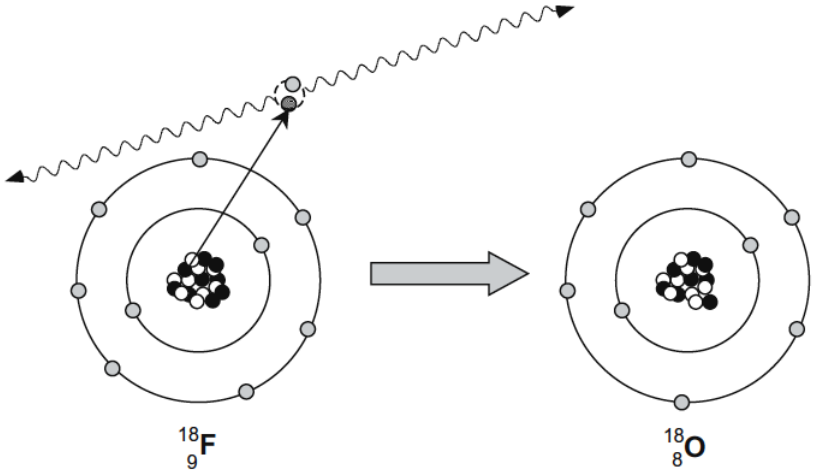

Figure 1.1. Decay scheme of a β^+ radionuclide and the positron-electron pair annihilation. This figure conveys the basic principles of PET.

1.2. Physics principles

1.2.1. Beta decay

Beta particles are fast electrons or positrons produced in the (weak interaction mediated) decay of neutrons or protons in neutron or proton rich nuclei (Krane, 1987). In a neutron rich nucleus a neutron can transform into a proton via the process

$$n \rightarrow p^+ + e^- + \overline{\upsilon}_e \qquad (1.1)$$

where an electron and an antineutrino are emitted. Free neutrons also decay according to this disintegration scheme with a half-life of 10.25 minutes (Cherry *et al.*, 2003). The daughter nucleus now contains one extra proton so that its atomic number Z increases in one unit. This can be written as

$$X^{\,Z}_{N} \rightarrow X^{\,Z+1}_{N-1} + e^- + \overline{\upsilon}_e \qquad (1.2)$$

In proton rich nuclei, a positron and a neutrino are emitted in the complementary process (Krane, 1987) to the one previously described.

$$p^+ \rightarrow n + e^+ + \upsilon_e \tag{1.3}$$

This β^+ process cannot happen to free, isolated protons, due to energy constrains, but the corresponding decay in nuclei can arise when it is energetically possible (Powsner and Powsner, 2006) and it is written as

$$X_N^Z \rightarrow X_{N+1}^{Z-1} + e^+ + \upsilon_e \tag{1.4}$$

The daughter nucleus now contains one proton less after the decay; therefore the atomic number has decreased by one unit. There is also a third process in nuclei mediated by the weak interaction. It is called electron capture (Krane, 1987). In this process an atomic electron is captured by the nucleus

$$p^+ + e^- \rightarrow n + \overline{\upsilon}_e \tag{1.5}$$

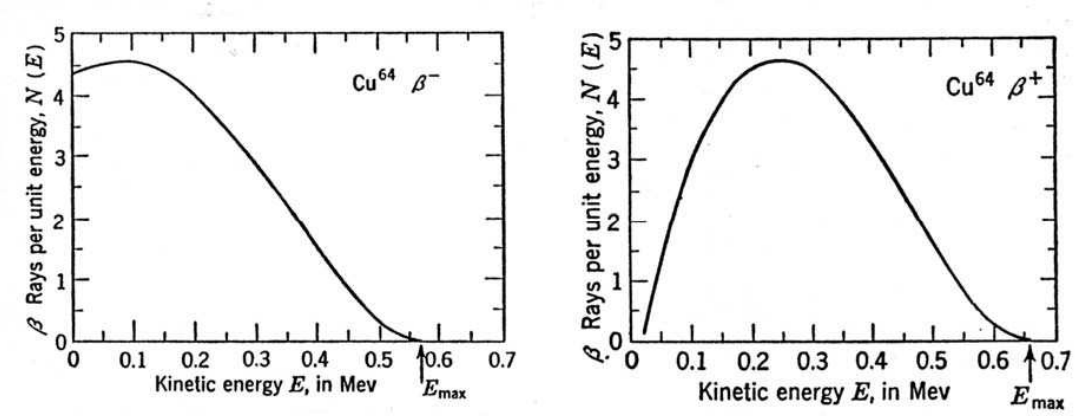

Figure 1.2. Experimental β-spectra obtained from decaying ^{64}Cu. β^- particles are affected by the electric field of the positively charged nuclei and thus the energy spectrum is shifted towards lower energies. β^+ particles, on the other hand, are repelled by the nuclei so the energy spectrum it is shifted towards higher energies.

A basic characteristic of the β-decay process is the continuous energy spectrum of the β particles. This is because the available energy in the decay is shared between the β particle and the neutrino or antineutrino. Typical energy spectra are shown in Figure 1.2 (Krane, 1987). The number of β particles emitted with momentum between p and $p + dp$ can be expressed as

$$N(p)dp = Cp^2q^2dp \tag{1.6}$$

where C is a constant and q is the momentum of the neutrino.

The distance from the emission point to the annihilation point is known as the *positron range*, that is one of the main limiting factors to the spatial resolution of PET (Levin and Hoffman, 1999). Positron range effects depend on the energy of the emitted positrons. The distance in the normal direction to the location of the decaying atom to the line defined by the annihilation photons is the *positron range blurring*, relevant for PET projection data (see Figure 1.3). Because positrons are emitted with a range of energy and follow a tortuous path in tissue, the positron range is a non-Gaussian distribution as described by Derenzo (Derenzo, 1979) and Levin and Hoffman (Levin and Hoffman, 1999).

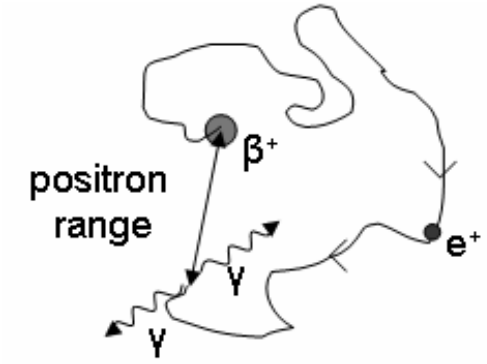

Figure 1.3. Scheme representing the definition of the positron range. From its emission, the positron follows an erratic path until the annihilation process.

When the positron reaches thermal velocities (a few eV), it either annihilates directly with an electron into two gammas, or first forms positronium in the singlet ($^1S_0$, para-positronium) or triplet ($^3S_1$, ortho-positronium) state (Berko and Hereford, 1956). Para-positronium decays only into two gammas with a lifetime of $\tau_{2\gamma}=1.26\cdot10^{-10}$ s (Patro and Sen, 1971), while ortho-positronium decays into three gammas with a lifetime of $\tau_{3\gamma}=1.42\cdot10^{-7}$ s (Westbrook *et al.*, 1987). These respective decay times were measured for positrons in metals with a 2γ/3γ branching ratio of 372 (Berko and Hereford, 1956). Also, for both positronium states, the pick-off annihilation is possible, where the positron annihilates with another electron from neighboring atoms before it is able to annihilate with its positronium partner (Colombino *et al.*, 1965).

As the majority of disintegrations occur with both positron and electron at thermal energies (much less than their rest masses), two photons with a characteristic energy of 511 keV are produced, for the majority of annihilations in water or tissue, with a relative angle of approximately 180º (DeBenedetti *et al.*, 1950). These almost collinear gammas can be used for PET because their direction includes information about the annihilation position. As the momentum of the positronium will be small, but in general non vanishing in the laboratory system, there is a slight deviation from collinearity, which is given by (Erdman, 1955):

$$\Delta\varphi = \frac{p}{m_e c} \tag{1.7}$$

DeBenedetti et al. (DeBenedetti *et al.*, 1950) measured $\Delta\varphi \approx 0.4^\circ - 0.5^\circ$. This photon non-collinearity is another limiting factor of spatial resolution in PET, because it introduces an uncertainty in the location of the annihilation point (Herraiz *et al.*, 2007).

There are just a few radionuclides, mainly ^{11}C, ^{13}N, ^{15}O, ^{18}F, and ^{82}Rb that have the adequate chemical and physical properties (see Table 1.1) which make them suitable for *in vivo* biochemical and physiological studies (Raichle, 1983). In particular, these radionuclides are isotopes of elements that can be incorporated into molecules that participate in metabolic processes and therefore enable the *in vivo* study of the behavior of these molecules. Furthermore, their short half-lives reduce significantly the radiation dose to both the subject and the people handling the radionuclides. The trade off is the need for a dedicated cyclotron (or of a generator for the case of ^{82}Rb) in the vicinity of the PET facility.

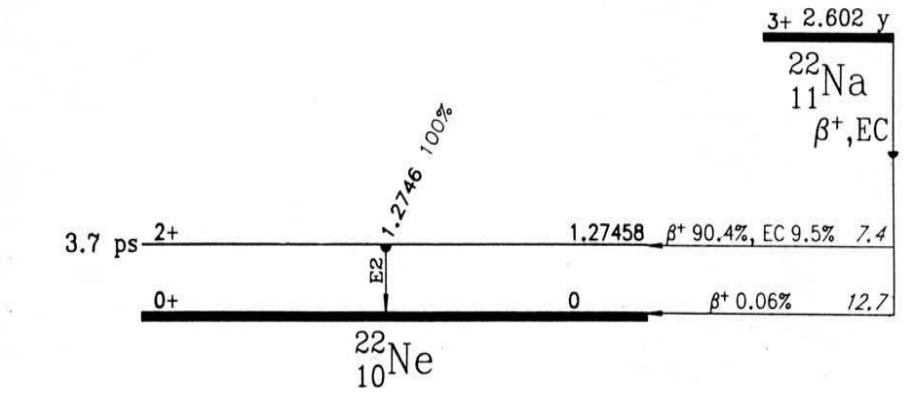

Figure 1.4: Level scheme showing the decay of ^{22}Na (Krane, 1987).

Table 1.1: Physical properties of positron emitters (Bailey *et al.*, 2004).

Radionuclide	Half-life (min)	Range in Water (mm)		Emission energy (MeV)	
		Max	Mean	Max	Mode
^{11}C	20.4	4.1	1.1	0.959	0.326
^{13}N	10.0	5.1	1.5	1.197	0.432
^{15}O	2.07	7.3	2.5	1.738	0.696
^{18}F	110.0	2.4	0.6	0.633	0.202
^{82}Rb	1.25	14.1	5.9	3.400	1.385

1.2.2. Interactions of gamma radiation with matter

When a monoenergetic gamma ray with intensity I_0 crosses matter, it interacts with the electrons of the material. As a result of these interactions, some gammas will be removed out of the incident ray by either photoelectric absorption (absorption coefficient τ), or Compton or Rayleigh effects (absorption coefficient σ), or pair production (absorption coefficient κ) (Knoll, 2000). An overall absorption coefficient μ results from these three individual absorption coefficients:

$$\mu = \tau + \sigma + \kappa \tag{1.8}$$

Thus the overall absorption can be described by

$$I = I_0 e^{-\mu x} \tag{1.9}$$

where I_0 is the incident and I the resulting intensity after crossing a distance x of material.

Photoelectric absorption

During photoelectric absorption, the incident gamma with energy E_γ is absorbed by an atom of the traversed material. An electron from the electron shell of this atom is then ejected with energy

$$E_{e^-} = E_\gamma - E_{bound} \tag{1.10}$$

where E_{bound} is the binding energy of the knocked out electron. The resulting hole in the electron shell is filled by the remaining electrons within the shell or by the capture of a free electron from the surrounding medium.

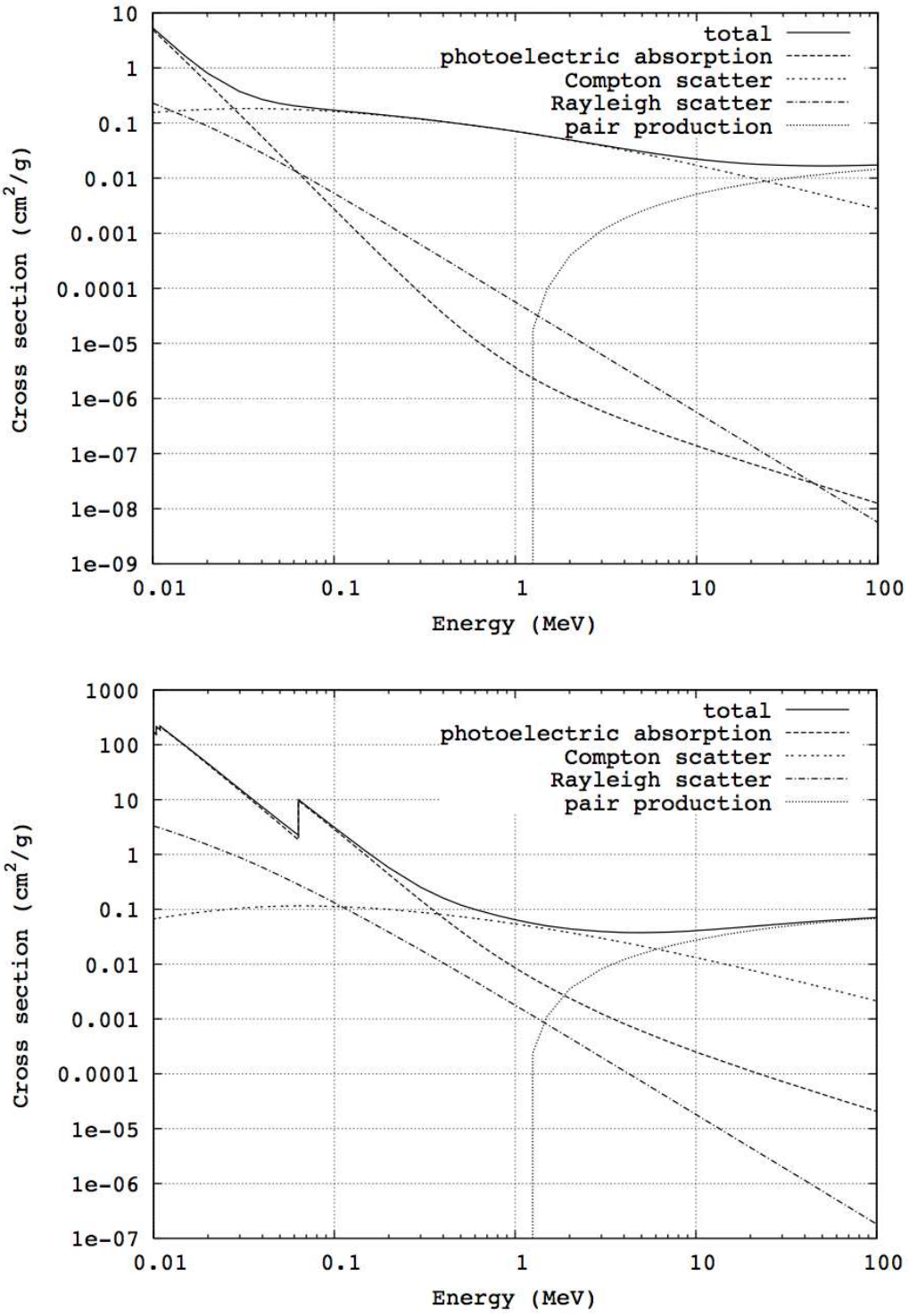

Figure 1.5. Cross secctions for the interacction of photons in water (top) and LSO (bottom). This figures include total, photoelectric absorption, Compton and Raleight scatter, and pair production. The main contribution to the total cross section at 511 keV in water is due to the Compton scatter while for LSO is shared between Compton scatter and photoelectric absorption. Rayleigh scatter is almost negligible in both cases (source: NIST XCOM data base).

Compton and Rayleigh scattering

A gamma of energy E_γ, that interacts with a shell electron of the traversed material by the Compton effect (Compton scattering), is deflected from its incident direction by an angle θ and loses an energy given by conservation of momentum as

$$E_{e^-} = E_\gamma - E_{bound} - E'_\gamma \tag{1.11}$$

where E'_γ is the energy of the gamma after the interaction. This amount of energy is transferred to the electron. E'_γ depends on the scatter angle θ according to (Knoll, 2000)

$$E'_\gamma = \frac{E_\gamma}{1 - \frac{E_\gamma}{m_e c^2}(1 - \cos\theta)} \tag{1.12}$$

$m_e c^2$ being the rest-mass energy of the electron (511 keV). The maximum energy transferred to the electron occurs when the scattering angle $\theta = \pi$.

$$E_{e^-,\max} = E_\gamma \left(\frac{2E_\gamma / m_e c^2}{1 + 2E_\gamma / m_e c^2} \right) \tag{1.13}$$

This gives rise to the Compton edge in the energy spectrum of monoenergetic gamma rays as seen in detectors of finite size (Knoll, 2000).

When elastic scattering occurs, the incident photon is scattered without ionizations nor other energy losses in excitations of the internal states of the constituents of the material. This process is known as Rayleigh scatter.

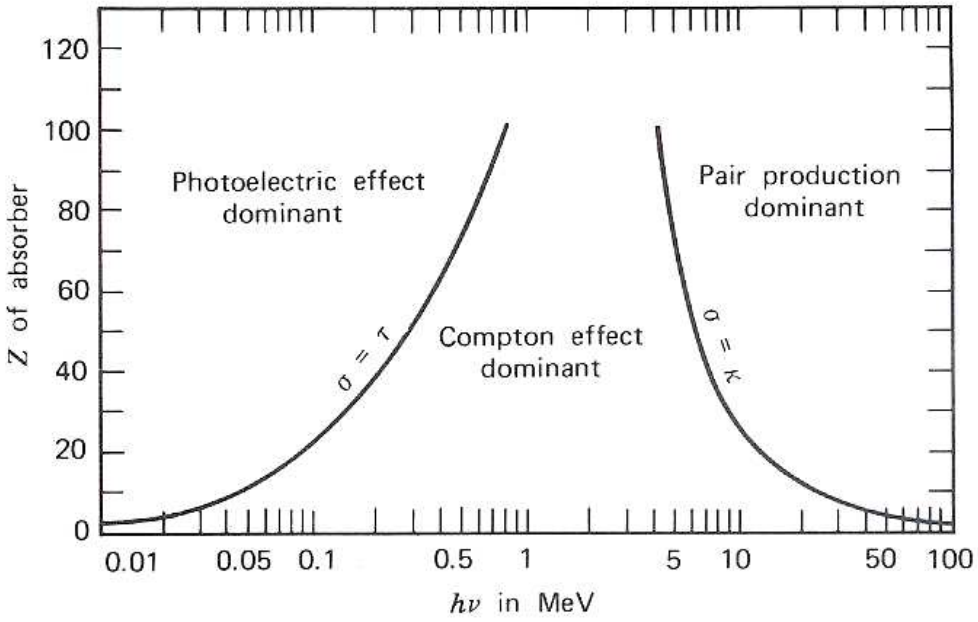

Figure 1.6. Relative importance of the three major types of gamma-ray interaction for different combinations of Z and Eγ is shown. For 511 keV gamma rays, only photoelectric and Compton interactions are relevant, whereas pair production can be neglected (Knoll, 2000).

Pair production

The energy threshold for pair production

$$\gamma \rightarrow e^{+} + e^{-} \tag{1.14}$$

is 2 × 511 keV = 1.022 MeV. This interaction can only take place in the presence of a third partner to pick up recoiling energy and momentum so that energy-momentum conservation can be verified. Additional energy of the gamma will be converted into kinetic energy of the electron, positron and recoiling partner. As this later is usually a relatively heavy nuclei, its recoiling energy can be neglected. Both electron and positron produced will undergo interactions with matter, and positron will finally produce annihilation radiation at the end of their path.

1.3. Detectors

Detection of gamma radiation is a very common technique in experimental nuclear physics. Existing knowledge in experimental nuclear physics has been adapted to the specific requirements of PET. In essence, a gamma detection system is a block of material where the gamma photon interacts. This block then transforms the absorbed energy of the gamma photon into a measurable property. If this measurable property is a number of visible photons, like in the scintillation detectors which will be described in the next subsection, it is usual to couple the block to a device that transforms this flux of visible photons into an electric signal. For energy measurements, the electric signal produced by the detector should be proportional to the measured energy. To look for coincidences in PET, in order to extract the coincidence events and to evaluate and store the energy and position of each coincidence event, the output signal is later processed and compared with the output signals of other blocks.

1.3.1. Scintillation detectors

An scintillation detector emits light (that is, photons in the visible energy range) when it is excited by radiation of higher energy. The energy range of the light emitted for most employed scintillators spans from the ultraviolet to the infrared ends (100 - 800 nm). There are several scintillating materials in use today: organic and inorganic scintillators in solid, liquid or gaseous forms. The advantage of inorganic scintillators lies in their greater stopping power, thanks to their higher density and atomic number Z (Knoll, 2000). They also have some of the highest light outputs (number of photons emitted per unit of deposited energy). High light output results in better energy resolution, because larger number of visible photons will be produced. This will reduce the broadening of the energy spectrum, because this later effect is basically due to statistical fluctuations. This makes these inorganic scintillators extremely suitable for the detection of gamma rays and, by far, the most employed materials in PET detectors.

The time structure of the light emitted by scintillators can often be approximated by (Ljungberg *et al.*, 1998)

$$N(t) = N_0 \frac{e^{-t/\tau_{FALL}} - e^{-t/\tau_{RISE}}}{\tau_{FALL} - \tau_{RISE}} \tag{1.15}$$

where $N(t)$ is here the number of photons emitted by the scintillators at time t, N_0 is the total number of photons emitted, and τ_{FALL} and τ_{RISE} are fall and rise constants of the scintillator. The time response of the crystal should be as fast as possible to avoid coincidences of

uncorrelated photons and pileup of consecutive pulses and to reduce the dead time of the system.

Table 1.2. physical properties of inorganic scintillator most used in PET (Bailey *et al.*, 2004).

	NaI	**BGO**	**LSO**	**GSO**
Composition	NaI:Tl	$Bi_4Ge_3O_{12}$	Lu_2SiO_5:Ce	Gd_2SiO_5:Ce
Density (g/cm^3)	6.67	7.13	7.40	6.71
Effective atomic number	51	74	66	59
Attenuación coefficient (cm^{-1})	0.34	0.92	0.87	0.62
Refractive index	1.85	2.15	1.82	1.85
Light yield [%NaI:Tl]	100	15	75	41
Wavelength for max. emission (nm)	410	480	420	430
Decay constant (ns)	230	300	40	56
Hygroscopic	Yes	No	No	No

PET systems not only need a detector with high efficiency but also the best possible spatial resolution. For that purpose, most systems use segmented scintillators that try to minimize the uncertainty in the location of the interaction. Current high resolution PET scanners employ arrays of pixelated scintillator crystals (Casey and Nutt, 1986). Scanners with blocks made of continuous crystal are less frequently used for high resolution scanners (Joung *et al.*, 2001).

1.3.2. Photosensors

A typical scintillation detector consists of a scintillating crystal coupled to a photomultiplier tube (PMT) all housed in a metallic shield. Photomultipliers are constructed from glass vacuum tubes which house a photocathode, several dynodes, and an anode. Incident photons strike the photocathode material which is present as a thin deposit on the entry window of the device, with electrons being produced as a consequence of the photoelectric effect. These electrons are directed by the focusing electrode towards the electron multiplier, where electrons are multiplied by means of secondary emission (Knoll, 2000).

The electron multiplier consists of several electrodes, called dynodes. Each dynode is held at a more positive voltage than the previous one. The electrons leave the photocathode, with the energy of the incoming photon, minus the work function of the photocathode. As they move towards the first dynode they are accelerated by the electric field and arrive with larger energy. After striking the first dynode, more low energy electrons are emitted and these, in turn, are accelerated toward the second dynode. The geometry of the dynode chain is such that a cascade occurs with an ever-increasing number of electrons being produced at each stage. Finally the electrons reach the anode where the accumulation of charge results in a sharp current pulse indicating the arrival of a photon at the photocathode. The PMT will give an electric pulse proportional to the number of scintillation light quanta that reaches the photocathode which is proportional to the energy deposited. Thus, energy spectroscopy is possible with scintillation detectors and PMTs. The gain is defined as the total number of electrons that arrive to the anode for the production of a single electron in the photocathode. Gains from 10^5 to 10^8 can be reached with these devices.

Photomultiplier tubes typically require a power voltage of 1000 to 2000 volts for proper operation. The most negative pole is connected to the cathode, and the most positive pole is connected to the anode. Voltages are distributed to the dynodes by a resistive voltage divider. The divider design influences aspects such as frequency response and rise time, and therefore may be critical to certain applications. While powered, photomultipliers must be shielded from ambient light to prevent their destruction through over excitation.

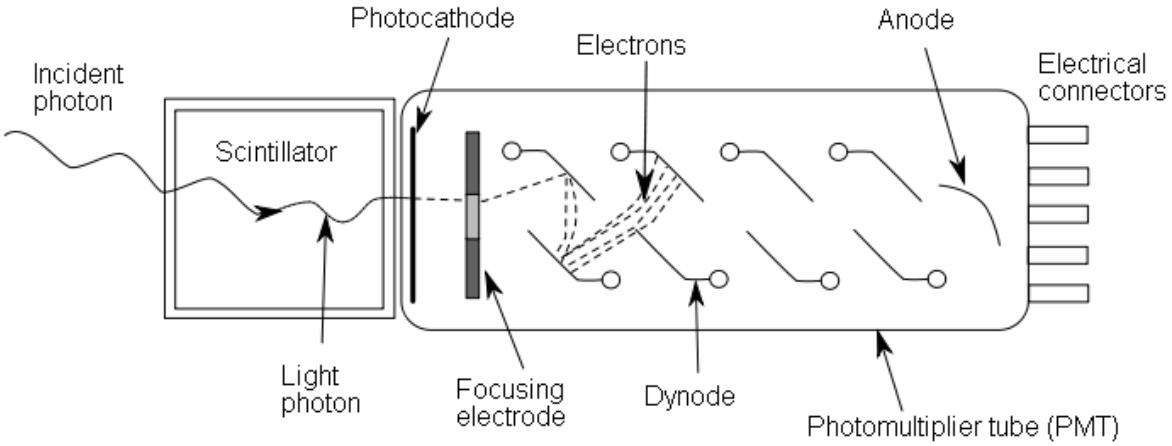

Figure 1.7. Principle of operation of a photomultiplier tube (PMT) (Knoll, 2000).

As mentioned before, spatial resolution is an important parameter in PET. Scintillation arrays are usually coupled to a single photomultiplier that must be able of localize the point where the light has entered the device. For this purpose, position sensitive photomultiplier (PS-PMT) were developed. These devices have an array of anodes where the collected charge is distributed. The distribution of charged among different anodes can be used to calculate the incident light position (Anger, 1969). Other devices as APDs (Pichler *et al.*, 1998), PIN-DIODES or more recently SiPMs are also being used (Otte *et al.*, 2005; España *et al.*, 2008).

1.3.3. Electronics

Pulse processing

In order to measure time intervals precisely, the arrival times of different events must be exactly derived to achieve optimal time resolution. To obtain good timing signals, Constant Fraction Discriminator (CFD) are employed. The output pulse coming from the anode of the PMT, is fed to the input of the CFD. In Figure 1.8 the principle of operation of a CFD is illustrated (Knoll, 2000).

The CFD is designed to trigger on a certain optimum fraction of the pulse height, thus making the performance (labeling of the onset of the pulse) of the CFD independent of pulse amplitude[1]. Furthermore, leading-edge discriminators are employed to provide energy selection. Events not with energy below the threshold will give rise to a signal from the CFD and thus will be excluded.

[1] Assuming all pulses have the same shape. Noise and baseline shifts can prevent this.

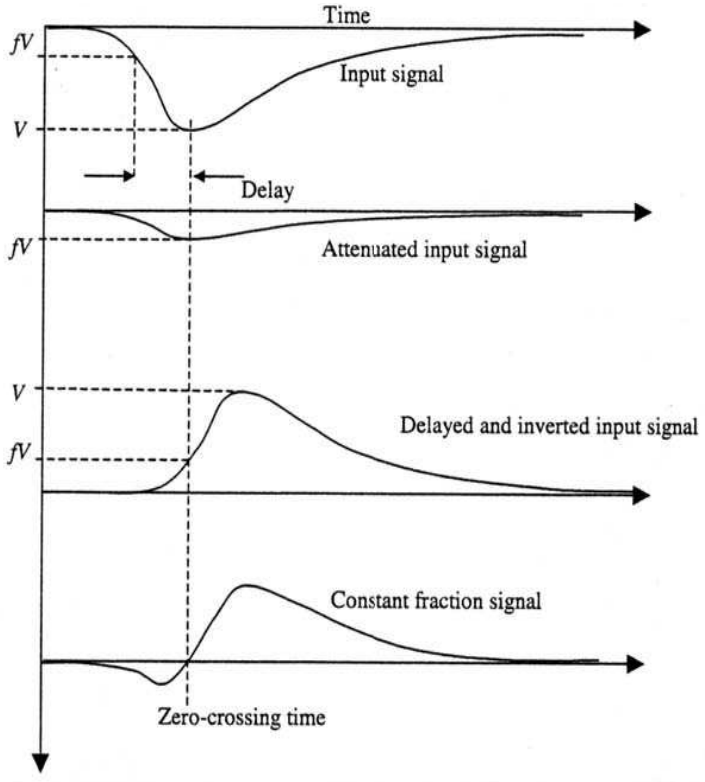

Figure 1.8. The formation of the constant-fraction signal.

The events triggered in a detector are fed into coincidence units that test whether each event is close enough in time to other events from other detectors, so that they can be considered as coincidence events. The time of flight taken by the gamma photons from the positron annihilation time to the detector is of the order of hundreds of picoseconds, what is less than the time resolution of most of PET scanners. However, scanners with time-of-flight (TOF) capabilities have been developed (Allemand *et al.*, 1980; Mullani *et al.*, 1981; Moszynski *et al.*, 2006). The time resolution achievable by the scanner is the result of a convolution of the time resolution of each scintillator, PMT and electronics. It is usually of the order of a few nanoseconds (Knoll, 2000).

Data acquisition system

Once pulses have passed all discriminators, the amplitude of the signal, that contains the energy information for the event, must be obtained. All output lines of the PS-PMT that have been triggered are integrated to obtain the total charge for the energy calculation and the location of the interaction. This is usually performed by electronic modules that, first, integrate the charge of each output line and convert the resulting integrated charge into a digital number (ADC conversion) that is transmitted and stored in a PC. The transmission of this information to the PC maybe performed via Ethernet, fireware, USB, PCI-X or other connections (Lewellen *et al.*, 2001).

1.4. Sorting of the data acquired

1.4.1. Look up tables

The measured energy and PMT XY location for each event must be processed in order to obtain energy and crystal identification. The energy is used to select which coincidence

events are accepted, usually when both single events of the coincidence are within a specific energy window. This energy window can vary depending of the purpose of the study, but it surely includes the 511 keV photopeak. Due to non-uniform gain in the photomultipliers, each crystal element must be individually calibrated in energy (Cherry *et al.*, 2003). In order to perform these energy calibrations, an energy spectrum must be acquired with a source phantom that irradiates all LORs as evenly as possible. This source must contain at least one distinguishable gamma emission with energy in the range 100 keV to 700 keV. Using gamma emissions with two different gamma energies makes it possible to establish a (most often linear) dependence of the integrated charge on the deposited energy. A simplified version of this method would employ only the 511 keV peak and assume that the zero channel of the ADC corresponds to zero energy of the gamma.

Crystal identification must be achieved from existing information. A similar acquisition to the one done during energy calibration is used, where the XY locations extracted from the PS-PMT signals are histogramed into a flood field image (Figure 1.9) (Cherry *et al.*, 2003). This image is then segmented by an algorithm that builds a correspondence between each region of the image and each crystal element.

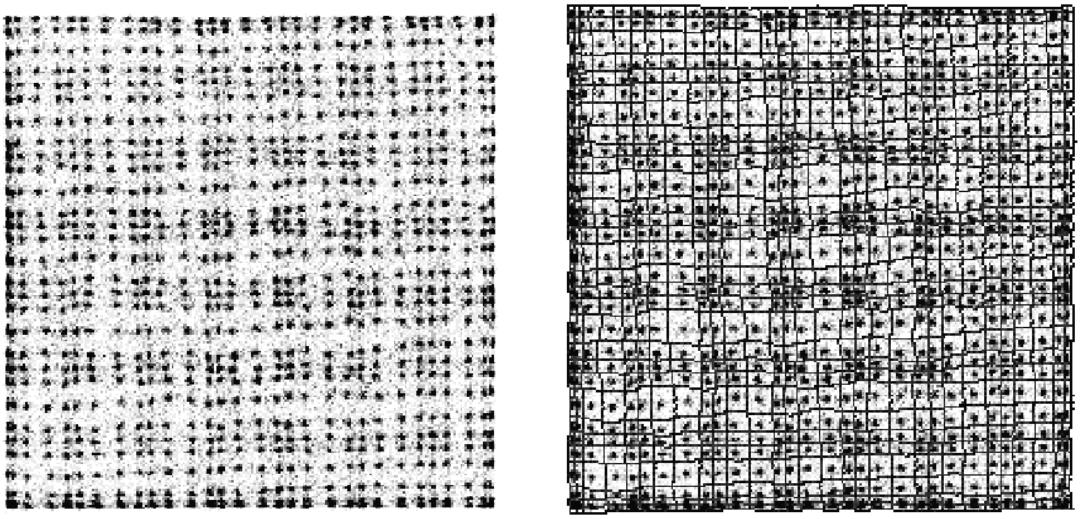

Figure 1.9. Flood field image of a crystal array coupled to a photomultiplier (left) and its look up table for pixel identification. Hamamatsu H8500 (8 × 8 anodes) coupled to a 30 × 30 MLS crystal matrix with 1.5 mm of pixel size (Vaquero *et al.*, 2005).

1.4.2. Data organization

List mode

One way to store the measured coincidence events for further processing is to write the information from prompt events in order of occurrence in the acquisition system. An event packet would include crystal number, energy, positioning, etc. In addition, gantry information (e.g. count rate and time information) as well as external data (e.g. gating and patient motion information) can be inserted into the list mode stream in the form of tag words (Byme, 2001; Parra and Barrett, 1998).

The event packets stored are processed afterwards and eventually transformed into sinogram data sets or LOR histograms (Kadrmas, 2004), while the timing information is analyzed so that the data set can be split into different time frames.

Projections and sinograms

A projection represents a set of parallel LORs at a specific angle ϕ (Bailey *et al.*, 2004)

$$p(s,\phi) = \int_{-\infty}^{\infty} f(x,y)dy_r \qquad (1.16)$$

where *f(x,y)* is a two-dimensional representation of the activity distribution, *s* is the radial coordinate, and y_r is the transversal direction coordinate.

The projections from all angles can be arranged in a matrix. Because a point source will be represented by a sine curve in this matrix representation (see Figure 1.10), said matrix is called a sinogram (Bailey *et al.*, 2004; Bendriem and Townsend, 1998). Sinograms are the basis of most of the image reconstruction schemes (Bendriem and Townsend, 1998).

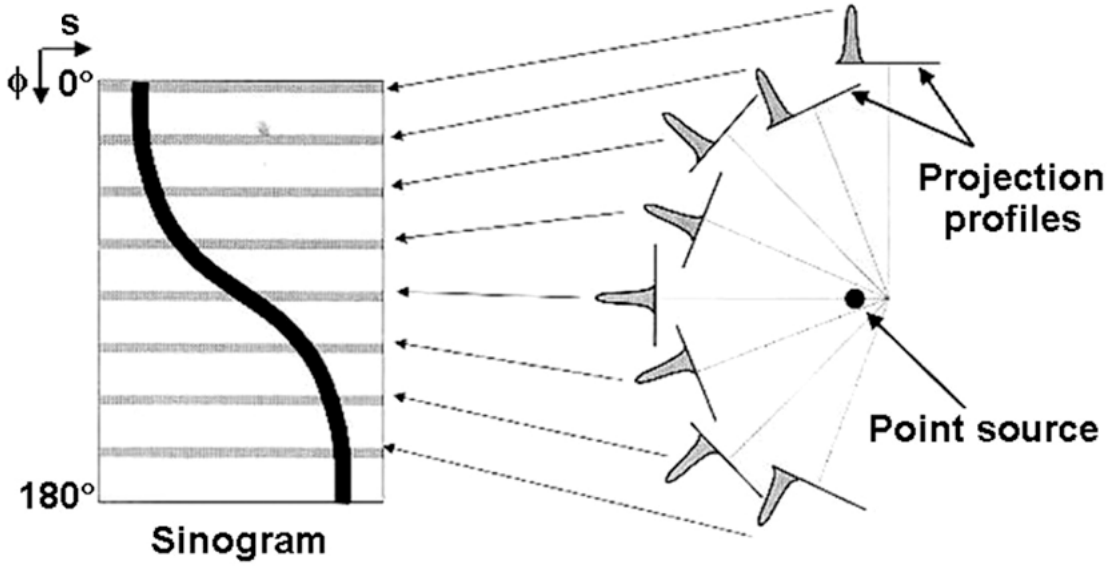

Figure 1.10. The projections of a point source at different angles (left) are represented with a sine curve in a sinogram representation the data acquired.

1.5. Corrections

Quantitative measurements and images free from artifacts require corrections to the acquired data before, during, and after reconstruction. This section introduces some of the corrections that are applied to PET acquisitions.

1.5.1. Decay

During multi-frame studies, tracer activity decreases due to radioactive decay of the radionuclide. Usually tracer activity is expressed at the time of injection of radiotracer to the patient with the following formula

$$A_0 = A_i D_i \qquad (1.17)$$

where A_i is the mean tracer activity during frame *I* and D_i is the decay correction factor

$$D_i = \frac{\Delta t_i \lambda e^{\lambda t_i}}{1 - e^{-\lambda \Delta t_i}} \tag{1.18}$$

with Δt_i the duration of the frame that was started at time t_i. D_i can be derived from the following considerations:

The number (N) of counts measured during the acquisition time Δt_i is

$$N = \int_{t_i}^{t_i + \Delta t_i} A(t) = \int_{t_i}^{t_i + \Delta t_i} A_0 e^{-\lambda t} = \frac{A_0}{\lambda} e^{-\lambda t_i} \left(1 - e^{-\lambda \Delta t_i}\right) \tag{1.19}$$

The initial activity A_0 can be calculated using this and

$$A_0 = \frac{N \lambda e^{\lambda t_i}}{1 - e^{-\lambda \Delta t_i}} \tag{1.20}$$

what yields equations (1.17) and (1.18) if $N = A_i \Delta t_i$ is used (Bailey *et al.*, 2004).

1.5.2. Attenuation

Attenuation correction is an important correction, required for quantitative PET. Annihilation photons in positron emission tomography (PET) are subject to attenuation as they travel through the imaged object. This effect reduces the number of photons detected in each line of response. If the material properties of the object are known, the measurement along each line of response can be corrected for this attenuation effect (Huang *et al.*, 1979). A coincidence event requires the simultaneous detection of both photons coming from the annihilation of a positron. If either photon is absorbed within the body or scattered out of the field of view, a coincidence will not occur. The probability of detection, therefore, depends on the combined path of both photons. Since the total path length is the same for all sources lying on the line that joins two detectors, the probability of attenuation is the same for all such sources, independently on source position.

The attenuation probability depends exponentially on the attenuation coefficient (μ) of the crossed material and the length travelled inside it. As both annihilation photons travel in the same direction, the total length is always the same. Thus, if the length travelled by one photon is x and the total length is D, the number of non attenuated coincidences is given by (Bailey *et al.*, 2004):

$$N = N_0 e^{-\mu x} e^{-\mu (D - x)} = N_0 e^{-\mu D} \tag{1.21}$$

This is true even if the source is positioned outside the body. In this case, the probability terms are e^0 and $e^{-\mu D}$ for the near and far detectors respectively (where D is the total thickness of the body), and the number of non attenuated coincidences is:

$$N = N_0 e^0 e^{-\mu D} = N_0 e^{-\mu D} \tag{1.22}$$

which is the same as it would be obtained from an internal source. Therefore, the problem of correcting for photon attenuation in the body is equivalent to the determination of the probability of attenuation for all sources lying along every line of response (Bailey *et al.*, 2004). The probability of attenuation for each line of response can be determined by comparing the count rate from an external (transmission) source with the unattenuated count rate from the same source when the patientis not in the tomograph. With the advent of dual

modality scanners capable of acquiring PET and CT data during the same imaging session, there has been considerable effort put into the development of methods to employ CT data for PET attenuation correction. When low statistic transmission scans are employed for attenuation correction, the segmentation into a small number of attenuation coefficient classes is frequently applied in order to reduce noise in the calculated attenuation coefficients (Papenfuss *et al.*, 2000).

1.5.3. Scatter

When a positron annihilates in the body, there is a reasonable chance that one or both of the annihilation photons will scatter in the body or in the detector itself. At the energy of annihilation photons (511 keV), the most likely type of interaction is Compton scattering. Since the coincidence LOR formed after one or both photons undergo Compton scattering is no longer collinear with the annihilation point, such events degrade the quality of PET image. Indeed, except for high energy resolution detectors (CZT, HPGe, Si(Li), BrLa(Ce)) (Vaska *et al.*, 2005; Cooper *et al.*, 2007), scattered coincidences are not easily discriminated from unscattered ones, solely based on their energy, and thus may significantly degrade both image quality (due to loss of contrast) and quantitative accuracy(Wirth, 1989). The proportion of accepted coincidences which have undergone Compton scattering prior to detection, is named as the *scatter fraction* and its magnitude depends on several factors, including size and density of the scattering medium, the geometry of the PET scanner and the width of the energy acceptance window. There are several characteristics of scattered coincidences which can be exploited to estimate their distribution (and potentially correct for it) in the measured data (Bailey *et al.*, 2004):

- LORs recorded outside object boundaries can only be explained by scatter in the object, assuming that random coincidences (see next subsection) have been subtracted.
- The distribution of scatter counts is very smooth, i.e., it contains mainly low spatial frequencies.
- The region of the coincidence energy spectrum below the photopeak has a large contribution from scattered events.
- Scattered coincidences that fall within the photopeak window are mainly due to photons that have scattered only once.

These various characteristics have given rise to a wide variety of approaches for estimating and correcting scattered coincidences in PET data (Bailey and Meikle, 1994; Levin *et al.*, 1995; Cherry *et al.*, 1993).

1.5.4. Random coincidences

Random coincidences arise when two unrelated photons are detected in opposing detectors, close enough in time to be accepted by the time-window criteria that the system employs to identify coincidences. Such events will be considered by the system as a coincidence event, in spite of whether or not they come from the same annihilation event. Random coincidences add uncorrelated background counts to PET images and hence decrease image contrast, if no correcting measures are taken (Bailey *et al.*, 2004).

The number of random coincidences detected can be reduced by choosing the scanner geometry so that the field of view (FOV) for single events is reduced (Badawi *et al.*, 2000) or

by reducing the time coincidence window of the system. The noise introduced by random coincidences can also be reduced by estimating their number of random counts on each LOR and taking this estimation into account in the reconstruction. The number of random coincidences on a particular LOR can be estimated in different ways (Cooke *et al.*, 1984). For instance, the rate of random coincidences R_{ij} on an LOR joining two detectors i and j is

$$R_{ij} = 2\tau r_i r_j \tag{1.23}$$

where r_i and r_j are the uncorrelated singles rates on detectors i and j respectively (Oliver and Rafecas, 2008), and τ is the time coincidence window of the system (Knoll, 2000). When the single rate is measured, all correlated and uncorrelated events will be detected. Thus, correlated single events, those that produce true coincidence events, must be substracted from the total singles rate in order to achieve a more accurate estimation of random coincidences.

Another way of estimating random coincidences employs a delayed coincidence channel. In this scheme, timing signals from one detector are delayed by a time significantly greater than the time coincidence window. In this way, all detected coincidences will be uncorrelated and the number of coincidences found will be a good estimate of the number of random coincidences in the prompt signal. This resulting estimate is then subtracted from the number of prompt coincidences to yield the combined number of true and scattered coincidences (Knoll, 2000). The advantage of this method is that the delayed channel has identical dead-time properties to the prompt channel. The disadvantage is that the statistical quality of the random coincidences estimate is poorer, as R_{ij}, r_i and r_j are subject to Poisson statistics and R_{ij} may be a significantly smaller quantity than either r_i or r_j (Casey and Hoffman, 1986).

1.5.5. Normalization

LORs in PET datasets have different sensitivity due to variations in detector efficiency, solid angle subtended, etc (Bailey *et al.*, 2004). Information on these variations is required for the reconstruction of quantitative, artifact-free images. Indeed, most algorithms require that these variations are removed prior to reconstruction. The process of correcting for these effects is usually known as *normalization* (Hoffman *et al.*, 1989; Badawi and Marsden, 1999a).

In a block detector system, detector elements vary in efficiency because of position of the element in the block, physical variations in the crystal and light guides and variations in the gains of the photomultiplier tubes or corresponding detector elements. Other causes of differenced sensitivity are the energy window selected for each crystal element and the time window alignment (Bailey *et al.*, 2004).

Accurate normalization is essential for good quantitation in PET. Traditional solutions to the normalization problem include direct and component-based methods. With indirect methods, a known source of activity is scanned, then the normalization factors are estimated as the ratio between the known ideal number of coincidences and those actually measured (Defrise, 1991). The main problem with this method is that it requires the accumulation of a very large number of counts in order to achieve acceptable statistical accuracy for each LOR. Component-based methods divide the normalization factors into detector efficiency and spatial distortion correction, intrinsic detector efficiency, geometric factors, crystal interference, dead time factors, etc (Badawi and Marsden, 1999a).

1.5.6. Dead-time

PET scanners may be regarded as a series of subsystems, each of which requires a minimum amount of time to elapse between successive events, for them to be registered as separated. Since radioactive decay is a random process, there is always a finite probability that successive events will occur within any minimum time interval, and at high count-rates, the fraction of events falling in this category can become very significant. The main effect of this phenomenon is a loss of the linear relationship between the number of coincidence events registered by the PET scanner and the total activity inside the FOV. The parameter that characterizes the counting behavior of the system at high event rates is known as *dead time* (Knoll, 2000). The fractional *dead time* of a system at a given count-rate is defined as the ratio of the measured count-rate and the count-rate that would have been obtained if the system behaved in a linear manner (Casey *et al.*, 1995).

One source of dead time is the integration time, that is, the time spent integrating the charge from the photomultiplier tubes (or corresponding devices) arising from a scintillation flash in the detector crystal. Other sources of dead time are the time needed for analog to digital conversion and the data transmission speed (Bailey *et al.*, 2004).

To measure the dead time behavior in a PET scanner as a function of count-rate, a decaying source experiment may be performed (Germano and Hoffman, 1988). A uniform source containing a known quantity of a short-lived positron emitter is placed in the field of view of the PET scanner. Repeated measurements of the singles, prompt and random coincidence rates are then made as the activity in the field of view decays. The incident count rate for a given level of activity in the field of view is obtained by linear extrapolation from the count-rate response measured when most of the activity has decayed away and dead time effects are small. The ratio between the incident and measured count-rate then gives the fractional count-rate losses.

Dead time correction schemes are usually constructed measuring the live time (1– fractional dead time) for each subsystem. If this is not possible, an analytic model incorporating knowledge of the system architecture is constructed, and fitted to data from decaying source experiments. The decay correction scheme then consists of applying a serie of measured and modeled correction factors to the data acquired. The live time in a sub-system may be measured in several ways. One possibility is to implementing a second circuit parallel to the measurement circuit for which the live time estimate needs to be made. Regular pulses are sent down from the second circuit to a counter (Daube-Witherspoon and Carson, 1991).

Dead time models usually treat system dead time as being separable into two components, described as paralyzable and non-paralyzable (Knoll, 2000). The paralyzable component describes the situation where the system is unable to process events for a fixed amount of time τ after each event. If an event arrives while the system is busy due to a preceding event, the system remains dead for a further τ seconds from the time of arrival of the second event. The relationship between the measured event rate m, the actual event rate n, and the dead time resulting from a single event is given by:

$$m = ne^{-n\tau} \tag{1.24}$$

In the non-paralyzable case, the system is again rendered dead for a time τ after each event, but while the system is dead, further events have no effect. For such systems, the

measured count rate tends asymptotically to a limiting value of τ^{-1} as the actual count-rate increases, and the relationship between m, n and τ is given by (Knoll, 2000)

$$m = \frac{n}{1 - n\tau} \tag{1.25}$$

1.5.7. Pile up

Pulse pile up occurs when a photon deposits energy in the detector crystal while the signal from the previous event is still being integrated. Pile up events cause two types of errors in PET data. The first one occurs when the pile up event provides a large enough signal to fall outside the energy window and the event is lost. Under this situation, deadtime corrections will be required for quantitative measurement. The second error is interaction misspositioning. In detection systems, which employ a 2-D matrix of crystals and analog logic to identify the crystal of interaction, the scintillation photons from all crystals are processed as a single event, and for pile up events the apparent location of the interaction results from an average of the crystals that absorbed radiation. If these events are not rejected, they will cause misspositioning of valid coincidence events. This will cause loss of resolution and contrast in the image, and cause a transfer of counts between image planes, leading to loss of counts in the originating plane and additional background events in the destination plane (Germano and Hoffman, 1990; Badawi and Marsden, 1999b) (see Figure 1.11).

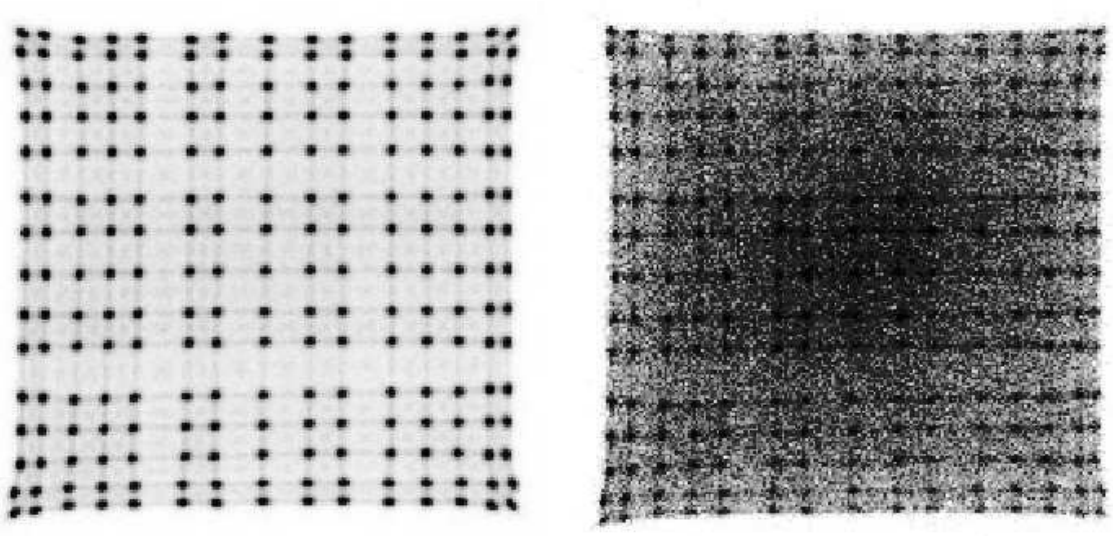

Figure 1.11. Simulated flood histogram for a Hamamatsu 8520-C12 coupled to an array of 15 × 15 LYSO crystals with (right, activity = 1mCi) and without (left, activity = 10 μCi) pile-up events. Pile-up produces misspositioned of detected photons.

1.6. Performance evaluation

1.6.1. Energy resolution

Energy resolution measures the precision with which the system can determine the energy deposited by incident photons. For a source of 511 keV photons, an ideal system would show a well-defined peak for 511 keV. Energy resolution is usually measured by histograming the energy of the events acquired and plotting the number of events versus the energy measured. In scintillation detectors energy resolution is a function of the relative light output of the scintillator, as well as its intrinsic energy resolution. The intrinsic energy

resolution accounts for non-statistical effects that arise in the energy measurement process. Good energy resolution is necessary for a PET detector in order to achieve good image contrast and to reduce background counts (Levin *et al.*, 2006).

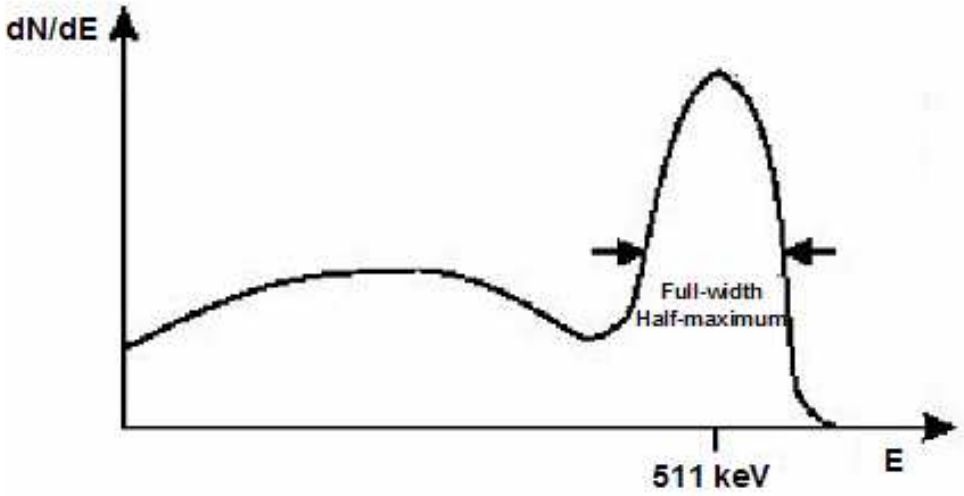

Figure 1.12. Energy spectrum of 511 keV gamma rays. Energy resolution is measured as the full width at half maximum of the photopeak.

1.6.2. Timing resolution

The timing resolution of a PET detector describes the uncertainty in the time determination of the arrival of the photon as measured by the detection chain, on an event-by-event basis, due to statistical fluctuations. Obtaining good timing resolution of a PET detector is a challenging goal because it involves detection of correlated photons that will arrive to detectors with time differences of a few hundreds of picoseconds. Since timing resolution represents the variability in the arrival times for different events, it needs to be properly accounted for when detecting coincident events. The size of the coincidence time window should be chosen taking into account the timing resolution of the system. Since random coincidences are proportional to the coincidence timing window, a narrow window helps reducing their occurrence. Hence, for PET imaging, fast scintillator with good timing resolutions are desirable in order to reduce the fraction of random coincidences.

1.6.3. Spatial resolution

Spatial resolution can be presented as the minimum distance between two point sources that allows them to be disentangled (Bailey *et al.*, 2004). Spatial resolution is usually determined measuring the width of the profile obtained when an object much smaller than the expected resolution of the system is imaged. A common method consists in imaging a point source and measuring the point spread function (PSF). Usually, the resolution is expressed as the full width at half maximum (FWHM) of the profile. A good approximation often employed for this profile is a Gaussian function (Bailey *et al.*, 2004).

There are many factors that influence resolution:

- Non-zero positron range after radionuclide decay.
- Non-collinearity of the annihilation photons due to the residual momentum of the positron.

- Distance between detectors.
- Width of detectors.
- Stopping power of the scintillator.
- Incident angle of the photon at the detector.
- Depth of the interaction of the photon.
- Number of angular samples.
- Reconstruction parameters (matrix size, reconstruction filter, ...).

Usually, the resolution along several directions across the FOV of the PET scanner is given, such as transaxial and axial resolution, as sampling is not necessarily equal in all these directions. Generally, ring-PET systems are over-sampled transaxially, while axial sampling is just enough to realize the intrinsic resolution of the detectors. Transaxial resolution is often measured for both radial and tangential directions at different distances off the central axis of the camera, as it varying in ring geometries due to differential detector penetration at different locations in the x-y plane (Bailey *et al.*, 2004).

1.6.4. Sensitivity

The sensitivity of PET scanners represents the ability of detecting coincident photons emitted from inside the FOV of the scanner. It is mainly determined by two parameters of the scanner: geometry and stopping efficiency of the detectors for 511 keV photons. The scanner geometry defines the fraction of the total solid angle covered. Small-diameter and large axial FOV geometries, typically lead to high-sensitivity scanners. The stopping efficiency of a PET detector is related to the type of detector being used. Usually, scintillation detectors provide high stopping power for PET imaging with acceptable energy resolution. The stopping power of the scintillation detector is dependent upon the density and Z_{eff} of the crystal used. A high stopping power, which allows for shorter crystals, is also desirable for the reduction of parallax error in the images acquired (Bailey *et al.*, 2004).

1.6.5. Scatter fraction

Scatter fraction is defined as the fraction of the total coincidences recorded in the energy window which have suffered scatter, in either one or two events of the coincidence pairs of valid coincidences (Bailey *et al.*, 2004). Scattered events decrease image contrast in PET by misplacing events, and cause errors in the reconstructed radioactivity distribution. The scatter fraction (SF) is also a critical component of the noise equivalent count rate (NECR) calculation (see next subsection), widely used as a golden measure to optimize acquisition parameters such as timing and energy windows, and for making comparisons among different clinical (NEMA, 2001) or preclinical (NEMA, 2008) scanners. Scatter can arise from three major sources: scatter inside the object, scatter at detector elements, and scatter from the gantry and surrounding environment. In human imaging, object scatter generally dominates (Cherry *et al.*, 2003). Standards have been developed for measuring the SF in clinical PET scanners (NEMA, 2001), and these methods are quite robust across a wide range of scanners and imaging parameters.

1.6.6. Count rate performance. NEC

Count rate performance refers to how many events the system can actually process in a given time. It is related to the time that the system needs to process a photon. After a photon is detected in the crystal, a series of optical and electronic steps take place, each of which requires a finite amount of time. As these combine in series, a slow component in the chain can introduce a significant delay. The determination of count rate losses for PET systems is employed to compare performance among different scanners (NEMA, 2001; NEMA, 2008). The method employed in PET for count rate and dead time determinations is the use of a source of a relatively short-lived tracer in a multi-frame dynamic acquisition protocol. Then, a number of data frames are recorded with short duration, over a number of half-lives of the source. Often, a cylinder containing a solution of ^{18}F in water is used. From this data, count rates are determined for true, random, and scatter components (Bailey *et al.*, 2004).

The purpose of estimating count rate performance is the desire to assess the impact on image quality of increasing the count rate. The noise equivalent count (NEC) rate (Strother *et al.*, 1990) provides a indicator of count rate performance of tomographs, or of the same scanner operating under different conditions (e.g., 2D and 3D acquisition modes). The noise equivalent count rate is the count rate which would have resulted in the same signal-to-noise ratio in the absence of scatter and random events. It is always less than the observed count rate. Indeed, the noise equivalent count rate is defined as (Bailey *et al.*, 2004)

$$NECR = \frac{\left[T_{total}\left(\frac{T}{S+T}\right)\right]^2}{\left(T_{total} + 2fR\right)} \tag{1.26}$$

where T_{total} is the observed count rate (including scattered events), T and S are the unscattered and scattered event rates respectively, f is the random field fraction that is, the ratio of the source diameter to the tomograph transaxial field-of-view, and R is the random coincidence event rate. Some caution is required when comparing NEC results from various systems, namely which scatter fraction was used and how it was determined, how the randoms fraction (R) was determined and how random subtraction was applied. However, NEC curves permit comparisons of count rate, and therefore are often employed to compare image quality among systems (Bailey *et al.*, 1991).

1.6.7. Partial volume effect. Recovery coefficients

In quantitative PET, the reconstructed image should map the radiotracer concentration with uniform accuracy and precision, throughout the field of view. However, due to partial volume effects (Hoffman, 1979), the bias in reconstructed pixel values may vary depending on the size of the structure being sampled and its radioactive concentration, relative to surrounding structures. The sensitive volume has dimensions approximately equal to twice the FWHM resolution of the reconstructed image. There are several approaches to correct or to minimize these partial volume effects. These include methods that attempt to recover resolution before or during image reconstruction and methods that use side information from anatomical imaging modalities such as CT and MRI (Rousset *et al.*, 1998).

Recovery coefficients (RC) are defined as the ratio of observed to true activity in a (PET) image. RC are usually measured for sources of different sizes and represents useful tool to relate measured and true activity (Bailey *et al.*, 2004).

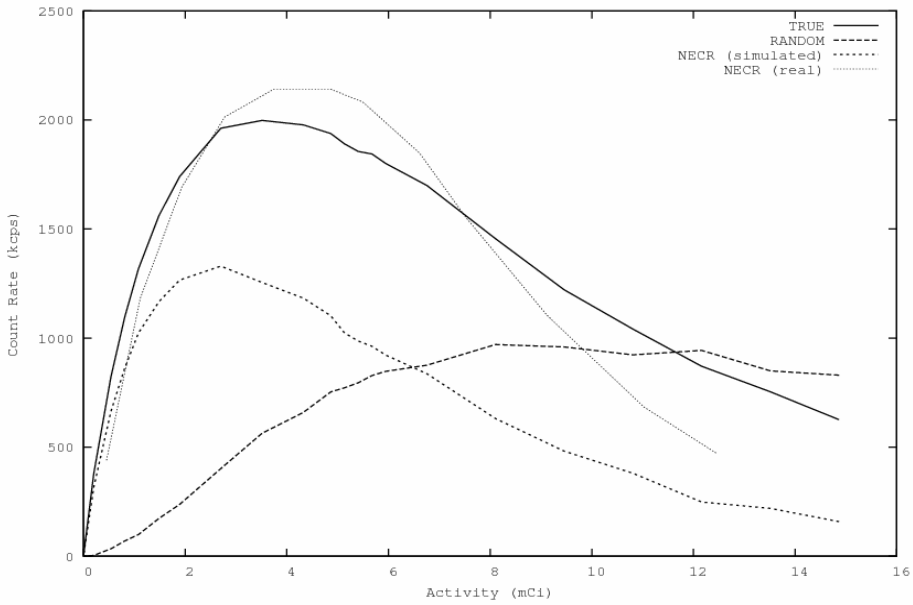

Figure 1.13. NEC rate simulated with PeneloPET (España *et al.*, 2006) for a mouse size phantom acquired in a Siemens Inveon (Kemp *et al.*, 2006) scanner, with an energy window from 350 to 650 keV. True and random components are also shown in the figure. As the random rate increases, the NECR reaches a maximum value and then starts decreasing.

1.7. The state of the art in small animal PET

Small animal PET scanners have been developed to perform imaging of small anatomical structures in laboratory animals. The dimensions of organs such as the brain in mice and rats are, respectively, nearly 8 times and 14 times smaller than in human subjects. The need to achieve much higher resolution and, at the same time, good sensitivity is a hard task (Green *et al.*, 2001; Myers and Hume, 2002; Chatziioannou, 2002b). In terms of design, the reduced size of scanners offers some advantages. It is known that the maximum spatial resolution is limited in PET by the non-collinearity of the two annihilation photons, besides positron range. Reducing the distance between detectors implies that the effect in the system resolution of non-collinearity of the photons can be reduced. Other advantages are raw material savings due to the smaller size of the system.

The detection systems in PET have mostly been developed using scintillator materials (Melcher, 2000; van Eijk, 2002; Humm *et al.*, 2003; Nutt, 2002; Zanzonico, 2004; Townsend, 2004). Inorganic crystals such as BGO, LSO (Ce) and GSO (Ce) have been employed in the construction of human scanners, and then used for small animal PET scanners (Lewis *et al.*, 2002; Chatziioannou, 2002a; Schafers, 2003). In order to achieve a high spatial resolution in scintillator based small animal PET scanner, the size of the scintillator crystals must be reduced compared to human tomographs. As a consequence, the solid angle covered by a single (small area) crystal and detector element is smaller than in human scanners.

Considerable effort has been put into the coupling scheme between scintillator and photomultiplier tubes, in order to optimize light collection and/or to simplify the design and maintenance of a PET detection system (Larobina *et al.*, 2006). Block detector (Nutt, 2002) represent a breakthrough that makes it possible the development of modular structures to detector rings reducing the number of photomultiplier tubes required. This technique is still in use. More recently, optical fiber coupling has been proposed to give more flexibility to the

design of scintillator arrays, with high packing fraction (Cherry *et al.*, 1996). Continuous light-guide backed to an array of photomultipliers, is another effective coupling scheme to improve light collection for large area continuous pixelated detectors (Surti *et al.*, 2000). Avalanche photodiodes (the solid state version of photomultiplier tubes) for the read-out of scintillation crystals has also been investigated (Surti *et al.*, 2000; Ziegler *et al.*, 2001), although these are only implemented in very few commercial PET scanners. Researchers are now exploring innovative solutions regarding both hardware (detector material, detector configuration and detector read-out) and software (3D reconstruction algorithms), to build systems with improved performance characteristics (Larobina *et al.*, 2006). For example, SiPMs (Otte *et al.*, 2005) are promising devices for the readout of scintillator detector in next generation of PET scanners.

High spatial resolution and sensitivity are important goals in positron emission tomography (PET), especially for small animal imaging applications. With the increased use of (translational research) mouse models in biology, there are many examples where the ability to visualize and accurately measure radiopharmaceutical accumulation, in structures that have dimensions of a millimeter or less in size, is important (Larobina *et al.*, 2006). Obvious examples include early detection and evaluation of metastasis disease in mouse models of human cancer, and the study of cell dynamics in relation to the immune system and novel stem cell therapies. Achieving these goals requires the highest possible spatial resolution and sensitivity. While other considerations, such as tracer specific activity and concentration of biologic target within the animal are also critical in determining whether a specific signal is measurable by PET, the range of applications for which small animal PET is suitable will clearly be dictated, to a large extent, by the resolution/sensitivity trade off of the imaging system.

The sensitivity of most current small animal PET scanners is in the range of 0.5–10% (Lage *et al.*, 2008; Wang *et al.*, 2006; Visser *et al.*, 2009). This indicates that a large number of decays do not lead to recorded events. There are two major ways in which events are lost. First, one or two of the 511 keV photons may not intersect the detector system. This can be fixed by designing PET systems with large solid angle coverage. Current animal PET scanners have an average solid angle coverage of less than 20%. Second, if a photon intersects a detector, it may not interact in the detector. To improve on this, detectors with larger intrinsic efficiencies will be required. Typical efficiencies are in the range of 20–70%, and of course depend on the detector material and thickness.

The path towards much higher sensitivity, small animal PET systems, without increasing cost, requires the design of high-efficiency (>60%) detectors with adequate depth of interaction capability. These detectors can be brought in close to the animal, reducing the detector area required per unit of solid angle coverage. This approach should yield system sensitivities in the range of 10–20% (Larobina *et al.*, 2006).

The other major issue of animal PET design is spatial resolution. The intrinsic spatial resolution of PET detectors is determined by many factors, including positron decay physics, photon interaction physics, and detector material and geometry (Larobina *et al.*, 2006). Current systems are based on scintillators with individual detector elements as small as 0.8 to 1 mm in cross section (Tai *et al.*, 2003). These detectors have reported resolutions ranging from 0.8 to 1.25 mm, which can be directly related to the size of the detector elements, with additional effects due to light production and collection, inter-crystal scatter and electronic multiplexing. More recently, solid state detectors have shown promise as room temperature detectors for nuclear medicine applications (Vaska *et al.*, 2005). Direct detection eliminates

the complications related to scintillation light collection and detectors can also be manufactured with smaller pixels than what is readily achievable in scintillation crystals. To determine whether further significant gains can be made in PET detector resolution, and to identify possible detector configurations that can achieve such gains, it is necessary to understand how much each these factors contributes to the overall resolution of PET detectors. Since these factors cannot be easily isolated to study them experimentally, Monte Carlo simulation and modeling is the most feasible approach for exploring the resolution limits, and for predicting the performance of new detector designs (Braem *et al.*, 2004).

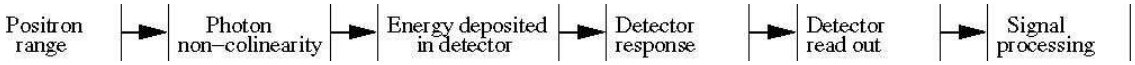

Figure 1.14. Linear system model of sources of resolution degradation in PET (Bailey *et al.*, 2004).

1.7.1. Depth of interaction

For research studies in biomedical sciences, small animal PET scanners must be highly sensitive. Much effort has been devoted to improve the spatial resolution of small animal PET scanners (Kitamura *et al.*, 2004), but the requirement of high sensitivity have not been satisfied. The scanner should contain long crystals in the radial direction and have a larger solid angle to increase its sensitivity; however, parallax error would prevent realizably both conditions simultaneously. Depth of interaction (DOI) detectors are one way of achieving high sensitivity without being affected by parallax (Seidel *et al.*, 1999) errors. Many types of DOI detectors have been proposed: a phoswich-type detector using the difference of scintillation decay time of the materials that form the scintillator layers (Seidel *et al.*, 1999), a multiple layer detector with insertions between crystals producing a shift in a two-dimensional projection of the collected light on the PMT (Murayama *et al.*, 1998), a detector that uses the signal ratio of two photo detectors coupled at both ends of crystal elements (Braem *et al.*, 2004), among many other methods.

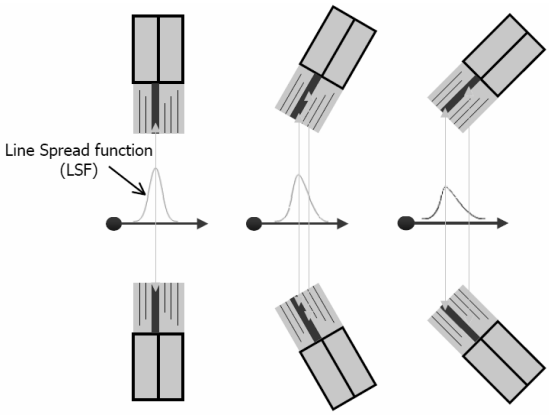

Figure 1.15. This figure shows the line spread function across lines of response with different incident angles.

2. Basics of image reconstruction

2.1. Introduction

The goal of PET image reconstruction is to obtain the most accurate three dimensional map of source distribution, using the information of the data acquired with the scanner. There is a large variety of reconstruction methods that can be used to achieve this. In this chapter, the main features of these methods will be described.

One way of representing the imaging system is by means of the following linear relationship (Bendriem and Townsend, 1998; Herraiz *et al.*, 2006)

$$p = SRM \cdot f + n \qquad (2.1)$$

where p is the set of observations (the data), SRM is the known system model, f is the unknown image, and n is the error present in the observations, or any effects not included in the SRM. The goal of the reconstruction is to find the image f that most adequately reflects the data p, represented as projections through the unknown object.

The standard parameterization of 2D PET data employs sinograms. For a fixed plane, Figure 2.1 defines the variables s and Φ used to parameterize a straight line (LOR) with respect to a Cartesian coordinate system (x, y) in the plane. The radial variable s is the signed distance between the LOR and the center of the coordinate system. The angular variable Φ specifies the orientation of the LOR.

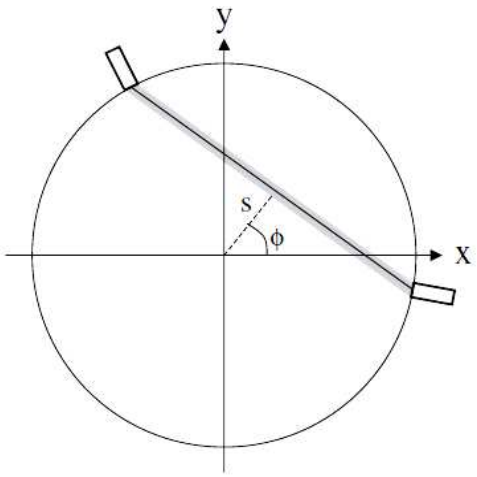

Figure 2.1. Schematic representation of a ring scanner. The tube of response between two detectors is represented in grey containing the corresponding LOR, which connects both detectors. The sinogram variables s and Φ define the location and orientation of the LOR.

The function $p(s,\Phi)$ is referred to as a sinogram and contains the line integrals across the object $f(x, y)$. For a fixed angle $\Phi = \Phi_0$, the set of parallel line integrals $p(s,\Phi_0)$ is a 1D parallel projection of f.

2.2. Analytical methods

The central-section theorem states that the Fourier transform of a one-dimensional projection is equivalent to a section, or profile, at the same angle through the center of the two-dimensional Fourier transform of the object (Kak and Slaney, 1988). Figure 2.2 shows a pictorial description of the central-section theorem, where $\Im_1\{p(s,\phi)\}$ is the one-dimensional

Fourier transform of a projection, $\Im_2\{f(x,y)\}$ is the two-dimensional Fourier transform of the image, and υ_x is the Fourier space conjugate of x. The central-section theorem indicates that if we know $P(\upsilon_s,\phi)$ at all angles, then we can fill in values for $F(\upsilon_x,\upsilon_y)$. The inverse two dimensional Fourier transform of $F(\upsilon_x,\upsilon_y)$ will give $f(x,y)$.

$$P(\upsilon_s,\phi)=\Im_1(p(s,\phi))=\Im_2(f(x,y))\Big|_\phi=F(\upsilon_x,\upsilon_y)\Big|_\phi \tag{2.2}$$

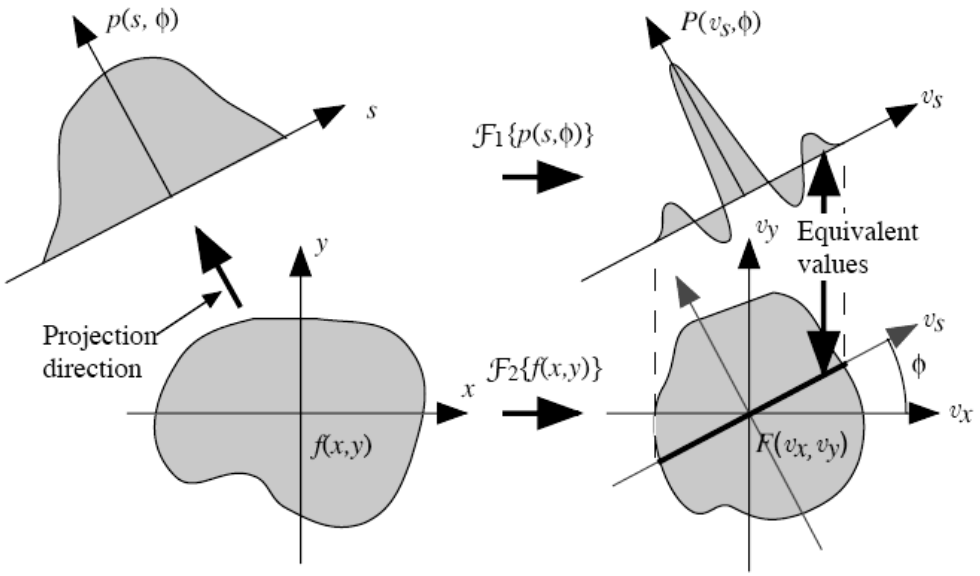

Figure 2.2. Pictorial illustration of the two-dimensional central-section theorem, showing the equivalency between the one-dimensional Fourier transform (top right) of a projection at angle Φ (top left) and the central-section at the same angle (bottom left) through the two-dimensional Fourier transform of the object (bottom right) (Bailey *et al.*, 2004).

Backprojection is the adjoint operation to the forward projection process that yields the projections of the object. Figure 2.3 shows the backprojection along a fixed angle *Φ*. Conceptually, backprojection can be described as placing a value of *p(s,Φ)* back into an image array along the appropriate LOR but, since the knowledge of where the values came from was lost in the projection step, a constant value is placed into all elements along the LOR (Henkin *et al.*, 2006).

One might assume that a simple backprojection of all the collected projections will be enough to return a good image, but this is not the case due to the oversampling in the center of the Fourier space. In other words, each projection fills in one slice of the Fourier space resulting in over sampling in the center and less sampling at the edges.

The over sampling in the center of Fourier space needs to be filtered in order to have equal sampling throughout the Fourier space. Basically, the Fourier transform of the backprojected image must be filtered with a ramp filter $\left(\upsilon=\sqrt{\upsilon_x^2+\upsilon_y^2}\right)$. This cone filter accentuates the values at the edge of the Fourier space and deaccentuates the ones at the center of the Fourier space.

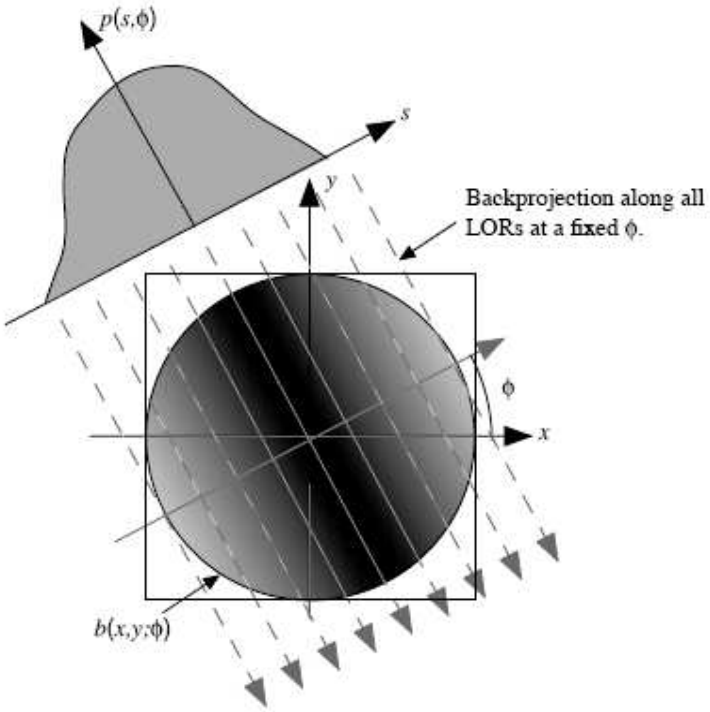

Figure 2.3. Backprojection, *b(x,y,Φ)*, into an image reconstruction array of all values of *p(s,Φ)* for a fixed value of *Φ* (Henkin *et al.*, 2006).

The filtered-backprojection (FBP) reconstruction method is probably the most well known standard method for reconstruction which applies the concept of backprojection and filtering explained before. Within FBP, the general expression employed to calculate the source distribution from projection data is (Herman, 1980):

$$f(x,y)=\int_0^{\pi}\Im_1^{-1}\left\{|\upsilon_s|\Im_1\left\{p(s,\phi)\right\}\right\}d\phi \qquad (2.3)$$

The inverse problem of equation (2.1) is generally considered *ill-posed* in several ways (Bailey *et al.*, 2004). In particular, its solutions are unstable, in the sense that small perturbations of the data (i.e. noise) can lead to unpredictable changes in the estimation of the reconstructed image. As photon detection is a stochastic process, some form of regularization is required to constrain the solution space to physically acceptable values.

The most common form of regularizing the image reconstructed is by means of simple smoothing. Within the FBP algorithm this can be written as:

$$f(x,y)=\int_0^{\pi}\Im_1^{-1}\left\{W(\upsilon_s)|\upsilon_s|\Im_1\left\{p(s,\phi)\right\}\right\}d\phi \qquad (2.4)$$

where $W(\upsilon_s)$ is the smoothing function, that can take any shape that is deemed most advantageous based on the image SNR, or other considerations (Henkin *et al.*, 2006). A very common smoothing function is the Hamming function (see Figure 2.4) (Bendriem and Townsend, 1998).

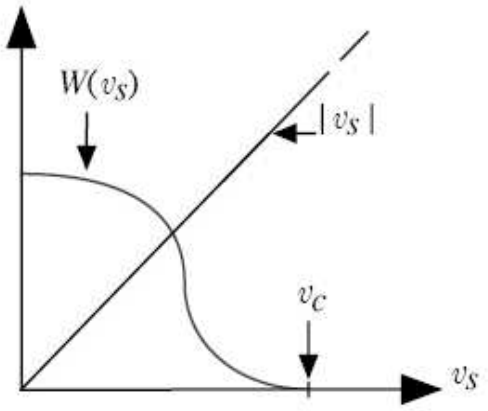

Figure 2.4. Illustration of the use of an apodized ramp filter $W(\upsilon_s)$ to suppress amplification of high-frequency noise above the cut-off frequency (Bendriem and Townsend, 1998).

2.3. Rebinning

Rebinning algorithms allow for the sorting of data from oblique sinograms of a 3D data set into the corresponding planes of a 2D data set. In this way, it is possible to reconstruct a 3D data set with conventional 2D reconstruction schemes, while maintaining the sensitivity of 3D acquisitions. Mainly two approaches are used in clinical routine: single slice rebinning (SSRB) (Daube-Witherspoon and G., 1987) and Fourier rebinning (FORE) (Defrise *et al.*, 1997).

2.3.1. SSRB

This approximate algorithm (Daube-Witherspoon and G., 1987) is based on the assumption that each oblique LOR measured crosses only a single transaxial section within the support of tracer distribution. SSRB defines the rebinned sinograms by (Bailey *et al.*, 2004):

$$p_{ssrb}(s,\phi,z) = \frac{1}{2\theta_{\max}(s,z)} \int_{-\theta_{\max}}^{\theta_{\max}} p_s(s,\phi,\zeta=z,\theta)\, d\theta \qquad (2.5)$$

$$\theta_{\max}(s,z) = \arctan\left(\frac{\min[z, L-z]}{\sqrt{R_d^2 - s^2}}\right) \qquad (2.6)$$

where θ_{max} is the maximum axial aperture for an LOR at a distance s from the axis in slice z, R_d is the scanner radius, and L the number of transaxial sections sampled. The algorithm is exact for tracer distributions which are linear in z. For realistic distributions, the accuracy of the approximation will decrease with increased transaxial FOV radius and with increased θ_{max}. Axial blurring and transaxial distortions, which increase with the distance to the axis of the scanner, are the main drawbacks of the SSRB approximation.

2.3.2. FORE

The approximate Fourier rebinning algorithm (Defrise *et al.*, 1997) is more accurate than the SSRB algorithm and extends the range of 3D PET studies that can be processed using rebinning algorithms. The main characteristic of FORE is that it proceeds via the 2D Fourier

transform of each oblique sinogram. Rebinning is based on the following relation between the Fourier transforms of oblique and direct sinograms (Bailey *et al.*, 2004)

$$P_s(\nu, k, z, 0) \simeq P_s\left(\nu, k, \zeta = z + k\tan\theta/(2\pi\nu), \theta\right) \tag{2.7}$$

where k is the azimuthal Fourier index. The FORE method amplifies slightly the statistical noise, as compared to SSRB, but results in significantly less azimuthal distortion.

2.4. Iterative methods

2.4.1. EM-ML

The most widely applied algorithm for finding the maximum-likelihood (ML) estimation of activity f given the projections p, is the expectation maximization (EM). This was first applied to the emission tomography problem by Shepp and Vardi (Shepp and Vardi, 1982). ML, though, is a general statistical method, formulated to solve many different optimization problems of physics, biology, economy and others. The EM-ML algorithm can be written as (Herraiz *et al.*, 2006)

$$f^{it+1}(V) = f^{it}(V)\frac{\sum_L SRM(L,V)\dfrac{p(L)}{\sum_{V'} SRM(L,V')\, f^{it}(V')}}{\sum_L SRM(L,V)} \tag{2.8}$$

where f is the reconstructed image, p is the data acquired and SRM is the system response matrix. The SRM is a precalculated matrix that contains the probability that one emission occurred at voxel V is detected in a detector element L. The accuracy of this matrix will be extremely important for the quality of the images resulting from the reconstruction method (Mumcuoglu *et al.*, 1996).

Usually, iterative algorithms based on ML statistical models assume that the data being reconstructed retain Poisson statistics (Shepp and Vardi, 1982). However, to preserve the Poisson statistical nature of data, it is necessary to avoid any pre-corrections (Qi *et al.*, 1998) to the data. Corrections for randoms, scatter and other effects should be incorporated into the reconstruction procedure itself, rather than being applied as pre-corrections to the data. At times, sophisticated rebinning strategies are employed to build sinograms into radial and angular sets. This also changes the statistical distribution of the data, which may no longer be Poisson like (Kadrmas, 2004).

A serious disadvantage of the EM procedure is its slow convergence (Lewittt *et al.*, 1994). This is due to the fact that the image is updated only after a full iteration is finished, that is, when all the LORs have been projected and back projected at least once. In the ordered subset EM (OSEM) algorithm, proposed by (Hudson and Larkin, 1994), the image is updated more often, which has been shown to reduce the number of necessary iterations to achieve a convergence equivalent to that of EM:

$$convergence: \ Subiterations = Iterations \times Subsets \tag{2.9}$$

According to the literature, EM methods have another important drawback: noisy images are obtained from over-iterated reconstructions, and this is usually attributed to either the fact that there is no stopping rule in this kind of iterative reconstruction (Johnson, 1987) or

to the statistical (noisy) nature of the detection process and reconstruction method (Bettinardi *et al.*, 2002; Biemond *et al.*, 1990). In practice, however, an image of reasonable quality is obtained after a few iterations (Hudson and Larkin, 1994) (see Figure 2.5).

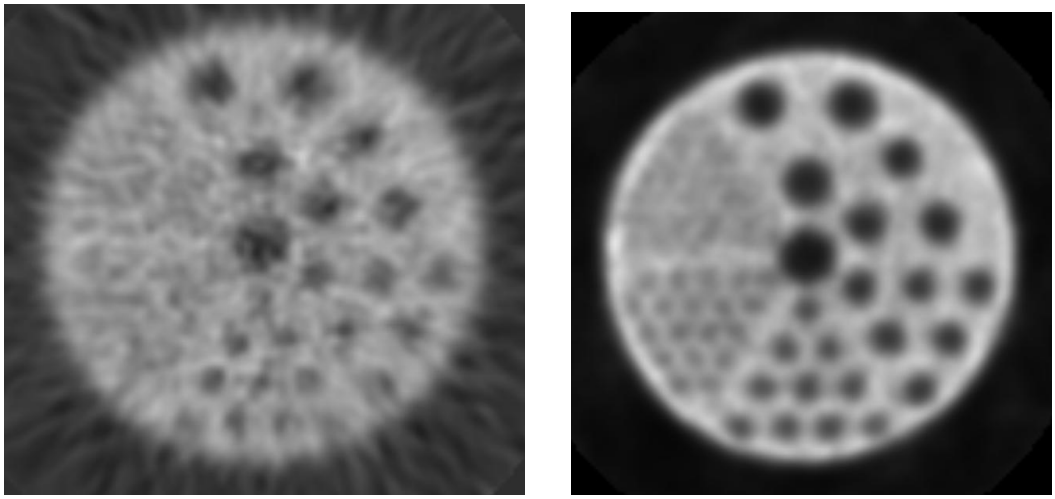

Figure 2.5. Reconstructed images of a cold Derenzo phantom filled with FDG and acquired with the VISTA scanner. The left image has been reconstructed using a FORE-2DFBP method and the right image has been reconstructed using a 3DOSEM method. This is an example of the improvement in resolution and level of noise that can be achieved when statistical methods are employed.

Several techniques have been proposed to address the noisy nature of the data: filtering the image either after completion of the reconstruction, during iterations or between them (Slijpen and Beekman, 1999), removal of noise from the data using wavelet based methods (Mair *et al.*, 1996) or smoothing the image with Gaussian kernels (Sieves method) (Snyder *et al.*, 1987; Liow and Strother, 1991).

Maximum *a priori* (MAP) algorithms are also widely used (Green, 1990). MAP adds *a priori* information during the reconstruction process, the typical assumption being that, due to the inherent finite resolution of the system, the reconstructed image should not have abrupt edges, at least not more abrupt that what one can expect from the resolution of the system. Thus, MAP methods apply a penalty function to those voxels which differ more than a certain threshold from their neighbors. Whether the maximum effective resolution achievable is limited, by the use of these methods, is still an open issue (Alessio *et al.*, 2003). On the other hand, a proper choice of reconstruction parameters, such as number of iterations, the use of an adequate system response and a smart choice of subsetting, can yield high quality images by means of the EM procedure (Herraiz *et al.*, 2006).

3. Monte Carlo simulations

3.1. Introduction

There is a class of numerical methods employed to solve complex problems, based on simulations that are at least partially stochastic, that is, they use random numbers (Kalos and Whitlock, 1986). These methods allow for simulations of complex physical processes in cases where a realistic solution is impossible (or very hard) to find by analytic means. For instance, in the description of radiation-matter interaction, there are many variables to be considered, that define the path and fate of each particle. Simulations are a common resort to study the interaction of radiation with materials (Briesmeister, 1993; Baró *et al.*, 1995; Agostinelli, 2003).

Simulations can yield information over the processes under study with several advantages over experiments. For any given model, it is very easy to change the parameters of the simulation and to investigate the effect of these changes in the performance of the system under study. Optimization of the design of imaging systems can largely benefit from the use of simulations (Braem *et al.*, 2004). Furthermore, by means of simulations one can study directly, properties of the scanner that cannot be measured experimentally. For example, it is impossible to accurately measure the scatter component of the radiation emitted from a distributed source, independently on the unscattered component. By using Monte Carlo techniques that incorporate the known physics of the scattering process, it is possible to simulate events scattered at the object and to determine their effect on the final image. Hence, simulations can help to understand the underlying processes, since all the history of simulated events is accessible (Ljungberg *et al.*, 1998).

3.2. Random numbers

Monte Carlo simulations employ random numbers. A sequence of random numbers is such that it is impossible to predict which will be the next number in the sequence. Sequences of perfectly random numbers are almost impossible to generate, by definition. Instead, pseudo-random numbers are employed. These pseudo-random numbers are generated by an algorithm that produces sequences of reasonably unpredictable appearance and with very long repetition cycles. These algorithms use a seed or initial number as a starting point for the generation of the sequence. Two sequences will be identical if they are generated from the same seed and algorithm and therefore, different seeds must be used in each simulation. In addition, these sequences of random numbers are often built so that they produce random variables that follow an uniform distribution in a specific range of values, that is, the probability of appearance of any number in the interval would be the same (Kalos and Whitlock, 1986).

Most programming languages include algorithms to generate sequences of random numbers uniformly distributed in the interval (0, 1). These are used as the basis for the generation of more complex distributions suitable for Monte Carlo methods. In what follows we introduce a few statistical definitions that will be useful for Monte Carlo methods.

The probability distribution function (PDF) of a continuous variable x ($p(x)$) is the function that contains the probability for x taking a specific value. This function must be positive and normalized to unity in a range of values (x_{min}, x_{max}) (Ljungberg *et al.*, 1998).

$$p(x) \geq 0 \qquad \int_{x_{\min}}^{x_{\max}} p(x)\,dx = 1 \tag{3.1}$$

The cumulative distribution function (CDF) of a variable x is the function that contains the probability that the value of the random variable falls within a particular interval $[x_{min}, x]$. It is therefore a non-decreasing function from $P(x_{min})=0$ to $P(x_{max})=1$ (Ljungberg *et al.*, 1998).

$$P(x) \equiv \int_{x_{min}}^{x} p(x')\,dx' \tag{3.2}$$

The first ingredient of a Monte Carlo calculation is the numerical sampling of random variables with specified PDFs. Different techniques to generate random values of a variable x, distributed in the interval (x_{min}, x_{max}) according to a given PDF $p(x)$, are explained below and in more detail for instance in (Sempau *et al.*, 2003).

3.2.1. Inverse transform method

The cumulative distribution function of $p(x)$ is a non-decreasing function of x and, therefore, it has an inverse. The transformation $\xi = P(x)$ defines a new random variable that takes values in the interval (0, 1), owing to the correspondence between x and ξ.

Therefore, the variable x defined as $x = P^{-1}(\xi)$ is randomly distributed in the interval (x_{min}, x_{max}). This method is called the inverse transform and is used when the inverse of $p(x)$ can be found analytically.

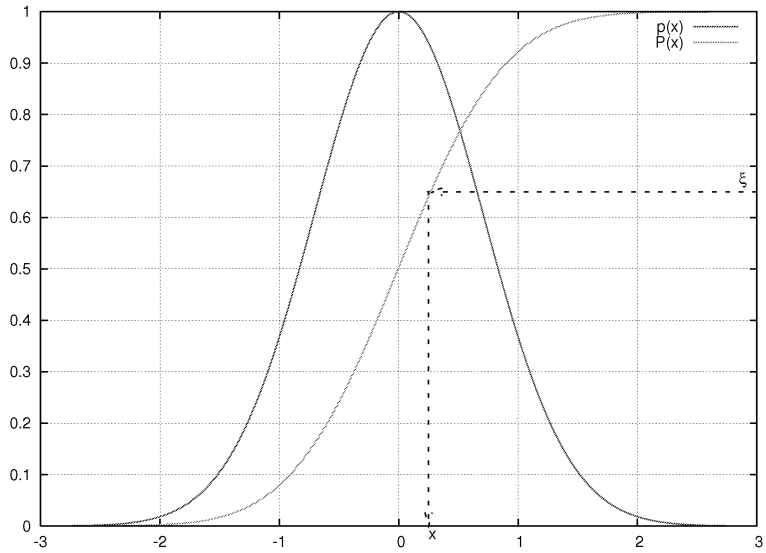

Figure 3.1. PDF p(x) and the corresponding CDF P(x). Uniform random numbers and their corresponding CDF can be used to generate random numbers that follow a particular PDF. One takes a uniformly distributed random number ξ in the (0, 1) interval. The inverse of the PDF will be applied to the ξ value to yield the x value of the random variable distributed with the desired PDF.

As an example, consider the exponential distribution of the free path x of a particle between interaction events,

$$p(x) = \frac{1}{\lambda}\exp(-x/\lambda) \tag{3.3}$$

where λ represents the mean free path. In this case the equation can be solved using the method described above.

$$\xi = \int_{x_{\min}}^{x} \frac{1}{\lambda} \exp\left(-x'/\lambda\right) dx' \Rightarrow x = -\lambda \ln\left(1-\xi\right) \tag{3.4}$$

The inverse transform method can also be used efficiently for random sampling of a continuous distributions *p(x)* given in numerical form, or that is too complicated to be solved analytically. This can be achieved by using an *a priori* calculation of the CDF for *N* values of x_n, keeping constant the difference between the PDF of consecutive values.

$$\mathrm{P}\left(x_n\right) = \int_{x_{\min}}^{x_n} p\left(x\right) dx = \frac{n}{N} \tag{3.5}$$

The accuracy of the simulation will depend on the number of points employed to subdivide the range of interest. A way of choosing values of x_n in the simulation with this method is to generate a random number ξ and to consider the quantity $y \equiv \xi N$, which takes values in the interval (0, *N*) (Sempau *et al.*, 2003).

3.2.2. Rejection methods

The inverse-transform method for random sampling is based on a one-to-one correspondence between *x* and ξ values, which is expressed in terms of a single-valued function. There is another kind of sampling method that consists of sampling a random variable from a certain distribution, different to *p(x)*, and subjecting it to a random test to determine whether it will be accepted for use or rejected. These rejection methods lead to very general techniques for sampling any PDF (Kalos and Whitlock, 1986).

First of all, a function *G(x)* is chosen such that $G\left(x\right) \geq p\left(x\right)$, and a random number *x* is obtained using any method according to that function. After this, another random number *y* uniformly distributed between 0 and *G(x)* is chosen. *x* values are rejected if *y* lies above *p(x)* or accepted if *y* lies below *p(x)*. This process gives rise to values of *x* distributed according to *p(x)*.

The efficiency of the method (the fraction of accepted *x* trials) can be calculated with the following expression:

$$\varepsilon = \frac{\int_a^b p\left(x\right) dx}{\int_a^b G\left(x\right) dx} \tag{3.6}$$

3.2.3. Variance reduction methods

Monte Carlo simulations can be time consuming. This is particularly true when the majority of photon histories generated by a standard Monte Carlo simulation are likely to be rejected, for example when simulating a point source at a large distance from a small detector, so that the probability that a photon would hit the detector is small.

Variance reduction techniques can then be applied in order to improve the efficiency of the simulation, and hence the statistical properties of the images produced. These techniques are based on computing a weight *W* for each photon history. This weight represents the probability that the photon passes through a particular history of events. These techniques are based on assumptions about probability functions of the physical processes, either to reduce the variance per history or to speed up the simulation to allow more histories

to be simulated during the same CPU time. To achieve this, to each photon is associated a weight *W*, which is the quotient between the true probability distribution and the fictitious probability distribution that the photon goes through a particular series of events (Ljungberg *et al.*, 1998).

In applying variance reduction techniques to the simulation of random walk processes (such a photon passage through matter), various techniques can be used. An initial weight is attached to each particle history as it is being generated. The history weight is then updated event by event by multiplying it by the correct weight factor for the variance reduction technique, if any, used at that step of the simulation. As an example, we consider a method where we *force* all the interactions to reach the detectors. The weight of the history in this case, will simply be given by the probability of a random interaction to reach the detector, which can be computed by simple geometrical arguments, and thus only photons whose paths intersect the detector need to be simulated.

3.3. Use of Monte Carlo techniques in Nuclear Medicine

Historically, it was in nuclear medicine that most of the early Monte Carlo calculations in radiation physics were performed. Today, the use of Monte Carlo simulations in this field continues to increase. The energy range of the photons used in nuclear medicine calls for a minimum emphasis on the production of secondary charged particles and high-energy processes that yield an electromagnetic cascade; at the other extreme, very low-energy photon can be practically ignored. On the other hand, the need for detailed simulations of complicated geometry configurations, is shared today by many other applications, and nuclear medicine is not exception in adopting the enormous potential provided by some of the major public Monte Carlo codes and their advanced geometry capabilities (Agostinelli, 2003; Briesmeister, 1993).

Currently there are many Monte Carlo simulation packages with different characteristics, suitable for either PET (Positron Emission Tomography) or SPECT (Single Photon Emission Computer Tomography) processes, at different levels of reliability. Accurate and versatile *general-purpose* simulation packages such as EGS4 (Rogers, 1984), MCNP (Briesmeister, 1993), and most recently PENELOPE (Baró *et al.*, 1995) and Geant4 (Agostinelli, 2003) have been made available. These last packages require a lot of expertise in order to model emission tomography configurations. Further, SimSET (Harrison *et al.*, 1993), GATE (Jan *et al.*, 2004), Eidolon (Zaidi and Scheurer, 1999) and PETSIM (Thomson *et al.*, 1992) are powerful simulation codes for specific applications in PET and SPECT. Nowadays, SimSET and GATE are probably the most extensively used (Barret *et al.*, 2005; Du *et al.*, 2002; Lazaro *et al.*, 2004; Chen *et al.*, 2006). Table 3.1 shows the principal features of these Monte Carlo codes.

3.3.1. SimSET

SimSET (Harrison *et al.*, 1993) uses Monte Carlo techniques to model the physical processes and instrumentation employed in emission imaging. First released in 1993, SimSET has become a primary resource for many nuclear medicine imaging research groups around the world (Barret *et al.*, 2005; Du *et al.*, 2002). The University of Washington Imaging

Research Laboratory keeps on the development of SimSET, adding new functionalities and utilities (Schmitz *et al.*, 2007; Harrison *et al.*, 2003). SimSET is freely available[2].

Table 3.1. Main features of PET Monte Carlo codes. Voxelized attenuation body and activity distributions are employed to define very complex geometries. Simulation of positron range and non-collinearity is mandatory to achieve realistic results. If pixelated detector capability is included, the reflector material placed among crystals can be considered. Random coincidences are very important when simulating high count rates. Some of the codes have been validated against experimental data.

	Voxelized att / act distrib.	Positron Range / Non-collinearity	Pixelated Detectors	Randoms	Validated
PETSIM	No	Yes	Yes	Yes	No
GATE	Yes	Yes	Yes	Yes	Yes
Eidolon	Yes	Yes	Yes	No	No
SimSET	Yes	Yes	No	No	Yes
PeneloPET	No / Yes	Yes	Yes	Yes	Yes

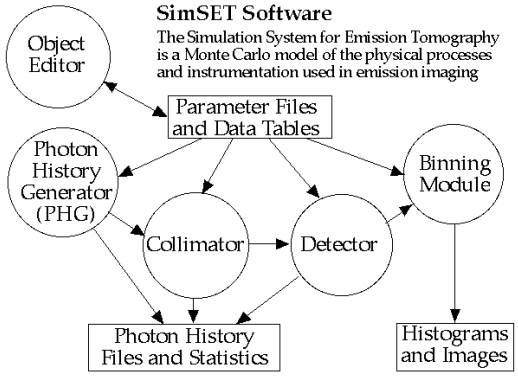

Figure 3.2. Block diagram illustrating how the different modules fit together in the SimSET package.

A diagram of SimSET modules is shown in Figure 3.2. The software is written in modular form, and the core module is the Photon History Generator (PHG), which models photon creation and transport through heterogeneous attenuators for both SPECT and PET. The Collimator Module receives photons from the PHG and tracks photons through the collimator being modeled. The Detector Module receives photons either directly from the PHG module or from the Collimator module. It tracks photons through the specified detector, and records the interactions within the detector for each photon. Each module can create a Photon History File that contains information on the photons it has tracked. The Binning Module is used to process photon and detection records, and can be used on-the-fly or on pre-existing history files.

All the modules in SimSET are configurable by the user. Configuration is achieved by editing ascii text files. The PHG, Detector and Collimator modules are configured using Parameter Files and Data Tables. Digital phantoms for the PHG (Activity and Attenuation

[2] http://depts.washington.edu/simset/html/simset_main.html

Objects) can be created. SimSET also comes with a range of utilities for manipulating datasets and history files. It does not handle randoms nor the time-structure of PET-counts.

3.3.2. GATE

The first version of GATE (GEANT4 Application for Emission Tomography) is available[3] since 2003 (Jan *et al.*, 2004). It is a generic simulation platform based on a general purpose code GEANT4 (Agostinelli, 2003) and designed for PET/SPECT applications. Several research institutes dealing with SPECT and PET are involved in the development and validation of GATE within the OpenGATE collaboration (Thiam *et al.*, 2008; Lazaro *et al.*, 2004). In particular, GATE allows for the description of time-dependent phenomena such as source or detector movement and source decay kinetics. It includes geometry modeling tools for complex scanner geometries, models for detector electronic response, and visualization utilities. Modeling of CT scans and estimation of dose can also be performed with GATE (Chen *et al.*, 2006; Thiam *et al.*, 2008).

GATE combines the GEANT4 physics models, geometry description, and visualization and 3D rendering tools, with original features specific to emission tomography. It consists of several hundreds of C++ classes. Mechanisms to manage time, geometry, and radioactive sources from a core layer of C++ classes close to the GEANT4 kernel (see Figure 3.3) are available to the user. An application layer allows to implement user classes derived from the core layer classes, e.g. to build specific geometrical volume shapes and/or to specify operations on these volumes such as rotations or translations. As the application layer implements all needed features, the use of GATE does not require C++ programming. A dedicated scripting mechanism, that extends capabilities of the native command interpreter of GEANT4 allows to perform and to control Monte Carlo simulations of realistic setups.

Modifications of the geometrical elements are synchronized with those of the sources. For this purpose, the acquisition is subdivided into time-steps during which the elements of the geometry are considered at rest. Decay times are generated within these time-steps so that the number of events decreases exponentially from time-step to time-step, and decreases also inside each time-step, according to the decay kinetics of each radioisotope. This allows to model time-dependent processes such as count rates or detector dead-time on an event-by-event basis. Detector electronic response is modeled as a chain of processing modules designed by the user to reproduce e.g. the detector cross-talk, its energy resolution, or trigger efficiency. It allows to define of detector dead-time and coincidence time windows which will significantly effect NEC curve estimation (Assie *et al.*, 2004).

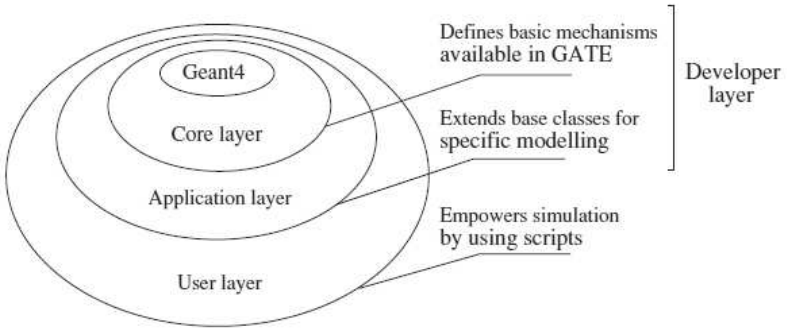

Figure 3.3. Sketch of the layered architecture of GATE (Jan *et al.*, 2004).

[3] http://opengatecollaboration.healthgrid.org/

3.3.3. PeneloPET

A new PET Monte Carlo code has been developed and will be presented in the next chapter (España et al., 2009). The main purpose of this new PET simulator is the optimization of the design of small animal PET scanners. Most often these scanners are made of multiple scintillator arrays read by Anger-like logic, arranged in complex geometries with millions of lines of response. Design optimization requires to perform many high statistics test simulations, each of them with different settings for the scanner, varying geometry (scanner diameter, crystal size), materials (scintillator, shielding and other scatter elements), electronics (integration time, dead time, coincidence window, pile up rejection). For this purpose it is of paramount importance to have the fastest possible simulation tool, capable of running in parallel in clusters of computers, and providing an easy way of executing many simulation instances with small changes of scanner definition. While the ample variety of detector philosophies that the combination GEANT4/GATE allows for is appealing, it is also true that it comes at the price of an important software overhead that makes the simulations with GATE in need of much computing resources. Indeed, GEANT4 offers a broad selection of physics models that are thus available for GATE users, but this also makes GATE simulations rather slow (Jan De *et al.*, 2007).

PeneloPET is based on PENELOPE (Baró *et al.*, 1995), a Monte Carlo code which is written using FORTRAN. The FORTRAN language is highly standardized and is available in any computer architecture aimed to scientific computing. FORTRAN compilers are optimized for speed and accuracy. Being written in FORTRAN, PENELOPE is bound to be both fast and portable.

4. PeneloPET, a Monte Carlo PET simulation tool based on PENELOPE

4.1. Introduction

Monte Carlo simulations play an important role in PET imaging, as an essential tool for the research and development of new scanners and for advanced image reconstruction. One of the main purposes of this thesis was to develop a PET Monte Carlo tool, which will be introduced in this chapter. The availability of powerful computers has encouraged the use of PET-dedicated simulation codes in the last few years. Examples of areas that benefit from extensive simulations are the design of new PET scanners (Braem *et al.*, 2004; Heinrichs *et al.*, 2003), the development and assessment of image reconstruction algorithms (Herraiz *et al.*, 2006) and of correction techniques (Levin *et al.*, 1995), among other applications (Zaidi, 2000; Ay and Zaidi, 2006; Ortuño *et al.*, 2003; Ortuño *et al.*, 2006; Torres-Espallardo *et al.*, 2008). Simulations make it possible not only to refine the design parameters of PET scanners, but they also help to identify bottlenecks regarding count rate, resolution, sensitivity, etc.

There are several Monte Carlo codes (for a short and recent review see Buvat and Lazaro 2006) that simulate the transport of radiation through matter, e.g. GEANT4 (Agostinelli, 2003), MCNP (Briesmeister, 1993), EGS4 (Kawrakow and Bielajew, 1998), and PENELOPE (Baró *et al.*, 1995; Salvat *et al.*, 2006). Either based upon these codes, or in tables of photon cross-sections, a number of tools for PET simulation have been developed, such as SIMSET (Harrison *et al.*, 2003), PETSIM (Thomson *et al.*, 1992) or Eidolon (Zaidi *et al.*, 1998), based on MCNP, and GATE, based in GEANT4 (Jan *et al.*, 2004). Probably (Buvat and Lazaro, 2006) one of the most widely known is GATE which, being based in GEANT4, can include a large variety of photon detectors and targets the large community of high energy and nuclear physics users that have acquaintance with GEANT4. GEANT4 is powerful and flexible enough to simulate PET scanners; however, its learning curve is both steep and long. A superficial knowledge of C++ is insufficient to optimally use GEANT4, and the installation process requires more than basic computer skills. This is why GATE was developed. GATE consists of hundreds of classes that provide useful functionalities for PET simulations. No C++ programming is involved and thus it is easier to learn and use, unless there is a need to create new classes to address specific problems.

We have chosen PENELOPE as the core of our PET simulation tool. PENELOPE is a Monte Carlo code for the simulation of the transport in matter of electrons, positrons and photons with energies from a few hundred eV to 1 GeV. It is then less generally aimed as GEANT4, but it suits well PET needs, it is fast and robust, and it is extensively used for other medical physics applications, particularly for dosimetry and radiotherapy (Sempau and Andreo, 2006; Panettieri *et al.*, 2007; Vilches *et al.*, 2007). PENELOPE is written in the FORTRAN programming language.

4.1.1. Why another PET simulator?

The main purpose of our PET simulator is the optimization of the design of small animal PET scanners. Most often, these scanners are made of multiple scintillator arrays read by Anger-like logic, arranged in complex geometries, with millions of lines of response. In order to optimize the design of the scanner, many high-statistics simulations have to be made and studied, each of them with different scanner settings, as for instance geometry (scanner diameter, crystal size), materials (scintillator, shielding and other scatter elements),

electronics (integration time, dead time, coincidence window, pile-up rejection), etc. Thus, it is desirable to have the fastest possible simulation tool, capable of running in parallel in clusters of computers, and able of providing an easy way of executing many simulation instances with small changes of the scanner definition. The ample variety of detector configurations allowed by the combination GEANT/GATE is appealing, but it comes at the cost of increased need for computing resources (Buvat and Lazaro, 2006).

The FORTRAN language is highly standardized and it is available in many computer architectures aimed to scientific computing, to which FORTRAN compilers have been adapted and optimized for speed and accuracy. Written in FORTRAN, PENELOPE is bound to be both fast and portable. On the other hand, while still widely used by physicists and mathematicians, FORTRAN is not the most popular programming language among young researchers, and lacks the object-oriented structure that is appealing when writing modular codes. On these grounds, we have developed PeneloPET, a FORTRAN package that allows to easily define complete simulations of PET systems within PENELOPE. PeneloPET is capable of preparing sophisticated simulations just by editing a few simple input text files, without requiring knowledge of FORTRAN or any other programming language. Simulations prepared with PeneloPET are straightforward to be run in parallel in clusters of computers.

4.1.2. Introduction to PeneloPET

The basic components of a PeneloPET simulation are detector geometry and materials definition (including non-detecting materials, like shielding), source definitions, non-active materials in the field of view of the scanner, and electronic chain of detection. All these components are defined with parameters in the input files. Different levels of output data are available for analysis, from sinogram and LORs histogramming to fully detailed list mode. These data can be further exploited with the preferred programming language, including ROOT. The detailed list mode generates a file with all the hits, single or coincidence events, and the corresponding information about interaction coordinates, deposited energy in the detectors, and time and type of coincidence: random, scatter, true, with pile-up, etc.

In this work we have performed several comparisons with another PET-dedicated code (GATE) and with studies obtained from four commercial PET scanners. The agreement between PeneloPET simulations and the results obtained in real scanners, confirms PeneloPET as a powerful tool for PET research and development, as well as for quality assessment of PET images. PeneloPET can be obtained under request from the authors. The reader interested can visit http://nuclear.fis.ucm.es/penelopet for details.

A few definitions

A coincidence event is noted as *pile up* when at least one of the single events has suffered pulse pile up. A coincidence is considered as a *scatter* coincidence when at least one photon that triggers the detectors has suffered one interaction before reaching the scintillator. A coincidence is considered as a *random* count when the two photons in the coincidence pair come from two different, uncorrelated, annihilation process. A *self-coincidence* event arises when the same photon produces both triggers of the *single* events. The remaining coincidences are considered as *true* events, that is, those for which both photons that produce the triggers are originated in the same annihilation process, do not interact before reaching the scintillator and no pulse pile up has occurred in any of the detectors that take part in the coincidence event.

4.2. Main features of PeneloPET

4.2.1. Source code

Our goal with PeneloPET has been to develop an easy to use program that includes all the physical and electronic processes involved in PET. PeneloPET requires a moderate time investment for the preparation of the simulation setup and it runs very efficiently, with modest computational burden compared to other PET simulation tools. It can be ported to any platform and operating system capable of compiling FORTRAN programs. We have tried PeneloPET under Windows, Linux/Unix, and Mac OS X platforms and with different FORTRAN compilers (gnu-g77[4], Absoft[5], Intel[6]) without porting problems.

The source code consists of two main modules. The first one deals with the PENELOPE simulations and the level of detail chosen for these, and takes care of the information about scanner detectors and materials, source and decay. This module includes the routines involved in the distribution of isotopes and emission of particles generated in the decay processes, as well as their interactions.

The second module post-processes the decay and interaction data generated by the first module. It takes into account, for instance, the Anger logic for positioning the interaction inside the crystal array, detector pile-up, energy resolution in the scintillator, and aspects of the electronics, such as coincidence time window, dead time, time resolution, and integration time. No PENELOPE routines are generally involved in this second module. Energy windows can be applied in this second module. Continuous or pixelated detectors can be managed by this second stage of the simulation package.

In order to run the simulations on clusters of computers, a simple and portable Python[7] script is provided with the code. The use of a Python enables to run the script under Windows, Linux/Unix, and Mac OS X. After configuring PeneloPET for the execution of the desired setup in a single-CPU, the Python script launches the simulation on the number of CPUs desired, with different random seeds, and takes care of the initial activity and the acquisition time for each sub-process, in order to simulate the same number of decay events as the equivalent single-CPU run. In this way, the simulation time is reduced proportionally to the number of CPUs employed.

4.2.2. Description of PeneloPET input files

Four input files have to be prepared by the user in order to set up a simulation. As an example, Table 4.1 shows these input files for the simulation of a point source in the SUINSA rPET scanner (Vaquero *et al.*, 2005). The first input file in Table 4.1 (main.inp) contains the general parameters of the simulation, such as the acquisition protocol and acquisition time. It also enables simulation of secondary particles, if desired, and controls whether positron range and non-collinearity are taken into account. This file contains options also for scanner rotation, energy and coincidence windows, contributions to dead time, output format, and type of study.

[4] http://www.gnu.org/software/fortran/fortran.html

[5] http://www.absoft.com/Absoft%20Compilers.htm

[6] http://www.intel.com/cd/software/products/asmo-na/eng/compilers

[7] http://www.python.org/

Table 4.1. PeneloPET input files needed to simulate a point source in the rPET scanner (Vaquero *et al.*, 2005). Full detail about these input files and options can be found in the PeneloPET manual. In this input file, 'F' stands for false or disabled option, while 'T' stands for true or enabled option.

	--- GENERAL PARAMETERS --- (main.inp)
12345 54321	!Random number generator seeds
9000 1 F	!Acquisition time (sec); Number of Frames; Read Frame List File
1000	!Limit number of interactions for each particle
F T T	!Secondary Particles Simulation; Positron Range; Non-Collinearity
0 180 3000 40	!Initial & Final ang pos (deg); Numb of Steps per cycle; time per cycle (sec)
0.	!Lower Level Energy Threshold (eV)
1000000.	!Upper Level Energy Threshold (eV)
5	!Coincidence Time Window (ns)
0.1	!Trigger's Dead Time (ns)
150	!Integration Time (ns)
1200	!Coincidence's Dead Time (ns)
F F T	!Hits LIST; Singles LIST; Coincidences LIST
F	!Write LOR Histogram
T 117 190 4.49684	!Write Sinogram; radial bins; angular bins; maximum radio
F 99 99 55 4.48 4.2	!Write Emission Image; X Y Z voxels, Transaxial & Axial FOV (cm)
F	!Hits checking
T	!Verbose
F	!Neglecting events if more than 2 singles in the coincidence time window
	--- SCANNER PARAMETERS --- (scanner.inp)
4	!Number of Detectors per Ring
1	!Number of Detectors in Coincidence in the same Ring
1	!Number of Rings
0.	!Gap Between Rings (cm)
30	!Number of transaxial crystals per detector (columns)
30	!Number of axial crystals per detector (rows)
1	!Number of crystal layers per detector
1.2 13 0.26 1 40 0.01	!LAYER: Length (cm); Mat; E Resol.; Rise & Fall Tim (ns); Tim Error (ns)
0.16 0.16	!Pitch: Distance between centres of adjacent crystals (cm)
8.	!Radius: Centre FOV - Centre Front of Detector (cm)
	--- BODY PARAMETERS --- (object.inp)
C 1 0. 0. 0. 0. 1.62 5.0 0. 0.	!Shape Mat X Y Z R1 R2 HEIGHT (cm) PH TH (deg)
	--- SOURCE PARAMETERS --- (source.inp)
P 1E6 F 1 0.5 1. 2. 0. 0. 0. 0. 0. 0. 0. 0. 180 ! Shap Act Units Isot X Y Z R1 R2 H PH TH TH1 TH2	

In the second file (scanner.inp), which contains the scanner definition, multiple rings and layers of crystals can be specified. Although our main goal was to simulate pixelated detectors for high-resolution small animal PET imaging, PeneloPET is also suitable for continuous scintillator blocks or even detectors not based on scintillators (such as CZT or silicon strips) with small or no changes.

Non-radioactive materials other than the scintillator (already defined in the file scanner.inp), such as surrounding materials and shielding, are defined in a third file (object.inp). The radioactive source is defined separately in a fourth input file (source.inp), which contains source geometry and information about activity and isotope. Keeping separated definitions for sources and materials simplifies the comparison of simulations of ideal sources, without scatter or attenuation, to more realistic sources. Details about PeneloPET input files and options can be found in the PeneloPET manual[8].

Typical materials for crystals, shielding and phantoms are predefined in PeneloPET and, if necessary, new materials can be created in a straightforward way. The visualization tools built in PENELOPE (gview2d, gview3d (Salvat *et al.*, 2006)) are also available in PeneloPET to display and test geometries. This is specially useful during scanner design stages (see Figure 4.1). Note that the definitions in Table 4.1 do not correspond to the scanner depicted in Figure 4.1.

Although the examples presented in this work deal with preclinical scanners, PeneloPET is also capable of simulating clinical PET scanners.

4.3. Description of PeneloPET output files

Output files generated by PeneloPET can offer three different levels of detail. At the highest level, all the information about each interaction is recorded for further analysis. At the intermediate level, just the single events and the information needed for their analysis is recorded. The possibility of pile-up and cross talk is taken here into account. At the third, and lowest, level of detail, only coincidence events are recorded in a compact LIST mode. Information about pile-up, scatter, random and self-coincidence events, obtained from the simulation, is also summarily available.

A coincidence event is labeled as pile-up when at least one of the single events has suffered pulse pile-up. A coincidence is considered to be a scatter coincidence when at least one of the photons that trigger the detectors has interacted before reaching the scintillator. A coincidence is considered as a random one, when the two photons in the coincidence pair come from two different, uncorrelated, annihilation process. Self-coincidence events may arise when the same photon, after scattering in a first detector, reaches a second detector. If the energy deposited in each detector is above the detection threshold, it may trigger two single events and yield a self-coincidence count. The remaining coincidences are considered as true events.

PeneloPET generates several output histograms that help to understand the results of the simulations, as for instance sinogram projections, LOR histogram, single and coincidence maps, and energy spectrum. In order to simplify the reconstruction of simulated data, the format of the sinograms conforms to that expected by the STIR library[9].

ROOT (Brun and Rademarkers 1997) is an object-oriented data analysis framework that provides tools for the analysis of experimental data. PeneloPET LIST files can be converted into ROOT format. As an example, Figure 4.2 shows a two dimensional energy histogram of the single events that yield the coincidence events, which has been plotted with ROOT.

[8] http://nuclear.fis.ucm.es/penelopet/

[9] http://stir.sourceforge.net

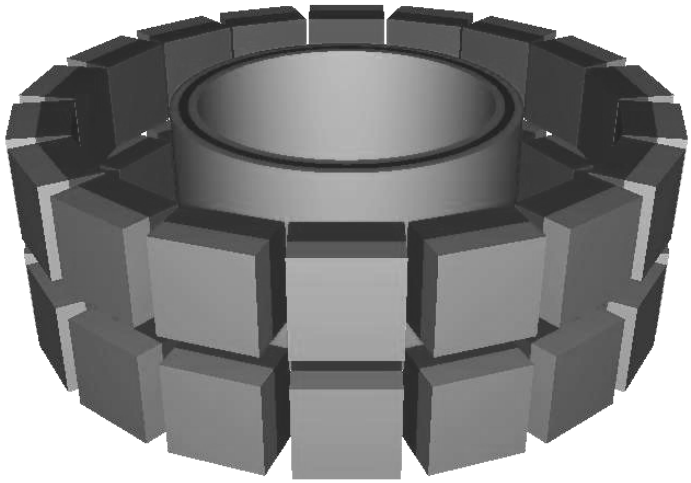

Figure 4.1. View of the SUINSA ARGUS (Wang *et al.*, 2006) scanner obtained with the gview3d application distributed with PENELOPE. An annulus phantom can also be observed, centered in the FOV.

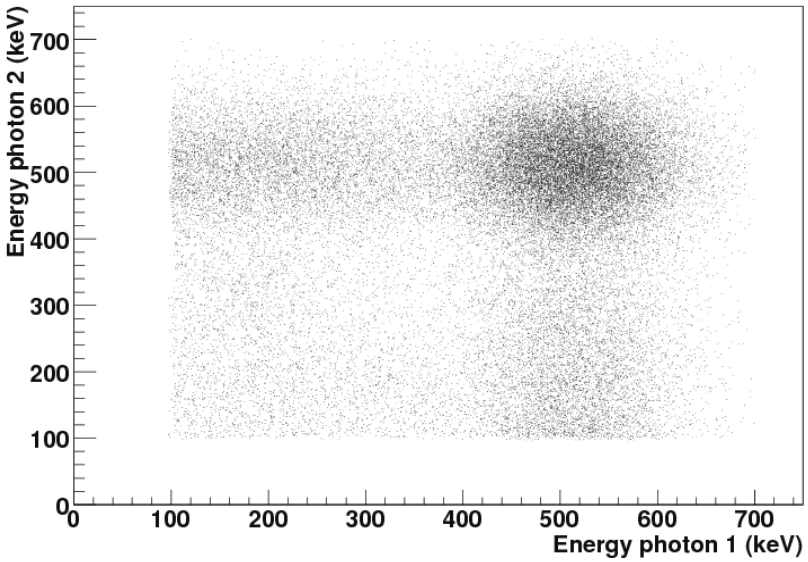

Figure 4.2. A two-dimensional energy histogram of single events belonging to the same coincidence, histogrammed with ROOT, from the file generated with the ROOT-output option of PeneloPET.

4.4. PENELOPE

PENELOPE is a code for the Monte Carlo simulation of coupled transport of electrons and photons. It is suitable for the range of energies between 100 eV and 1 GeV, and allows for complex materials and geometries. Due to its accuracy and flexibility, PENELOPE is being broadly employed, with numerous applications in the field of medical physics (Sempau and Andreo, 2006; Panettieri *et al.*, 2007).

PENELOPE consists of a package of subroutines, invoked by a main program that controls the evolution of the stories of particle counters and accumulates the magnitudes of interest for each specific application. These subroutines are written in the FORTRAN77 programming language, and are distributed by Nuclear Energy Agency - Organization for Economic Co-operation and Development (NEA-OECD). The authors are Francesc Salvat

and Jose M. Fernández-Varea of the Physics Department of the Universidad de Barcelona and Josep Sempau of the Institute of Energy of the Universidad Politécnica de Cataluña.

The simulation of electrons and positrons includes the following types of interactions:

- Hard elastic collision ($\theta > \theta_c$).
- Hard inelastic collision ($\theta > \theta_c$).
- Hard Bremsstrahlung emission.
- Delta interaction.
- Artificially soft event ($\theta<\theta_c$).
- Inner-Shell impact ionization.
- Annihilation (only for positrons).
- Auxiliary interaction (an additional mechanism that may be defined by the user, e.g., to simulate photonuclear interactions).

The simulation of photons includes the following interactions:

- Coherent scattering (Rayleigh).
- Incoherent scattering (Compton).
- Photoelectric absorption.
- Electron-Positron pair production.
- Delta interaction.
- Auxiliary interaction.

For further explanation of the physics included in these interaction the reader is referred to (Sempau *et al.*, 2003).

Each interaction can lead to secondary particles which can be later tracked and simulated. For example, the positron annihilation leads to γ photons and the photoelectric effect will lead to free electrons.

The use of PENELOPE requires to prepare a main program which will be responsible for calling the PENELOPE subroutines and for storing the information about the trajectories of the particles simulated. The main program should provide PENELOPE with the information about the geometry and materials, and also other parameters as type of particle, energy, position and direction of movement of the particle to be simulated. Through appropriate use of these tools, the user can create a simulation environment to carry out the desired studies. PENELOPE is of relatively common use in experimental nuclear physics and medical physics (Panettieri *et al.*, 2007).

PENELOPE includes a subroutine for generating sets of random numbers, that is based in an algorithm due to (L'Ecuyer, 1988). This algorithm yields 32-bit real numbers distributed uniformly over an open interval between zero and one. Its period is approximately 10^{18}, which is infinite for most practical purposes.

4.5. PeneloPET in more detail

PeneloPET is a Monte Carlo simulation environment for positron emission tomography (PET). The PENELOPE package is used to simulate the physics of the interaction of radiation with the matter. The application makes use of PENELOPE subroutines and other new subroutines that deal with the remaining emission and detection processes. This section details the operation of these subroutines.

At the first level of simulation, the PENELOPE subroutines are used. The information obtained here is the type of particle, and its initial coordinates, as well as the coordinates of all its interactions, deposited energy and body/material of each interaction. Four different kinds of information are stored in this simulation level:

- Angular position of the scanner (in the case of a simulation of a rotating scanner).
- Decay position.
- Starting position of secondary particles, such as annihilation photons.
- Interaction coordinates, with indication of the body of material and energy deposited in the interaction.

For every interaction event the following information is stored: block detector number, crystal number inside the block, energy deposited, decay number, annihilation photon number, scatter flag, and time stamp.

Once the buffer is filled (typically 500,000 events), the first photon track is analyzed. If the first interaction of the photon occurs out of the detector material, it is flagged as a scattered photon, that then would contribute a scatter count. The first interaction inside a detector activates a trigger mark and a time flag (this time flag is somewhat blurred using the time jitter value input in the simulation definition). If more interactions occur in the same activated detector, all of them are stored with the same trigger time until the end of the integration process. The coincidence window for all detectors connected with this one is open and all the detectors in coincidence are looked for triggers inside the coincidence window. If in one or more detectors a trigger is found before closing the coincidence window, a predefined coincidence matching is used to sort them for further processing. While the integration time of the marked detector has not finished, all interactions produced at the mentioned detector are stored. Once the integration time is elapsed, the total charge collected from the beginning of the trigger to the end of the integration time is computed. This process can include the tails of previous pulses and the heads of later pulses.

Single events are later matched to form coincidence-pairs which are also stored with the following information: block number, crystal identification number and energy deposited at both single events, time difference between the coincidence events, time stamp, and coincidence type. There are five different coincidence types:

- Pile-up: at least one of the single events has suffered pulse pile-up.
- Scatter: at least one photon that triggers the detectors have suffered one interaction before reaching the scintillator.
- Random: the two photons in the coincidence pair come from two different, uncorrelated, annihilation processes.
- Self-coincidence: the same photon produces both triggers of the single events.
- True: the remaining coincidences that do not fall into the four former categories, are considered *true* events, that is, those for which both photons that produced triggers are originated in the same annihilation process, do not interact before reaching the scintillator and no pulse pile-up has occurred in any of the detectors that belong to the coincidence event.

4.5.1. How to use PENELOPE subroutines

The first step is to define geometry and materials of the system. Geometry definition requires to prepare a file written in the specific format of PENELOPE. All bodies must be characterized by their limiting surfaces so that all surfaces are defined first, and finally bodies are constructed by combining several of these surfaces. The subroutine that extracts the information from the geometry file is called GEOMIN.

Table 4.2. First lines of GEOMIN subroutine.

```
SUBROUTINE GEONMIN (PARINP, NPINP, NMAT, NBOD, IRD, IWR)
C This subroutine
C initializes the geometry package for Monte Carlo
C simulation of particle transport.
C
C Input arguments:
C PARINP ....array containing optional parameters, which may
C replace the ones entered from the input file.
C NPINP .....number of parameters defined in PARINP (. ge.0).
C IRD .......input file unit (opened in the main program).
C IWR .......output file unit (opened in the main program).
C Output arguments:
C NMAT ......number of different materials in full bodies (excluding void regions).
C NBOD ..... Number of defined bodies.
```

Materials that composes each body must be specified in the geometry file. The cross sections of the materials employed shall be concatenated in a different file, that the PEINIT subroutine reads. The order in which the cross sections are concatenated must agree with the numbering used in the geometry file.

Table 4.3. First lines of PEINIT subroutine.

```
SUBROUTINE PEINIT (Emax, NMAT, IRD, IWR, INFO)
C
C Material input of data and initialization of simulation routines.
C Each material is defined through the input file (unit = IRD), which is
C created by the program 'material' using information contained in the
C database.This file can be modified by the user if more accurate information
C teraction data are available. Data files for different materials must
C CONCATENATE be in a single input file, the M-th material in this
C file is identified by the index M.
C Input arguments: Emax
C ...maximum particle energy (kinetic energy for electrons and
C positrons) used in the simulation. Note: Positrons with
C E may produce energy photons with energy E 1022 E6.
C NMAT ...number of materials in the geometry.
C IRD ....input unit.
C IWD ....output unit.
C INFO ...determines the amount of information that is written on
C the output file,
C INFO = 1, minimal (composition data only).
C INFO = 2, medium (same information as in the material
C definition data file, useful to check that the StruCad -
C ture of the latter is correct).
C INFO = 3 or larger, full information, including tables of
C interaction properties used in the simulation
```

Initial information for every particle such as type of particle, its energy, spatial coordinates and direction of movement, must be fixed at the beginning of the simulation of the particle track.

The remaining subroutines that must be used in the main program in order to simulate every particle are:

- CLEANS: This subroutine initializes the list of secondary particles. It must be called before starting the simulation of each primary particle.

- LOCATE: This subroutine determines the body that contains the point with coordinates (X, Y, Z) where the particle interacts. The output values are:

    - IBODY: the body that contains the particle.

    - MAT: material of that body.

- START: For electrons and positrons, this subroutine forces the following interaction event to be a soft *artificial* one. It must be called before starting a new primary or secondary track and also when a track crosses an interface. For photons this subroutine has no physical effect. However, it is advisable to call START for any kind of particle because it checks

whether the energy is within the expected range, and it can thus help to detect bugs in the main program.

- JUMP: It computes the free path from the point of departure to the position of the next interaction, and the probability of occurrence of the different types of interactions. The output value is:
    - DS: free path of the particle
- STEP: This subroutine computes the final coordinates, using the initial coordinates and direction. Furthermore, it returns the new body and material where the particle is placed after this step.
- KNOCK: It simulates the interaction. The output parameters are:
    - DE: energy deposited by the particle in the material.
    - ICOL: type of interaction suffered by the particle.
    - (U, V, W): new direction of the particle after the interaction.
- SECPAR: This subroutine returns the initial parameter of the next secondary particles to be simulated and removes them from the list of secondary particles. The output value is:
    - LEFT: number of secondary particles remaining in the list of secondary particles.

An initial call to subroutine LOCATE returns the body and material where the particle is at the beginning. CLEANS initialized the list of secondary particles. Each time the simulation of a particle is finished, it must be verified whether there are secondary particles remaining to be simulated in the list. The START subroutine must be called each time the simulation of a primary or secondary particle is started, the particle enters into a new body. Once the particle comes into a new body, the JUMP subroutine must be called to compute the free path before next interaction. The new particle location is updated using the STEP subroutine. An interaction will be valid if it occurs in the same body of start. If the final body is different, the distance from the start to the exit points of the body is stored, and subroutines START, JUMP and STEP must be called again, taking as starting point the entry point into the new body. The simulation of the interaction is therefore conditioned by the distance traveled across previous bodies. Once it is verified that the starting and interaction bodies are the same, the subroutine KNOCK should be called, and it simulates the event of interaction. The call to the subroutines START, JUMP and STEP should continue until the particle has lost all its energy, off a predefined cut-off energy. Once the simulation of a particle is finished, a call to SECPAR returns the number of secondary particles in the list, and the whole process is repeated until a null value for the number of remaining secondary particles is obtained. All this is transparent to the user.

4.6. Description of some specific PeneloPET routines

A set of additional subroutines have been implemented to perform full simulations of PET scanners, with just a few lines of input codes.

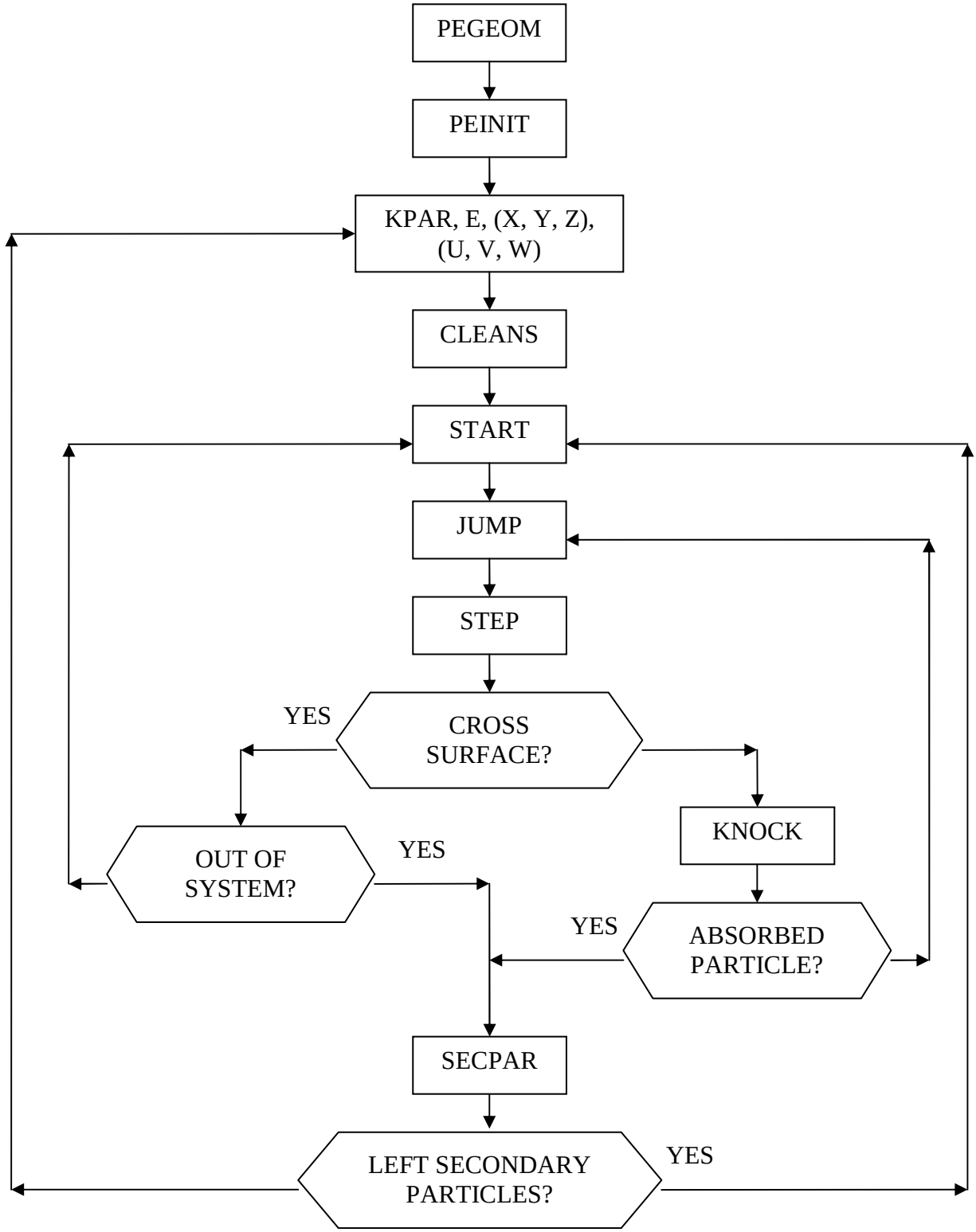

Figure 4.3. Flowchart of the basic kernel of interaction between PENELOPE and PeneloPET.

4.6.1. Geometry of the system

As we saw in the previous section, the definition of the geometry must be supplied to PENELOPE routines. To ease this task, several subroutines have been implemented that automatically build the geometry file required by PENELOPE, for common PET scanner configurations. The definition of the geometry has been divided into two sections, one that defines the detection system (scintillation crystals) and other that deals with the remaining bodies (shielding, source, ...).

Scanner definition

Many modern PET scanners are made of blocks consisting of a crystal matrix of one or more layers of scintillators (Wang *et al.*, 2006). Each crystal, usually of square or rectangular cross-section, has a length much larger than the side of its cross-section. Therefore, blocks have a prismatic shape with rectangular base. The input parameters that define the geometry of the blocks and the scanner as a whole are defined in a plain text input file (see table 4.4). The number of blocks, number of crystals per block, and the size and material of each scintillator crystal, are typical information that must be specified in the input file.

Table 4.4. Input file used for the definition of the scanner.

------ SCANNER PARAMETERS ------
10 ! Number of Detectors by Ring
3 ! Number of Detectors in Coincidence in the same Ring
36.0 ! Angle Between adjacent Detectors
2 ! Number of Rings
0.5 ! Gap Between Rings [cm]
20 ! Number of transaxial crystals by Detector [COLUMNS]
20 ! Number of axial crystals by Detector [ROWS]
1 ! Number of crystal layers by Detector
1.5 4 ! Length and materials for each crystal layer [cm] [table materials]
0.10 ! Pitch: Distance between center of the adjacent crystals [cm]
7.0 ! Radio: FOV Center - Center Front of Detector [cm]

PeneloPET subroutines create a geometry file for PENELOPE that contains the definition of the surfaces and bodies, and a predetermined numbering for both. This body numbering is used inside PeneloPET routines to locate the block where the particles interact. Each block and layer of crystal is defined as an independent body.

Other bodies

Objects that are not part of the detection system can be easily defined. Common objects to define are the shielding of the scanner and the phantom or activity sources. The list of objects to be simulated must be defined in an independent file (see Table 4.5), indicating their shape (spherical, cylindrical, prismatic ...), size, location, orientation and composition. The definition of these objects is important in order to take into account the effects of the scattering and absorption of annihilation photons.

Table 4.5. Input file used to define shielding and phantom bodies.

```
------ OBJECT PARAMETERS ------
 S10. 0.0.2.3.0.TYPE MATER XC YC ZC RI RE H [cm]
 C10. 0.0.2.3.1.TYPE MATER XC YC ZC RI RE H [cm]
 R50. 0.0.3.3.5.TYPE MATER XC YC ZC LX LY LZ [cm]
 ----------------------------------------------
```

An example of geometry input file generated for PENELOPE is shown in Table 4.6, and the resulting scanner is shown in Figure 4.4.

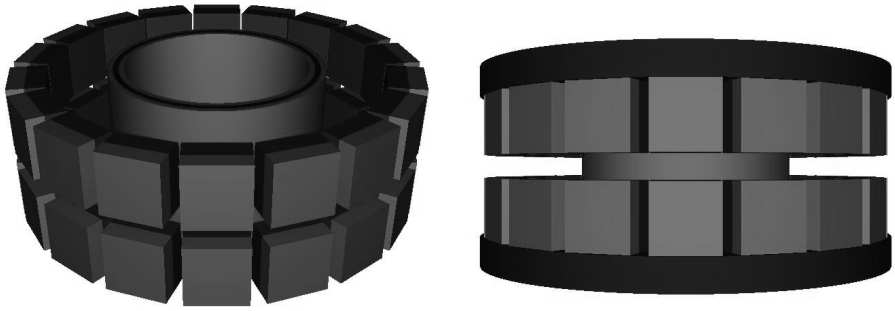

Figure 4.4. Graphical display of the Argus drT scanner with a normalization annulus phantom inside the FOV, as defined from a PeneloPET input file similar to the one in table 4.4. The right panel includes shielding materials, presented in dark colour. The gview3d.exe program included with the PENELOPE distribution was used to draw these figures.

Table 4.6. Typical appearance of a PENELOPE geometry input file generated from PeneloPET scanner definition of table 4.4. All surfaces is defined in first place, and the bodies are later built from the intersection of the predefined surfaces.

```
0000000000000000000000000000000000000000000000000000
SURFACE ( 001)
INDICES=( 0, 0, 0, 1,-1)
Z-SCALE=(+0.200000000000000E+01,  0)
0000000000000000000000000000000000000000000000000000
SURFACE ( 002)
INDICES=( 0, 0, 0, 1,-1)
Z-SCALE=(+0.200000000000000E+01,   0)
THETA=(+0.120000000000000E+03,   0) DEG
0000000000000000000000000000000000000000000000000000
.
0000000000000000000000000000000000000000000000000000
BODY    ( 001)
MATERIAL( 002)
SURFACE ( 003), SIDE POINTER=(+1)
SURFACE ( 004), SIDE POINTER=(-1)
SURFACE ( 005), SIDE POINTER=(-1)
SURFACE ( 006), SIDE POINTER=(-1)
SURFACE ( 001), SIDE POINTER=(-1)
```

```
SURFACE ( 002), SIDE POINTER=(-1)
00000000000000000000000000000000000000000000000000
.
```

4.6.2. Definition of materials

PENELOPE includes a database with the necessary information about elements. Furthermore, cross section files for elements, compounds or mixture of compounds can be easily built if needed. Cross section files for many materials used in PET have been included in PeneloPET (LSO, GSO, BGO, NaI, LaBr, CZT, lead, steal, copper, aluminium, water, delrin...). When a simulation is performed, all required cross section files must be concatenated in a single file in the same order as in the geometry file. PeneloPET includes subroutines to perform this.

4.6.3. Isotopes

PeneloPET is ready to simulate common β^+ isotopes. Isotopes are defined in an input file (see Table 4.7) that can easily be extended by the user. Each isotope is referenced by its half life and a list of emitted particles that includes the type of particle, emission energy (in the case of electrons and positrons, this refers to the value of Q, or maximum kinetic energy) and the fraction of occurrence, or branching ratio.

Table 4.7. Input file with isotopes pre-defined in PeneloPET.

```
---------- ISOTOPES -------------------------
1       6586.2          9       F18     !Order-label    Half_Life[sec]  Z       Isotope_name
B+      633.5E3         0.9673          !Type   Energy Fraction
-----------------------------------------------------
2       1223.4          6       C11     !Order-label    Half_Life[sec]  Z       Isotope_name
B+      960.2E3         0.9976          !Type   Energy Fraction
-----------------------------------------------------
3       597.9           7       N13     !Order-label    Half_Life[sec]  Z       Isotope_name
B+      1198.5E3        0.9980          !Type   Energy Fraction
-----------------------------------------------------
4       122.24          8       O15     !Order-label    Half_Life[sec]  Z       Isotope_name
B+      1732.0E3        0.9990          !Type   Energy Fraction
-----------------------------------------------------
5       8.210972E+07    11      Na22    !Order-label    Half_Life[sec]  Z       Isotope_name
B+      545.7E3         0.9033          !Type   Energy Fraction
G       1274.54E3       0.9994
-----------------------------------------------------
```

4.6.4. Distribution of activity

The activity distribution can be defined by means of simple geometrical shapes or by means of a voxelized distribution.

Predefined geometrical shapes.

Emission points homogeneously distributed at random within defined regions will be chosen. There are subroutines for the following basic geometries:

- *Rectangular prism*. Cartesian coordinates (x, y, z) are employed because the probability distribution is uniform in all of these coordinates, and they are independent.

$$p(x)=p(y)=p(z)=1$$
$$\xi_x=\frac{x-x_{min}}{x_{\max}-x_{\min}}\Rightarrow x=\xi_x\left(x_{\max}-x_{\min}\right)+x_{\min} \tag{4.1}$$

- *Cylindrical region.* Cylindrical coordinates are used to maximize the efficiency of the choice of random emission points. Azimuthal and vertical distribution of emission points are homogeneously produced, while the radial distribution varies linearly according to the Jacobian for the transformation from cylindrical to Cartesian coordinates:

$$p(\varphi)=p(z)\,;\,p(r)=r$$
$$\xi_r=\frac{\int_{r_{\min}}^{r} r\,dr}{\int_{r_{\min}}^{r_{\max}} r\,dr}=\frac{\frac{r^2-r_{\min}^2}{2}}{\frac{r_{\max}^2-r_{\min}^2}{2}}\Rightarrow r=\sqrt{\xi_x\left(r_{\max}^2-r_{\min}^2\right)+r_{\min}^2} \tag{4.2}$$

- *Spherical region.* The use of spherical coordinates is more efficient in this case. The azimuthal angle is distributed homogeneously, while the radial distribution varies as the square of the radius, and the polar angle distribution follows the cosine of the polar angle, according to the Jacobian transformation from spherical to Cartesian coordinates:

$$p(\varphi)=1\,;\,p(\theta)=\sin(\theta)\,;\,p(r)=r^2$$
$$\xi_r=\frac{\int_{r_{\min}}^{r} r^2dr}{\int_{r_{\min}}^{r_{\max}} r^2dr}=\frac{\frac{r^3-r_{\min}^3}{3}}{\frac{r_{\max}^3-r_{\min}^3}{3}}\Rightarrow r=\sqrt[3]{\xi_x\left(r_{\max}^3-r_{\min}^3\right)+r_{\min}^3}$$
$$\xi_\theta=\frac{\int_{\theta_{\min}}^{\theta}\sin\theta d\theta}{\int_{\theta_{\min}}^{\theta_{\max}}\sin\theta d\theta}=\frac{\cos\theta_{\min}-\cos\theta}{\cos\theta_{\min}-\cos\theta_{\max}}\Rightarrow \tag{4.3}$$
$$\Rightarrow\theta=\arccos\left(\xi_\theta\left(\cos\theta_{\max}-\cos\theta_{\min}\right)+\cos\theta_{\min}\right)$$

Voxelized distribution

Any complex distribution can be defined using a voxelized definition with the initial activity for each voxel. This type of source definition does in fact not result in any increase of computational time. Mixture of different isotopes can be employed in the same simulation.

4.6.5. Direction of the particles emitted

The direction of the particles emitted after the decay of radioactive nuclei or resulting from the annihilation of positronium, is distributed isotropically. The emission direction is defined by the polar and azimuthal angles, in spherical coordinates. For most studies, it is desirable to reduce the range of possible emission directions assuming that the particles emitted in directions outside some range do not contribute to the final outcome of the simulation. In this case, a correction factor to the simulated efficiencies, equivalent to the fraction of the angular range employed to the total solid angle subtended (4π), is automatically applied.

4.6.6. The Gaussian probability distribution

Gaussian distribution appears when simulating physical processes. The Gaussian probability distribution is defined as follows:

$$p(x) = \frac{1}{\sqrt{2\pi\sigma}} \exp\left(-\frac{(x-\mu)^2}{2\sigma^2} \right) \tag{4.4}$$

where σ is the standard deviation of the distribution, and μ is the mean. There is no analytical solution to the inverse transformation method for the Gaussian distribution. This is why the Box-Muller algorithm (Bratley *et al.*, 1983) explained below, was implemented. This algorithm is based on the product of two Gaussians with the same σ.

$$\begin{aligned} p(x)\,p(y)\,dxdy &= \frac{1}{2\pi} \exp\left(-\frac{x^2+y^2}{2} \right) dxdy = \\ &= \left[r \exp\left(-\frac{r^2}{2} \right) dr \right] \left[\frac{d\theta}{2\pi} \right] \\ x = r\cos\theta \;;\; y &= r\sin\theta \end{aligned} \tag{4.5}$$

in this way, a cumulative distribution function is obtained which is separable in r and θ:

$$\begin{aligned} \xi_r &= \frac{\int_0^r r \exp\left(-\frac{r^2}{2} \right) dr}{\int_0^\infty r \exp\left(-\frac{r^2}{2} \right) dr} = \frac{1 - \exp\left(-\frac{r^2}{2} \right)}{1} \Rightarrow r = \sqrt{-2\ln\xi_r} \\ \theta &= 2\pi\xi_\theta \end{aligned} \tag{4.6}$$

Therefore, each time a pair of random numbers (ξ_r, ξ_θ) is generated; two other random numbers, according to a Gaussian distribution, will be obtained by means of.

$$\begin{aligned} x &= \sqrt{-2\ln\xi_r}\cos(2\pi\xi_\theta) \\ y &= \sqrt{-2\ln\xi_r}\sin(2\pi\xi_\theta) \end{aligned} \tag{4.7}$$

To get a distribution with mean μ and standard deviation σ, the following transformation should be used:

$$x = \frac{x' - \mu}{\sigma} \Rightarrow x' = \mu + \sigma x \tag{4.8}$$

4.6.7. Range of positrons

When a positron is generated in a decay process, it has a kinetic energy that depends on the energy shared with the neutrino created in the same process. This yields a continuum energy spectrum distribution, which is easily computed from theoretical grounds, either for allowed or superallowed transitions, and including the Coulomb correction factor (see for instance equation (13) in (Levin and Hoffman, 1999)) after (Richardson and Kurie, 1936). In PET positron range simulations, this latter Coulomb correction factor is often either neglected or only treated in a nonrelativistic approach. PeneloPET uses the exact expression for the Coulomb correction factor, which, albeit relatively close to one for light nuclei and positron emission, it may significantly distort the beta spectrum for medium to heavy nuclei, particularly in the case of electron emission. Figure 4.5 shows the normalized positron spectra corresponding to ^{18}F, and ^{68}Ge/^{68}Ga, with and without Coulomb correction.

PeneloPET has two possibilities for incorporating positron range. The first one tracks the path and energy spectrum for each positron coming from the decay process. This will lead to accurate results, but at the expense of an increase of computational time. In the second approach the profile of the positron range in water is generated, from a detailed simulation (like the one described for the previous approach), run only once with high statistics, saving the resulting profile for later simulations, where the positron annihilation point will be randomly generated from these pre-computed positron range profiles. Positron range profiles for β^+ isotopes widely used in PET are included with PeneloPET (see Table 4.8). Profiles for other isotopes can be added with the tools provided with PeneloPET. By default, uniform positron range across the FOV is considered in this second case. Non-uniform positron range can only be considered within the first, more detailed and computationally expensive (more than 10 times slower), approach.

4.6.8. Non-collinearity

When an annihilation process takes place with the positron and electron at rest, two photons are produced with the same energy, 511 keV. To conserve energy and momentum, both photons should be emitted along the same line but in opposite directions (Knoll, 2000). Because usual annihilation takes places with thermal electrons and positrons, that is, electrons and positrons of a few eV of energy, the emission of photons is not exactly collinear. Note, a few events would be produced where the positrons have not been showed down to thermal energies. For these events, the non-collinearity is expected to be much higher. However these are a tiny fraction of all events, (Halpern, 1954). This non-collinearity is included employing a Gaussian distribution of 0.5 degrees FWHM that seems to agree with the experimentally measured (Harrison et al 1999).

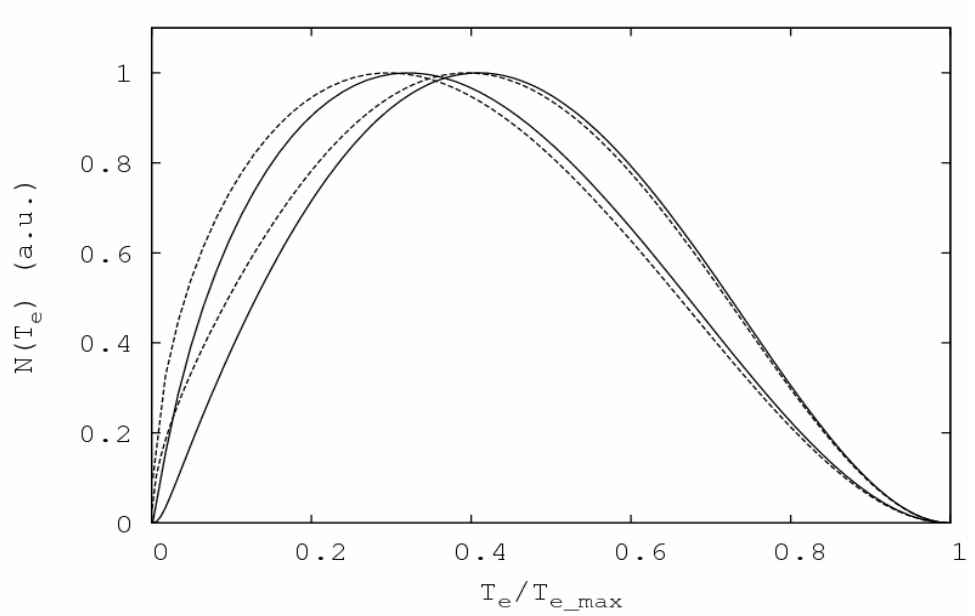

Figure 4.5. Simulated positron spectra obtained with PeneloPET and employed in positron range calculations. From left to right, ^{18}F, ^{68}Ge/^{68}Ga, dashed lines without Coulomb correction, solid lines with Coulomb correction. The horizontal axis represents the kinetic energy normalized to the maximum value of each spectrum.

Table 4.8. List of β+ isotopes already defined in PeneloPET, with available positron range profiles.

Isotope	Half Life
^{11}C	20.4 min
^{13}N	9.97 min
^{15}O	2.04 min
^{18}F	110 min
^{22}Na	2.6 y

4.6.9. Distribution of radioactive emissions

Activity is the number of decays that are produced in a certain amount of radioactive material per second (Knoll, 2000). The decay constant (λ) is the probability of decay for a nucleus per time unit and has a characteristic value for each isotope. The Poisson distribution describes the statistics of radioactive decay. This distribution is a special case of the binomial distribution when the probability of success (p) is close to zero and the number of attempts (N) tends to infinity, so that the product of both has a ($N \cdot p$) finite value. The decay constant is usually very small and the number of nuclei (attempts) in a radioactive sample is always very high, hence the Poisson distribution is appropriate for this case. The probability of observing r decays following the Poisson distribution is (Leo, 1994):

$$P(r) = \frac{\mu^r e^{-\mu}}{r!} \tag{4.9}$$

where μ is the mean, given by the product $N \cdot p$:

$$P(r) = \frac{(\lambda N)^r e^{-\lambda N}}{r!} \tag{4.10}$$

This function (see Figure 4.6) represents the probability to obtain r decays in a sample of N nuclei with a decay constant λ in an interval of 1 second.

The simulation of the decay rate should assign an emission time coordinate to each decay process. To achieve this goal, the probability distribution of time between two consecutive decays, for a specific activity and decay constant, must be obtained. The probability for any decay during a time interval δt is:

$$P(0) = \frac{(\lambda N \delta t)^0 e^{-\lambda N \delta t}}{0!} = e^{-\lambda N \delta t} = e^{-A\delta t} \tag{4.11}$$

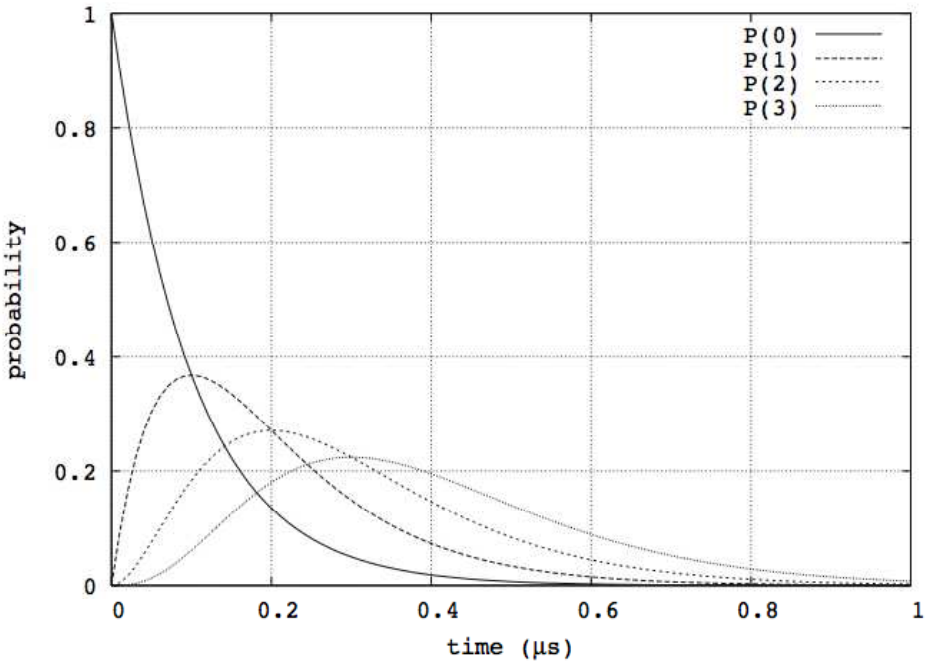

Figure 4.6. Time distribution of the probability of occurrence of 0, 1, 2 and 3 decays for 10^7 Bq of ^{18}F.

Therefore, a distribution of random numbers is generated as follows (see chapter 3):

$$\xi = \frac{\int_0^{\delta t} e^{-A\delta t} d(\delta t)}{\int_0^{\infty} e^{-A\delta t} d(\delta t)} = \frac{A\left(1 - e^{-A\delta t}\right)}{A} \Rightarrow \delta t = \frac{-\ln(1-\xi)}{A} \tag{4.12}$$

When a photon deposits energy larger than a given threshold in a detector, a pulse (*a single event trigger*) is generated. The shape and duration of this pulse is defined in the simulation definitions input file. Due to the finite time response of the scintillator, an integration of the pulse during, typically, a hundred of nanoseconds, is needed in order to measure the energy deposited by the photon and to proceed to the localization of the interaction. If any other photon interacts with the same detector within this integration period of time, an overlap of both pulses (detector pile-up) will result (see Figure 4.7) (Knoll, 2000). This will cause incorrect energy and pixel crystal identification. The time response of the

detectors and the acquisition electronics, can be taken into account in high detail with PeneloPET, which allows for realistic implementation of pulse pile-up. Pulse pile-up rejection in the electronics can also be simulated. Figure 4.8 shows the distortion of the energy spectrum due to pulse pile-up, as obtained from PeneloPET simulations (España *et al.*, 2007a).

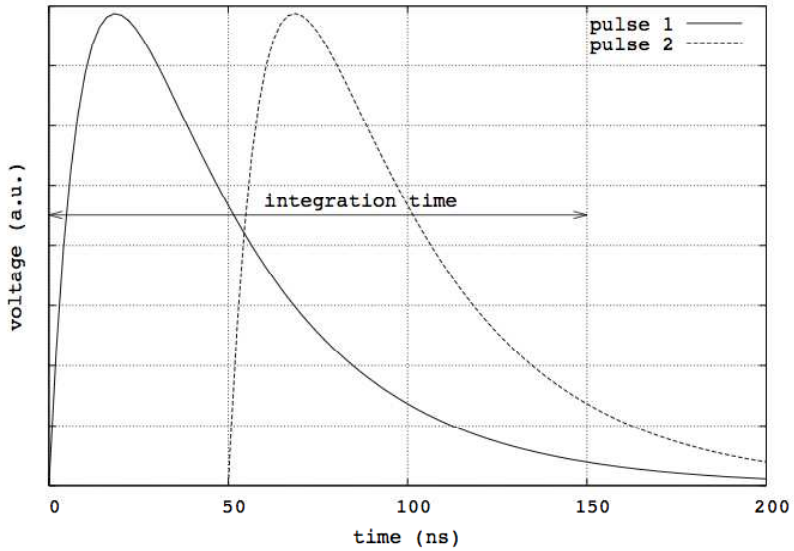

Figure 4.7. Signal, showing stacked (piled-up) pulses due to the arrival of a second pulse within the integration time of the first one.

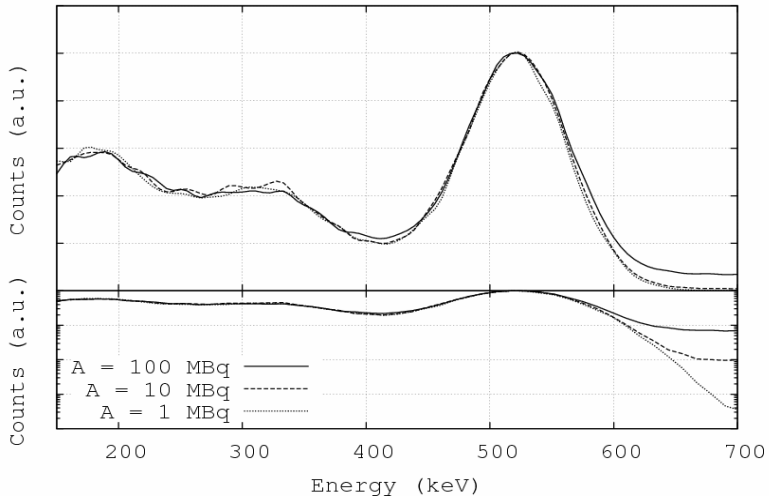

Figure 4.8. Energy spectrum for acquisitions simulated at different activity levels, with linear (top panel) and log (bottom panel) scales. This simulation was performed for a rat-size phantom filled with ^{18}F in the ARGUS scanner. Counts at the right of the photopeak are due to detector pile-up events, whose contribution is more conspicuous for larger activities. Pile-up events also fill in slighly the region around the Compton edge.

4.6.10. Resolution in energy

PENELOPE does not simulate the details of the photo-emission and detection of visible photons in the PMT, or similar devices. Thus, the energy measured by the detectors according to PENELOPE must be blurred in order to take into account the finite energy resolution of the detection system. By default, energy blurring is assumed to be of Gaussian

shape. In the input file, the FWHM in energy for the 511 keV photopeak is introduced (usually taken from comparisons to actual experiments) while blurring for other energies is computed assuming ΔE proportional to $E^{-1/2}$.

When a gamma photon interacts within the detector, that interaction should be assigned to a specific crystal of the array. Although of course it is well known from the simulation, in most actual scanners the location of the interaction inside a pixel crystal is not available (Dongming *et al.*, 2006). Once the interaction is determined to take place inside a pixel crystal, the transverse central point of that crystal is taken as the interaction point. Additional Gaussian blurring can be added to crystal identification in order to match the observed (experimental) results for particular scanners. When the photon interacts in more than one crystal, the energy centroid is computed using all *illuminated* crystals weighted by the energy deposited on each one. This is a procedure similar to the one introduce by Anger (Anger, 1969) and mimics the behavior of many scanners. Variations of the Anger algorithm can be easily implemented in PeneloPET. With this algorithm, X and Y coordinates (as well as energy E) are assigned to each interaction. Simulations can be employed to determine the percentage of success (that is, of events with the right crystal of interaction assigned) for these algorithms (see chapter 7).

$$\begin{aligned} E &= \sum_{i=1}^{N} E_i \\ X &= \sum_{i=1}^{N} \left(E_i \times X_i\right) / E \\ Y &= \sum_{j=1}^{N} \left(E_j \times Y_j\right) / E \end{aligned} \qquad (4.13)$$

4.6.11. Time coincidence window

To implement the effect of the time coincidence windows in the scanner, two parameters must be defined: the resolution time of the detection system and the time coincidence window. The arrival time of a photon to a detector is randomly blurred following a Gaussian distribution according to the time resolution of the system. The time of flight of the photon can easily be included in the simulation. When a photon reaches a detector producing a single event trigger, all detectors allowed in coincidence (this is included in the definition file for the scanner) are looked for another single event trigger within the time coincidence window. If more than two events are detected inside the coincidence window, a decision protocol is used to sort these events in coincidence. PeneloPET includes different protocols to handle multiple events in coincidences which can be chosen in the input files, for instance, it can get rid of these events, or it can choose one of these events randomly, or use an average of them.

4.6.12. Dead time

Dead time occurs when the acquisition mechanism is busy analyzing previous events. In general, gamma detectors suffer from several contributions to dead time. First of all, in the detection process, a trigger flag is activated above some energy threshold. This single trigger flag will not be ready to measure new events for a (usually very short) time (single-trigger dead time). Events are accepted if a coincidence is by a hardware pre-coincidence filter (if the scanner works in coincidence-mode acquisition). Moreover, for single-mode acquisitions,

every single event is acquired and converted, and coincidence sorting only occurs later in software. In either case, an additional acquisition dead time during which no other photon can be detected by the same electronic input (single dead-time or coincidence dead-time, depending on the acquisition mode) can be considered. This dead time usually lasts from the time that the trigger flag was set and until when all integration and electronics conversions are performed by the acquisition electronics. Once the information from the gamma interaction has been recorded (typically by an ADC gate) it must be sent to the computer for further processing. Very high count rates can produce event losses during the transmission to the computer. Further, CPU dead time can also cause a loss of events. All sources of dead time can be included in PeneloPET and are explained in what follows:

- Coincidence window: All detectors connected in coincidence can produce coincidences for single trigger events, within a time difference smaller than the coincidence window. If more than two single events reach the coincidence unit while the coincidence window is open, some of them can be lost depending of the matching protocol.

- Trigger dead time: A single trigger event is produced when a photon reaches an inactive detector. The time that must be elapsed until a next single trigger event can be resolved, is fixed by this parameter. Only registered triggers can produce coincidence events.

- Integration time: During the integration process of a detector, the singles from all photons that reach the detector will not produce any further single trigger event but instead they will be integrated together with the one that triggered the detector and thus affect the energy and location values resulting from the ADC procedure.

- Singles dead time: There is usually an additional time after the integration stage that is needed to perform digital conversion. During this stage the detector can not process additional interactions, that is, no further single trigger events will be processed. These interactions will not contribute to pile-up, contrarily to those described in previous paragraph.

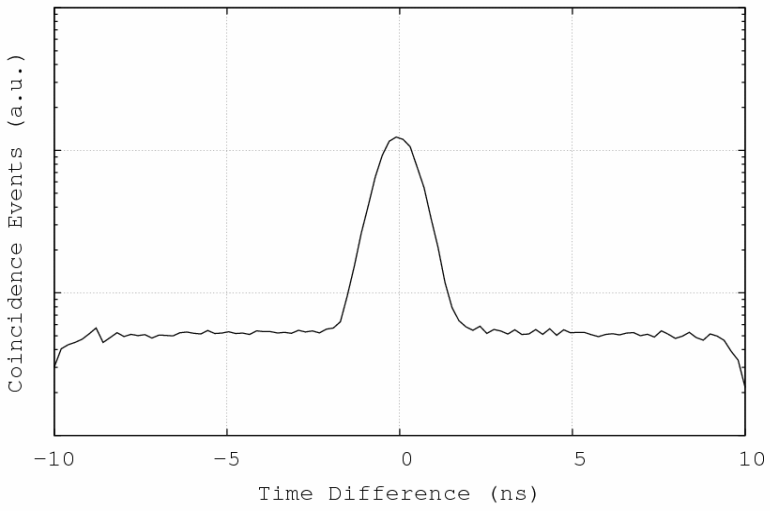

Figure 4.9. Histogram of time-differences for the two single events in coincidence pairs. This simulation was performed using a rat-size phantom filled with 71 MBq of ^{18}F for the ARGUS scanner. Log scale is used for the y axis. A time-resolution of 2 ns FWHM been chosen to reproduce the behaviour of the actual scanner.

Table 4.9. Lines in the main.inp file that set possible deadtime effects. The first line sets the maximum difference in the arrival of two single events to be considered as a coincidence event. The third line establishes the time during a pulse is integrated. The fourth line sets the total time that needs to be elapsed from the trigger for an integrated event until the detector is ready for further analysis.

3	[Coincidence Time Window (ns)]
200	[Trigger Dead Time (ns)]
220	[Integration Time (ns)]
1200	[Single Dead Time (ns)]

4.6.13. Constraints in energy and type of particle

PeneloPET offers all the possibilities of PENELOPE for constraining the energy and the kind of particle that is included in the simulation (Salvat *et al.*, 2006). Depending on the purpose of the simulation, the user may choose tracking all photons, electrons and positrons, including every secondary particle, or just some of them. It is also possible to track only the particles with energy above a certain threshold or to stop tracking a particle when its energy is below a low energy threshold. Faster simulations can be performed by tracking only annihilation photons. This should be a good approximation since the mean free path of secondary particles is short enough for the case of intermediate energy photons employed in medical imaging (Ljungberg *et al.*, 1998).

4.6.14. Response of the system

Iterative reconstruction methods require the knowledge of the system response matrix (SRM) (Herraiz *et al.*, 2006). The SRM contains the elements representing the probability of detection of an event coming from a voxel, at an specific LOR. PeneloPET includes the possibility of building the SRM for a specific LOR. For this purpose a point source of the selected isotope is placed in different locations along the channel of response (CHOR), or region of space that is connected (that is, can produce a coincidence event) to the LOR (Herraiz *et al.*, 2006). Parameters can be chosen to define how fast and accurate the results should be. The SRM can be also computed for rotating scanners, for which the probability of detection for each sinogram bin, instead of for each CHOR would be computed (Herraiz *et al.*, 2006). PeneloPET can be employed to compute the SRM specifying just a few lines in the input files.

Table 4.10. Detail of the *main.inp* file required to compute system response simulation. First and second lines establish whether it will a LOR-based or Sinogram-based response calculation. Third and fourth lines establish the periodicity and size of the sampling volume. The last line specifies the allowed angular range around the direction of the LOR for the emitted photons, and the number photons used for the calculation of every coefficient of the SRM.

T			[System Response Simulation: LOR-RESPONSE]
F			[System Response Simulation: SINOGRAM-RESPONSE]
21	21	19	[Chord points - Transaxial Axial Longitudinal]
0.5	0.5	10.0	[Chord size: Transaxial; Axial; Longitudinal(cm)]
2	5E6		[Chord Aperture, Decays/Point]

4.7. Conclusions

We have developed PeneloPET, an easy to use simulation package for PET simulations. For its versatility, speed, and easy-to-analyze outputs, PeneloPET is a tool useful for scanner design, system response calculations, development of corrections methods, and many other applications. PeneloPET emerges as a powerful tool for PET simulations. Some applications will be shown in the following chapters.

5. Validation of PeneloPET

5.1. Introduction

In the previous chapter PeneloPET has been presented. Validation of the code must be performed in order to assess its reliability simulating each specific scanner. Simulation parameters must be tuned for each scanner until good agreement between real and simulated data is obtained. Once the code is validated for a scanner, it can be used for research and development in that specific scanner in order to improve its performance. This chapter presents the results of simulations obtained with PeneloPET and compares them to real scanner measurements and to results from other simulation packages.

To start with the validation, a comparison between results obtained with PeneloPET and those provided by the GATE simulation toolkit is shown. An axial sensitivity profile for a simple configuration based on rPET (Vaquero *et al.*, 2005) scanner was estimated, from both PeneloPET and GATE simulations. In the remainder of this section, we compare simulated measurements with real measurements for four commercial small-animal PET scanners: rPET (Vaquero *et al.*, 2005), ARGUS (Wang *et al.*, 2006), Raytest CLEARPET (Heinrichs *et al.*, 2003) and Siemens INVEON (McFarland *et al.*, 2007). The real measurements from ARGUS, CLEARPET and INVEON scanners were taken from (Wang *et al.*, 2006), (Sempere Roldan *et al.*, 2007), and (Blake *et al.*, 2006) respectively. The simulations tried to reproduce as accurately as possible, with the information available, the geometry and materials mentioned in said references.

5.2. SUINSA rPET scanner

rPET (SUINSA Medical Systems, (Vaquero *et al.*, 2005)) is a rotating scanner consisting of 4 PMT detector modules, each one coupled to a single layer array of 30 × 30 MLS crystals (Pepin *et al.*, 2001). Pitch size is 1.6 mm, individual crystal length is 12 mm, and the ring diameter is 16 cm. A point source has been simulated at several axial positions along the axis of the transaxial FOV. Figure 5.1 shows the ratio of detected coincidences to annihilations at the source, for three different energy windows. Source activity was kept low enough so that dead time, random and pile-up effects could be considered negligible. The number of positron (e^+) annihilations simulated per second using one core of an Intel Xeon X5472 3.00 GHz quad-core processor, were 75000 e^+/sec and 12000 e^+/sec, for PeneloPET and GATE codes, respectively. In both cases, only annihilation photons of 511 keV were simulated, no angular restrictions were imposed, and no secondary particles nor X-rays were considered.

Regarding the accuracy of results, there are small quantitative differences (about 5%) between the sensitivity predictions for the case of the 100-700 keV energy window. For GATE simulations, the GEANT4 standard electromagnetic (EM) model was chosen. Three EM models are available in GEANT4, and thus also in GATE: The standard one, the low energy one and the same PENELOPE model that we employ in PeneloPET. It has been found in several works that these three models produce slightly different predictions (Poon and Verhaegen, 2005). Some authors (Chen *et al.*, 2006) have suggested that the PENELOPE model may be more adequate for Compton interactions, the low energy model for Rayleigh scattering, and the standard EM model of GEANT4 for photoelectric absorption of photons. One must be aware that we simulate not only the interaction of annihilation photons with biological tissue, but also with detector materials, such as scintillator and shielding. Thus

Compton scattering and photoelectric absorption of photons are equally relevant for our simulations. In any case, the differences between these three models are not large, except for the lowest energy photons, which are of little relevance for the results of PET simulations.

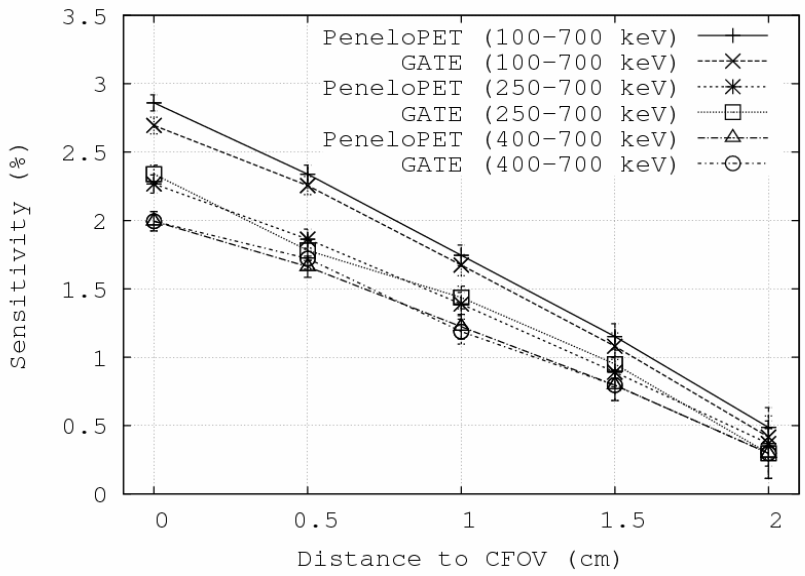

Figure 5.1. Axial sensitivity profile for the rPET scanner, obtained from simulations of a low activity ^{18}F point source. PeneloPET results agree with those obtained with GATE, within error bars, except for the energy window with the lowest energy threshold, for which GATE sensitivities are larger than PeneloPET ones by about 5%. The error bars are taken as ± the standard error obtained from four runs of simulations with different random seeds.

Furthermore, real and simulated sinograms from a mouse phantom acquisition were compared. The real acquisition was performed at Hospital General Universitario Gregorio Marañón, in Madrid. The mouse phantom was made of a rod filled with ^{18}F, 1 cm off-centered in a water cylinder of 2.5 cm of diameter and 6 cm in length (see appendix A). In this comparison we show the radial profiles of coincidences for two different angles. The initial activity was 250 μCi and no energy window was applied. Figure 5.2 shows that there is good agreement between real and simulated data in both peak and background areas.

5.3. SUINSA ARGUS scanner

The ARGUS small-animal PET scanner (Wang et al., 2006) consists of 36 PMT detector modules, each one coupled to a dual layer array of 13 × 13 LYSO+GSO scintillation crystals. Each pixel crystal has a cross section of 1.45 × 1.45 mm^2 separated by a white reflector 0.1 mm thick. The resulting pitch size is 1.55 mm and the length of the LYSO and GSO layers is 7 and 8 mm respectively. The 36 modules are arranged in two rings of 18 modules each, with a diameter of 11.8 cm. All the measurements described in this section are taken from (Wang et al., 2006) except the one regarding the annulus phantom, which was obtained at Hospital General Universitario Gregorio Marañón, in Madrid.

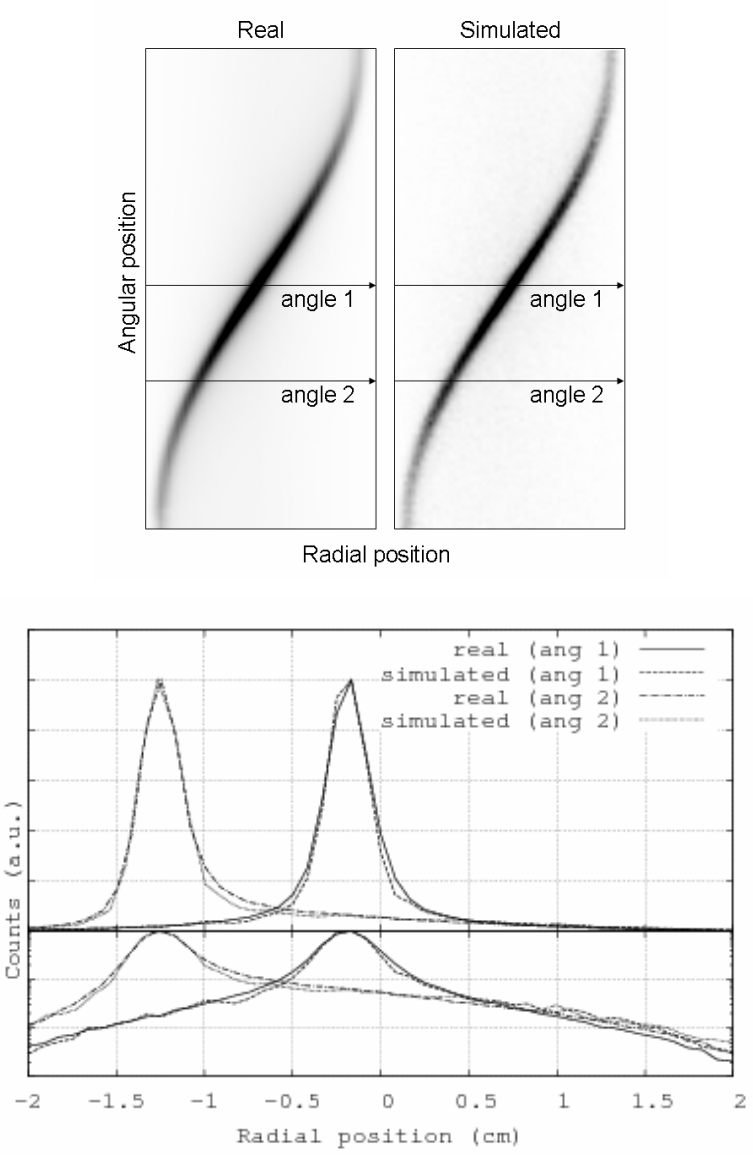

Figure 5.2. Comparison of real and simulated sinograms of a water filled cylinder plus an off-centered rod with ^{18}F (250 μCi), acquired with the rPET scanner. Radial profiles at two different angular positions are shown in the bottom panel with both log (bottom part of the figure) and linear vertical scales. The two arrows in the sinogram of the top panel indicate where the radial profiles shown in the bottom panel are located.

For the first measurement, an annulus phantom made of epoxy containing ^{68}Ge was acquired. This annulus is normally employed to perform normalizations and calibrations of the scanner. It has an inner diameter of 6.92 cm, its walls are 2 mm thick, and its total activity is about 500 μCi. Acquisitions were obtained with three energy windows (100-700 keV, 250-700 keV and 400-700 keV). Figure 5.3 shows a comparison of count profiles resulting from all coincidence events coming from crystals in the same axial row, with the ones from the simulation. The overall shape of these profiles is well reproduced by the simulations. The discontinuity at the center of the profile is due to the gap between the two detector rings. Both real acquisitions and simulations have a very large number of events, so that the statistical error is negligible. The ripple observed in the real profiles may be due to a non uniform axial distribution of shielding and other scanner materials, combined with edge effects of the PMTs, and with the unavoidable (although small) differences in the positions of the real crystals with respect to their *ideal* locations. In the simulation, ideal geometries for the crystal

arrays, PMTs and photocathodes, as well as shielding have been employed. It is thus reasonable to expect a more uniform axial structure for the profile of simulated counts than that exhibited by an actual machine. In any case, this ripple observed in the real acquisitions is about 5% and the difference observed with the simulated results is in the same order.

We can notice a change in shape of the axial profiles according to the energy window selected. From the simulations we can obtain separated contributions to the axial count profiles from true, random and scatter counts, as well as from counts that are affected by pile-up. According to the simulations, we can attribute the largest contribution to this change in shape of the profiles to scatter counts. Further, there is a noticeable difference in the fraction of scatter coincidences registered with the 100-700 keV energy window, as compared to the narrowest one (400-700 keV). The annulus acquisition provides with the necessary normalization information and it is also very useful in order to tune the system response employed by iterative reconstruction codes (Herraiz *et al.*, 2006).

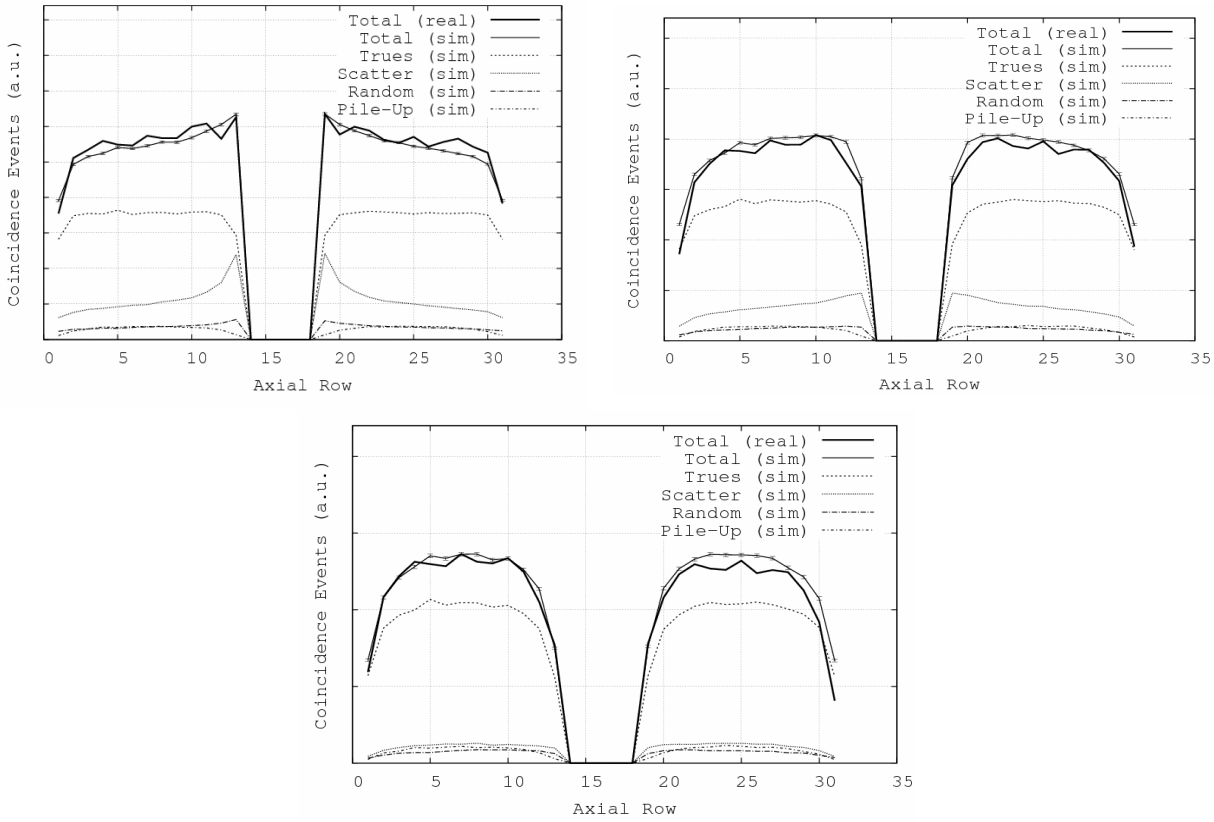

Figure 5.3. Profiles of coincidence counts for crystals in the same axial row, from a 500 μCi ^{68}Ge annulus. Different energy windows are shown: (top-left) 100-700 keV, (top-right) 250-700 keV, (bottom) 400-700 keV. Real (thick solid lines) and simulated (thin solid line) results from PeneloPET are presented. Also, for the simulations, contributions of true, random and scatter counts, as well as counts that are affected by detector pile-up are displayed separately. The small error bars (visible only in the simulated profiles) indicate the expected statistical error[10].

Table 5.1 presents the results for the scatter fraction, real and simulated with PeneloPET. Real values were taken from (Wang *et al.*, 2006). Differences between real and simulated values are below 5% for both the 250-700 and 400-700 keV energy windows. For

[10]In this work the term 'statistical error' denotes the variation in the measured magnitude induced by statistical fluctuations, that is, a variation of $\pm\sqrt{N}$, being N the number of counts accumulated for said measurement.

the 100-700 keV energy window, the simulated values are systematically lower (by about 10%) than the real ones, most likely due to the fact that the simulations did not include secondary particle emissions, such as X-rays, that can contribute at low energies. The expected relative statistical error of the simulations is ± 5%.

Table 5.1. Scatter fraction for the ARGUS scanner.

Energy window (keV)	Mouse phantom		Rat phantom	
	Real	Simulated	Real	Simulated
100-700	33 %	29 %	48 %	42 %
250-700	27 %	27 %	37 %	38 %
400-700	19 %	20 %	29 %	29 %

Figure 5.4 shows the comparison of simulated axial sensitivity profiles against real data from the ARGUS scanner. The agreement of the simulations with the data is very good at the centre of the scanner (they agree within 5%), while there are somewhat larger differences (about 10%) in the relative minima of the sensitivity profile, corresponding to the center of each ring. Outside these two minima, the differences between simulations and real data are below 5%. Overall, the agreement between simulation and data is good.

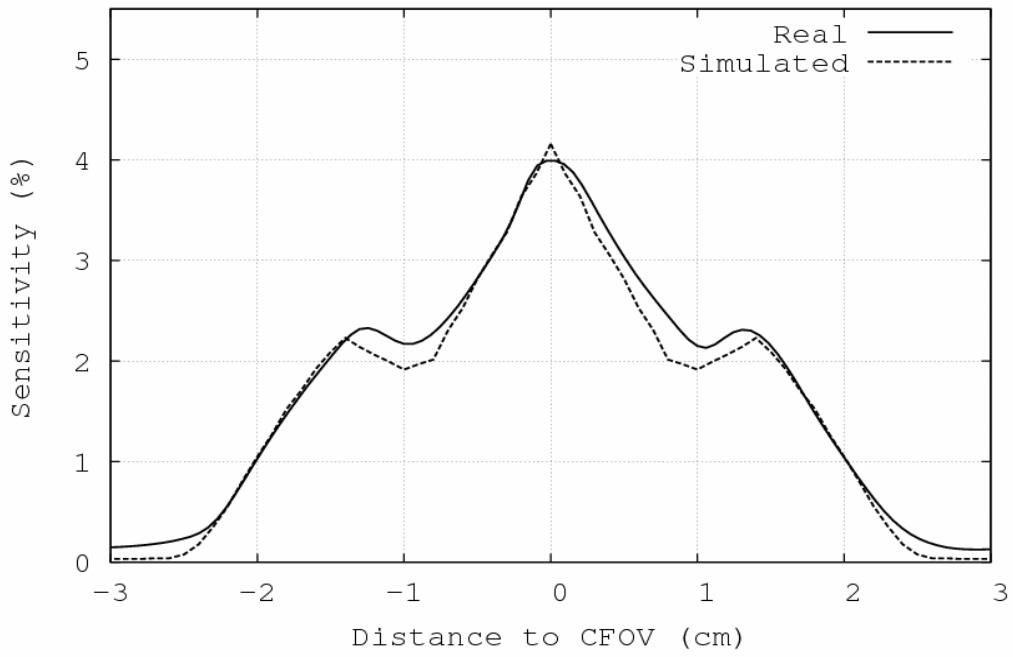

Figure 5.4. Axial sensitivity profile of the ARGUS scanner measured with a 18F point source shifted in small steps along the central axis of the FOV, compared to PeneloPET simulations. Data are from Wang et al (2006). The simulations include inert material and shielding.

Figure 5.5 presents a comparison of radial resolution measured for a ^{22}Na point source placed at different radial distances from the scanner axis, for real and simulated data. The resolution obtained from the simulation is in very good agreement with the experimental data at the center of the FOV while for larger offsets, small deviations of the simulations to the measured results (of no more than 7%) can be observed.

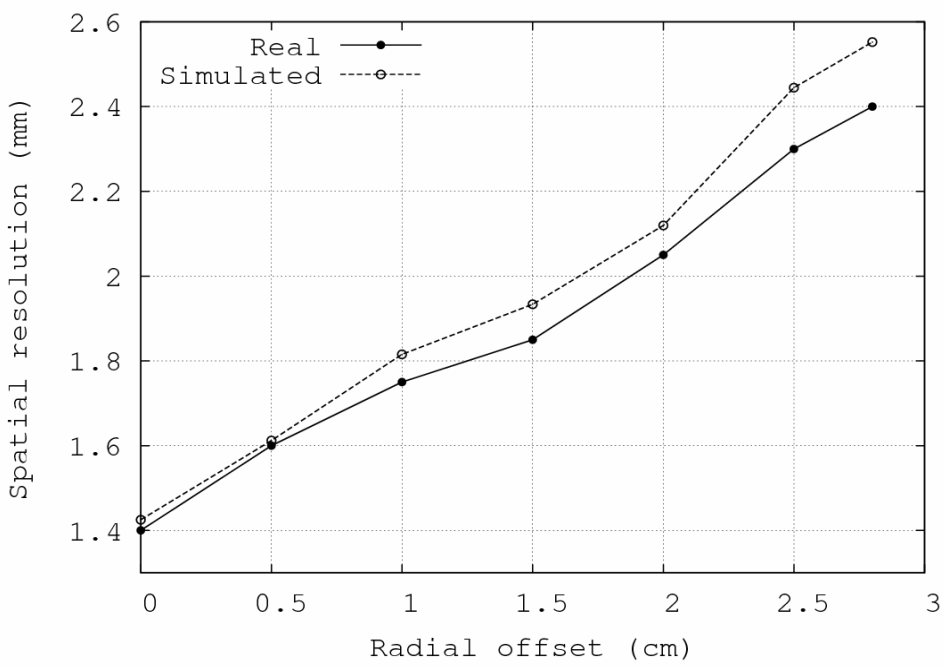

Figure 5.5. Radial resolution of the ARGUS scanner measured with a ^{22}Na point source placed at different radial positions in the central axial slice.

Finally, simulations to obtain the noise equivalent count rate (NECR) for a rat-size phantom have been performed. NECR peak values obtained from real data were taken from (Wang *et al.*, 2006). NECR data simulated with PeneloPET were analyzed to find the position of the NECR peak. Agreement of simulated and real NECR values is good, as shown in Table 5.2. Due to the fact that a finite number of steps are employed to find the maximum of the NECR curves, we estimate that these figures are affected by a relative error lower than 5%, in both position and value of the peak.

Table 5.2. Peaks of the NECR curve of a rat-size phantom for three energy windows, for the ARGUS scanner.

NECR (kcps) [Activity (kBq/cc)]	100-700 keV	250-700 keV	400-700 keV
Real	120 [92]	140 [78]	145 [43]
Simulated	125 [86]	130 [74]	150 [40]

5.4. Raytest CLEARPET scanner

The CLEARPET (Heinrichs *et al.*, 2003) scanner consists of 80 PMT detector modules, each one coupled to a dual layer array of 8 × 8 LYSO+LuYAP scintillation crystals. Each pixel crystal has a cross section of 2 × 2 mm^2 and there is a reflector 0.3 mm thick between crystals. Pitch size is 2.3 mm and the length of both LYSO and LuYAP layers is 1 cm. The 80 modules are arranged in four rings of 20 modules with a diameter of 13.5 cm. Every four contiguous modules in the axial direction form a *cassette*. Every second cassette is alternatively shifted by ± 9.2 mm in the axial direction.

The axial sensitivity profile for the CLEARPET scanner was simulated for configurations with different number of detectors. Simulations of a ^{22}Na point source placed in the axis of the FOV at many positions along the axial direction, are compared to real data taken at 18 positions of the point source along the scanner axis The sensitivity was calculated as the ratio of the number of coincidence events measured inside the energy window of 250 to 750 keV, and the total number of decay processes occurred during the acquisition time. Figure 5.6 shows this comparison. There is good agreement in the central region of the axial profile, where simulation and data are within few percent of each other, and a worse agreement towards the edges of the axial FOV. This is most likely due to the fact that, in this case, the simulation did not include any shielding materials. Shielding material can increase the number of events, due to photons that first interact in the shielding and are then back scattered into a detector. This should have a more noticeable effect near the edges of the axial FOV, increasing the sensitivity there.

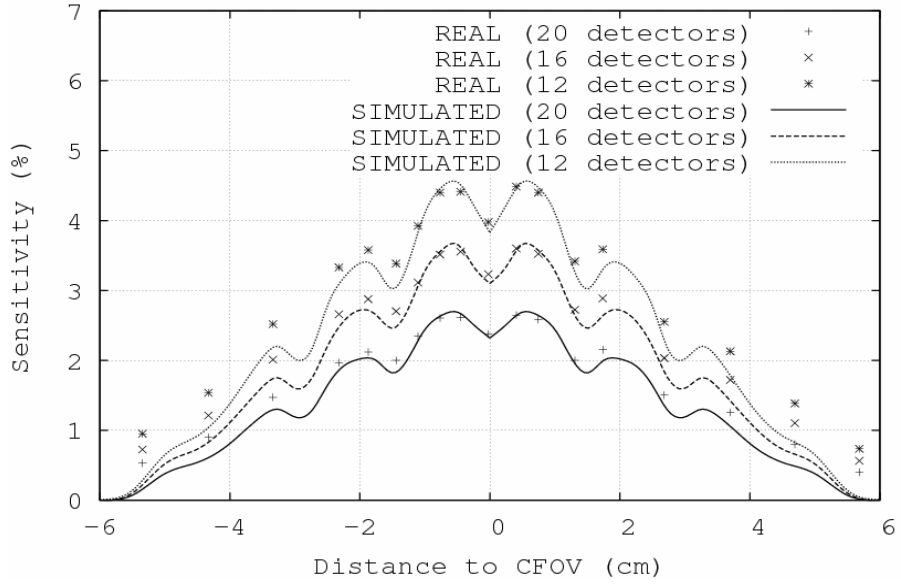

Figure 5.6. Axial sensitivity profile of the CLEARPET scanner. The figure shows measurements and results from simulations for three different scanner configurations (12, 16, and 20 detectors per ring) with a detector diameter of 13.5 cm. Real data are taken from (Sempere Roldan *et al.*, 2007) and are represented with points.

5.5. Siemens INVEON scanner

The INVEON (McFarland *et al.*, 2007) scanner consists of 64 PMT detector modules, each one coupled to a single layer array of 20 × 20 LSO scintillation crystals. Each crystal has a section of 1.55 × 1.55 mm^2 and are separated with a reflector 0.05 mm thick. Pitch size is 1.6 mm and the length of LSO crystals is 1 cm. The 64 modules are arranged in four rings of 16 modules with a diameter of 16.1 cm.

An estimation of the sensitivity of this scanner was made with a line source 14 cm long filled with 1.3 MBq of ^{18}F and placed along the central axis of the scanner. The simulation included all materials of the line source in order to take into account attenuation effects at the source. The sensitivity obtained for the line source activity was converted to equivalent sensitivity for a centered point source, as explained in (Kemp *et al.*, 2006). The sensitivity estimated from real measurements by (Kemp *et al.*, 2006) was 52.0 cps/kBq. The

sensitivity estimated from the simulations was 52.7 cps/kBq, in good agreement with the real measurement.

Figure 5.7 shows the noise equivalent count rate (NECR), obtained from a simulation of a mouse size phantom of plastic material with a 3.6 mm hole, 1 cm off-centered. A line source filled with FDG is introduced in the hole, and an acquisition with an energy window from 350 to 650 keV is performed. This simulation mimics the setup described by (Kemp *et al.*, 2006) to measure the INVEON NECR curve. We have taken the acquisition performance parameters (time and energy coincidence window, etc) according to the values quoted by (Kemp *et al.*, 2006). Figure 5.7 shows the components of NECR obtained from the simulation and the simulated NECR compared to the real measurements. Good agreement for the position of the NEC peak and the maximum NEC counts is found. Agreement is worse at higher rates, probably due to differences in dead time and pile-up rejection mechanisms of the real scanner and the ones included in the simulation.

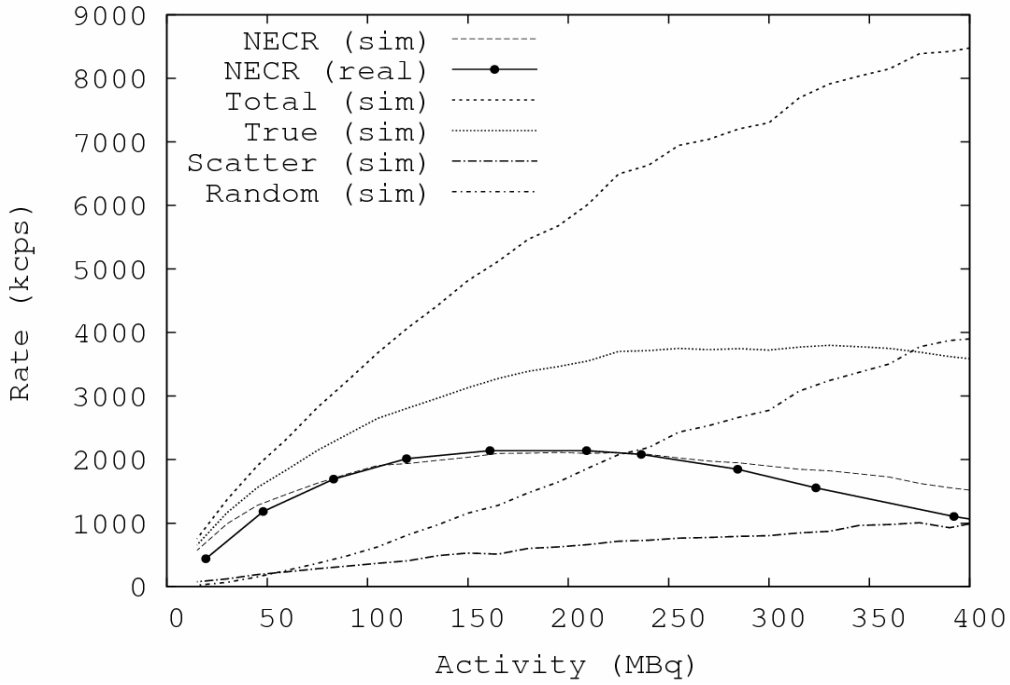

Figure 5.7. NECR curve for a mouse-size phantom acquired with the INVEON scanner. Simulated results are compared to the measurements of reference Kemp et al (2006). Total coincidence rates and true, scatter and random counts contribution are also shown for the simulation.

5.6. Simulation speed

The number of decay events simulated per second (simulation rate) depends strongly on the geometry of the scanner, shielding and surrounding materials included in the simulation. A ^{18}F point source placed at the centre of the FOV, without any other material, apart from detector scintillating material, has been simulated for the four different scanners studied in this work. The simulations tracked only annihilation photons. Results are reported in Table 5.3. Simulation rates correspond to a core of an Intel Xeon X5472 3 GHz quad processor. The parallel version of the code can use the four cores of the processor obtaining a four-fold increase in these simulation rates. The numbers in the table correspond to the actual rate of processed decays, without any angular restriction for the direction of the photons emitted.

Table 5.3. Number of decay events simulated per second (simulation rate) for a ^{18}F point source at the center of the FOV and different scanner geometries.

Scanner	Simulation rate
rPET	75000 e^+/s
ARGUS	12000 e^+/s
CLEARPET	11000 e^+/s
INVEON	17000 e^+/s

5.7. Conclusions

Due to its versatility, good simulation speed, and easy-to-analyze outputs, PeneloPET is a useful tool for scanner design, system response calculations, development of corrections methods, and other applications. Though a detailed comparison between GATE and PeneloPET was not the goal of this work, for the purpose of validation of this new PET simulation tool, we have compared PeneloPET to GATE in one instance, showing that PeneloPET seems to be faster than GATE, while producing results that differ less than few percent of GATE's predictions. Detailed comparisons of GATE and PeneloPET simulations will be dealt in further works. We have also compared simulations of PeneloPET against real measurements from four different small-animal PET scanners. We have compared both integral or extensive properties of scanners, such as sensitivity, axial profile of counts, scatter fraction, and NEC rates as well as intensive ones, namely sinogram profiles and spatial resolution, finding in general good agreement between simulated and real data (España *et al.*, 2009).

6. Estimation of the system response matrix

6.1. Introduction

Previous chapters introduced and validated PeneloPET (España *et al.*, 2009), our Monte Carlo tool for PET applications. In this chapter, we apply PeneloPET to the calculation of the system response matrix (SRM) for statistical reconstruction methods. The main goal would not be only to store a very accurate SRM but also to reduce its size as much as possible, in order to achieve fast reconstructions.

Small animal PET scanners require high spatial resolution and good sensitivity. To reconstruct high-resolution images in 3D-PET, iterative methods, such as OSEM, are superior to analytical reconstruction algorithms, although their high computational cost is still a serious drawback (Johnson *et al.*, 1997; Herraiz *et al.*, 2006). The performance of modern computers could make iterative image reconstruction fast enough and able of dealing with the large number of probability coefficients of the system response matrix, in high-resolution PET scanners, which is a difficult task that prevents the algorithms from reaching peak computing performance. Considering all possible axial and in-plane symmetries, as well as certain quasi-symmetries, it has been possible to reduce the memory needed to store the system response matrix (SRM) well below 1 GB, which allowed us to keep the whole response matrix of the system inside the RAM present in ordinary industry-standard computers, so that the reconstruction algorithm can achieve near peak performance. If the SRM does not fit in RAM, the performance of the reconstruction is affected significantly, due to the large time required to access the hard disk. In our implementation, the elements of the SRM are stored as cubic spline profiles and matched to voxel size during reconstruction. In this way, the advantages of *on-the-fly* calculation and of fully stored SRM are combined. The *on-the-fly* part of the calculation (matching the profile functions to voxel size) of the SRM accounts for 10–30% of the reconstruction time, depending on the number of voxels chosen. This approach has been tested with real data from a commercial small animal PET scanner. The results (image quality and reconstruction time) show that the technique proposed is a feasible solution.

Statistical 3D reconstruction methods such as expectation maximization (EM) (Shepp and Vardi, 1982; Browne and de Pierro, 1996; De Pierro and Yamagishi, 2001) have shown superior image quality than conventional analytic reconstruction techniques. Moreover, EM has some desirable properties, such as conservation of the number of counts, non-negativity, good linearity and dynamic range. One of the key advantages of statistical reconstructions is the ability to incorporate accurate models of the PET acquisition process through the use of the system response matrix (SRM). However, SRM for 3D systems are of the order of several billions of elements, which imposes serious demands for statistical iterative methods in terms of the time required to complete the reconstruction procedure and the computer memory needed for the storage of the SRM. A new EM-based reconstruction methodology has been designed, developed, implemented and tested, that provides fast reconstructions while remaining very flexible. With this approach, the usual difficulties of iterative reconstruction methods regarding the large size of the SRM, or the use of unrealistic estimates of it, are overcome by means of a compressed and realistic SRM. The efficiency of the proposed method relies on the design and method of storing this SRM. The imaging process of obtaining the *y(i)* counts on each of the *i* pair of detectors, from an object discretized in *x(j)* voxels, can be described by the operation

$$y(i) = \sum_j A(i,j)\,x(j) \qquad (6.1)$$

where *A(i,j)* is the SRM, the vector *x(j)* corresponds to the voxelized image and *y(i)* to the measured data. Each element *A(i,j)* is defined as the probability of detecting an annihilation event coming from image voxel *j* by a detector pair *i*. This probability depends on factors such as the solid angle subtended by the voxel to the detector element, the attenuation and scatter in the source volume and the detector response characteristics.

The forward projection operation just introduced above, estimates the projection data from a given activity distribution of the source. Backward projection is the transposed operation of forward projection; it estimates a source volume distribution of activity from the projection data. The operation corresponds to

$$b(i) = \sum_i A(i, j)\, y(i) \tag{6.2}$$

where *b(j)* denotes an element of the backward projection image. Both the forward and backward projection operations require the knowledge of the SRM (Frese *et al.*, 2001; Rafecas *et al.*, 2004). Iterative reconstruction algorithms repeatedly use the forward and backward projection operations, which are the most time-consuming parts of iterative reconstruction programs. Some implementations trade accuracy for speed by making approximations that neglect some physical processes, such as positron range, scatter and fractional energy collection at the scintillators or visible light loses in the detectors (Vaquero *et al.*, 2004; Lee *et al.*, 2000; Yamaga and Murayama, 2002-2003). This approach simplifies these operations to gain speed, but this trade-off often leads to non-optimal images.

The evaluation and storage of SRM elements is a very active subject of research. Ideally, the SRM could be calculated, using MC methods (Rafecas *et al.*, 2004) or from empirical data (Frese *et al.*, 2001), and stored once and for all before the beginning of the reconstruction process. In practice, memory requirements for doing this have become prohibitive so far. A number of methods have been proposed to compute and handle huge sparse matrices, like usual SRMs. Some implementations compute the elements *A(i,j)* on the fly, only if and when they are required (Kudrolli *et al.*, 2002), thus avoiding the need to store the whole SRM.

Table 6.1. Vista parameters (Wang *et al.*, 2006).

Ring diameter	11.8 cm
Aperture	8 cm
Axial FOV	4.8 cm
Number of DOI detector modules	36 position-sensitive PMTs
Number of dual-scintillator DOI elements	6084
Crystal array pitch	1.55 mm
Total number of crystals	12 168
Total number of 3D coincidence lines	28.8×10^6

In other approaches, the SRM has been factorized as a product of independent contributions: geometry, attenuation and detector sensitivity (Qi *et al.*, 1998). However the simplifications required by *on-the-fly* or factorized calculations, often overlook important effects (Lee *et al.*, 2004).

Due to the fact that SRMs are very large, but sparse, they may be kept on disk using sophisticated storage schemes and taking advantage of system symmetries (Johnson and

Sofer, 1999) that allow for reducing the size of the SRM to a few tens of gigabytes. Due to the fact that accessing the SRM from disk for every forward and backward projection operation is very slow, it will considerably slow down the reconstruction. Our approach involves compressing the SRM to an extent that enables its allocation in the RAM memory of industry-standard computers, avoiding disk access during reconstruction. In this way, it is possible to achieve a sustained performance of around 50% of the theoretical peak computing capability of the processors.

6.2. System response matrix (SRM)

The SRM is composed of all the $V \times L$ probability elements $A(i,j)$, $i = 1,...,L$, $j = 1,...,V$, representing the probability of detecting an event coming from voxel $V(j)$ at detector LOR $L(i)$. Forward and backward projections require the knowledge of all of these elements. This matrix depends on factors such as the physics of beta decay, attenuation and scatter in the source volume, solid angle subtended from voxel to detector element and intrinsic detector response characteristics. For a reconstruction method to be accurate, all these effects should be considered. The equipment used in this study is an eXplore Vista-DR (GE) small animal PET scanner (Vaquero *et al.*, 2004). It is a ring-type scanner with a diameter of 11.8 cm, a transverse FOV of 6.8 cm and an axial FOV of 4.6 cm. Vista technology is based on scintillator detector modules with depth-of-interaction (DOI) capabilities (Lee *et al.*, 2000) arranged in single (SR) or double rings (DR). The detector modules are composed of a 13 × 13 crystal array with 1.55 mm pitch size. The number of LORs in this scanner is over 2.8×10^7 (see Table 6.1). DOI determination enables both spatial resolution and sensitivity to be improved simultaneously (Yamaga and Murayama, 2002-2003).

From the data of Table 6.1, and at nominal image resolution of 175 × 175 × 62 voxels (near 1.9 millions of voxels), the number of elements in the SRM (number of LORs × number of voxels) is of the order of 5×10^{13}. Storing all the elements of the SRM would require more than 10 TB (Rafecas *et al.*, 2004). This exceeds the resources of any ordinary workstation, making it necessary to disregard all redundant elements and to perform approximations, in order to be able to store the SRM in the limited amount of RAM of ordinary workstations. Three techniques have been used to achieve this goal: null or almost-null element removal (matrix sparseness), intensive use of system symmetries and compression of the resulting SRM employing quasi-symmetries.

6.2.1. Sparseness of the SRM

Every detector pair can receive coincidence counts only from a relatively small portion of the FOV. Thus, most matrix elements of the SRM are null and only the non-zero elements should be stored, reducing considerably the storage requirements. To estimate how many non-zero elements of the SRM have to be taken into account, we have proceeded as follows: the voxels connected to a given LOR (that is, the voxels from which positron decay can produce with non-negligible probability a valid coincidence count in the detectors that define the LOR) constitute the so-called tube of response or TOR (Michel *et al.*, 2002) for that LOR. Extensive simulations determine the maximum size of the TOR needed and only the SRM elements that are part of some TOR are stored. A voxel will be considered as not connected to a LOR (i.e., not being part of the TOR) when the probability that a positron emitted from that voxel yields a count in the corresponding detector pair is smaller than one-thousandth of the maximum value of all the voxels for such given TOR. For the scanner considered here, it has been used a nominal number of voxels of 175 × 175 × 62 in XYZ to cover the FOV. This yields a voxel size of 0.38 × 0.38 × 0.76 mm^3 (see Table 6.1) and an average number of

voxels in a TOR of about 6000 for a typical TOR size of 150 (longitudinal) × 10 (transverse width of the TOR in the transaxial XY plane of the scanner) × 4 (transverse width in the axial or Z direction scanner) voxels (Johnson and Sofer, 1999). With these choices, the number of non-zero elements of the SRM is then 28.8×10^6 LORs × 6000 connected voxels on average or 10^{11}elements. That is, only around 0.2% of the elements of the SRM are non-zero. Yet, storing these non-zero elements as floats (4 bytes per SRM element) will require about 600 GB of disk space, still too high for the current RAM amount of industry-standard computers.

6.2.2. System symmetries

An additional reduction factor of approximately 40 in the number of non-null SRM elements to be stored can be achieved by assuming that (exact) axial (translation and reflection) and in-plane symmetries exist (Johnson and Sofer, 1999). Voxels are chosen in an orthogonal grid oriented along X, Y and Z-axis, with Z being the axis of the scanner. If an integer number of voxels is employed for the width of the TOR in the Z-axis, then there is a Z-translation symmetry, due to the fact that voxels in the same relative position of the TOR and belonging to parallel TORs should have equal values (see Figure 6.1).

It must be noted that although our SRM exhibits indeed this translational symmetry, in real scanners, due to edge and block effects, it is only an approximate symmetry.

There is also another axial symmetry, Z-reflection symmetry. Using both parallel and reflection Z-symmetries, the number of elements to be stored is reduced considerably. Each pair of blocks has (2×13×13)×(2×13×13) LORs, but using symmetries, only 2×13×(2×13×13) need to be stored. A factor 13 of reduction is achieved.

Another symmetry, namely reflection symmetry among blocks in the XY plane, also holds. Using this, the number of pairs of detectors that have TORs with different values is reduced by a factor of 3. Using them all, as already mentioned, these symmetries allow to reduce by a factor or near 40 the number of different elements of the SRM that must be stored. Storage needs can thus be reduced to a few (slightly less than 10, for the considered scanner) GB, small enough to fit in hard disks, yet too much to be maintained in RAM.

6.2.3. Compressed SRM

The last step of the method proposed uses additional non-exact symmetries, or quasi-symmetries, in order to obtain additional reduction of the SRM. Allowing for relatively small differences between quasi-symmetric elements of the SRM (versus no difference *a priori* in the case of the exact symmetries), we can group certain LORs into sets of the same quasi-symmetry class. The differences between elements of the SRM for LORs belonging to a given class should be much smaller than between LORs from different classes. Quasisymmetry classes can be obtained, for instance, by grouping together LORs from crystals with different, but close, LOR-crystal orientations. The differences among the elements of the same quasi-symmetry class are about 5–10%, depending on the amount of compression (reduction in size) desired (Herraiz *et al.*, 2006).

In Figure 6.1 to Figure 6.3, this procedure is illustrated with an example taken from the simulations. MC events were generated at different positions inside a TOR. As shown in Figure 6.2, LORs 1–3 are parallel or almost parallel to the crystals and thus the probability values along these three TORs should be very similar. Analogously, LORs 4–6 have a large LOR-crystal angle, similar for the three of them. In Figure 6.3, longitudinal profiles along these LORs are shown. Indeed, the results of the MC simulations for the calculation of the probabilities for LORs 1–3 (and 4–6), shown by the data points (which include statistical

error bars), are very similar. It could even be possible to say that these are the same within error bars. In Figure 6.4, now the profiles of the TORs along the transverse direction to the LORs (s-coordinate) are shown at several values of the l-coordinate. As in the case of the longitudinal profiles, it can be seen that the results of the simulated data for the near equivalent LORs 1–3 or 4–6 are very similar. Moreover, it has been realized that the variation of probability inside a TOR is smooth, which allows us to fit the simulated points to profiles with an smooth interpolating cubic spline. The differences among the results of the interpolating curves for LORs 1–3 are marginal and the three interpolating curves could be considered identical within the statistical error bars of the MC points. A similar observation can be made for TORs 4–6. Our quasi-symmetry assumption means that the same profile functions will be employed for TORs 1–3 that belong to the same quasisymmetry class. TORs 4–6 belong to another quasi-symmetry class and are represented by one set of profile functions, different from those of the other quasi-symmetry classes.

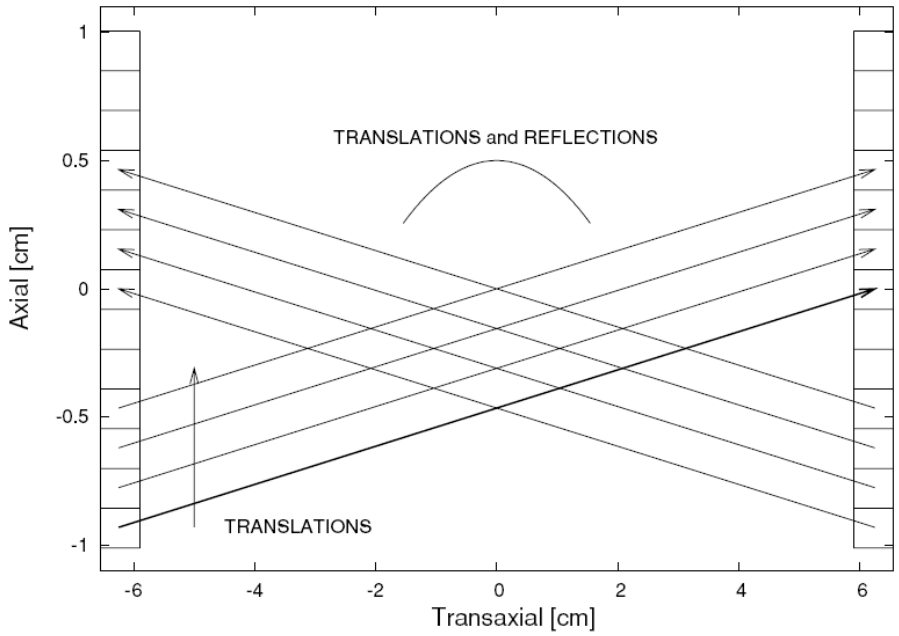

Figure 6.1. Schematic drawing of a Vista small animal PET scanner detector pair, showing the (exact) translation and reflection symmetries employed in this work. All the elements of the SRM belonging to parallel LORs are, by symmetry, equivalent.

Depending on the geometry of the system, the use of quasi-exact symmetries allows us to obtain a number of quasi-equivalent LOR classes (that is, TORs with non-equivalent values) which may be 9 (in the example so far discussed) to 25 (for up to five different LOR-crystal angles in the same quasi-symmetry class, allowing for larger differences among the profiles within the same quasi-symmetry class) times smaller than the number of classes obtained with only exact symmetries. The elements of this notably reduced SRM are encoded as transverse and longitudinal profile functions, obtained by cubic spline interpolation of MC sampled points. For each transversal or longitudinal profile, MC estimates of probability at 20 points along or across the TORs, are employed to determine the cubic spline profile functions. At reconstruction time, the probability element of the SRM corresponding to each voxel inside a TOR is obtained by interpolation of the profile functions. If the voxel size chosen is large, it averages several values interpolated from the profile functions at different points inside the voxel, in order to compute the probability for each voxel. The interpolation and averaging of probability from profile functions inside each voxel is compared with the results

of average of points obtained directly from the MC simulations. From these comparisons, it is possible to conclude that, for a number of voxels above or below a factor of 3 of the nominal number of voxels of 175 × 175 × 62, the interpolation procedure differs typically by less than 5% from the results of direct MC simulation, in the example shown in Figure 6.2 to Figure 6.4 (three different LOR-crystal angles) and by less than 10% for larger quasi-symmetry class (five different LOR-crystal angles).

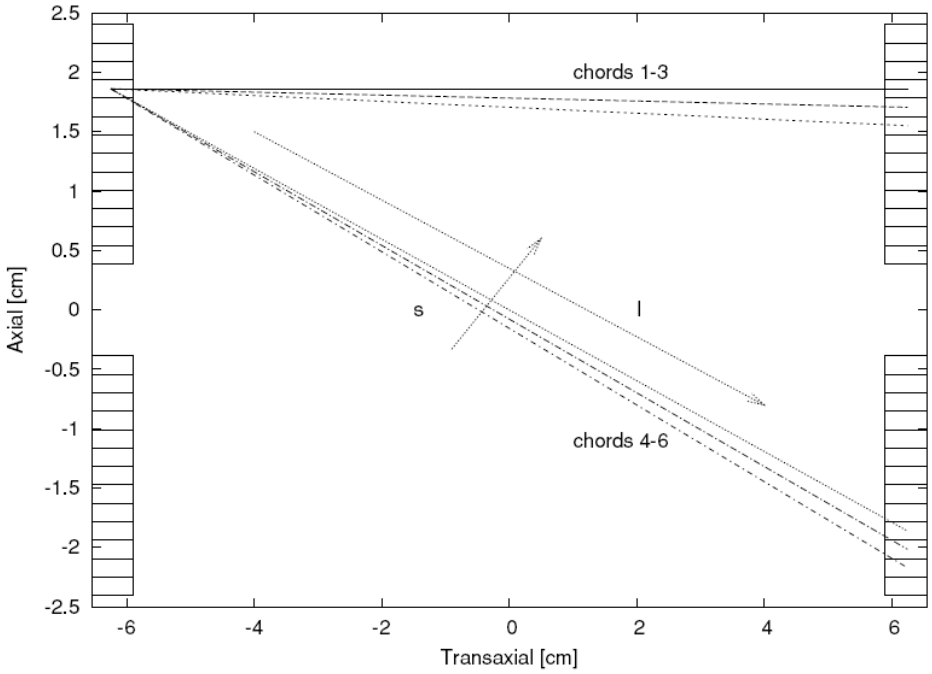

Figure 6.2. Schematic representation of several lines of response (LOR) considered for the discussion on quasi-symmetries. Three LORs (numbered 1–3 from top to bottom) with a small relative LOR-crystal angle and three (numbered 4–6, also from top to bottom) with large relative LOR-crystal angle are depicted. l and s are the coordinates along the LOR direction and normal to it, respectively.

In short, the same quasi-equivalent profiles can be used to build the non-zero SRM elements for a reasonable range of voxel sizes. The optimal voxel size that should be employed for each reconstruction may be different depending for instance on the number of counts of a particular acquisition. This profile function approach makes it possible to generate reconstructions with different voxel sizes, without the need to recompute the SRM elements. Eventually, this process leads to a compressed SRM that fits in 30–150 MB, depending on the degree of quasi-symmetry assumed.

To end this section, it will be commented on the storage strategy that is also useful to save space. All the cubic spline coefficients for the profiles of a quasi-symmetry class (or superTOR) are rescaled in order to convert (and store) them as integer values. Two bytes are employed to represent every coefficient, which allows us to represent ratios of more than 60 000 to 1 inside the same TOR. The scale factors (maximum and minimum values of the coefficients for all the profiles in each superTOR) are also recorded as two additional floating numbers. During reconstruction, the integer values are converted into the adequate float ones on the fly. The FOV is divided in voxels arranged in an orthogonal grid. For a given TOR, voxels are visited from bottom to top, left to right and back to front directions. Every voxel in the superTOR is visited in order and the SRM element corresponding to that voxel–LOR combination is obtained by interpolation of the cubic spline profiles. Then, the superTOR

values are stored as a list of numbers formed by the probabilities of each voxel of the superTOR visited in the assumed order. Once the superTOR is obtained (decompressed) on the fly, all the operations (forward or backward projections) that involve the TORs in the quasi-symmetry class are performed.

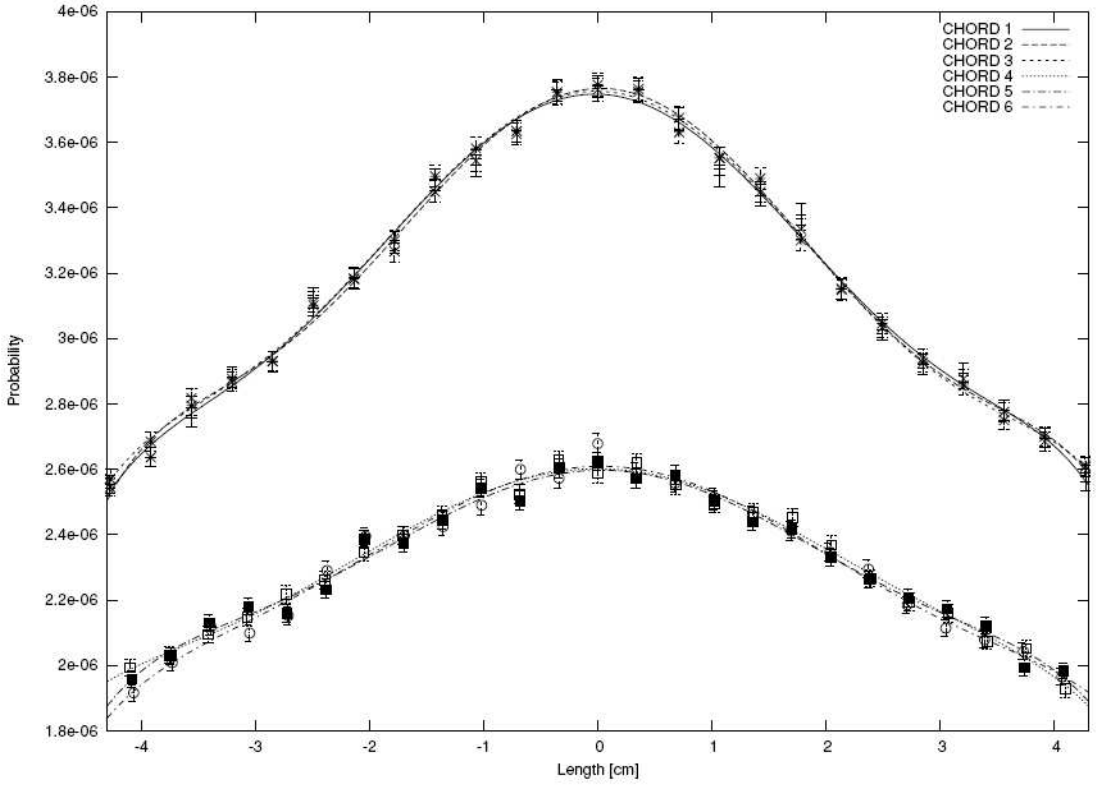

Figure 6.3. Longitudinal profiles of the probability elements for the LORs shown in Figure 6.2. The probability of detection of a coincidence count in LORs 1–6 per every positron decay in the axis of the TOR as a function of the distance to the centre of the TOR is shown. The data points represent the results for the MC simulation described in the text, the error bars are given by the statistical uncertainty. Symbols employed are as follows: 1, plus (+) sign; 2, times (×) sign; 3, star (*) sign; 4, empty square; 5, solid square; 6, empty circle. Profiles fitted to the points by means of cubic splines are also shown. The small crystal-LOR angle (1–3) profiles are very similar among them, but rather different from the large crystal-LOR angle ones (4–6).

6.2.4. MC simulation

Given the fact that the compressed SRM fits in RAM, it does not need to be computed during reconstruction, nor read from disk once loaded in memory at the beginning of the reconstruction. Thus, the SRM can be computed using a very realistic model and stored once and for all. Monte Carlo (MC) methods are, in principle, well suited to provide realistic estimates of SRM elements. In this case, a self dependent MC model, PeneloPET (España *et al.*, 2009), has been used. It includes scatter and incomplete collection of energy in the scintillator crystals, positron range and non-collinearity effects. Positron range is dependent on the object. In order to incorporate its effect in the SRM, in our simulations the range is computed assuming that water fills uniformly the whole FOV. Most importantly, the scatter of gamma photons when they reach the scintillator crystals has been included too. The comparison of simulated phantoms with actual acquisitions reveals that the simulation is very realistic indeed.

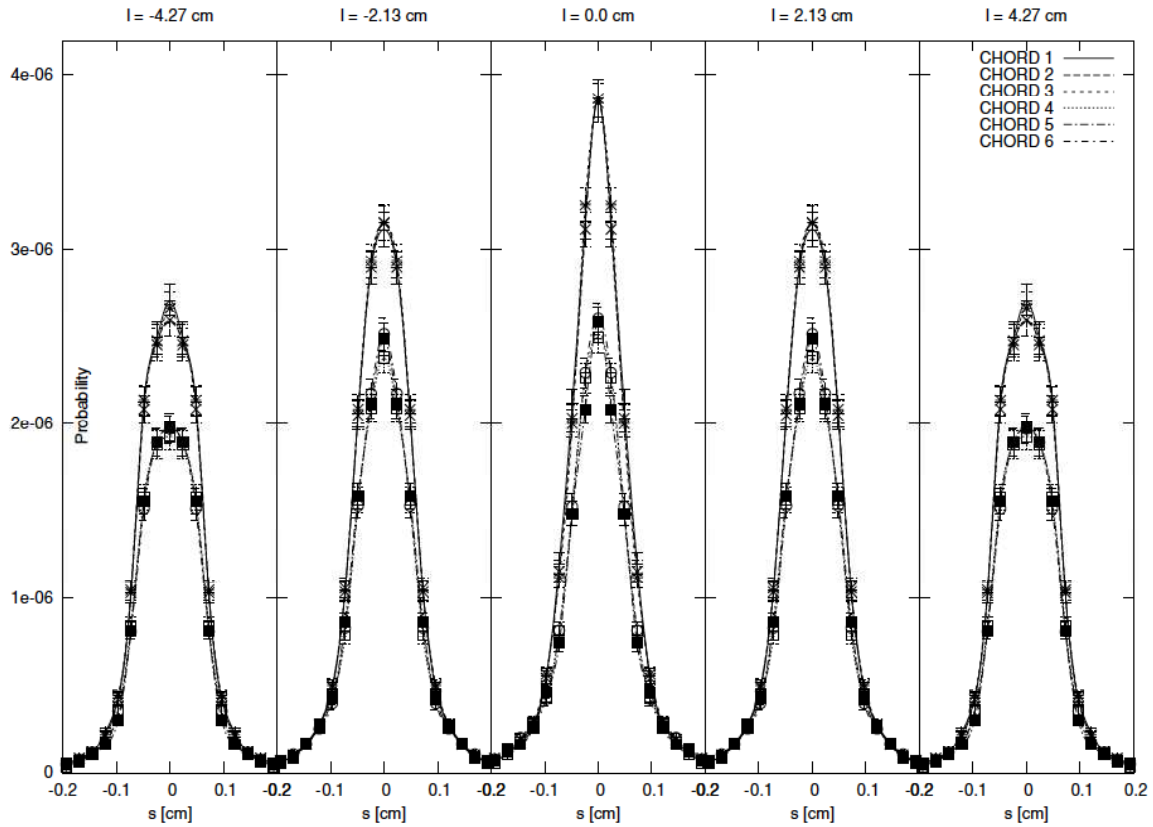

Figure 6.4. Transverse profiles of LORs 1–6 of Figure 6.2. Data points and curves as in Figure 6.3. Several profiles at different distances l to the centre of the LOR are shown. The transverse width of the TORs shown in the figures is around 4 mm, or three crystal widths.

A large number of simulated events are accumulated until the statistical uncertainty is below 5% at the centre of a typical LOR. Several weeks of computing time were required for the calculation of the SRM in a cluster composed of 100 cores AMD Opteron processors. The total time employed for the full MC simulation is 2 days.

6.3. Iterative algorithms for image reconstruction

To test the accuracy of the compressed SRM obtained, it has been used one of the most widely applied algorithm for finding the maximum-likelihood (ML) estimation of activity x given the projections y, that is, expectation maximization (EM). This was first applied to the emission tomography problem by Shepp and Vardi (Shepp and Vardi, 1982). ML, though, is a general statistical method, formulated as a method for solving many different optimization problems.

Usually, iterative algorithms obtained from the ML statistical model assume that the data being reconstructed retain Poisson statistics. However, to preserve the Poisson statistical nature of data it is necessary not to perform any pre-corrections (Qi *et al.*, 1998). Corrections for randoms, scatter and any other effects should be incorporated into the reconstruction procedure itself, rather than being applied as pre-corrections. At times, sophisticated rebinning strategies are employed to build sinograms into radial and angular sets, which changes the statistical distribution of the data, which may no longer be Poisson like (Kadrmas, 2004). Furthermore, much attention must be paid in order that sinogram rebinning does not cause a loss in the potential accuracy of the reconstruction. Our approach does not involve

sinograms in any way, thus preserving all the information obtained during the acquisition. Uncorrected data, binned into raw 3D-LOR histograms, should maintain Poisson statistics (Kadrmas, 2004).

A serious disadvantage of the EM procedure is its slow convergence (Lewitt and Matej, 2003). This is due to the fact that the image is updated only after a full iteration is finished, which implies that all the LORs have been projected and back projected at least once. In the ordered subset EM (OSEM) algorithm, proposed by Hudson and Larkin (Hudson and Larkin, 1994), the image is updated more often, which has been shown to reduce the number of necessary iterations to achieve a convergence equivalent to that of EM.

According to the literature, EM methods have another important drawback: noisy images are obtained from over-iterated reconstructions, and this is usually attributed to either the fact that there is no stopping rule in this kind of iterative reconstruction or to the statistical (noisy) nature of the detection process and reconstruction method (Bettinardi *et al.*, 2002; Biemond *et al.*, 1990). In practice, however, an image of reasonable quality is obtained after a few iterations. Several techniques have been proposed to address the issue of the noisy nature of the data: filtering the image either after completion of the reconstruction, during iterations or between them (Slijpen and Beekman, 1999), removal of noise from the data using wavelet based methods (Mair *et al.*, 1996) or smoothing the image with Gaussian kernels (Sieves method) (Snyder *et al.*, 1987; Liow and Strother, 1991).

Maximum a priori (MAP) algorithms are also widely used (Green, 1990). MAP adds *a priori* information during the reconstruction process, the typical assumption being that, due to the inherent finite resolution of the system, the reconstructed image should not have abrupt edges. Thus, MAP methods apply a penalty function to those voxels which differ too much from their neighbors. Whether the maximum effective resolution achievable is limited, or even reduced, by the use of these methods is still an open issue. On the other hand, a proper choice of the reconstruction parameters, such as the number of iterations, the use of an adequate system response and a smart choice of subsetting, allows to obtain high quality images by the EM procedure (Herraiz *et al.*, 2006).

An OSEM algorithm has been implemented (Herraiz *et al.*, 2006) that includes the possibility of MAP by means of a generalized one-step late MAP-OSEM algorithm, similar to the one described in Lewitt and Matej (Lewitt and Matej, 2003) and Kadrmas (Kadrmas, 2004):

$$x^{n,s+1}(j) = x^{n,s}(j)\left[\frac{\sum_{i\in SubsetS} A(i,j)\dfrac{y(i)}{\left(R_i^n + S_i\right)}}{\sum_{i\in SubsetS} A(i,j)\left(1+Penalty(j,n)\right)}\right] \qquad (6.3)$$

where the parameters and functions are defined as follows: *x(j)* is the activity of voxel *j (j = 1*, maximum voxel number *V*), $x^{n,s}(j)$ is the expected value of voxel *j* at iteration *n* and subiteration *s*, *A(i, j)* is the probability that a photon emitted from voxel *j* is detected at LOR *i*, *y(i)* is the projection from the object measured at LOR *i* (experimental data), S_i is the object scatter and random coincidences at LOR *i*, *Penalty(j,n)* is the penalty value at voxel *j* and iteration *n*, R^n is the projection estimated for the image reconstructed at iteration *n*:

$$R_i^n = \sum_{j=1}^{Voxels} A(i,j)\,x^n(j) \qquad (6.4)$$

This MAP-OSEM algorithm can be considered as a generalization of the ML–EM. It incorporates a penalty MAP function which can be chosen in different ways (Stayman and Fessler, 2001, Yu and Fessler, 2002, Nuyts and Fessler, 2003), and scatter and random counts estimates, that may require additional modeling of these processes. OSEM reconstruction without MAP regularization is obtained by setting the penalty function to zero. However, it can be noted that in this chapter are mostly interested in the way to compress the SRM and not in the effect of MAP on the image quality, and thus all the reconstructed images presented here are obtained with zero penalty.

With regard to attenuation, as it is a relatively minor effect for small animal PET (Yao *et al.*, 2005) and our main aim is to test the adequacy of our compressed SRM and not the importance of attenuation, it has not been included in the reconstructed images shown.

6.4. Results of simulations

6.4.1. Test set

To test our methodology, it was first reconstructed data from different simulated phantoms: uniform cylinders and point sources in different axial and transaxial positions and simulated microresolution and Defrise phantoms. In order to study the linearity of the reconstruction method as well as the conservation of the number of counts and noise properties, a *spiral phantom* was designed (Figure 6.8 and Figure 6.9). It was comprised of three cylinders (background) of 11.5 mm in diameter, each with two spirals inside: a hot one (activity four times greater than the background) and a cold one (activity four times lower than the background). The diameter of these spiral shape cylinders are 1.4, 2.2 and 2.6 mm. Events were generated from these test sets using our own MC (España *et al.*, 2009; Herraiz *et al.*, 2006) method, taking into account positron range and non-collinearity effects. Neither attenuation nor scatter within the object were included for these simulations. The response of the detector was also realistically simulated considering the main physical effects contributing to the spread of the energy among crystals due to scatter in the scintillators. For each study, 10^{10} events were simulated and stored as projection data. It has been realized that the realistic model of detector response resulted in wider TORs, which contained many more voxels than when more simplistic models of the system response are used. The images reconstructed from these simulations have a resolution of 175 × 175 × 62 voxels. The size of the phantoms and the images were chosen to be the same as the FOV of the eXplore Vista-DR (GE), namely 65 mm in diameter. Thus, the voxel size is 0.38 × 0.38 × 0.78 mm^3.

6.4.2. Evaluation

Initial tests were run to verify that the compressed SRM and the uncompressed SRM yielded images of similar quality and with no artifacts (see Figure 6.5). The effect of compression in the SRM on the reconstructed images will be commented in more detail in the next section.

In a second step, an estimate of the point spread function (PSF) was obtained by using a phantom consisting of an array of small sources located at different radial and axial positions and separated by 5 mm. Resolution obtained from reconstructions of simulated projections as well as from real phantoms are shown in Table 6.2, revealing that submillimetre resolution can be obtained from real projections. As shown in the figures and summarized in Table 6.2, very uniform values of resolution (as measured by FWHM)

throughout the FOV of 0.7 mm (at centre of the scanner) to 0.9 mm (2.5 cm off axis) were obtained.

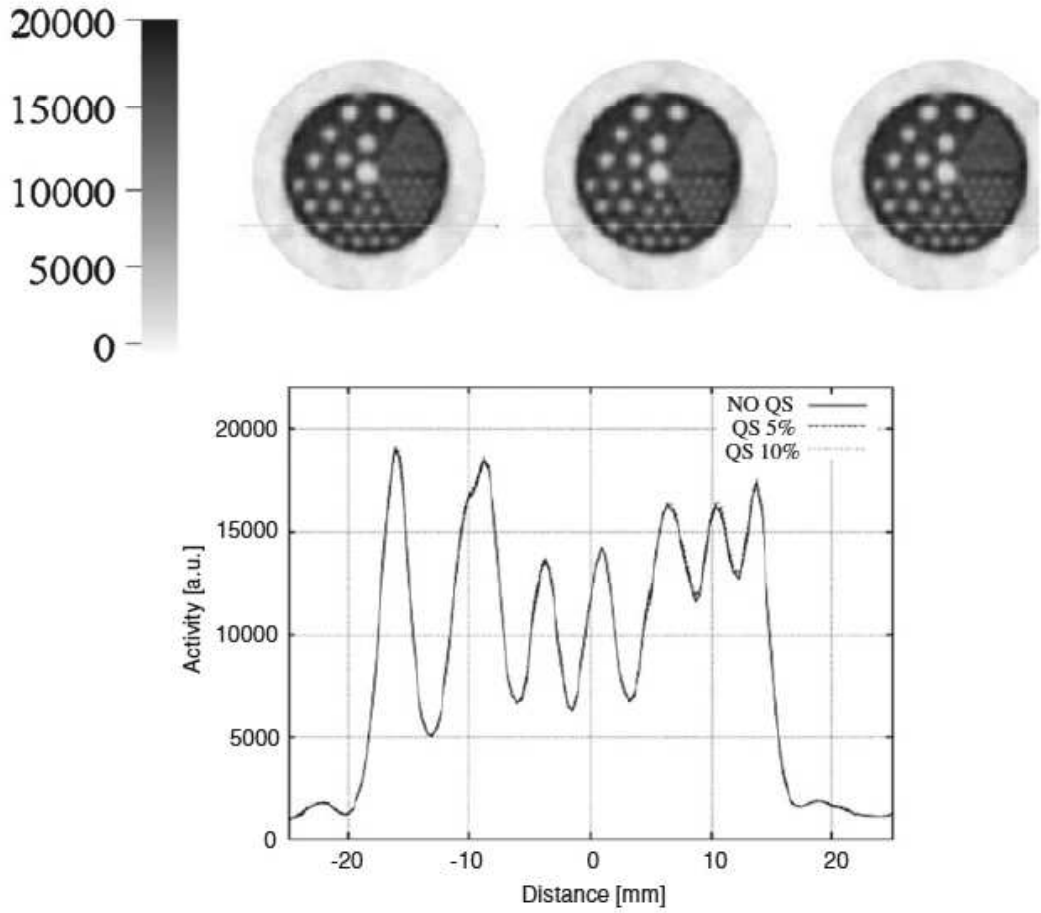

Figure 6.5. Reconstructions with different degree of quasi-symmetry assumptions. Transaxial slices of a 1 iteration of 100 subsets, 3D-OSEM reconstruction, of a cold Derenzo phantom (1 mCi of ^{68}Ge, 90 min acquisition time) are shown at the top panel. Left slice is obtained without quasi-symmetries. The central one has been reconstructed using the quasi-symmetries explained in Figure 6.2 to Figure 6.4. With this degree of quasi-symmetry, differences of less than 5% inside superTORs are found. The right slice has been obtained with a higher degree of quasi-symmetries (and compression), meaning up to 10% of difference of the profiles inside a superTOR. At the bottom panel, the activity profile against the distance (in mm) from the centre of the line drawn in the slices is shown. Small differences in the activity profile begin to be visible at the highest level of quasi-symmetry. Horizontal scale in mm. Darker grey in the figure corresponds to larger activity values.

Table 6.2. Spatial resolution.

Measured	R = 0 mm	R = 25 mm
Radial	0.7 mm	0.9 mm
Tangential	0.7 mm	0.9 mm
Simulated (MC)	R = 0 mm	R = 25 mm
Radial	0.6 mm	0.8 mm
Tangential	0.6 mm	0.8 mm

These results of resolution can also be observed with the microresolution phantom reconstruction displayed in Figure 6.6, where the uniform resolution, almost constant along the radial direction, can be observed.

With regard to linearity, Figure 6.7 and Figure 6.8 show an spiral phantom and the reconstructed (OSEM) image after 1 iterations of 100 subsets. Note the very linear response exhibited by the reconstructed image: the hot spiral to background and background to cold spiral activity ratios are preserved after reconstruction.

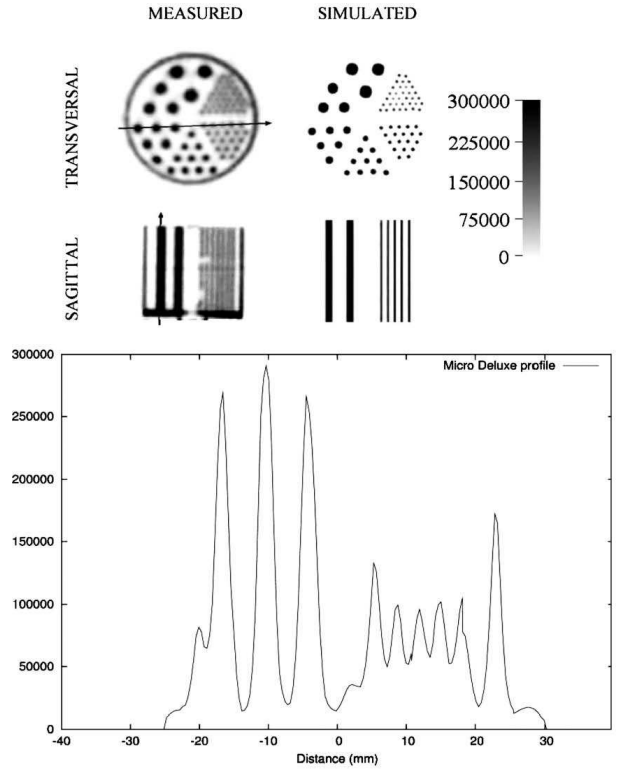

Figure 6.6. Microresolution phantom, Data Spectrum Co., Hillsborough, NC. Top: image reconstructed from real measured projections and from projections obtained after a simulation. Transverse and sagital views. Rod diameters: 1.2, 1.6, 2.4, 3.2, 4.0 and 4.8 mm. Separation = twice diameter. Bottom: transverse line profile of the measured microresolution phantom along the arrow indicated in the figure is shown.

6.5. Evaluation of the effect of compression

To study the effect of the implemented quasi-symmetries, it has been chosen a 90 min acquisition of a cold Derenzo phantom of 1 mCi activity of ^{68}Ge. In Figure 6.5, it is shown a slice of the phantom reconstructed after one 3D-OSEM iteration of 100 subsets where the SRM was dealt for in three ways. (a) Without making use of the quasi-symmetries. (b) With the quasi-symmetries explained in previous sections, and quasi-symmetry classes (superTORs) built from profiles that typically differ by less than 5%. This allows for a reduction in a factor of approximately 9 in the size of the SRM that needs to be stored. (c) With a larger degree of compression, which allows for a reduction factor in size of the SRM of approximately 25, with superTORs that represent profiles that differ approximately by less than 10%.

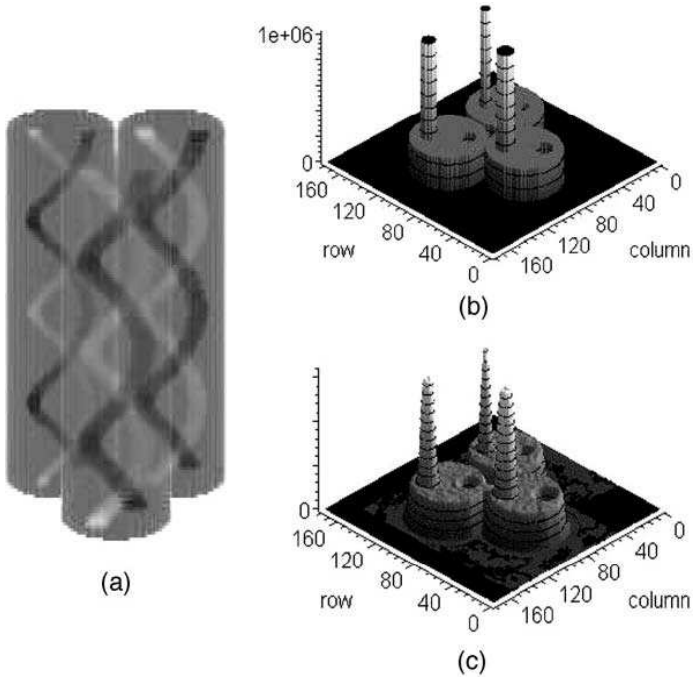

Figure 6.7. (a) Spiral phantom and (b) 3D representation of a transverse section of the original spiral phantom. Z-axis represents counts. (c) 3D representation of the OSEM-3D reconstructed image after three iterations (25 + 25 + 50 subsets). The three large cylinders are 11.5 mm in size, and there are two small ones inside each large cylinder, a hot one, with activity four times larger than the average on the large cylinder, and a cold one, with activity four times smaller than the average one. Small cylinders are 1.4, 2.2 and 2.6 mm in diameter.

In the bottom part of the figure, the activity profiles along the lines indicated in each slice of the upper part of the figure are shown. While the activity profile of the reconstruction obtained without quasi-symmetry (solid line) and the one of the reconstruction obtained with moderate compression (labeled QS 5%, medium dashed line) are hardly distinguishable, the reconstruction obtained with the most compressed SRM (labeled QS 10%, short dashed line) begins to deviate slightly from the uncompressed result.

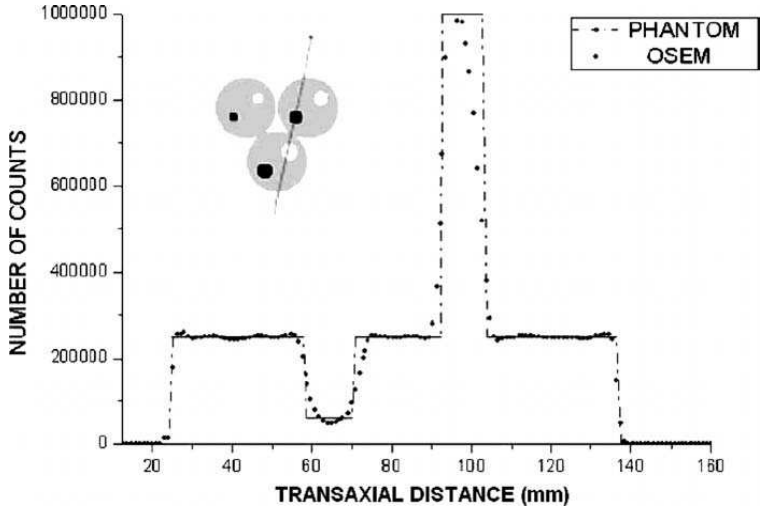

Figure 6.8. Profiles across the spiral phantom study showing the activity distribution: phantom (solid line), OSEM reconstruction (dots) (1 iteration 100 subsets). Voxel size is 0.38 (X) × 0.38 (Y) × 0.78 (Z) mm^3.

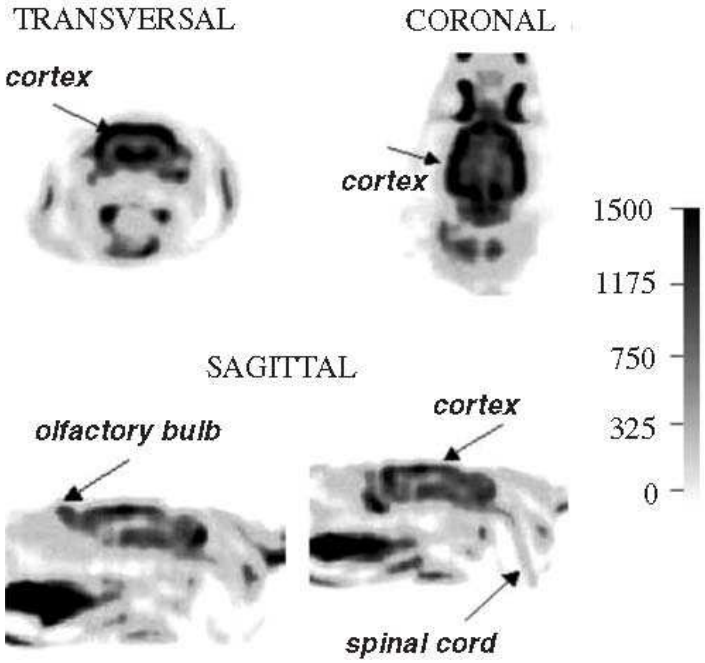

Figure 6.9. Single bed study of the head of a 185 g rat. 35 min intake of 1 mCi of FDG and 60 min scan acquisition in an eXplore Vista (GE) drT PET scanner. 3D-OSEM with 1 iterations of 100 subsets was employed.

Apart from this figure where the effect of quasi-symmetries has been studied, in the remaining of this work, the moderate amount of quasi-symmetries was employed, which implies, for the Vista drT scanner, an SRM size of 150 MB.

6.6. Results for small animal data

Our reconstruction software was also tested on real mice data. ^{18}F (fluorine) and FDG mice wholebody projections were acquired with a Vista (GE) drT PET scanner (Vaquero *et al.*, 2004). Figure 6.9 and Figure 6.10 show the reconstructed images obtained using the 3D-OSEM algorithm with 1 iterations of 100 subsets. The number of voxels is 175 × 175 × 62 for the rat head depicted in Figure 6.9 and 175 × 175 × 168 for the whole body (three beds) mice of Figure 6.10. In all cases, the voxel size is 0.38 × 0.38 × 0.78 mm^3. As indicated by the study from phantoms and simulated data, submillimetric details can be observed in the images of the mice and the rat head. In the rat head, cortex, spinal cord and olfactory bulb are easily identified. For the mice results, the fluorine image clearly shows small details such as ribs and spinal bones, and the small bones in the front legs. The FDG image shows the usual accumulation of activity at the mouse urinary bladder, but no artifacts are produced in its vicinity.

6.7. Analysis of performance

6.7.1. Optimization techniques in 3D-OSEM reconstruction

Considering all the strategies previously described, an accelerated version of OSEM that can optionally incorporate a penalty function in the reconstruction process (MAP-OSEM) has been implemented. The number of subsets in each iteration can be freely chosen between 1 and 100, not limited by system symmetries. Subsetting strategies require that all subsets have TORs evenly distributed along the FOV. In order to achieve this, superTORs are picked

in random order and consecutively assigned to each subset. As all the TORs belonging to a superTOR lie within the same subset, it can be taken advantage of symmetries and quasi-symmetries to speed up decompression of the SRM, because every TOR needs to be decompressed once and only once during each iteration. Subsets are thus chosen so that they include all members of a quasi-symmetry class. From 1 to 100 subsets, there are plenty of choices to build the subsets that fulfil this requirement of including all the members of the classes comprised in a subset. Symmetry classes are just chosen in each subset at random. Beyond 100 subsets, however, problems arise because every subset will then include too few symmetry classes.

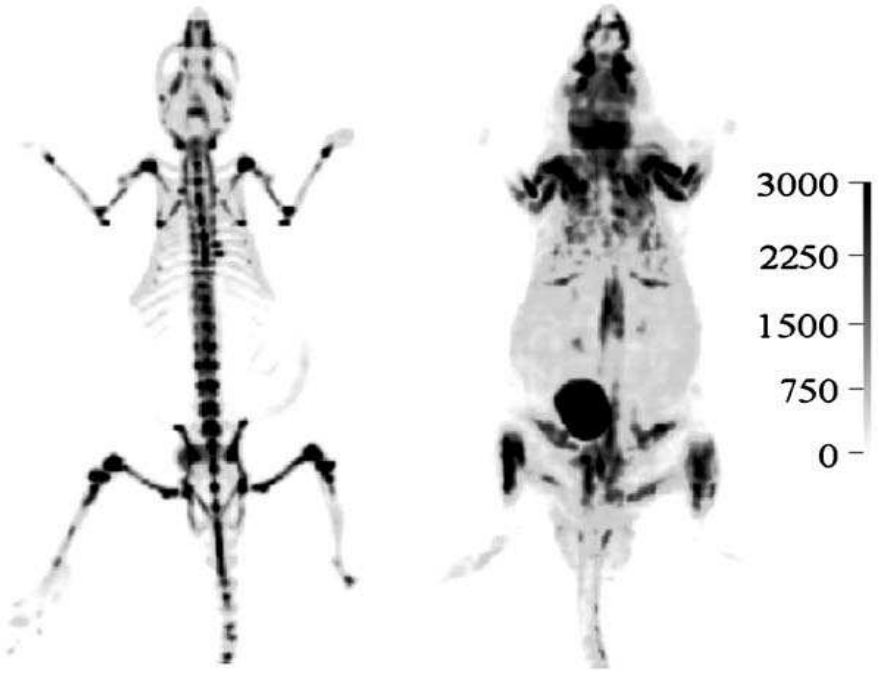

Figure 6.10. Reconstructed images of (a) ^{18}F (fluorine) and (b) FDG mouse study acquired with an eXplore Vista (GE) drT PET scanner. A three-bed scan of a 25 g mouse, with 5 min scan acquisition per bed, four slices overlap between beds, 45 min uptake of 250 μCi of FDG (right) or ^{18}F (left). 3D-OSEM with 1 iteration of 100 subsets was employed in both cases.

Always keeping in mind flexibility as a goal of design, the number of subsets as well as the number and size of voxels or the size of the FOV employed can be changed at any time during reconstruction, even before full iterations are completed. In this way, different sizes of voxel, number of subsets and iterations can be tried and the best combination in terms of speed, quality of the reconstruction or both can be found. For instance, during the first stages of reconstruction, when only the low frequencies (gross details) of the image are recovered, the use of a high number of voxels is a waste of computer power. The number of voxels employed to represent the image may be increased as the high frequency components of the reconstructed image begin to appear. This strategy has been described in detail in Raheja et al (Raheja *et al.*, 1999) and it has been named multiresolution. It can be noted that the images and execution times quoted in present work have been obtained without resorting to this feature.

With regard to reconstruction times, a full iteration of an acquisition covering the whole axial FOV (that is, an acquisition of one bed or 175 × 175 × 62 voxels) typically takes 20 min using 1 CPU (Opteron 244, 1.8 GHz, 2 GB RAM). Thus 60 min are needed for the single-bed, one-iteration reconstructions shown in Figure 6.9 of this work in a single-CPU

computer. For larger animal like rats that span a length larger than the axial FOV of 4.8 cm, the bed that supports the animal is displaced during acquisition and thus several scans (bed positions) are acquired consecutively in order to cover the whole body. More axial slices will be acquired and reconstruction time will be increased proportionally to the size of the axial FOV. The increase of performance of computers makes it very difficult to keep up to ate the computing time estimates. Most recent implementation of the code on quad cores reduces this time substantially (see table 6.3)

Reconstruction time scales approximately with the product of the number of LORs (2.9×10^7) and the number of voxels in a LOR (on average 6000 for the standard resolution employed of $175 \times 175 \times 62$ voxels). Without compression, a similar reconstruction needs to access above 3 GB worth of SRM elements from disk for every subset, which slows downs the reconstruction by a factor of 10–50, depending on disk speed and network activity.

The reduction of the storage needs for the SRM allows us to keep it in RAM. The code is implemented in a way that no disk I/O is needed in order to forward and backward project. The SRM is read at once at the beginning of the execution and the image is written to disk only after a full iteration is finished. Except for the short initial and final periods of intense disk I/O, the common Unix tools measure a CPU use larger than 99%, which indicates that the elapsed time during execution is mostly CPU bounded. Determining the performance of computer codes, however, is a very subtle and non-trivial task. A program can be CPU bounded yet it may be wasting CPU cycles doing nothing useful.

CPU manufacturers often quote peak performance of modern CPUs, referring to ideal situations where no cache misses occur, burst mode access to memory is possible, the CPU internal pipelines are fully used, etc. For instance, a peak performance of two flops per CPU cycle is quoted for AMD Opteron CPUs, which refers to a single multiply and add instruction performed in a clock cycle. Real life applications depart from the ideal conditions and thus peak CPU performance is hardly achieved during sustained execution of complex codes. In order to assess the performance of the code, FIRST was compiled with the 8.1 version of the Intel Fortran compiler. The Intel vtune performance analysis and profiling tool was employed to determine performance and number of flops required by each routine. It can be concluded that during reconstruction 50% of peak performance was obtained in sustained fashion. It was also determined that when our compressed SRM that fits in RAM memory is employed, the decompression time measured was in the range of 10–30% of total reconstruction time, depending on the number of voxels chosen.

6.7.2. Parallel implementation

Parallel computing on multiple processors is an attractive option to reduce computational time. The use of protocols like message passing interface (MPI[11]) enables clusters of networked industry-standard PCs (Beowulf clusters) to be relatively easy configured as a multiprocessor unit. Several parallel implementations of the OSEM algorithm have been presented in other works (Johnson and Sofer, 1999; Chen, 1998). A parallel version of the Fast Iterative Reconstruction Software (FIRST) has been implemented to run in Beowulf clusters of several CPUs in a master/slave configuration, characterized by the use of a master process and several (usually as many as the number of available CPUs) slave processes. The master distributes the job among the slaves and continuously balances the workload to achieve the best performance taking into account differences in individual speed

[11] http://www-unix.mcs.anl.gov/mpi/

or workload on each CPU. In spite of its name, the master process does not perform any intensive calculations, though. On startup, the master process reads from disk (once and for all) the SRM elements and sends them to the slave processes. Enough RAM memory to store the full compressed SRM must be available for each slave process. After startup, the master process decides which part of each subset (i.e., which actual superTORs of such subset) is forward and backward projected by each slave process. Once all the slave processes have finished with their share of each subset, the master process updates the image, that is also stored in memory, and broadcasts the new image to all the slave processes. Upon completion of the reconstruction, the master process updates the image on disk. The slave processes are highly CPU intensive, as they are continuously performing the forward and backward projection operations.

Table 6.3. Elapsed time for FIRST reconstructions (Herraiz *et al.*, 2006) of 50 subsets for one bed of 175 × 175 × 62 voxels are displayed for a dedicated machine with two cuad-core Intel Xeon X5472 3.00GHz. Code is compiled with Intel Fortran compiler 10.1 and 32 bits libraries on a Fedora core 8.0 x86-i386 operating system. At least 1 GB per CPU is available in all cases. The elapsed time in minutes is shown.

CPUs	Version	CPU class	Elapsed time (min)
1	Non-parallel	Intel Xeon X5472 3GHz	8.3
1	1 master + 1 slave	id.	8.9
2	1 master + 2 slaves	id.	4.5
4	1 master + 4 slaves	id.	2.7

The master process only takes part in the reconstruction whenever one of the slave processes finishes its share of the reconstruction task and claims for more or when all the TORs of a subset have been visited by all the slave processes and then the image must be updated and broadcasted. Multitask capabilities of modern computers and operating systems make it possible to have as many slave processes as available CPUs, yet having an additional master process that will occupy a few cycles of one of the CPUs that is running one of the slave process. Balance of the workload among different CPUs is easily achieved as the slave processes that run faster (because they are executed by a less busy or faster CPU) will claim for their share of subsets more often than the ones that run slower. The only caution that must be taken is that the initial workload sent to each slave process is similar but not identical for all of them. In this way, the possibility that more than one slave process claims the attention of the master process at the same time, is minimized. In practice, the tasks assigned to the slave process take from a few seconds to near a few tenths of seconds to be completed, before requesting the action of the master process. The master process, on the other hand, can comply with the task required by the slave process in just a fraction of a second.

Overall, the implementation is simple and efficient. In Table 6.3, it has been quoted the elapsed time in minutes taken by the reconstruction of one iteration of 50 subsets at nominal number of voxels of 175 × 175 × 62. Tests were made in a single CPU and two core system comparing parallel to the nonparallel versions. A master plus a slave process parallel reconstruction in a single CPU takes less than 10% longer than the nonparallel (only one process in one CPU) version of the code, working in the same single-CPU system. The additional time is due to the overhead of sending the SRM from the master to the slave, as well as the elements of the image after updates, using the MPI interface. On the other hand, the parallel version of FIRST working over several CPUs reduces the elapsed reconstruction time by a factor equal to the number of CPUs available. For relatively small clusters with very

powerful cores with up to 4 CPUs, the results shown in Table 6.3 indicate that the implementation with only one master process is rather efficient. When two or more CPU cores are available, the master process uses less than 2% of the total computing time required for the reconstruction, according to the CPU use stated by the Unix common tools function *ps*. If a number of CPU cores larger than eight is to be used, benefits will be found by using more than one master process. In Table 6.3, a summary of elapsed times with one master process is shown.

6.8. Conclusions

FIRST (Herraiz *et al.*, 2006), a fully 3D-OSEM or 3D-MAP-OSEM non-sinogram-based reconstruction algorithm, using a compressed SRM that contains the resolution recovery properties of EM, has been implemented in this work. The full SRM for eXplore Vista GE can be stored in less than 150 MB of storage. Reconstructed images are indistinguishable from the ones obtained without compression. The use of the compressed SRM allowed for a reconstruction with a more realistic response of the system. In this work, an own PeneloPET MC model of the scanner was used, which incorporates physical effects such as positron range, non-collinearity and scatter in the scintillator material. Although it took several weeks, the SRM was computed only once. It was stored in compressed form so that the reconstruction program could keep it in dynamic memory.

Thanks to this, near peak performance of the algorithm is achieved with just a slight overhead (10–30%) due to the decompression procedure. This resulted in short reconstruction times, even if the realistic SRM implies wider TORs and thus more voxels are involved in every projection and back projection operation than when simplified SRM are used. The algorithm has been validated against simulations as well as real data. Acquisitions of phantoms and mice from a commercially available high-resolution PET scanner were reconstructed. A realistic SRM from our own MC model of the scanner with optimal resolution recovery was used. This fact, together with the intrinsic high resolution (small crystal pitch of 1.55 mm) of the scanner, resulted in very high quality images with submillimetre resolution, as shown in Figure 6.6, Figure 6.9 and Figure 6.10. The reconstruction time needed by the algorithm enables real time operation in a small cluster (less than 3 min per bed and iteration in a recent quad core computer cluster (Herraiz *et al.*, 2006)) of industry-standard PCs. The results from real acquisitions in terms of resolution and linearity agree with what is expected from the simulated projections that use the same SRM as the reconstructions. This indicates that the SRM derived from our Monte Carlo simulations accurately reflects the response of the real scanner. Very uniform resolution and linearity is exhibited by the reconstructed images.

The flexibility, reduced reconstruction time, accuracy and resolution of the resulting images prove that the methodologies used to implement the FIRST reconstruction can be applied to real studies of high-resolution small animal PET scanners. The use of quasi-symmetries to reduce (compress) the size of the SRM seems an adequate way of dealing with the problem of storing the huge SRM resulting from modern high-resolution PET scanners.

7. Improved image resolution using *a priori* estimates of single pixel events

7.1. Introduction

In this chapter we exploit the information that can be obtained from Monte Carlo simulations about events detected in a PET scanner. In the previous chapter we showed how to calculate a realistic system response matrix (SRM) in an efficient way. Here we will explain how to include *a priori* information about the counts in the SRM in order to improve the reconstructed images.

Most small animal PET scanners are based on arrays of pixelated scintillator crystals. Electronics read out of individual crystals is too expensive and thus the identification of the crystal of interaction, is usually made by center of energy methods based for instance on the Anger logic (Anger, 1969). This provides with X and Y information that are employed for the positioning of the interaction of each event. A look up table can be built from this information that assigns events to individual crystal pixels (Dongming *et al.*, 2006). If only X and Y information is employed, as it can be the case that the event actually corresponds to a multiple hit in the detector due to, for instance, inter crystal scatter or if detector pulse pile-up has occurred, the X Y information obtained with this method will produce an erroneous crystal identification, and it will result in a deterioration of the image obtained.

There are several factors that contribute to the degradation of spatial resolution in pixelated detector arrays. For instance, counts coming from oblique lines of response have an increased uncertainty in the photon positioning, due to the effect of the penetration in the crystal. During the decoding (crystal assignment) process, statistically distributed mispositioning of the crystal of interaction occurs (Yiping *et al.*, 1996). Scatter within the detector also contributes to errors in the crystal identification. The ideal situation where the degradation of spatial resolution due to scatter within the detector is minimal, corresponds to the case for which a photon interacts only in one crystal, either because it interacts only once or because all the interactions for said photon occurs in the same pixel of the array. We refer to those events as *single-crystal* events (España *et al.*, 2007a). When a photon goes through a scintillator detector, it can undergo photoelectric or Compton interaction. If photoelectric absorption takes place, all the energy is deposited in the same crystal but the probability of this is less than 50% for the scintillator materials used in PET (van Eijk, 2002). If the photon is Compton scattered, it continues *flying* with less energy and subsequently there are three alternatives: The photon can leave the scintillator with less than 511 keV of energy, having thus produced a *single-crystal* event, or it can undergo another Compton of photoelectric interaction. In the latter case, the photon can interact in the same crystal of the first interaction or in a different one. This latter situation will contribute to degradation of the spatial resolution. Multiple points of light emission from the array lead to errors in the assignment of the crystal of interaction. These *multiple-crystal* events could be, at least partially, identified with a detailed study of the flood field image built from the Anger logic centroids. Indeed, events with an X, Y signal in regions close to the maximum of the peak of each crystal, would correspond more likely to single-crystal events. Conversely, events falling in inter-peak or valley regions, would come from multiple-crystal events, more often that those events that fall in the maximum of the flood image.

In order to quantify these statements, Monte Carlo simulation were performed and the different type of events, contributing to the flood field images (see Figure 7.1), were studied.

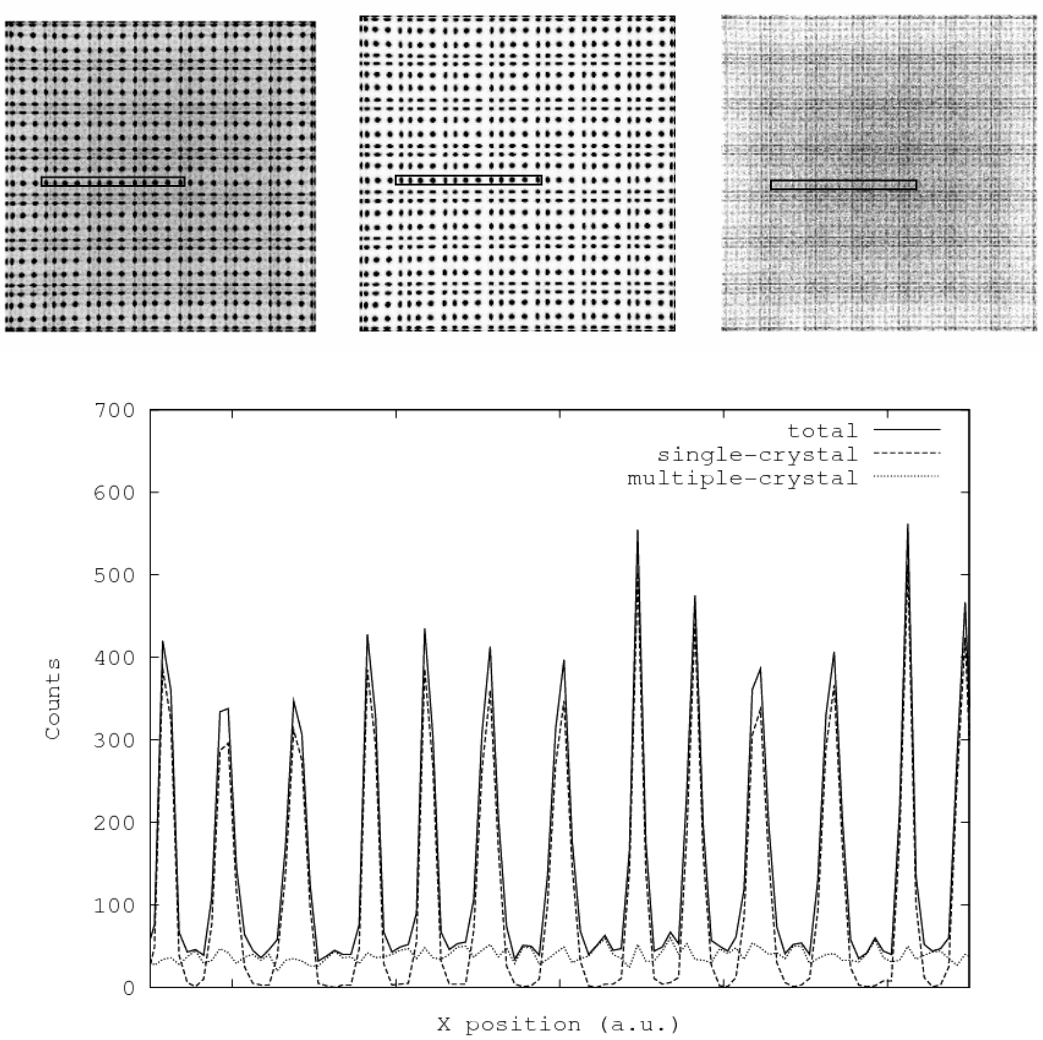

Figure 7.1. Flood field images obtained with detailed simulation with PeneloPET, for a 30 × 30 LYSO array with pixel dimensions of 1.5 × 1.5 × 12 mm^3 coupled to a Hamamatsu H8500 PS-PMT. The block is illuminated uniformly with a low activity ^{18}F radioactive source. Contribution of pile up events is negligible for the low activity employed. Total (top left), single-crystal (top middle), and multiple-crystal events (top right) flood field images are shown at the top panel. The panel at the bottom shows line profiles through the rectangular area indicated in the flood field images. As expected, peak regions are composed mostly of single-crystal events, while the valley regions receive a noticeable contribution from multiple-crystal events.

As mentioned, *single-crystal* events are not only composed of photons which interact once in the detector (single-hit), but also by photons which interact several times (multiple-hit) but whose interactions take place in the same pixel crystal. Table 7.1 shows the quantitative results for each kind of counts, according to the simulation performed.

In most cases, the way of assigning events to individual pixel elements is completely deterministic, in the sense that every accepted event is attributed to one and only one crystal, with 100% certainty. The criteria for accepting events can be tightened in aiming to reduce *multiple-crystal* contribution in the acquisitions. For instance, using a more restrictive look up table (LUT) that does not assign accept events that do not fall into the (narrow) predetermined XY range for each crystal. These restricted LUT acquisitions produce somewhat better resolution in the images, but at a high cost in the efficiency.

Table 7.1. Percentage of single and multiple hit events (left) and single and multiple crystal events (right) for the simulation performed. Results show how single crystal events get about a 10% contribution from multiple hit events.

Single hit	Multiple hit	Single crystal	Multiple crystal
51 %	49 %	60 %	40 %

In this work (España *et al.*, 2007a; España *et al.*, 2009), we propose an alternative method that, in order to improve the quality of the reconstructed images, makes full use of the information obtained by the scanner for every coincidence event, typically XY position estimates and deposited energy in the detector. This method uses a kind of fuzzy logic, where every coincidence is not just accepted or rejected according to the fulfillment of certain energy and XY range restrictions in a binary logic way, but rather, with the aid of extensive comparisons with real and simulated data, a combination of both energy and position information that represents the likelihood of the event for being single-crystal is built. Indeed, the combined criteria is adjusted to yield the right estimates for single-crystal events at different count rates, compared to realistic simulations (España *et al.*, 2006; España *et al.*, 2007b). Events identified with a high likelihood of coming from a single-crystal interaction in the detector, are given above average reliability, while others are considered as being less reliable. The assignation of measured counts to individual crystals in this method is thus not just 0 or 1, but any number in between, depending on the likelihood of the count for being single-crystal. The hypothesis of this work is that image quality obtained with small animal PET scanners can be improved using *a priori* estimation of the probability of being a single-crystal event.

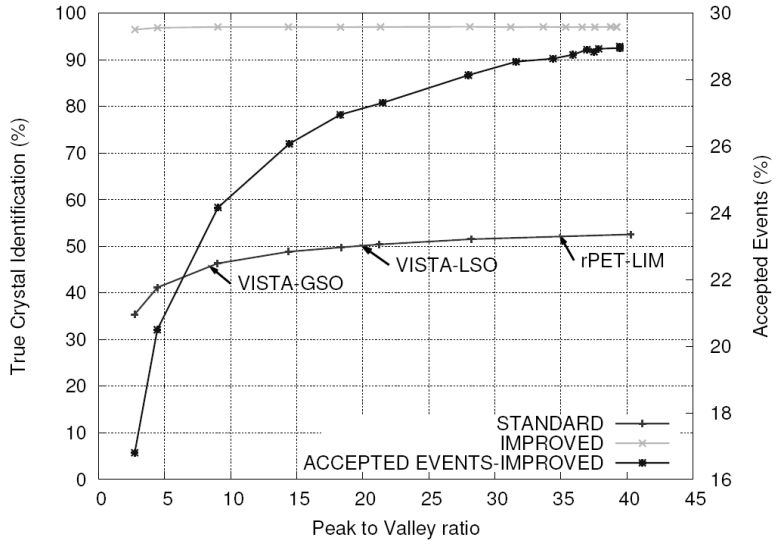

Figure 7.2. Red line shows the percentage of events that are assigned to the crystal where the first interaction takes place (true crystal identification) when using standard identification methods. Different points were calculated using different light output on a H8500 PMT with 30 × 30 crystals with a size of 1.5 × 1.5 × 12 mm^3. The results obtained for different real scanners (rPET (Vaquero *et al.*, 2005) and LYSO and GSO scintillator layers from VISTA (Wang *et al.*, 2006)) are superimposed in the figure. The green line shows the same results yielded by the improved method, and the blue line shows the percentage of effectively accepted events by the improved method each peak to valley ratio.

7.2. Method and results

The method proposed has been tested for the VrPET scanner (Lage *et al.*, 2008). The VrPET detection system is based on 4 flat-paneltype PS-PMTs (Hamamatsu, H8500) and MLS arrays (30 × 30 crystals of 1.5 × 1.5 × 12 mm^3). A rotation of the gantry is performed during the acquisition in order to obtain full angular sampling. This scanner performs acquisitions where the data are stored in list mode. For each event, XY centroids computed with Anger logic, and the raw energy for both single-events of each coincidence detected is available in the list file.

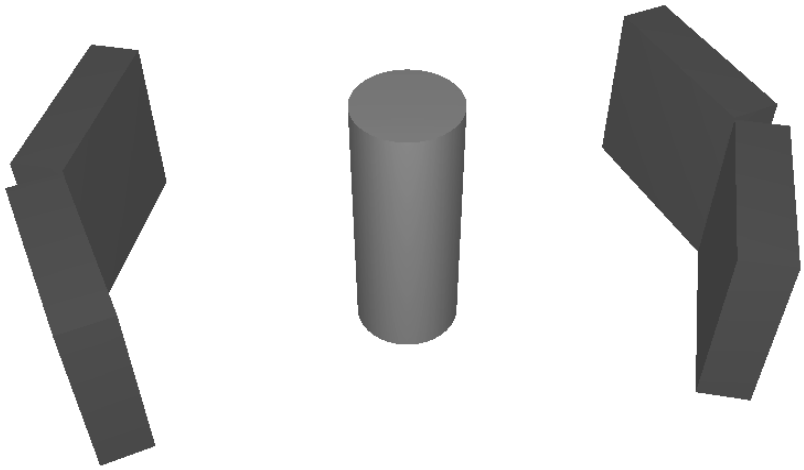

Figure 7.3. VrPET scanner diagram showing the arrangement of block detectors in the gantry. A cylindrical phantom is plotted inside the FOV (Lage *et al.*, 2008).

Each coincidence is obtained from the two single events detected in opposing block detectors. The probability of each coincidence (L_{12}) for being a single-crystal one corresponds to the product of the likelihood for both single events (L_1, L_2) for being *single-crystal*, as in both detection processes the probabilities of being single-crystals are uncorrelated:

$$L_{12} = L_1 L_2 \tag{7.1}$$

The estimation of the likelihood of a single event for being *single-crystal* is obtained by means of a combination of real and simulated acquisitions. Indeed, the likelihood of each single-event for being *singe-crystal* will be obtained as the product of one factor from the Anger location (L_{XY}) and another from the deposited energy (L_E):

$$L_1 = L_{XY_1} L_{E_1} \tag{7.2}$$

In the flood field image, the pixel with maximum number of counts for each peak is considered as the center of the crystal, where the percentage of *single-crystal* events is also the highest. The variation of the likelihood with the distance to the center of the peak is obtained from simulations where the detector is illuminated uniformly with a ^{18}F radioactive source. Once this variation is obtained, a LUT image containing the likelihood for a counted at each sub-pixel of this image of being *single-crystal*, is computed. As pile-up event contribution depends on the activity, this LUT image depends on the single-event rate, and thus it must be calibrated by comparison to acquisitions at different activity levels, where the

peak to valley ratio variation with the activity can be determined (Figure 7.4). Simulations are tuned to reproduce the behavior seen in the data.

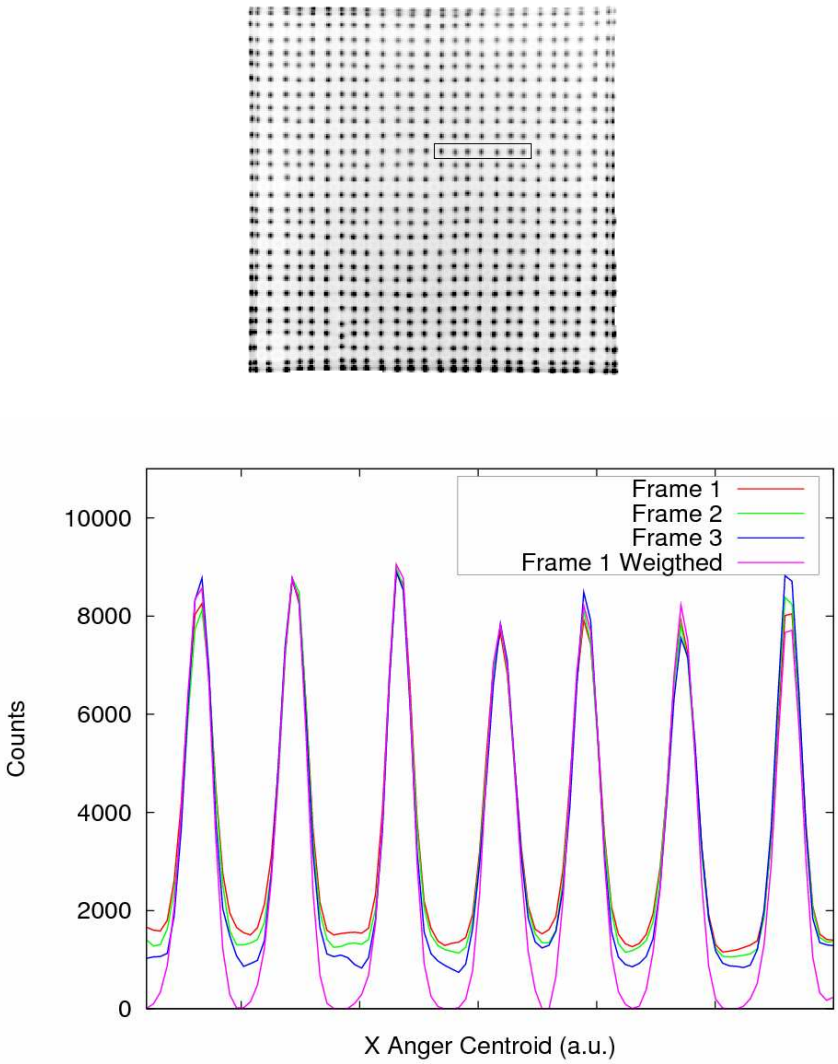

Figure 7.4. Flood field image (top) obtained for a multiframe acquisition of a decaying FDG mouse cylinder phantom, acquired with the VrPET scanner. Every frame is 30 minutes long and starts two hours later than previous one. At the bottom panel, line profiles through the peaks contained in the rectangular area marked in the flood field image, are plotted for three frames with different activities. The profiles are normalized to the same peak values, in order to compare the background level of each one. An extra line (pink) shows the flood field profile of the frame 1, when the likelihood of each count for being single-crystal is applied, and each count is 'weighted' by its probability of being single-crystal. Notice that the background baseline level due to photon detector pile-up and multiple-crystal events is cleanly removed by the weighting procedure.

A similar approach is also employed to obtain the dependence on the deposited energy of the likelihood of each count for being single-crystal (see Figure 7.5). Due to the fact that this dependence change with the source distribution, several likelihood-energy profiles have been obtained from simulations of a line source in air, inside a mouse size cylinder, and inside a rat size cylinder (see Figure 7.6). The distribution most suitable for each acquisition performed, according to the size and distribution of scattering material in the phantom or patient, will be employed each time.

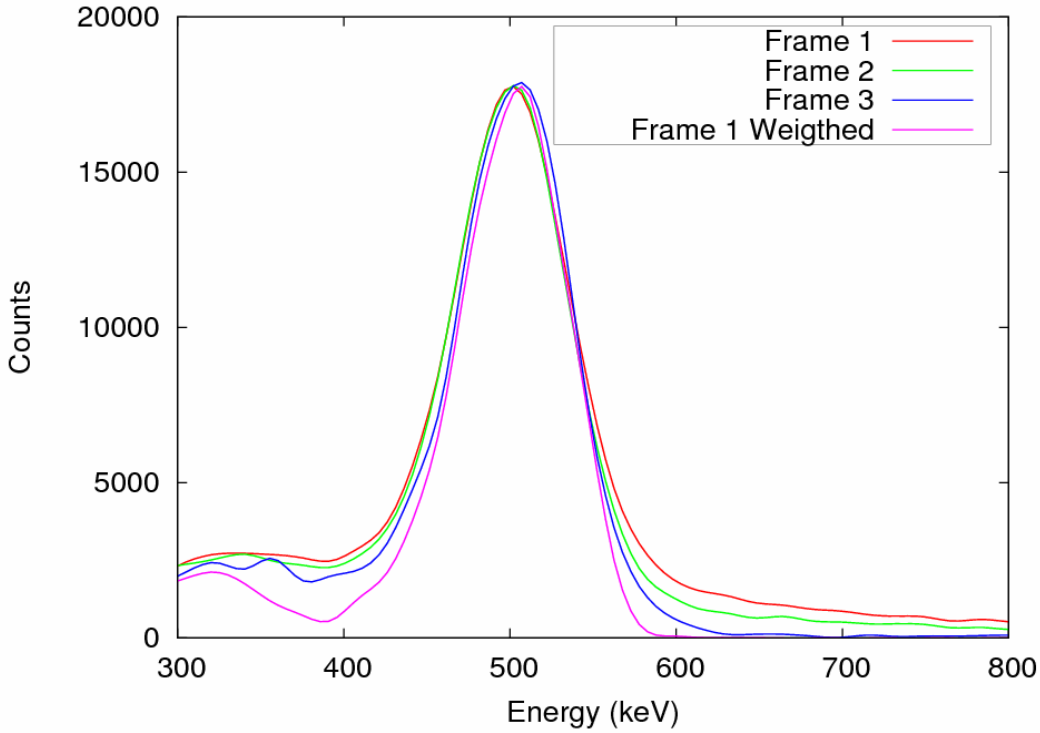

Figure 7.5. Energy spectrum for the acquisition mentioned in Figure 7.4. Profiles are normalized to the same peak values in all frames. Again, an extra line (pink) shows the energy spectrum for frame 1 after weighting every count with its single-hit likelihood. It can be seen that this procedure effectively removes the high energy tail due to photon pile-up at the detector and the background due to these events that fills up the Compton edge for the acquisitions of either frame.

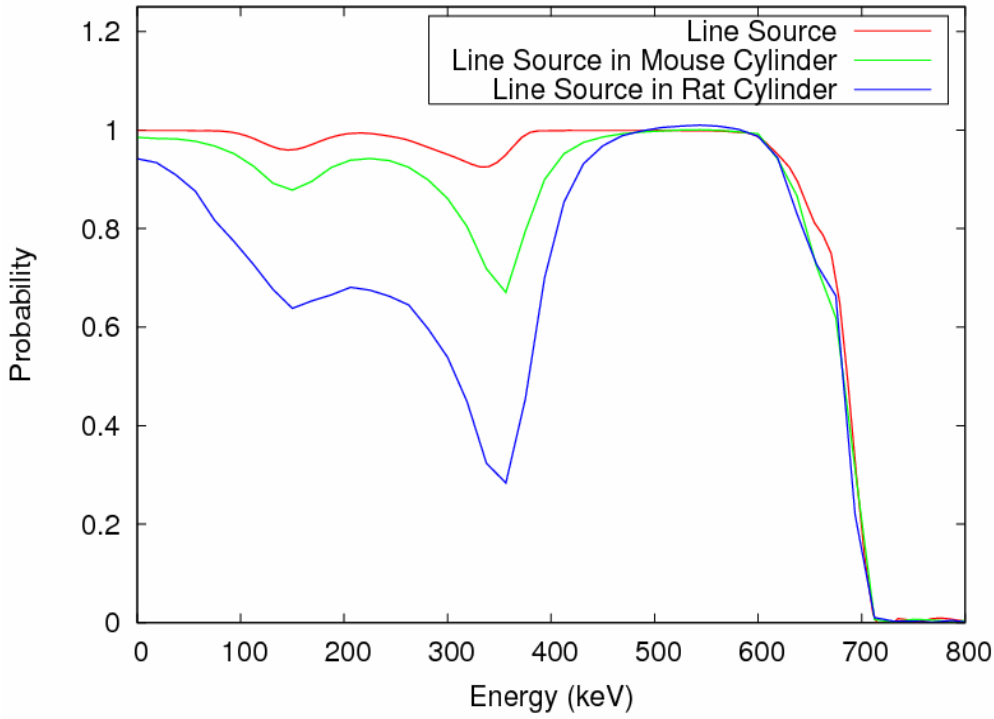

Figure 7.6. Likelihood of single-crystal events versus energy deposited in the detector. Results were obtained from simulations of three different phantoms acquired in the VrPET scanner.

Using the estimated likelihood for a count of being single-crystal, the average single-crystal probability and the histogram of single-crystal likelihood values for acquisitions at different rates were obtained. Figure 7.7 shows how the average likelihood decreases as the coincidence rate increases and Figure 7.8 shows how the highest single-crystal likelihood values appear more often, at lower activity levels. Note that these results are obtained for the VrPET scanner and could be quantitatively different for other scanners, but qualitatively similar.

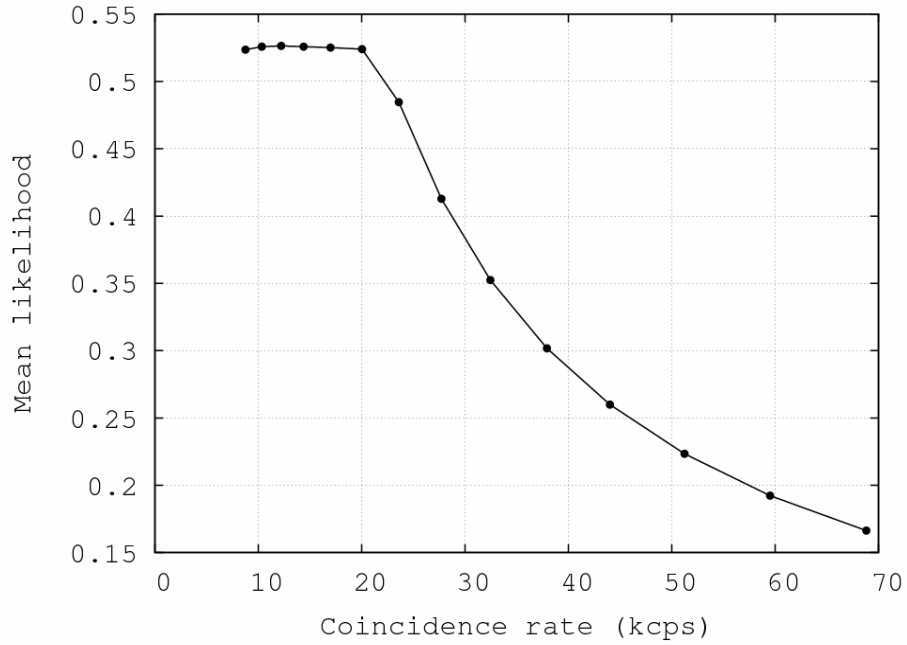

Figure 7.7. Average values of single-crystal likelihood for coincidences versus coincidence rate. High count rate acquisitions have smaller single-crystal likelihood, due to pulse pile-up.

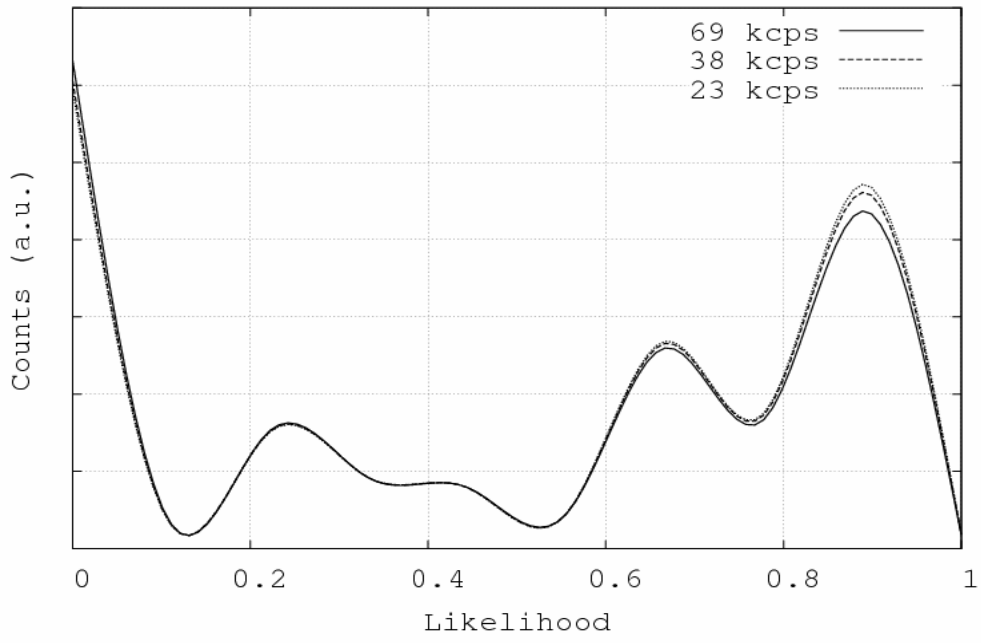

Figure 7.8. Histogram of single-crystal likelihood values of every coincidence for a multiframe acquisition. Curves are rescaled to have the same number of total counts.

Once the estimation of the *single-crystal* likelihood is obtained, two procedures for improving the image by means of this information have been studied. The first method computes the sinogram prior to the reconstruction of the image, by weighting every coincidence with the likelihood of it being *single-crystal* in both single-events that form the coincidence. Thus, the sinogram contains an enhanced contribution from single-crystal events and a reduced contribution from *multiple-crystal* events. Using this procedure, images with better spatial resolution are obtained but with an increase of statistical noise, because counts with low probability of being *single-crystal* are effectively removed from the image. An advantage of this procedure is that it can be employed by both FBP and iterative reconstruction methods. However, in this chapter, only results obtained with fully iterative EM 3D (3D-OSEM) methods will be shown.

In the second procedure, the *single-crystal* likelihood is fed into the iterative reconstruction algorithm, so that all counts are effectively taken into account. In our implementation, four sinograms are built for each acquisition, each one formed from coincidence events with a different combination of *single-crystal* likelihoods. The four combinations are: a) Obtained from the contribution of the probability that first and second events are *single-crystal* (SC-SC). b) Coming from the probabilities that first event is *single-crystal* and second event *multiple-crystal* (SC-MC). c) First event *multiple-crystal* and second event *single-crystal* (MC-SC). d) First and second events *multiple-crystal* (MC-MC).

The likelihood of having a *multiple-crystal* event is computed as the complementary probability to having a *single-crystal* event. In this way, every coincidence contributes to the four sinograms with a different weight to each one, as follows:

$$\begin{aligned} L_{SC-SC} &= L_{SC_1} L_{SC_2} \\ L_{SC-MC} &= L_{SC_1} L_{MC_2} = L_{SC_1} \left(1 - L_{SC_2}\right) \\ L_{MC-SC} &= L_{MC_1} L_{SC_2} = \left(1 - L_{SC_1}\right) L_{SC_2} \\ L_{MC-MC} &= L_{MC_1} L_{MC_2} \end{aligned} \tag{7.3}$$

And the total weight associated with each count, when the four sinograms are considered, is one.

Using this approach, a specific system response matrix for each sinogram is employed by the 3D-OSEM. These SRM are obtained from simulations, weighting the simulated data with similar factors as the experimental ones. The SRM for SC-SC events contains tubes of response that are much narrower than those events where gamma ray hits in more than one pixel crystal. This capability of projecting every type of sinogram with a more accurate system response matrix is what allows for images with higher signal to noise ratio.

Complete system response matrices for each type of sinograms have been computed with PeneloPET (España *et al.*, 2009). As mentioned, the same single-crystal likelihood maps employed for the real data are used during the system matrix estimation. In Figure 7.9, the transverse profiles of several CHOR for the four different SRM are shown.

Three different image reconstructions were performed with the 3D-OSEM algorithm (see table 7.2): standard, single-crystal and improved. i) The standard reconstruction uses a sinogram computed with the standard LUTs. ii) Single-crystal mode uses sinograms where the *single-crystal* likelihood of both single-events of the coincidence is employed to weight the counts in the sinogram. iii) The improved mode uses four sinograms as explained before.

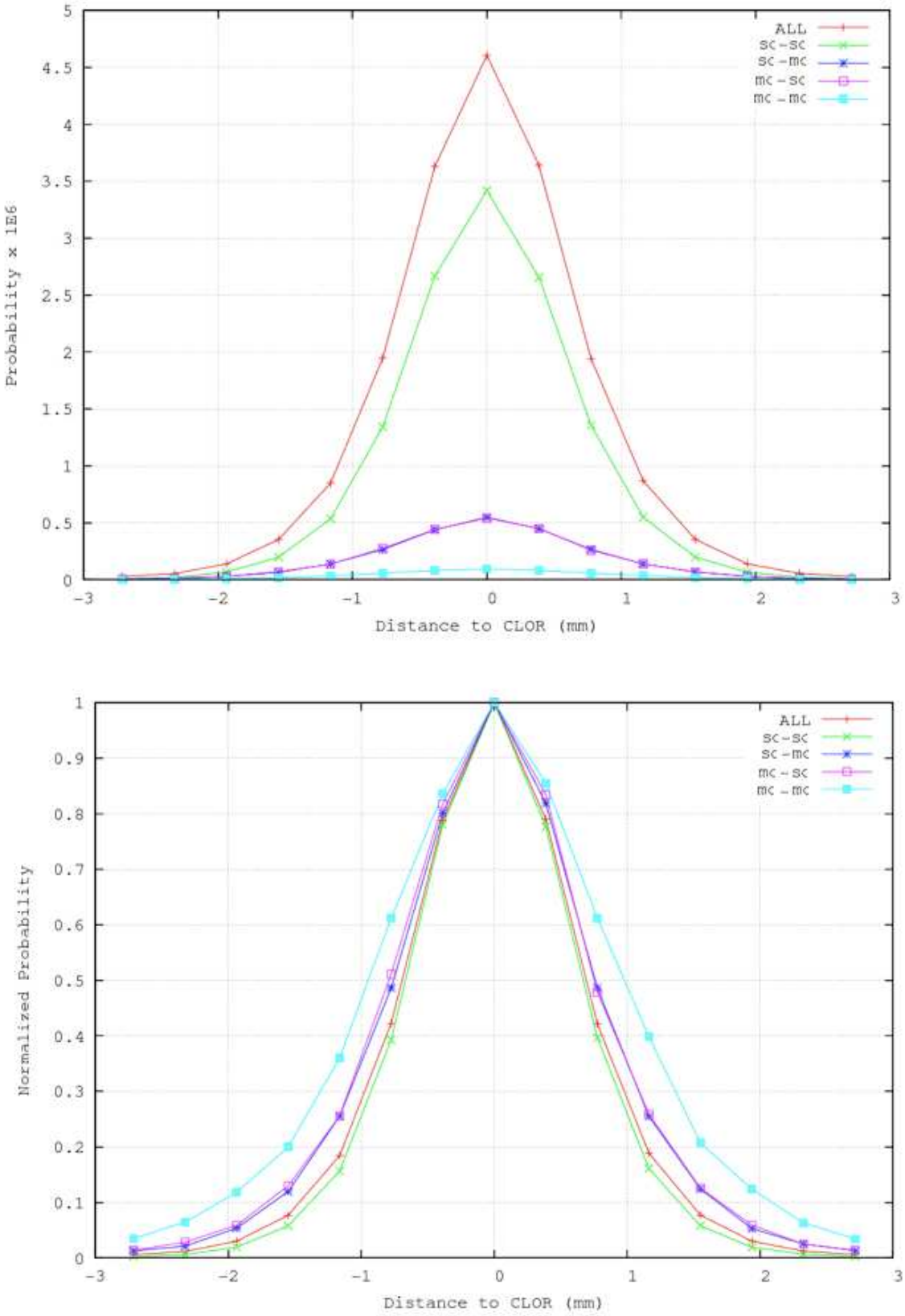

Figure 7.9. Transversal profile along a tube of response of one LOR showing the different values at the maxima (top) and different shapes (bottom, where all the profiles are rescaled at the same peak value) for the different SRM. They are also compared to the profile of the TOR of the standard SRM.

Table 7.2. Different types of reconstructions to be compared.

Standard reconstruction	Use standard LUT to compute the sinogram
Single-crystal reconstruction	Use sinograms including only single-crystal events.
Improved reconstruction	Use four sinograms with different combinations of single and mulple-crystal events.

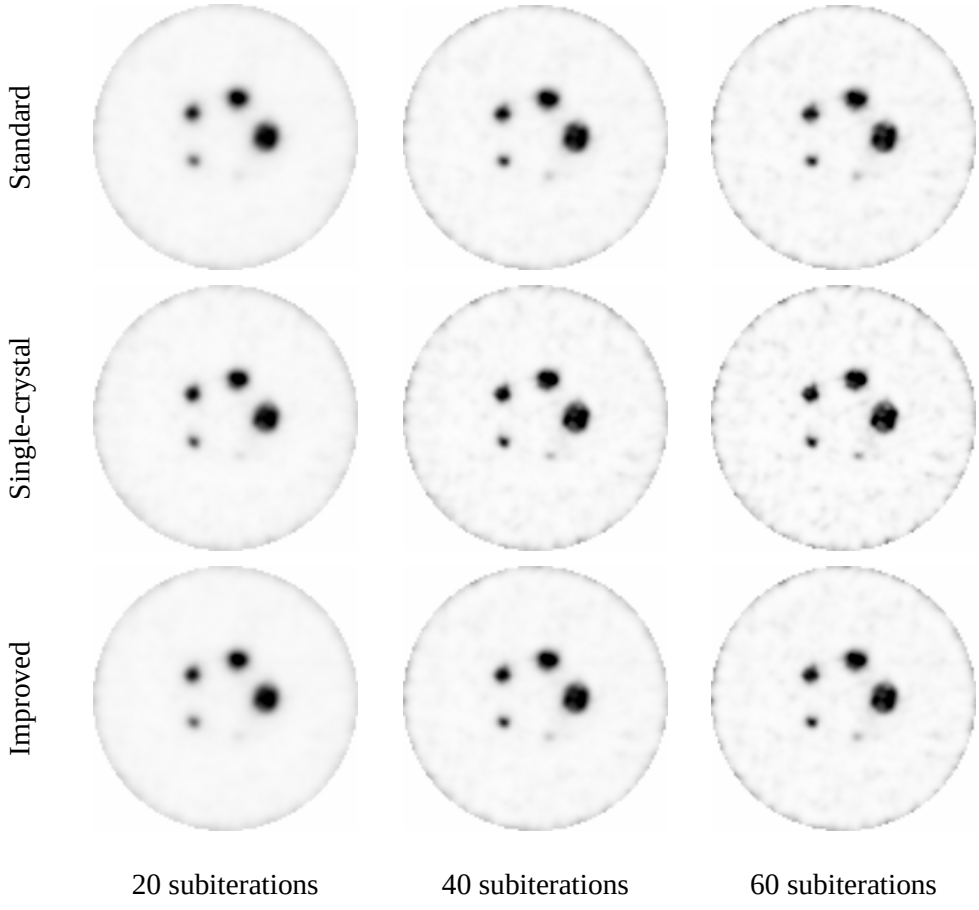

Figure 7.10. Slice of the 3DOSEM reconstructed images for a simulated acquisition of an IQ phantom (see appendix A) acquired with the VrPET scanner. Results with different number of subiterations are shown. The single-crystal reconstruction shows better detectability for the smaller rod but with a considerable increase of the noise in the background, due to the loss in sensitivity. The improved and standard methods show similar detectability for the smaller rod, with lower level of noise for the first one.

In order to compare the images obtained with the different methods (see Figure 7.10), NEMA protocols adapted for small animal studies (NEMA, 2008) have been applied to simulated acquisitions of VrPET scanner. First, the recovery coefficient for different rod diameters was studied. An image quality phantom (NEMA, 2008) filled with 100 μCi of ^{18}F was acquired during 20 minutes. This phantom is composed of a uniform region with a diameter of 30 mm, axially followed by five rods with diameters 1, 2, 3, 4, and 5 mm. The noise was measured in the uniform region and the recovery coefficient was studied for the

rod of 1 mm of diameter. Reconstructed images are stored every five subsets in order to evaluate the evolution of the recovery coefficient versus noise. Results of recovery coefficient versus noise for the three methods evaluated are shown in Figure 7.11. For the 1 mm rod, the recovery coefficient of the improved reconstruction is clearly better for all levels of noise, while single-crystal reconstruction shows slightly better results than the standard one until 10% of noise, from there on, the single-crystal results equals the standard one.

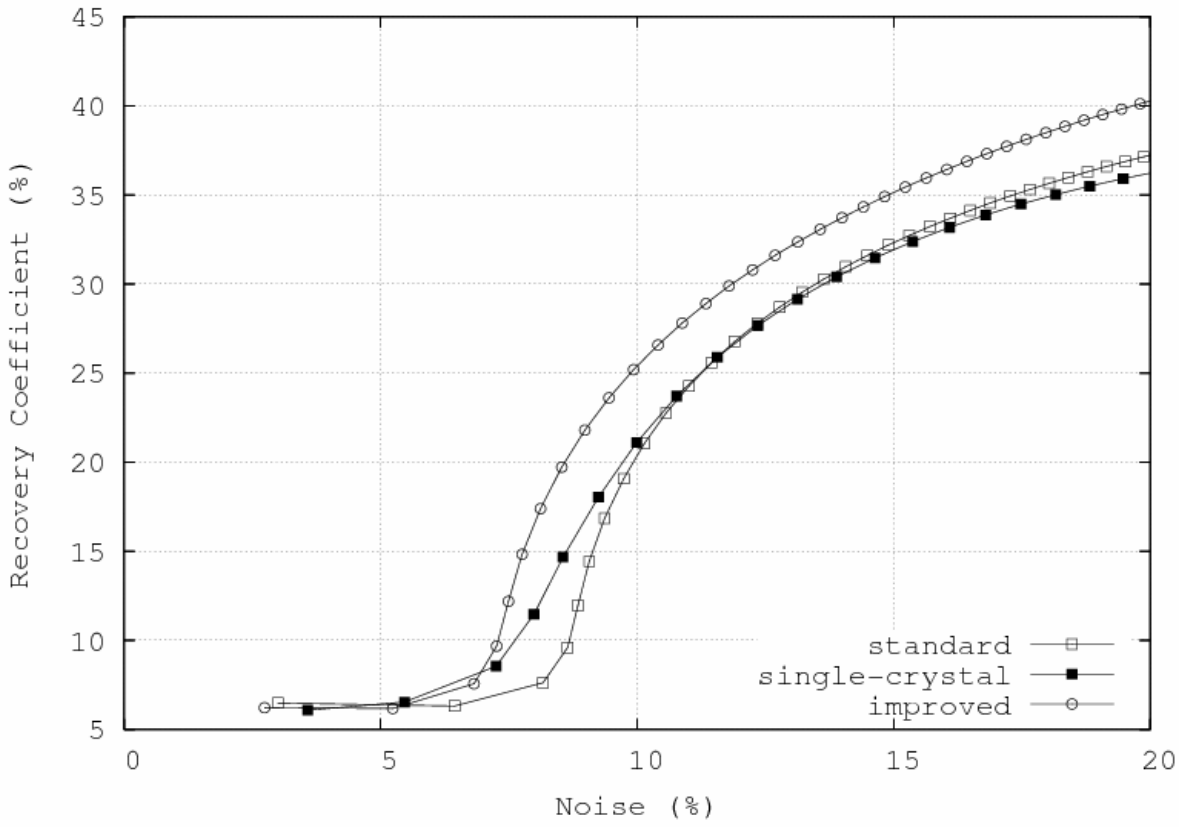

Figure 7.11. Recovery coefficients versus noise for a 3D-OSEM reconstruction for the 1mm rod of a simulated IQ phantom acquired with a VrPET scanner. Each point corresponds to five subiterations.

The simulation of a ^{22}Na point source placed at the center of a 1 cm^3 cylinder of water and acquired with the VrPET scanner was also performed to compare the spatial resolution of different methods. The point source was simulated at different radial positions, acquiring 10^5 prompt counts at each point. The radial, tangential, and axial resolutions were measured following NEMA protocols for small animal PET scanners (NEMA, 2008). The data acquired were reconstructed with 3D-OSEM (Herraiz *et al.*, 2006) using one iteration of 60 subsets. The results are shown in Figure 7.12. There is no difference in axial resolution, but the single-crystal reconstruction has better radial and tangential resolution (~10%) compared to standard and improved methods.

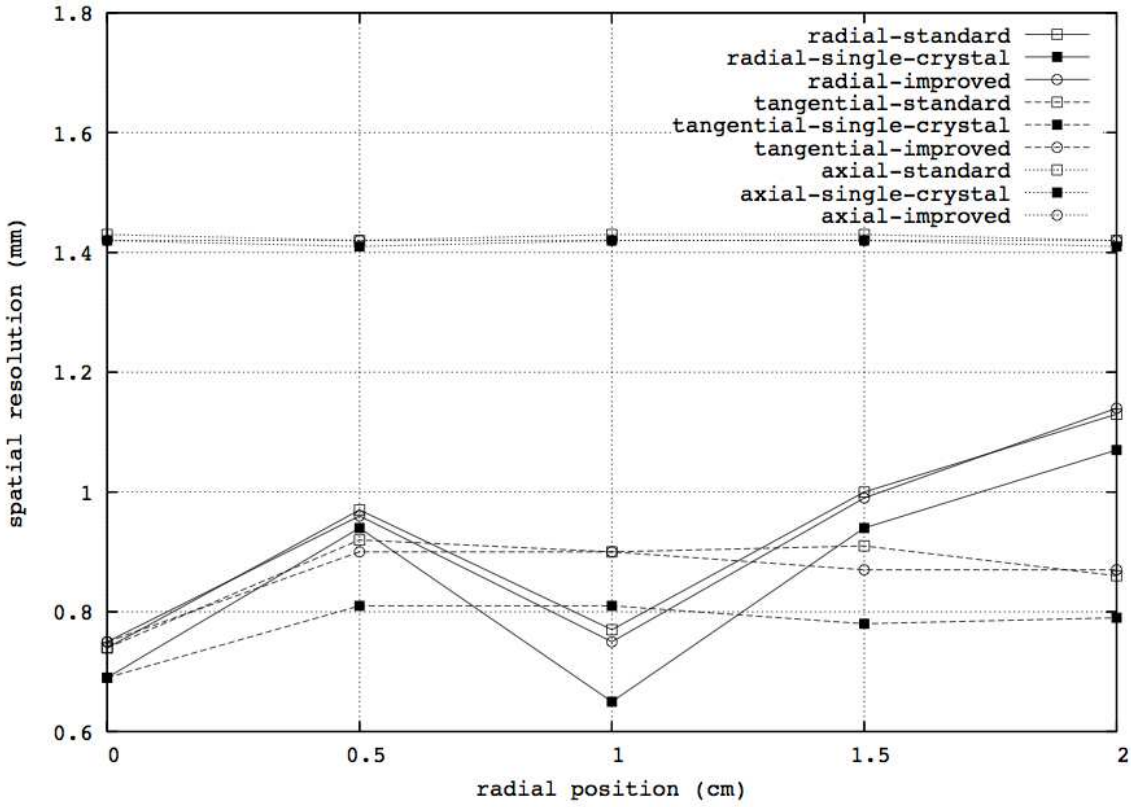

Figure 7.12. Spatial resolution variation with the radial position of the point source for the three evaluated methods. Radial (solid lines), tangential (dashed lines) and axial (dotted lines) resolution are plotted.

Comparing the results of recovery coefficient (RC) and spatial resolution, it can be noticed that best resolution is obtained with the single crystal method, while for the recovery coefficient, best results are given by the improved method. This may be due to the fact that resolution is measured on a point source with very good statistics and without presence of scatter and random coincidences. The reduction of the number of counts implied by working just with single-crystal events will not affect the resolution measure. On the other hand, recovery coefficients are measured with the Image Quality phantom comparing counts of an uniform region with counts in a thin capillary rod. Noise and background counts have an effect in the RC results and thus keeping all coincidences or neglecting some will be seen in the RC values.

A measurement of a Derenzo-like phantom (see appendix A) filled with FDG was performed with the VrPET scanner, in order to test the proposed method. The resulting images are shown on Figure 7.13 with differences of a few percent in peak to valley ratio and noise, but with slightly better images for the single-crystal and improved methods.

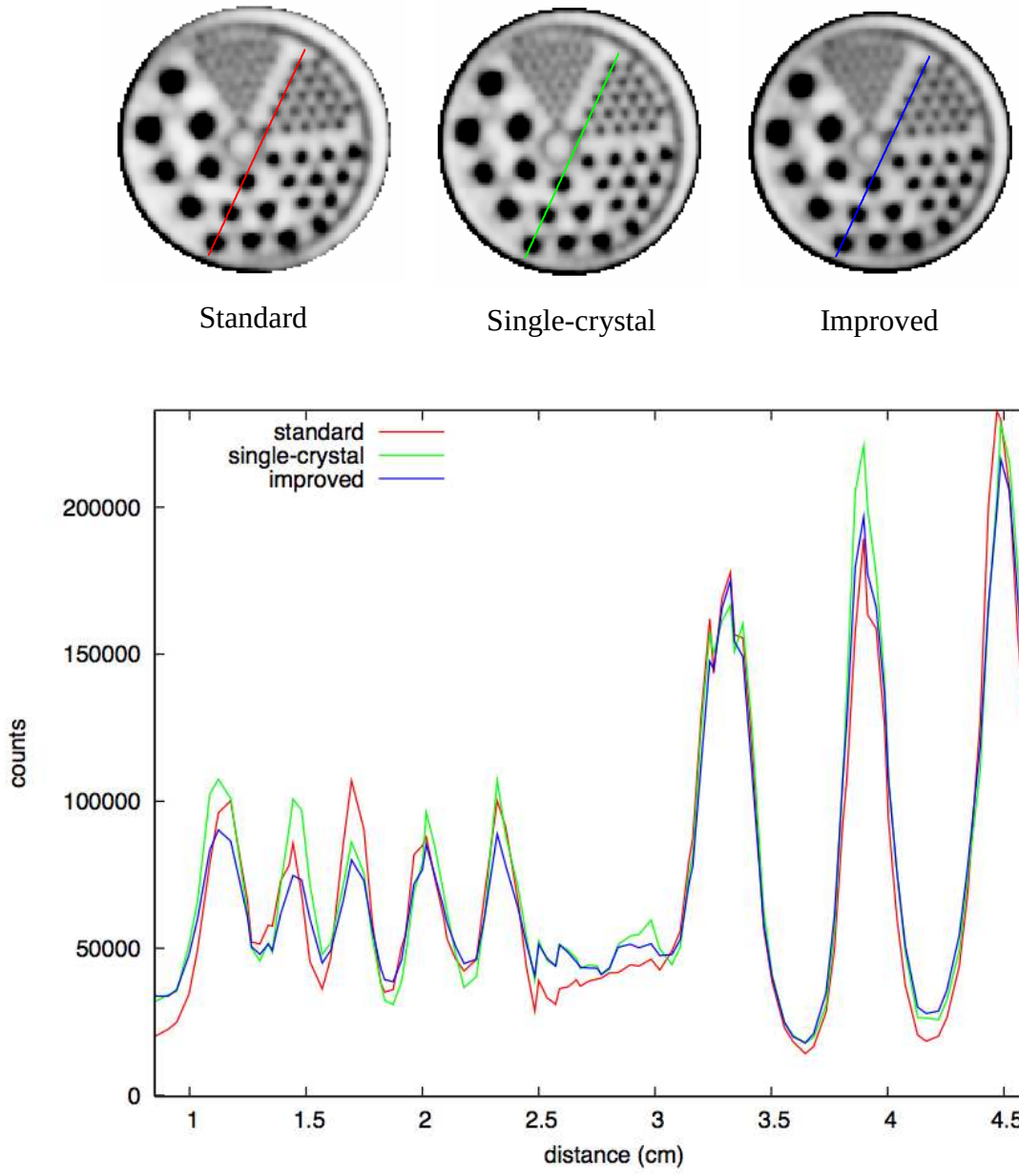

Figure 7.13. Top: 3DOSEM reconstructed images of a Derenzo-like phantom acquired with a real VrPET scanner (Lage *et al.*, 2008). The phantom was initially filled with 300 μCi of FDG and acquired during 5 hours. Bottom: line profiles across the lines drawn in the reconstructed images.

Additionally, we have performed some comparison between images obtained with the standard and single-crystal methods from data acquired with the rPET scanner (Vaquero *et al.*, 2005). Visual inspection of reconstructed images for a Micro Deluxe Resolution phantom (see Figure 7.14) and the heart region of a mouse (see Figure 7.15) shows better resolution and less background level for the single-crystal method. The main difference between the results obtained with rPET and VrPET scanners is the contribution of pile-up events. The integration time of the rPET scanner is about 200 ns while for VrPET is reduced to 130 ns. Thus, there is a higher contribution of pile-up events for the rPET scanner. As pile-up event are smoothly distributed in the flood histogram of one detector, reducing the contribution of events with centroid in the inter-peak regions will decrease more pile-up than true events.

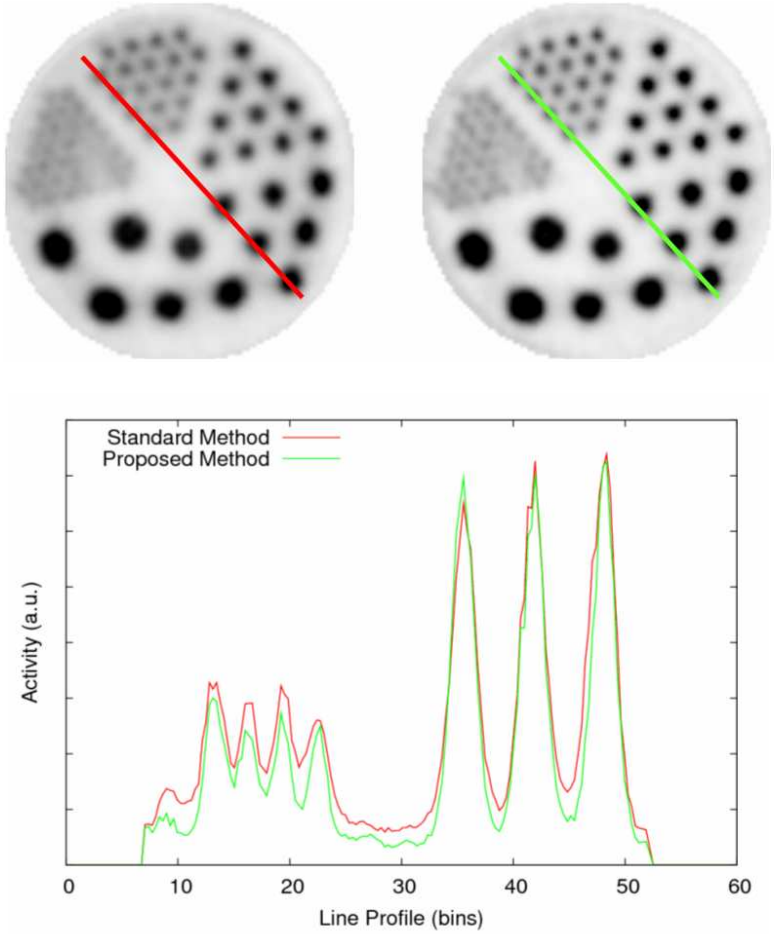

Figure 7.14. This figure shows the results for a Micro Deluxe Resolution phantom filled with FDG, acquired with rPET and reconstructed with the 3D-OSEM algorithm using standard (top left) and single-crystal (proposed in the figure, top right) methods. Improvements in resolution and overall reduction of the level of background are clearly seen.

7.3. Conclusions

A priori knowledge of the probability that detected events are single-crystal has been estimated using a combination of XY position information and energy deposited in the detector. This *a priori* information has been introduced in a 3D-OSEM iterative reconstruction method. A more specific system response matrix is used, accelerating the convergence of the algorithm and obtaining images with better resolution and recovery coefficients. If only single-crystal events are used during reconstruction, better resolution is obtained at the expense of a moderate increase of noise level in uniform regions, due to the fact that counts with less reliable pixel identification are effectively removed from the reconstruction. The recovery coefficient was evaluated using a simulated acquisition of an IQ phantom acquired with a VrPET scanner. These results show how, keeping all the counts and using specific SRM for each type of event, produces higher values of recovery coefficient and converge faster with a reasonable level of noise. The proposed methods show slight improvement when evaluating images from real measurements taken with VrPET, but the single-crystal method shows substantial improvement for acquisitions taken with rPET scanner, due to its capacity for reducing the contribution of pile-up events on the acquired data.

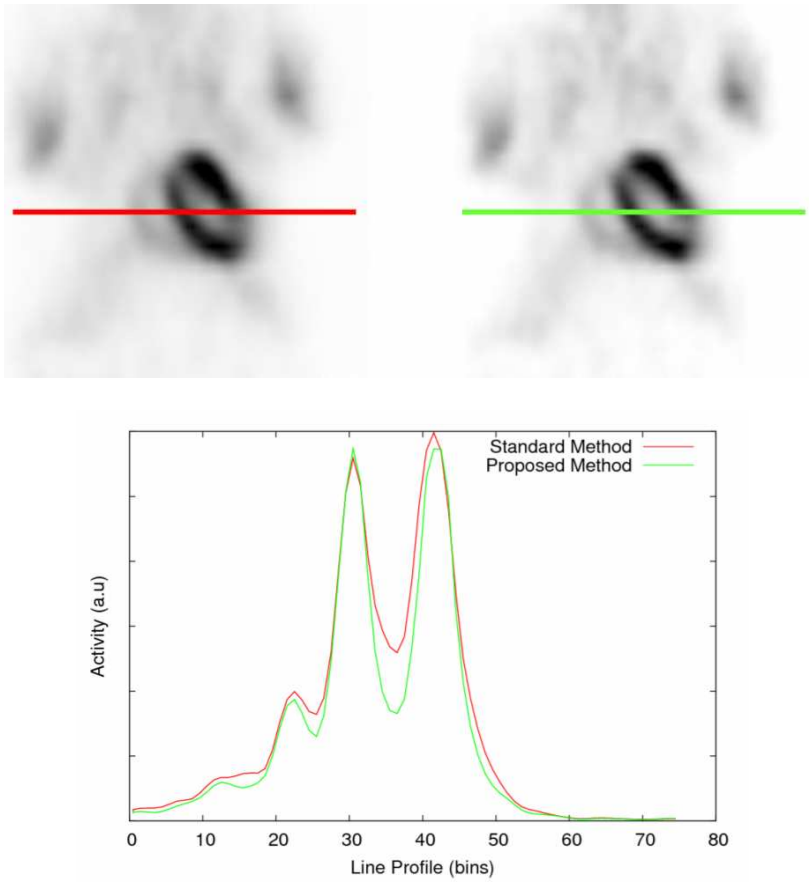

Figure 7.15. This figure shows the results from one mouse injected with FDG and acquired with the rPET scanner. Both standard (top left) and single-crystal (proposed in the figure, top right) methods are compared. Line activity profiles plot (bottom) show the improvement achieved in the heart region using the single-crystal method.

8. Considerations for the design of small animal PET scanners

8.1. Introduction

Previous chapters have shown some applications of Monte Carlo methods for improving the quality of the images obtained with existing PET scanners. All the experience gained until this point will now be applied to the design of a new PET scanner. We will try to determine the main bottlenecks that constrain performance of scanners in order to assess which configuration parameters need to be changed. PeneloPET shows its usefulness again on this chapter, allowing for exhaustive tests of scanner configurations in a short period of time.

Small animal PET scanners are in continuous development. New devices are produced with higher sensitivity, spatial resolution, and count rate capabilities (Wang *et al.*, 2006; McFarland *et al.*, 2007). The design of a new PET scanner is a very complex process that requires taking decisions of several kinds. Monte Carlo simulations have become an invaluable tool during this process, allowing for exhaustive studies of all the components that form the scanner (Heinrichs *et al.*, 2003). The purpose of this chapter is the study, by means of Monte Carlo simulations, of how the configuration parameters of a typical small animal PET scanner have an effect on its performance.

Current PET scanners are composed of block detectors (Wang *et al.*, 2006), of PS-PMTs coupled to scintillation crystal arrays. Block detectors are arranged in parallel rings that usually achieve better transaxial than axial spatial resolution. Different configurations have been evaluated. Parameters such as ring diameter, detector size, pixel size, scintillator material, and electronics have been exhaustively tested in order to assess the response of the scanner performance to variation of these parameters.

As a starting point, the desired values for the performance of the scanner were set. The sensitivity at the center of the FOV for an energy window from 250 keV to 700 keV should be around 10%. The spatial resolution at the center of the FOV should be better than 1.7 mm. Finally, both axial and transaxial FOV should be around 10 cm. High count rate capability is also a consideration of design. The methods employed to estimate these parameters are described in what follows.

There are four characteristics of PET scanners considered here: spatial resolution, sensitivity, FOV size and NEC Rate. Spatial resolution, FOV size and sensitivity depend on geometry and scintillator material, but not on electronics. On the other hand, obtaining good NEC Rate values depends on the geometry and, more essentially, on the electronics and the scintillator shaping time, that in turns depends on the scintillator decay constant. For instance, with the same scanner geometry and materials but different electronic resources, very different count rate capabilities can be achieved.

8.2. Spatial resolution and sensitivity

Spatial resolution and sensitivity are the most important parameters in the performance of a PET scanner. When designing PET scanners, hundreds or thousands of configurations must be exhaustively evaluated in order to obtain the best compromise between both parameters. One powerful figure of merit that has been used in this study is the representation of the spatial resolution as a function of sensitivity for each scanner configuration. However, the evaluation of these two parameters by simulating the NEMA protocols is an extremely tedious (and CPU-consuming) task when working with many configurations. In order to

simplify this process, an alternative method that reduces considerably the computation time has been employed to estimate both parameters, without performing reconstructions on simulated data.

Indeed, in this study we rely on the root mean square (RMS) (see eq. (8.1)) of the positioning error, computed as an estimation of the spatial resolution at any location inside the FOV. The positioning error is computed as the RMS difference between the sinogram coordinates for the true line that joints the real (known from the simulation) first interaction point in each detector of the coincidence pair, and the actual coordinates assigned to this same coincidence event inside the sinogram by the scanner, according to the simulation of Anger logic and other positioning algorithms.

$$RMS = \sqrt{\frac{1}{N}\sum_{i=1,N}\left[\left(\Delta\rho_i\right)^2 + \left(\rho_i \cdot \Delta\theta_i\right)^2\right]} \qquad (8.1)$$

Actual coordinates registered by the scanner may be blurred due to multiple interactions in each detector, photon-pile-up, noise, errors in the Anger-like procedure or crystal assignment, etc. This *detector-only* contribution to the blurring will be combined with other physical effects that contribute to the intrinsic blurring of PET, such as positron range. RMS values obtained in this way are compared with the radial spatial resolution obtained from FBP-reconstructed images for some well known scanners (nanoPET (Wyss *et al.*, 2006) and GE eXplore VISTA (Wang *et al.*, 2006)) for which the simulations employed here have been shown able of reproducing the experimental data with good accuracy (see chapter 5). Thus, simulated acquisitions of a ^{22}Na point source located at different radial positions where reconstructed using FORE+2D-FBP methods. The FHWM values obtained (from experiment as well as simulations) where represented as a function of the RMS computed from the simulations. The resulting curve indicated that a linear fit can describe adequately the dependence of the resolution on the RMS and the results of this fit were employed to assess a relation between resolution of the scanner and RMS of the simulations (see Figure 8.1).

We expect that this relationship holds valid for scanners with FOV of approximately similar size. Indeed, in this case the contribution from non collinearity and positron range would be equivalent, and the difference among the resolution obtained with different scanner configurations will be due to intrinsic detector blurring. The validity of this relationship at the +/- 15% level has not been contrasted only for the Vista and NanoPET scanners employed to obtain it. It has also been used to predict the resolution of other commercial scanners (Inveon (McFarland *et al.*, 2007), NanoPET (Wyss *et al.*, 2006)), obtaining good agreement with the measurements from several groups. We have also compared estimates of resolution obtained from the linear fit, with results of simulations of several configurations, where resolution was obtained with more conventional procedures, i.e., after reconstructing the images from the simulated data with an FBP method and measuring resolution from the FWHM of profiles in the images. Results were consistent with the ones derived from the RMS estimation within 15%.

With regard to scanner sensitivity, it is usually given at the center of the FOV. It was evaluated simulating a line source filled with ^{18}F along the central axis of the scanner in order to obtain the absolute central point sensitivity (ACS) (Wang *et al.*, 2006). The ACS value is calculated as two times the coincidence rate divided by the total activity that falls inside the FOV. Simulated measurements have also been compared to real acquisitions, validating PeneloPET ((España *et al.*, 2009) and chapter 4).

$$ACS = \frac{2 \times coinc/\sec}{activity_{FOV}} \tag{8.2}$$

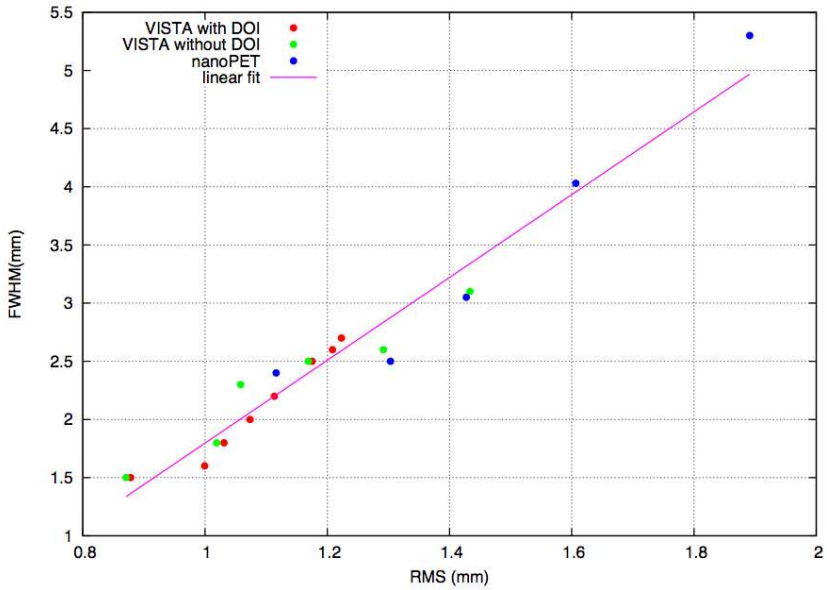

Figure 8.1. FWHM-RMS relation obtained from a linear fit to experimental points from known scanners. These scanners are NanoPET and VISTA (Wang *et al.*, 2006).

8.3. Field of view

The maximum axial FOV size achievable with a scanner is very approximately the axial length of the scanner. The maximum transaxial FOV can be estimated from the LORs density across the FOV. The radial bin of each LOR is estimated in the same way that for sinograms. The density of LORs contributing to a radial bin decreases very sharply at the edges of the FOV. The maximum useful achievable transaxial FOV can be considered as the limit where the LOR density falls to 50% of the average value. Figure 8.2 shows the LORs density for a scanner made of rings of 10 detectors similar to the VrPET one (Lage *et al.*, 2008), with diameters varying from 14 to 17 cm.

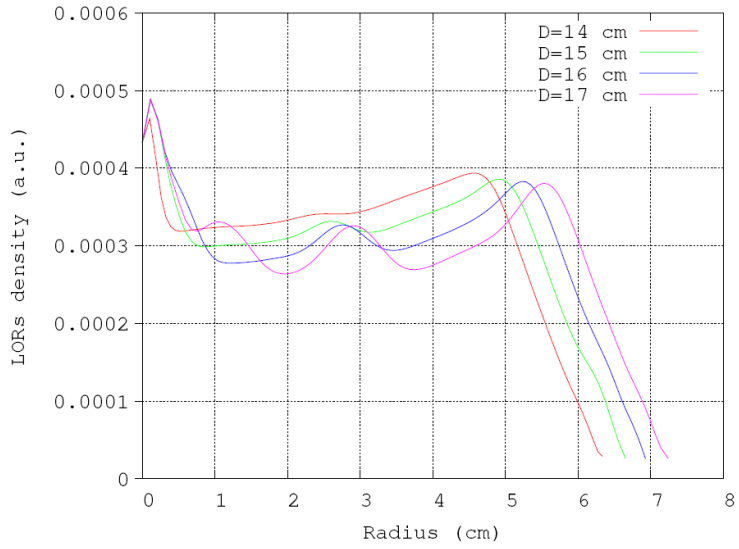

Figure 8.2. LORs density versus radial position for scanners with different diameters, all of them with 10 detectors per ring, similar to the nanoPET scanner (Wyss *et al.*, 2006).

8.4. Pitch size

Pitch size is the distance between centers of adjacent crystals. It is related to the transverse size of the pixel crystal and the thickness of the intercrystal reflector. Generally it is better to use a reflector thickness as small as possible, in order to increase the packing fraction of the detectors and, as a result, the sensitivity of the scanner (Phelps, 2004). A reflector thickness of 0.7 mm was chosen in what follows. Further, different crystal sizes were tested to compare the spatial resolution and sensitivity at the center of the FOV. For instance, the impact of pitch size in the resolution and sensitivity of a scanner composed of 2 rings of 10 detectors, like the rPET one, each one with LYSO crystals and a diameter of 14 cm, similar to the nanoPET scanner, has been studied. Crystal sizes from 1.2 to 1.9 mm were used to complete a block detector with a total width of 45 × 45 mm^2. The results of Figure 8.3 show some improvement in spatial resolution with the smaller crystal sizes, of up to 8%. Sensitivity keeps constant, as one would expect. As the effect of pitch size, within the ranges explored, is not very important, a fixed pitch size of 1.3 mm will be chosen in the remaining results of this chapter, unless noted otherwise.

8.5. Effect of the choice of scintillator crystal in spatial resolution and sensitivity

As mentioned before, block detectors are composed of a volume of scintillator coupled to a photosensor (typically photomultipliers or APDs) (Bailey *et al.*, 2004). These blocks form the basic elements of the scanner and their design will determine the sensitivity and spatial resolution achieved with the whole scanner. In order to define block geometry and composition, parameters such as scintillator material, pitch and crystal length were analyzed. As part of the comparison and evaluation of the performance achieved with different block configurations, the spatial resolution at the CFOV was studied as a function of the absolute central point sensitivity (ACS) for different scanner configurations. The energy window was fixed to 250-700 keV for all these studies. The desired axial and transaxial FOV are 10 cm.

Figure 8.3. Spatial resolution and sensitivity at CFOV for different pitch sizes for a two ring of detectors similar to VrPET with diameter of 14 cm, similar to nanoPET scanner (Wyss *et al.*, 2006).

Table 8.1. Properties of scintillator materials studied.

	LYSO	LSO	LuAP	BGO
Light output (photons/MeV)	25000	25000	10000	8000
Rise time (ns)	0.8	0.8	0.5	5
Fall time (ns)	40	40	17	300

Crystal length and scintillator material were changed in the simulations for different block configurations. The transverse size of individual crystal elements used during this study was fixed to 1.3 × 1.3 mm^2 and a 0.07 mm thick reflector was placed among them. Each block has 34 × 34 crystals for scanners with two or three rings, each with 10 blocks and a diameter of 14 cm. Note that coincidences among all rings were allowed. BGO, LSO, LYSO, and LuAP scintillator materials were simulated for crystal lengths from 8 to 11 mm. Figure 8.4 shows the results for all these combinations. If a sensitivity of 10% is pursued, it can be seen that the variation in spatial resolution is about 25%, depending on the block configuration. This figure should be very useful when deciding the final block design. It will be complemented with information on the count rate capabilities, to accomplish a better block detector definition.

From the Figure 8.4 the following points can be concluded:

- LYSO results show a worsening of resolution by about 0.06-0.1 mm and of sensitivity by 15% percent with respect to equivalent LSO crystals. This implies for instance a total sensitivity reduction from 10% to 8.5% when using LYSO instead of LSO.
- LuAP results are better than LSO ones in terms of sensitivity. As this also is a faster crystal, it will be possible to obtain also better NEC rates with this material.
- The best scintillator in terms of resolution and sensitivity, for a given crystal size, is BGO. It yields 20% more sensitivity than LSO and improves resolution by 0.2 mm. But it has a very slow decay time, which causes trouble with NEC, and a low light yield, that causes (small) problems with crystal identification (Jennifer and Simon, 2005; Smith, 2002).

8.6. Identification of the crystal of interaction

As mentioned before, BGO light output is much lower than the one of LSO and LYSO crystals. This lower photon yield will cause not only a loss of energy resolution, but also poorer crystal identification in the flood histogram. A simulation of the light collection process was performed for low and high count rate in order to evaluate the degradation on the flood field image for LSO and BGO crystals (Murphy-O'Connor, 2006; Cal-González, 2008). A 13 × 13 crystal array with a pitch size of 1.55 mm coupled to a Hamamatsu R7600 PMT was used for this study. Integration time of 600 ns was employed for BGO and 80 ns for LSO. Results of Figure 8.5 shows that crystal identification is not worsened very much but, at high count rate, the BGO detector has a higher background formed mainly by pile-up events due to the longer fall time of this scintillator.

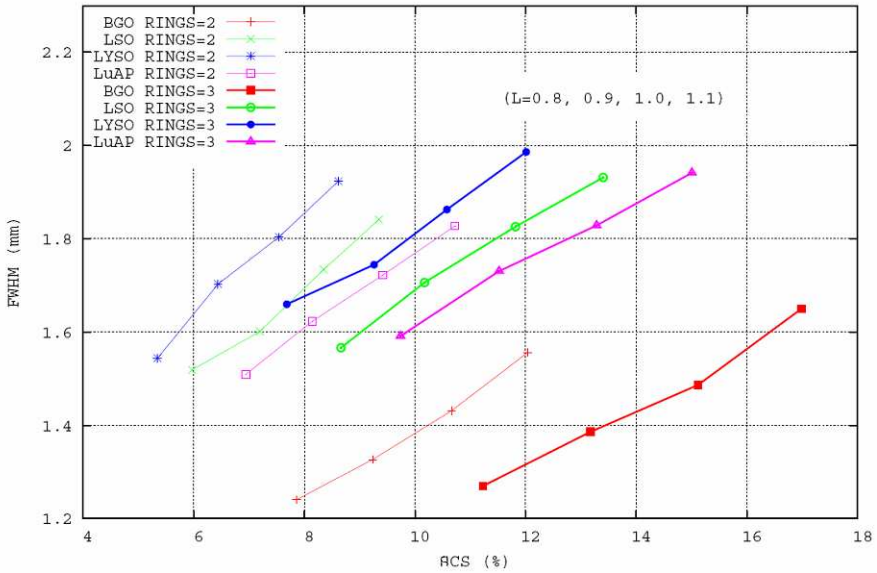

Figure 8.4. Spatial resolution at CFOV versus ACS using different block configurations. L represents the values given to the crystal length. Different crystal length of same materials are represented with points joined with a line of the same colour, where the shorter crystal lengths appear in the left part of the figure, that is, with lower sensitivity values but better spatial resolution.

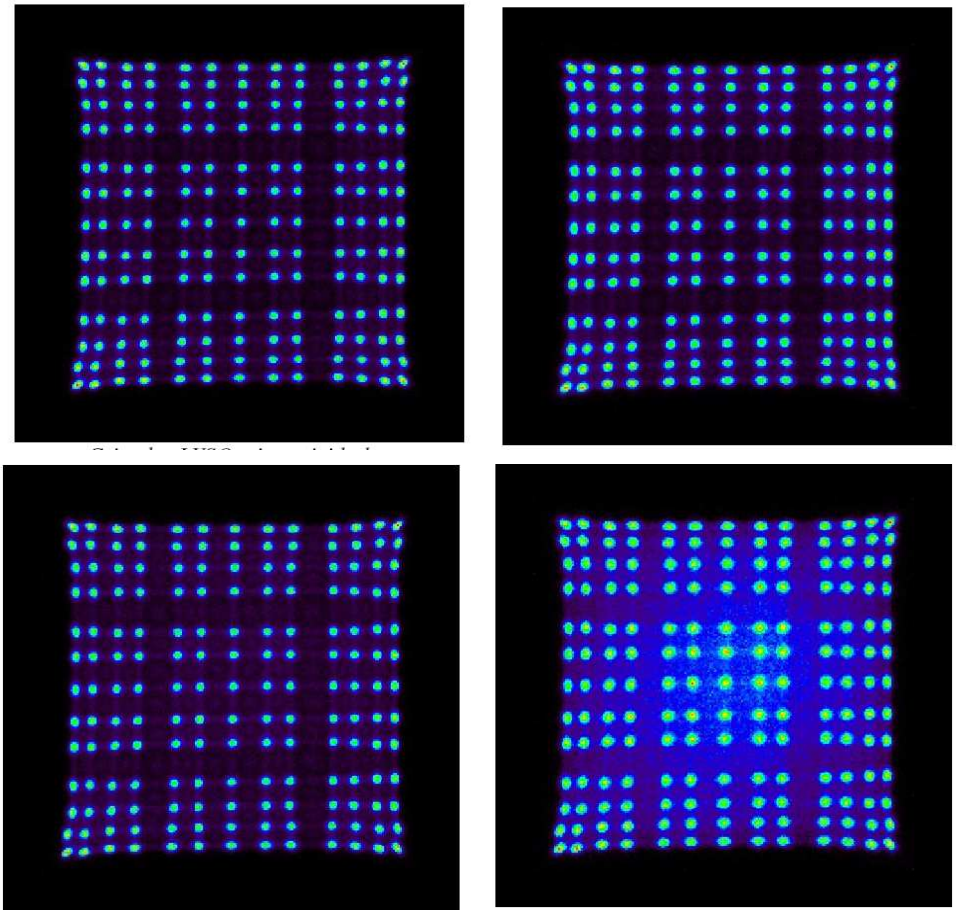

Figure 8.5. LSO (left) and BGO (right) flood field images for 13 × 13 crystals array coupled to a Hamamatsu R7600 PMT. Top images show results with low count rate and bottom images show results with 10^6 cps.

8.7. Considerations about the thickness of the scintillator

Annihilation photons have larger probability to undergo Compton scatter than photoelectric effect when passing through scintillation materials (Knoll, 2000). This gives rise to degradation in spatial resolution with the thickness of active material, independent of whether one or more layers of scintillator are employed (Bailey *et al.*, 2004). Figure 8.6 shows the dependence on the length of the scintillator crystals of the singles sensitivity for a 34 × 34 block of crystals with transverse size of 1.3 × 1.3 mm^2, irradiated with a ^{18}F point source placed at 8 cm of the front face of the detector. Results for BGO and $LaBr_3$ scintillation materials, for three different energy windows, are shown. These curves saturate when all the photons that go through the detector block are stopped. The thickness where saturation occurs represents the crystal length that would produce the maximum sensitivity in the scanner. For instance, using BGO crystals with a total length higher that 3 cm does not change sensitivity much. Comparing BGO and $LaBr_3$ results, it can be seen that 1 cm of BGO can stop more than twice photons than 1 cm of $LaBr_3$.

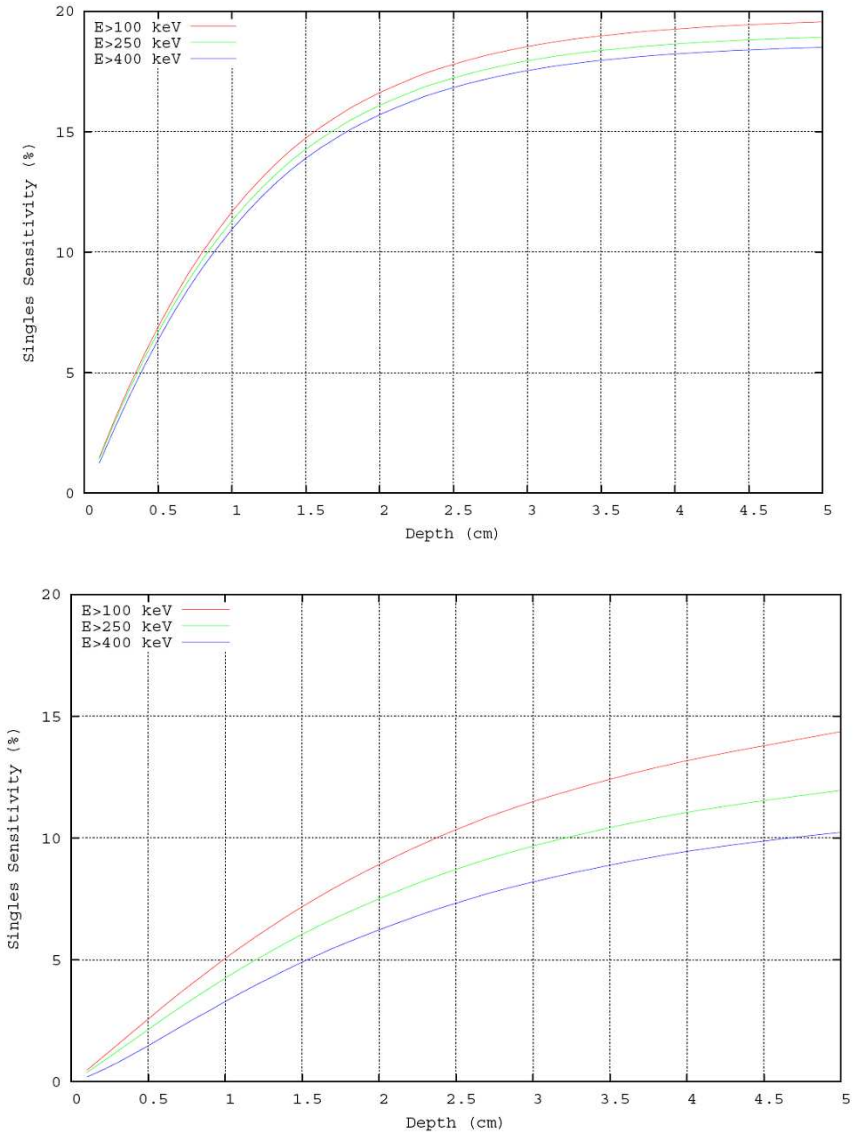

Figure 8.6. The sensitivity of the singles to the length of scintillator crystal for a 34 × 34 block (same as described before) irradiated with a ^{18}F point sourced placed at 8 cm from the front face of the detector. BGO (top) and LaBr (bottom) scintillator results are shown.

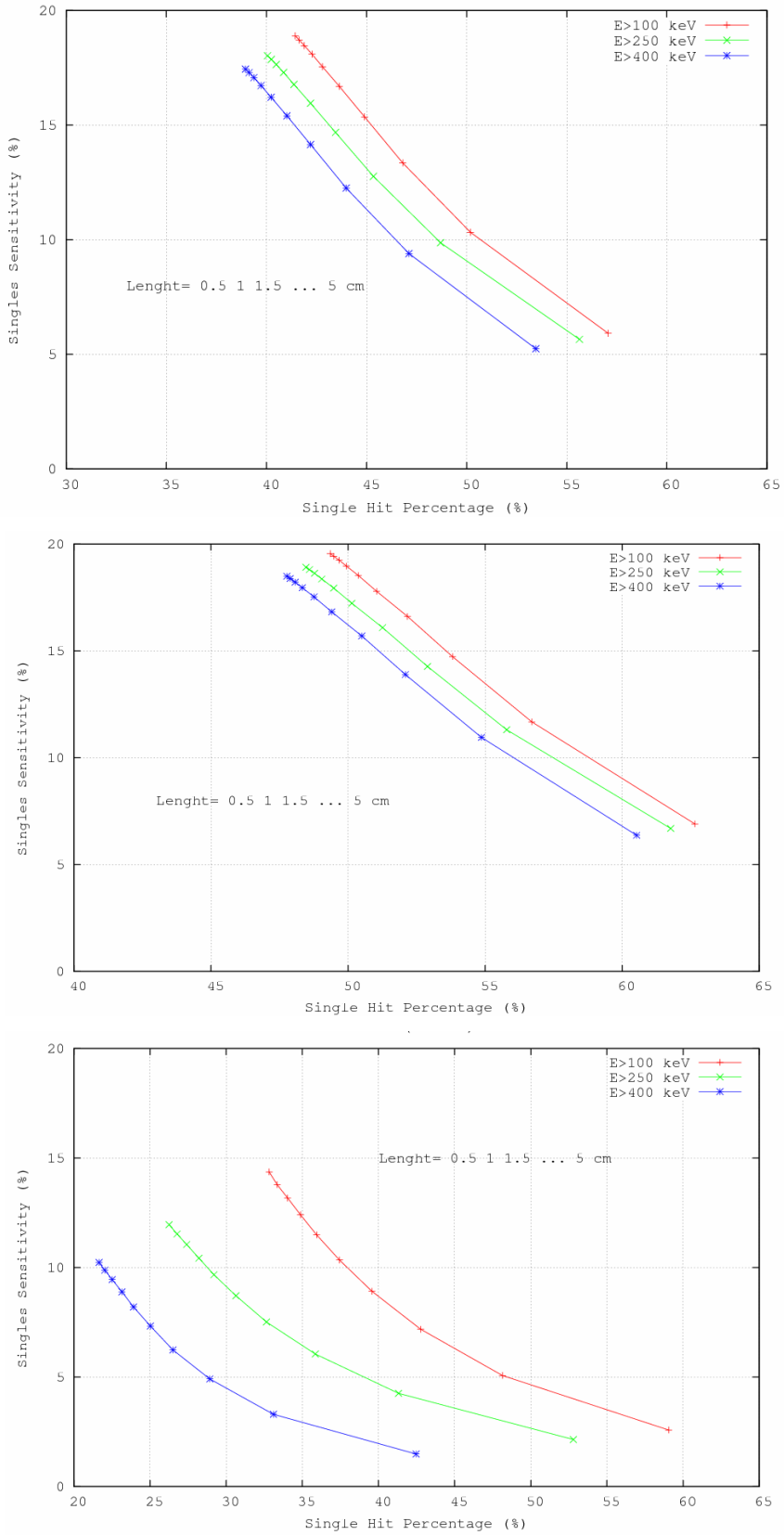

Figure 8.7. Single-events sensitivity versus single-hit percentage for LSO (top), BGO (middle) and LaBr (bottom) scintillation materials. Different crystal lengths results are joined with lines for the same energy window.

The singles sensitivity versus the percentage of photons that interacts just once in the detector is plotted in Figure 8.7. This figure allows to study how Compton scatter influences the detection properties depending on block thickness. LSO, BGO and $LaBr_3$ scintillation materials were studied with three different energy windows. It can be noticed that, for the thickest crystal, the percentage of photons that interact only once almost equals the photoelectric fraction obtained (than, thus, represents a lower bound for the single hit percentage), due to the fact that photons which undergo Compton scatter will produce additional hits inside the block and thus for infinite size crystals, (or very large ones), this fraction of single-interaction photons is just the one of the photons that only interact once and disappear. Higher single hit percentage translates into a better identification of the crystal of first interaction, and thus improves the resolution of the scanner. Due to its larger photoelectric fraction, BGO has the higher single-interaction photons fraction, followed by LSO and LaBr.

8.8. Improvement of spatial resolution of PET scanners

The spatial resolution of PET scanners can be improved, sacrificing sensitivity if a method based on the results presented in previous chapter is employed. This method consists in applying an estimation of the likelihood for having *single-crystal* events, to filter the detected events (see chapter 7). In order to estimate the improvement that can be obtained with this method, a ring of ten detectors, 16 cm diameter, with arrays of 34 × 34 crystals with transversal size of 1.3 × 1.3 mm^2 was simulated storing only the events for which the photon interacts only once (1 hit crystal) or, rather, the photons that interact only in one crystal. Conventional acquisitions were compared to the results of the improved one. Resolution versus sensitivity figures were obtained for three scintillator materials, BGO, LSO and LaBr, and different crystal lengths (from 0.1 to 5 cm). The results are shown in Figure 8.8. Larger crystal lengths appear to the rightmost part of the curves. The resolution and sensitivity obtained with BGO is always better than the ones obtained with LSO, both for normal acquisitions as well as for the ones that include only single-hit events. Single-hit results represent the ideal limit of maximum resolution, at the expense of much reduced sensitivity, that can be obtained with these improved acquisitions. Note that BGO results with conventional acquisitions are better to both respective LSO ones and also better than single-hit LSO results, for crystal lengths longer than 1 cm.

8.9. DOI and radial resolution

As it is well known, spatial resolution worsens away from the (transaxial) center of the FOV of scanners, due to depth of interaction (DOI) effects (Chien-Min *et al.*, 2000), caused by the finite length of the scintillator crystals. This degradation of resolution can be reduced using detectors with two or more layers of scintillator crystals (Kitamura *et al.*, 2004) or phoswich detectors (Seidel *et al.*, 1999). Multilayer detectors would be needed to maintain resolution across FOV and would be particularly useful if the scanner is made with small detector modules. To illustrate this effect and quantify it for small animal PET scanners, the variation of the resolution with the radial position of the source has been computed for a scanner formed of 2 rings of 10 detectors of 34 × 34 crystals with transverse size of 1.3 × 1.3 mm^2 and a diameter of 14 cm. Several detector configurations were tested in order to try different crystal lengths in phoswich configurations (see Figure 8.9). The purpose of this study is to evaluate differences in spatial resolution, thus sensitivity is not considered in this section. One must recall that the resolution at the center of the FOV cannot be improved with multi-layer scintillators, compared to detectors with the same total crystal length. It is only the

variation (degradation) of resolution across the FOV (farther away from the scanner axis) that is more favourable for multi-layer detectors (green line) compared to single layer ones (red line), for a given crystal thickness. Indeed, the best resolution that can be obtained with a given multi-layer arrangement would be the one obtained by keeping only the counts coming from the front layer (blue line). That is, the same resolution of a single layer arrangement with the length of the first layer of the multilayer detector (dark blue line) is recovered. It is interesting to note that resolution across the FOV can also be improved for one (or multi) layer detectors by means of the single-hit acquisition (pink line) explained in the previous chapter, but DOI effects would be similar to those of conventional acquisitions, in the sense that resolution will not be very uniform across the FOV.

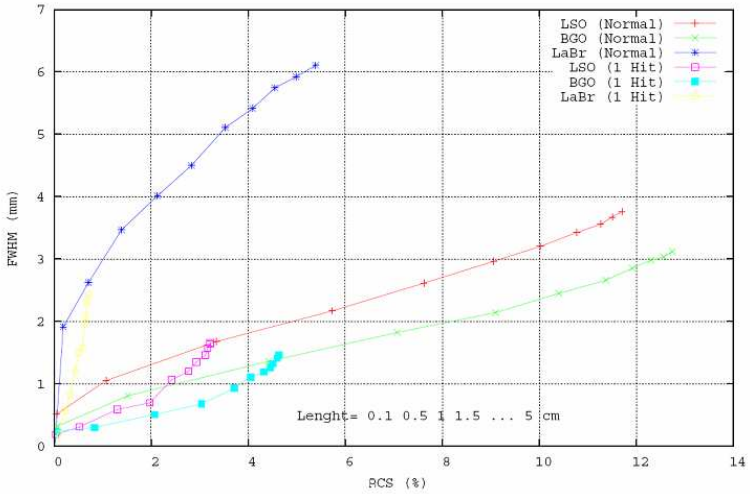

Figure 8.8. Spatial resolution versus sensitivity of conventional and single-hit acquisitions. A ring with 16 cm of diameter and 10 block detectors with 34 × 34 crystals with a transversal size of 1.3 × 1.3 mm^2 was employed for this measurements.

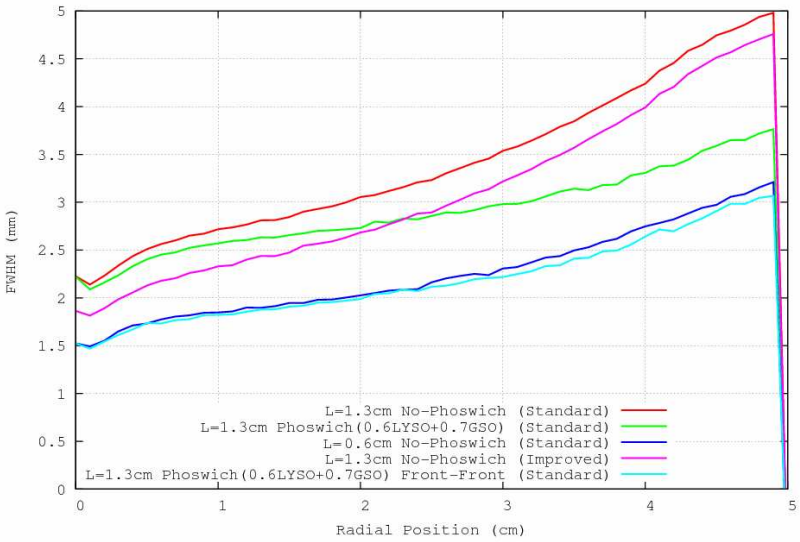

Figure 8.9. Comparison of radial resolution at different radial positions for scanners with multilayer detector compared to single-layer ones. Single (red) and multi-layer (green) detectors have the same resolution at CFOV but quite different at the edge of the FOV, due to the fact that oblique LORs are more affected by DOI. Keeping counts only from the first layer (blue), produces equivalent results to a single layer with the same total length than the first layer (dark blue). Single hit events (green) yield improved resolution, but with loss of sensitivity.

8.10. Count rate and NEC capabilities

The count rate capability of several scanner configurations was evaluated, using noise equivalent count (NEC) rate as indicator. NEC rate is computed for acquisitions of the same phantom at different activity levels. These NEC values obtained are represented as a function of the activity. The peak values of the NEC curves are used to compare count rate performance of different scanner configurations.

The maximum useful count rate obtained from a PET scanner depends on the geometry and material that compose the scanner, and also in a very important way on the configuration of its electronics, that is, on the integration time, coincidence time window, dead time, etc. Random and scatter coincidence events, dead time and pulse pile-up are the main contributions to effective count rate degradation. The images with the best signal to noise ratio are obtained, at a given activity values, usually when they are acquired at the maximum of the noise equivalent count (NEC) rate curve (Bailey *et al.*, 2004). A scanner with high sensitivity will not be useful if the dead time is high, or if it is formed with large scintillator blocks with a very slow decay component so that, at moderate rates, a high percentage of pulses suffered from detector pile-up (Germano and Hoffman, 1988, 1990).

In this section, NEC rates for several configurations of the electronics and acquisition system are presented in order to evaluate the effect that each ingredient of the electronics has on the count rate capabilities of the scanner. These simulations were performed with a large size cylindrical phantom (10 cm diameter and 15 cm length) acquired with three different energy windows (100-700, 250-700, and 400-700 keV). NEC curves were estimated from simulations of a scanner composed of two rings, each one with 10 PMTs of 34×34 crystals with a size of $1.3 \times 1.3 \times 14$ mm^3 and a diameter of 14 cm. Each PMT is connected in coincidence with the 5 opposite detectors of each ring, thus 10 PMT in total. In the next figures the NEC curves and coincidence rates, under several assumptions, are presented. Different integration and conversion times are combined and the effect of pile up rejection is also tested. In Table 8.2 typical values for the singles and coincidence rates expected in total and per detector for this setup, for activities of the order of 2 mCi, are listed.

When pile-up rejection is applied, singles with the initial trigger less separated of another trigger than a specified time are not accepted for coincidences.

Table 8.2. Rates measured for a scanner with two rings, each one with 10 PMTs. Acquisitions of a large cylinder phantom filled with 2 mCi of ^{18}F, with energy window of 250-700 keV, 75 ns of integration time, 100 ns of conversion time, and 10 ns of pile up rejection time.

	Total	Per detector
Singles rate	$3.8 \cdot 10^7$	$1.9 \cdot 10^6$
Coincidence rate	$1.02 \cdot 10^6$	$5.1 \cdot 10^4$
Trues rate	$7.5 \cdot 10^5$	$3.7 \cdot 10^4$
Randoms rate	$2.7 \cdot 10^5$	$1.3 \cdot 10^4$
Rate of accepted pile up events	$4.0 \cdot 10^4$	$2.0 \cdot 10^3$

First, the effect of conversion time is reviewed in Figure 8.10 and Figure 8.11, considering that a pile up rejection mechanism is available, and using 75 ns of integration time for both 100 ns or 1200 ns conversion time. Degradation in performance due to the worse conversion time is of the order of 50%. The position of the maximum of the NEC shifts

from 1.5 to 0.7 mCi and the rate of the maximum values of the NEC decreases from 160 kcps to 100 kcps (250-700 keV energy window) due to conversion time.

One important conclusion of these figures is that the narrowest energy window is the one with larger NEC values, showing that the larger rejection of scatter implied in the narrow energy window, compensates the loss of sensitivity.

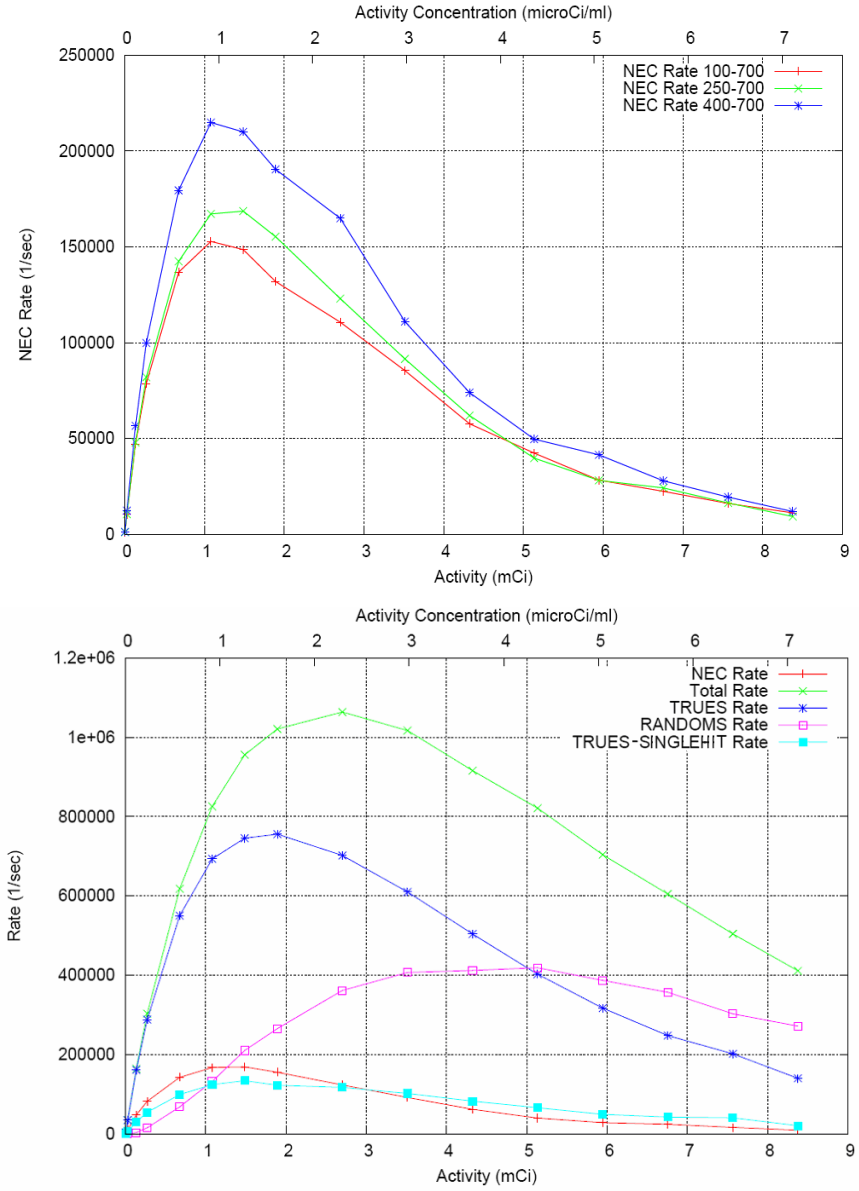

Figure 8.10. (Top) NEC rate measured for a big cylinder using different energy windows. (Bottom) Total, partial and NEC rates for an energy window of 250 to 700 keV. The integration time was fixed to 75 ns, conversion time to 100 ns and pile-up rejection to 10 ns.

The following test shows the effect of pile-up rejection (see Figure 8.12). For the same integration and conversion time as in Figure 8.11, for the 75+1200 case, pile up rejection is now switched off. We notice that the NEC peak is now found at less activity (0.6 mCi), and reaches merely 80 kcps, 20% less than when pile-up rejection was on but, more importantly, the rates that the machine should sustain are 800 kcps, versus 400 kcps when pile-up rejection is in effect. These larger singles rates produce an increase of randoms contribution. Furthermore, counts accepted without pile-up rejection will suffer from pile-up (and thus

wrong crystal identification) in a percentage of 30% at the peak of the NEC, while with pile-up rejection in place, there are virtually (< 5%) no counts accepted with pile-up. If pile-up events are not rejected prior to conversion, but rather after it, because they fall out of the energy window, the main bottleneck or contribution to the dead time of the scanner would be conversion time.

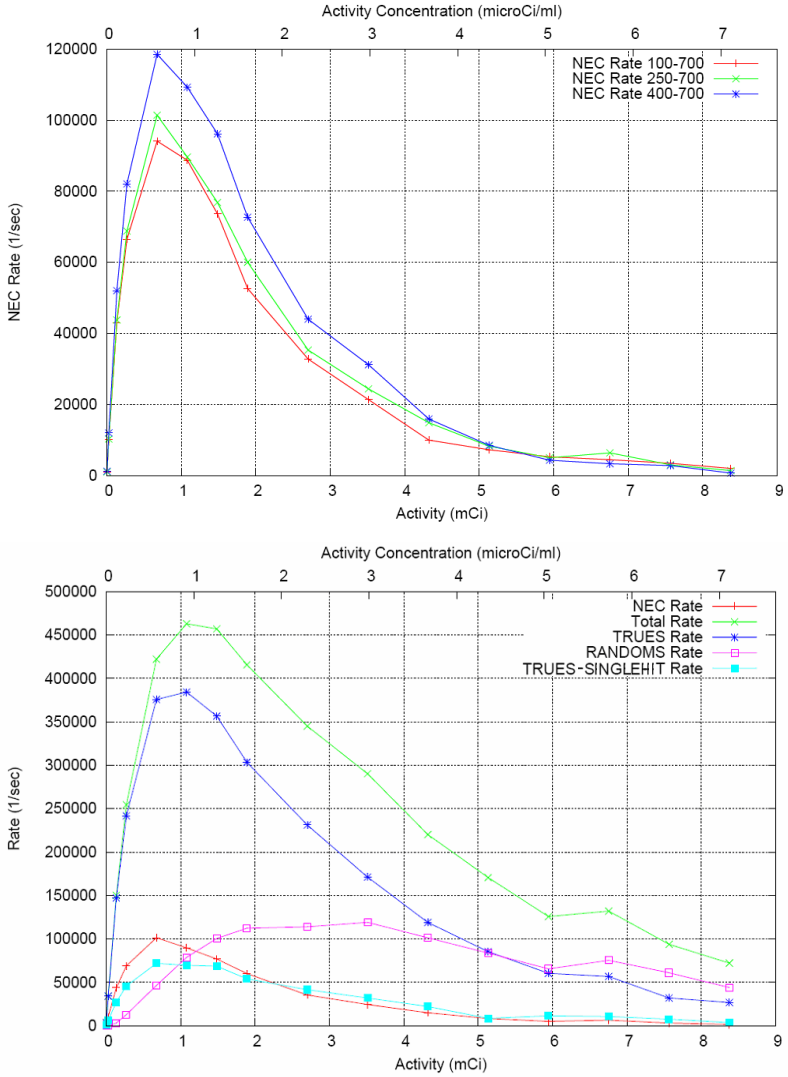

Figure 8.11. (Top) NEC rate measured with a big cylinder using different energy windows. (Bottom) Total, partial and NEC rates for an energy window of 250 to 700 keV. The integration time was fixed to 75 ns, conversion time to 1200 ns, and pile-up rejection to 10 ns.

Figure 8.13 shows the effect of reducing the integration time from 75 to 50 ns. Near a 20% increase in the NEC rate and activity at the peak of the NEC is obtained. Coincidence rate is increased to 1200 kcps.

8.11. Acquisition protocols

Some PET scanner have a reduced number of detectors, due to the high cost of the detection elements, at the expense of some sensitivity loss (Vaquero *et al.*, 2005). Complete angular sampling is achieved by rotating the detectors around the field of view. The widespread use of iterative statistical methods of reconstruction, together with the fact that

these iterative reconstruction methods are more tolerant to incomplete angular sampling, allows to explore the possibility of using different rotation schemes (i.e. continuous vs. step and shoot) of the detectors, in order to obtain the best image resolution with the minimum acquisition and reconstruction times.

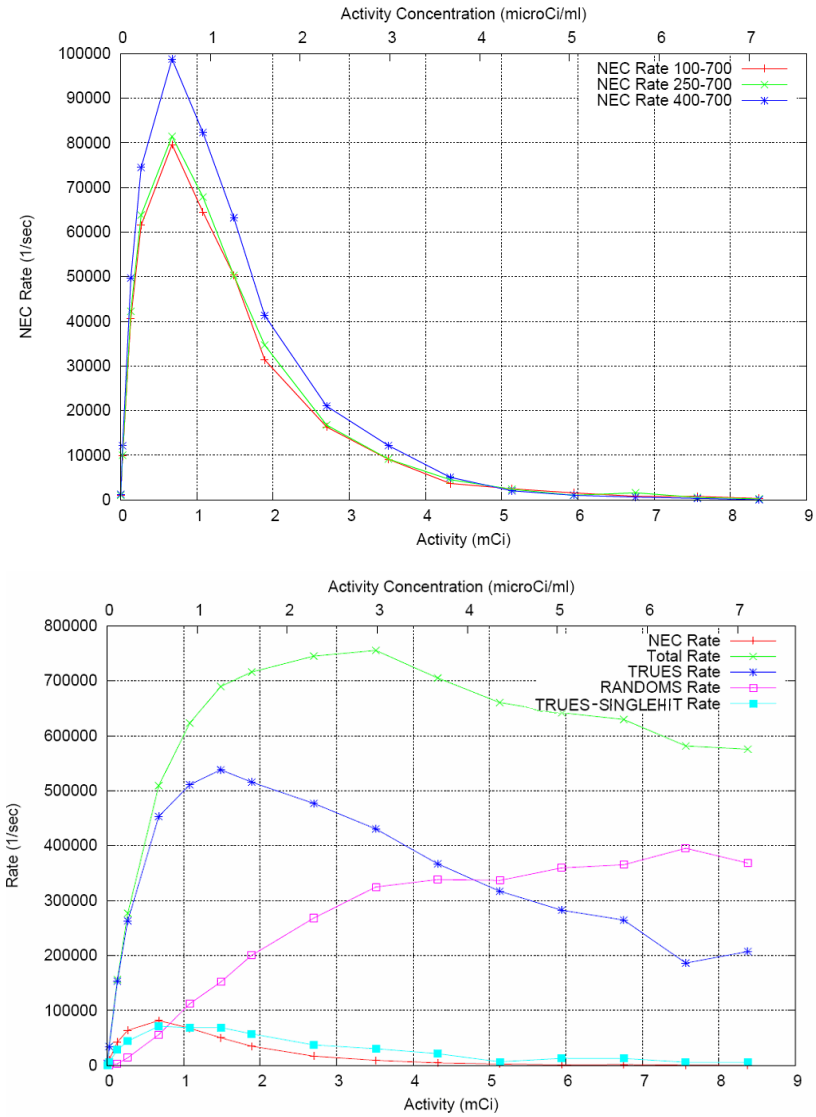

Figure 8.12. (Top) NEC rate measured for a big cylinder using different energy windows. (Bottom) Total, partial and NEC rates for an energy window of 250 to 700 keV. The integration time was fixed to 75 ns, conversion time to 1200 ns and no pile-up rejection was employed.

Organizing the data in LOR histograms (Kadrmas, 2004) keeps the spatial but not temporal resolution of the PET measurements. Continuously rotating scanners make extremely difficult the use of LOR histogramming for reconstruction. An alternative option is LIST mode reconstruction (Barret *et al.*, 1997) which keeps both spatial and temporal resolution. The computational cost of LIST mode reconstructions is highly dependent on the number of detected events (N_{counts}). A further alternative is to reconstruct data organized in sinograms. This causes a loss of spatial resolution due to the rebinning of the data acquired (Kadrmas, 2004). If the number of counts is much higher than the number of sinogram elements (N_{bins}), the best option for continuously rotating configurations would be reconstruction from sinograms. However, if step and shoot rotation schemes are used during acquisition of PET data, LOR histogramming would be possible. Step a shoot rotation

consists in acquiring data only while the scanner detectors are placed in a fixed angular position. Different fixed angular positions are used in order to complete angular sampling.

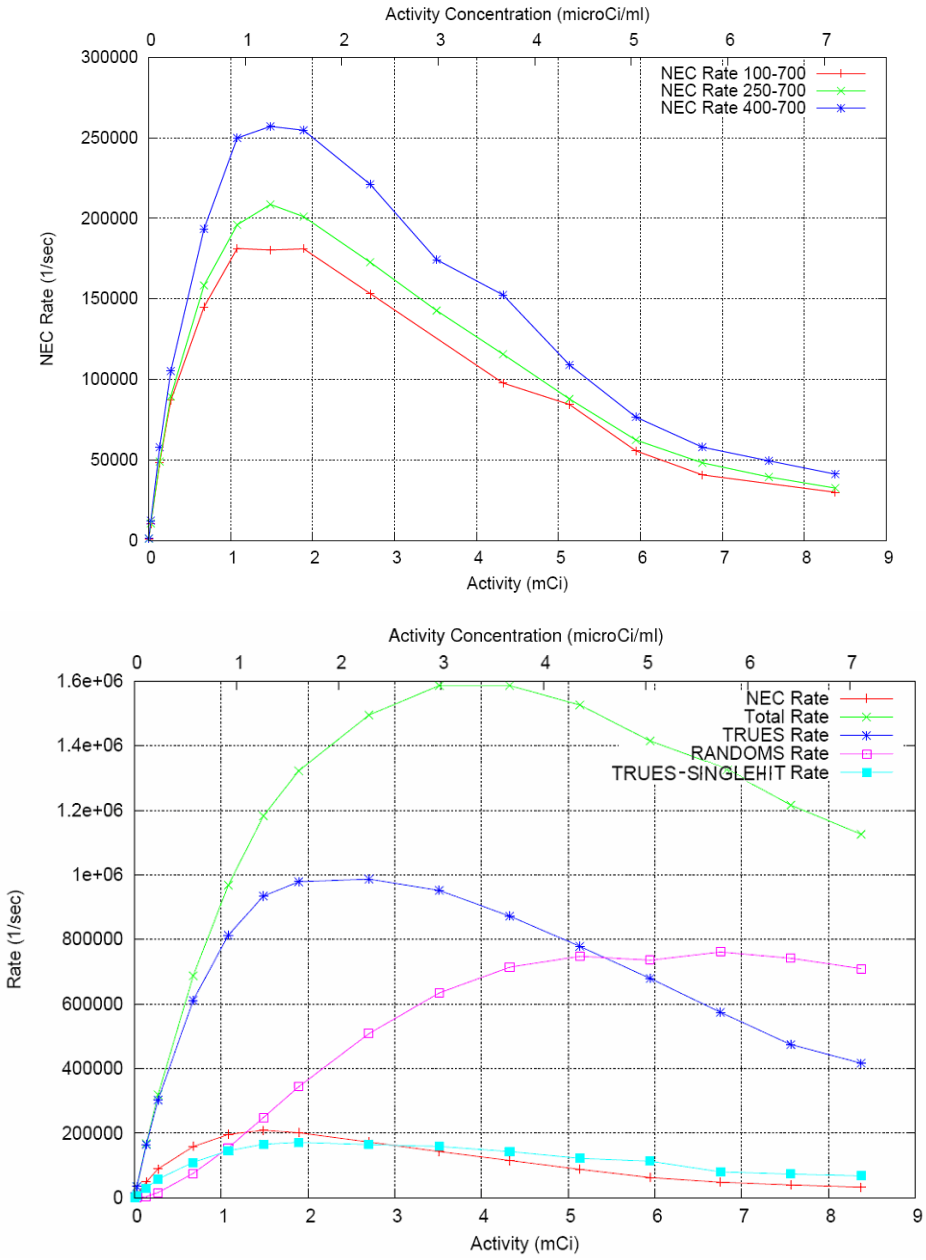

Figure 8.13. (Top) NEC rate measured for a big cylinder using different energy windows. (Bottom) Total, partial and NEC rates for an energy window of 250 to 700 keV. The integration time was fixed to 50 ns, conversion time to 100 ns, and pile-up rejection to 10 ns.

LOR histograming (Kadrmas, 2004) of data may be better suited for iterative reconstructions, because the physical characteristics of the scanner are related to the nature and placement of the detectors that define every LOR, rather than by their corresponding position inside the sinogram. This is why, in general, the best way to reconstruct using iterative methods is LOR histograming, which allows for optimal evaluation of the system response matrix (Herraiz *et al.*, 2006).

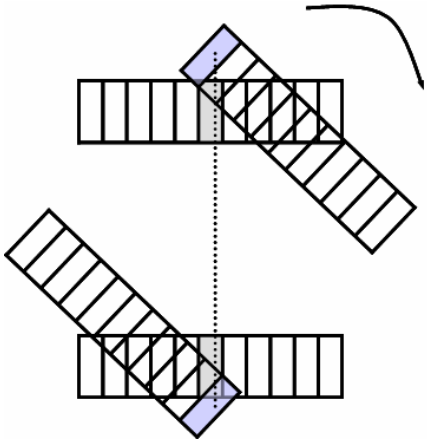

Figure 8.14. Events assigned to the same sinogram coordinates may have been acquired with different detector orientations, which implies a different response matrix (or detector configuration) that, in general, depends on the actual angular position of the detectors for each count.

Sinogram histogramming involves the combination of several LORs into the same radial bin, depending on their radial position (see Figures 8.14 and 8.15). This causes for instance that central radial positions have larger number of LORs per bin than those in the radial edge, as shown in Figure 8.15. This fact must be corrected by a normalization procedure that generally spoils or mask the statistical nature of the acquired data and thus prevents iterative methods to work at their best (Herraiz *et al.*, 2006; Kadrmas, 2004).

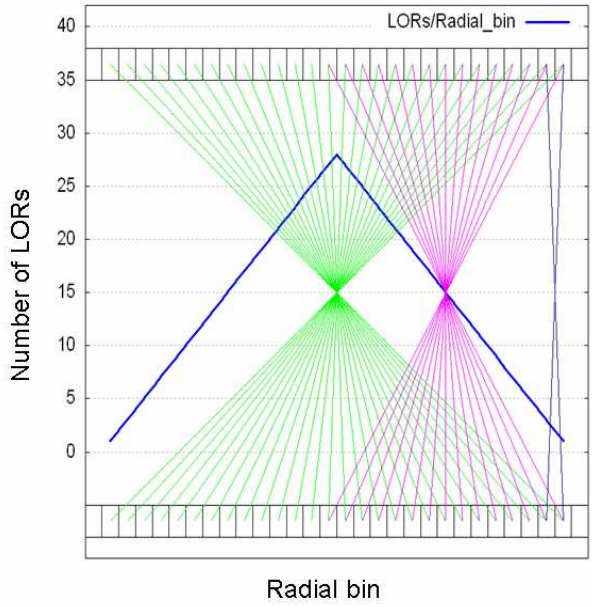

Figure 8.15. The number of LORs per radial bin depends on the radial position (blue line). Green and pink lines show the number of LORs that contribute to two different radial positions. Grey lines delimitate detector crystals.

Further, each radial bin receives counts from several LORs, so that the information about the physical position of the scanner for each individual coincidence event is lost in the sinogramming process. Figure 8.16 shows the mixed response shapes and their corresponding radial bin response. It shows how the response profile of LORs has more information about each coincidence event and that the sinogram bins receive contributions from many LORs with different detector response, which blurs the reconstructed image.

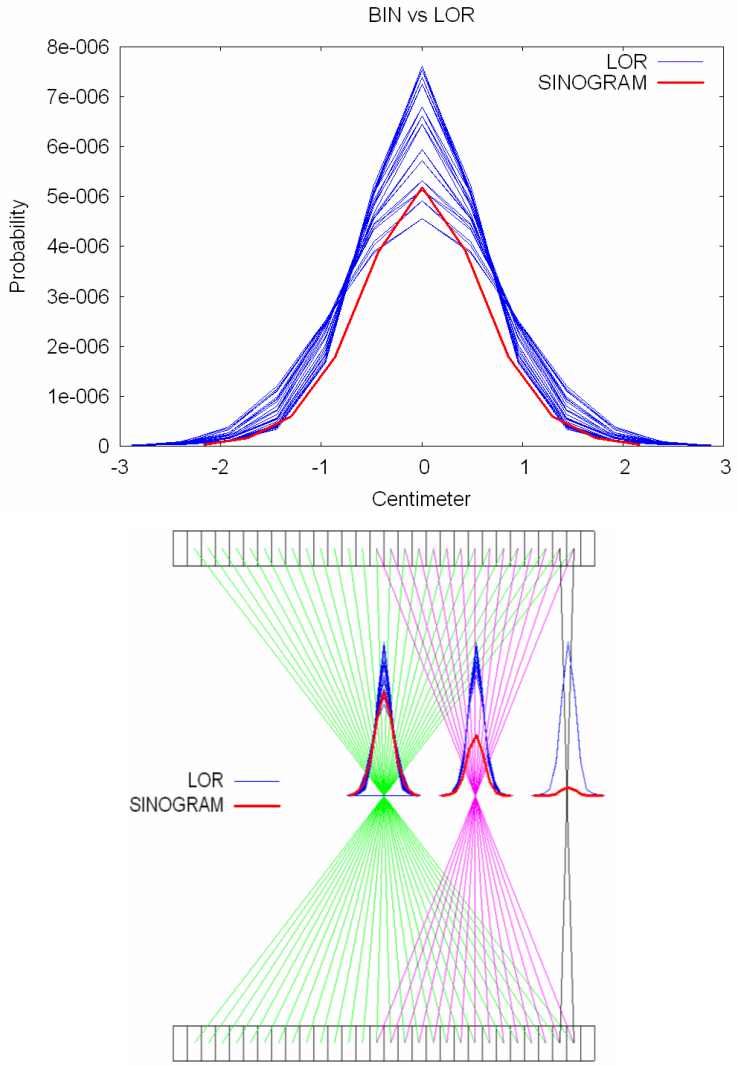

Figure 8.16. Comparison of the transverse response of a specific radial bin (red line) and the one of all the LORs (blue lines) that contribute to that radial bin. Central radial bin (top) and scheme for several radial bins (right).

PeneloPET Monte Carlo code (España *et al.*, 2009) has been used to simulate rotating PET scanners, producing simulated data which were reconstructed with a 3D-OSEM algorithm (Herraiz *et al.*, 2006). The spatial resolution achieved for different rotation schemes was compared. The first rotation scheme considered consists in acquiring data in a continuous rotating mode, arranged in sinograms, that is probably the method most often employed (Vaquero *et al.*, 2005). The other rotation schemes studied are several step and shoot schemes, with data sorted in LOR histograms. The results show that resolution can be improved by up to 30 % just by modifying the configuration of the rotation scheme and the prescription for histogramming the data.

A two detector block scanner, each block made of a 30 × 30 array of LYSO crystals of 1.6 mm in pitch and 12 mm in length, is employed to evaluate the improvement achieved with step and shoot acquisitions versus continuous rotation. The transaxial FOV is 4.8 cm diameter. This scanner is similar to the Suinsa rPET (Vaquero *et al.*, 2005) scanner, with two detectors instead of four. The number of sinogram bins used in this scanner is about $6 \cdot 10^6$, and a typical acquisition has about 10^7 counts, so that LIST mode reconstructions are not recommended.

For this study, a Derenzo-Like (Adam *et al.*, 2007) (see appendix A) phantom was used in the acquisitions simulated. The same initial activity of the source, as well as any other acquisition parameters, was used for all the acquisition schemes.

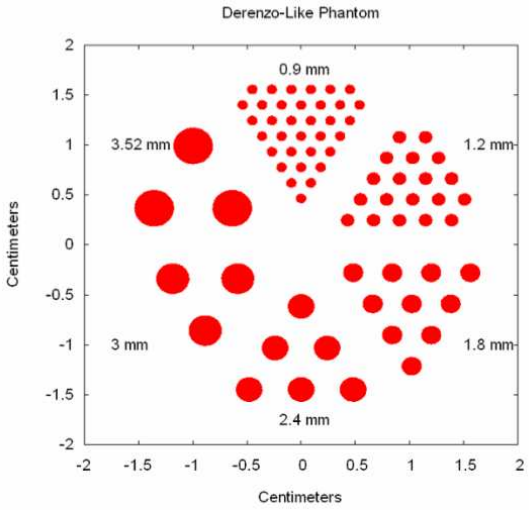

Figure 8.17. Derenzo-like phantom (Adam *et al.*, 2007) used for evaluation of the improvement achieved with step and shoot acquisitions.

Different numbers of steps that complete the angular sampling can be defined. From close examination of Figure 8.18, it can be extracted that if only 4 steps are employed, the images obtained are deformed due to incomplete angular sampling, while for 6 steps that deformation disappears and thus we can consider that angular coverage is good enough.

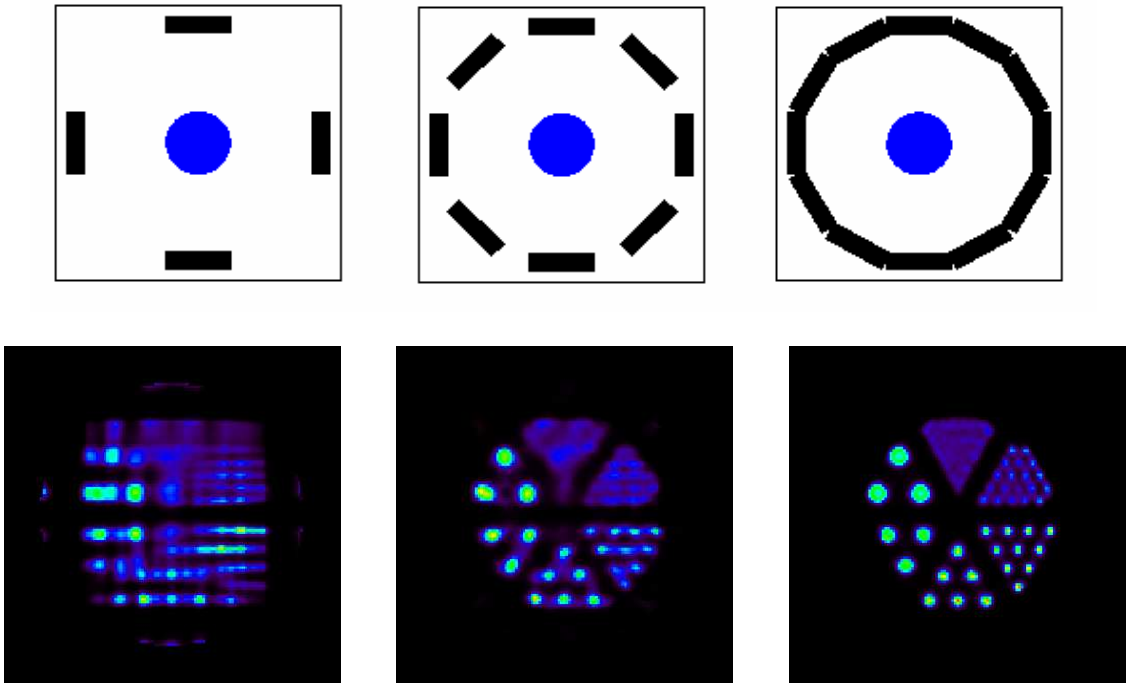

Figure 8.18. Reconstructed images obtained from acquisitions simulated of a Derenzo-like phantom, with different number of steps. Angular coverage is complete if five or more steps are chosen.

A comparison of the resolution obtained from the continuous rotating scheme and the step and shoot one with 6 steps, is shown in Figure 8.19 and Table 8.3. These results show how the resolution is improved in step and shoot acquisitions, which make it possible to distinguish the smaller rods.

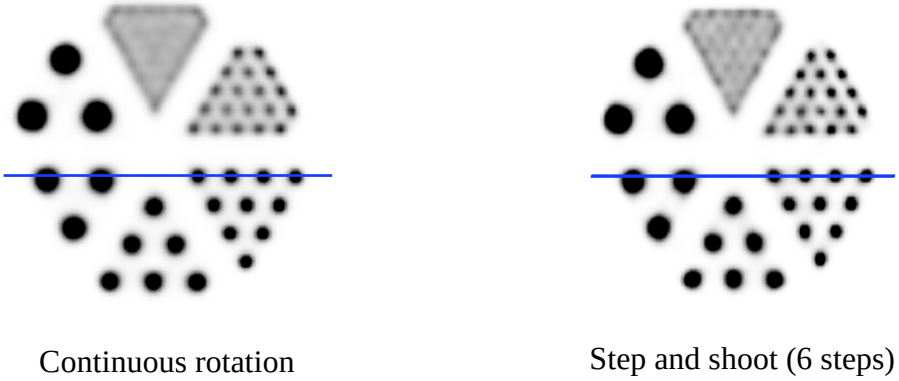

Continuous rotation Step and shoot (6 steps)

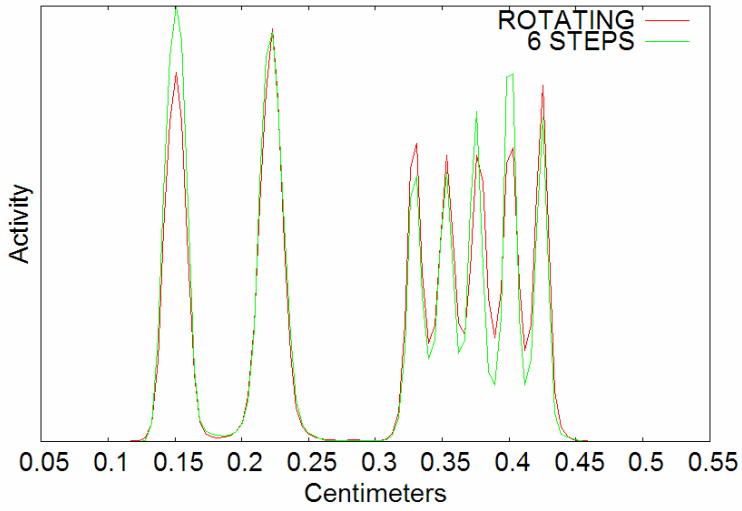

Figure 8.19. Comparison of images reconstructed from simulated acquisitions of a derenzo-like phantom, with continuous rotation (top-left) and step and shoot (top-right) modes. Line profiles along the yellow and blue lines of the image (top) are shown in the panel at the bottom of the figure.

Table 8.3. Spatial resolution measured over the images reconstructed for step and shoot versus continuous mode acquisitions. These resolutions are measured profiles as FWHM in mm.

Radial - **Tangentia**l (mm)	5 STEPS	6 STEPS	7 STEPS	CONTINUOUS
3 Iterations 50 Subsets	0.90 - **1.02**	0.73 - **0.85**	0.79 - **0.83**	1.06 - **1.27**
2 Iterations 75 Subsets	1.04 - **1.12**	0.75 - **0.87**	0.82 - **0.88**	1.07 - **1.30**
1 Iterations 150 Subsets	1.06 - **1.15**	0.92 - **1.00**	0.94 - **1.13**	1.09 - **1.32**

We can conclude that step and shoot acquisitions are an advantageous alternative to continuous rotating PET acquisitions, for scanners with incomplete angular sampling. The most accurate response of the system for each individual event that step and shoot acquisitions allow for, improves image resolution up to 30%, and the computational cost would be comparable, or less, than the one of the continuous rotation.

8.12. Conclusions

The design of a high resolution, small animal, PET scanner is a complex process. By means of Monte Carlo simulations, we have shown the effect of many design parameters of the scanner performance. Simulations emerge thus as an essential tool in scanner design. A few conclusions extracted from the results presented in this chapter are summarized here:

The spatial resolution depends more on crystal length than on pitch size, for usual high resolution scanner configurations. The best resolution would be achieved with shorter crystals and larger scanner diameters, but this would decrease sensitivity and would require more detector modules.

Assuming ideal electronics, pulse pile-up in the detector, due to photons arriving during scintillator light decay, along with random counts in the coincidence window, become the limiting factor of NEC rate. This bottleneck can only be solved with faster scintillator materials, that will allow for faster scintillator decay and narrower coincidence window, and/or with smaller volumes of crystal being read by each readout element (PMT, ADC, SiPM). Thus, for detector material of similar speed (rise and decay times) smaller detector arrays are superior with respect to NEC, if the electronics is good enough.

For rotating scanners, the step and shoot rotation protocols can achieve resolution up to 30% better than scanners with continuous rotation.

Conclusions of this thesis

In this thesis, Monte Carlo simulations have been used to improve the PET technique. Full advantage of realistic simulations has been taken to improve the quality of the images obtained with existing scanners, and for designing new PET scanner prototypes. The main contributions and conclusions of this work are summarized below:

- A PET Monte Carlo simulation tool (PeneloPET) has been developed. It allows for realistic simulations, including high detail in physics and electronics processing of detector pulses. We achieved fast simulations without loss of simulation detail. *Thanks to the reduction of simulation time,* the user can include more realism into the simulation as well as conduct studies in greater depth. Being capable of obtaining results in various formats, whether histograms or sinograms as well as list mode files, *helps to reduce the analysis time and to increase its possibilities*. A simple script, written in python language, allows for splitting simulations into many parallel processes suitable for clusters of computers or multi-core processors, with minimum effort.

- Exhaustive validations of our simulation package have been performed by means of comparisons to both results from other simulation packages as well as to real data taken by commercial small animal PET scanners. Very good agreement was found between real and simulated data, establishing the reliability of the code. *These extensive validations garantee PeneloPET to be suitable for improving PET scanners*.

- Several system response matrices (SRM), employed by statistical reconstruction methods have been computed by means of Monte Carlo simulations. These SRMs include a realistic description of physical processes, such as photon emission and detection, which yield images with high quality. Moreover, compression strategies used to store the SRM in RAM memory has made it possible to optimize the reconstruction process, getting the most out of computer resources, in order to obtain images in the shortest possible time. *The reduced size of the SRM also solves the problem of storing the huge SRM* of modern high-resolution PET scanners. *We can conclude that PeneloPET is suitable for the estimation of the SRM of small animal PET scanners.*

- A method to improve the quality of the images have been developed based on *a priori* knowledge of the probability of a detected event for coming to photon interactions in a single crystal of the detector array. *We have confirmed that the introduction of a priori knowledge of single-crystal events during the reconstruction* (obtained from a comparison of simulations with real data), *yields images with better signal to noise ratio and converging in less number of iterations than the standard method*. Higher recovery coefficients are obtained using this improved method, for reasonable noise levels. Results from real data were also compared, showing that keeping only single crystal events significantly reduces the background level for scanners with high contribution of pile-up events. *We can conclude that by using PeneloPET to obtain a priori information about the data acquired, it is possible to improve the quality of the reconstructed images.*

- Several configuration parameters involved in the design of small animal PET scanners have been studied. As a result of this study, *it has been established what the most important configuration parameters that must be considered when designing a PET scanner are* in order to obtain better spatial resolution, sensitivity

and counting rate capabilities. PeneloPET allows to estimate resolution versus sensitivity profiles for different values of one or more parameters. Crystal size and material can be chosen after extensive PeneloPET simulations. PeneloPET can simulate scanners with different block detector sizes, time response, and timing resolution in order to assess the configuration that gives the optimal count rate capabilities for the scanner. PeneloPET was also employed in a comparison of step and shoot rotation protocols versus continuously rotating schemes, yielding *an spatial resolution about 30% higher for the step and shoot case*. *Thus, we can conclude that PeneloPET is a powerful tool for the design of new small animal PET scanners*.

List of figures

List of tables

Bibliography

Adam A, Ken S and Paul K 2007 Statistical image reconstruction from correlated data with applications to PET *Phys. Med. Biol.* **52** 6133-50

Agostinelli S 2003 GEANT4 - a simulation toolkit *Nucl. Inst. Meth. In Phy. Res. A* **506** 250-303

Alessio A, Sauer K and Bouman C A 2003 MAP reconstruction from spatially correlated PET data. In: *IEEE NSS-MIC,* (Portland: USA) pp 1445-51

Allemand R, Gresset C and Vacher J 1980 Potential advantages of a Cesium Floride scintillator for time-of-flight positron camera *J. Nucl. Med.* **21** 153-5

Anger H O 1969 Scintillation Camera and Multiplane Tomographic Scanner *Kaku Igaku* **62** 125-48

Assie K, Breton V, Buvat I, Comtat C, Jan S, Krieguer M, Lazaro D, Morel C, Rey M, Santin G, Simon L, Staelens S, Strul D, Vieira J M and Van de Walle R 2004 Monte Carlo simulation in PET and SPECT instrumentation using GATE *Nucl. Inst. Meth. In Phy. Res. A* **526** 180-9

Ay M R and Zaidi H 2006 Assessment of errors caused by X-ray scatter and use of contrast medium when using CT-based attenuation correction in PET *Eur. J. Nucl. Med. Mol. Imaging* **33** 1301-13

Badawi R D, Kohlmyer S G, Harrison R L, Vannoy S D and Lewellen T K 2000 The Effect of Camera Geometry on Singles Flux, Scatter Fraction and Trues and Randoms Sensitivity for Cylindrical 3D PET - a Simulation Study *IEEE Trans. Nuc. Sci.* **NS-47** 1228-32

Badawi R D and Marsden P K 1999a Developments in component-based normalization for 3D PET *Phys. Med. Biol.* **44** 571-94

Badawi R D and Marsden P K 1999b Self-normalization of emission data in 3D PET *IEEE Trans. Med. Imag.* **46** 709-12

Bailey D L, Jones T, Spinks T J, Gilardi M-C and Townsend D W 1991 Noise equivalent count measurements in a neuro-PET scanner with retractable septa *IEEE Trans. Med. Imaging* **10** 256-60

Bailey D L and Meikle S R 1994 A convolution-subtraction scatter correction method for 3D PET *Phys. Med. Biol.* **39** 411-24

Bailey D L, Townsend D, Valk P E and Maisey M N 2004 *Positron emission tomography: basic sciences* (London: Springer)

Baró J, Sempau J, Fernández-Varea J M and Salvat F 1995 PENELOPE: An algorithm for Monte Carlo simulation of the penetration and energy loss of electrons and positrons in matter *Nucl. Inst. Meth. In Phy. Res. B* **100** 31-46

Barret H H, White T and Parra L C 1997 List-mode likelihood *J. Opt. Soc. Am. A* **14** 2914-23

Barret O, Carpenter T A, Clark J C, Ansorge R E and Fryer T D 2005 Monte Carlo simulation and scatter correction of the GE Advance PET scanner with SimSET and Geant4 *Phys. Med. Biol.* **50** 4823-40

Bendriem B and Townsend D 1998 *The Theory and Practce of 3D PET* (Dordrecht: Kluwer Academic Publishers)

Berko S and Hereford F L 1956 Experimental studies of positron interactions in solids and liquids *Rev. Mod. Phys.* **28** 299-307

Bettinardi V, Pagani E, Gilardi M C, Alenius S, Thielemans K, Teras M and Fazio F 2002 Implementation and evaluation of a 3D one-step late reconstruction algorithm for 3D positron emission tomography brain studies using median root prior *Eur. J. Nucl. Med. Mol. Imaging* **29** 7-18

Biemond J, Lagendijk R and Mersereau R 1990 Iterative methods for image deblurring In: *IEEE NSS-MIC,* pp 856-83

Blake E, Pressley D R, Lenox M, Swann B K, Newport D F and Siegel S 2006 A Data Acquisition, Event Processing and Coincidence Determination Module for a Distributed Parallel Processing Architecture for PET and SPECT Imaging. In: *IEEE NSS-MIC,* (San Diego: USA) pp 2439-42

Braem A, Chamizo Llatas M, Chesi E, Correia J G, Garibaldi F, Joram C, Mathot S, Nappi E, Ribeiro da Silva M, Schoenahl F, Séguinot J, Weilhammer P and Zaidi H 2004 Feasibility of a novel design of high resolution parallax-free Compton enhanced PET scanner dedicated to brain research *Phys. Med. Biol.* **49** 2547-62

Bratley P, Fox B L and Schrage L E 1983 *A Guide to Simulation* (New York: Springer-Verlag)

Briesmeister J F 1993 MNCP 4 A, Monte Carlo N-Particle Transport System. (Los Alamos, New Mexico: Los Alamos National Laboratory)

Browne J and de Pierro A B 1996 A row-action alternative to the EM algorithm for maximizing likelihood in emission tomography *IEEE Trans. Med. Imag.* **15** 687-99

Buvat I and Lazaro D 2006 Monte Carlo simulations in emission tomography and GATE: An overview *Nucl. Inst. Meth. In Phy. Res. A* **569** 323-29

Byme C L 2001 Likelihood maximization for list-mode emission tomographyc image reconstruction *IEEE Trans. Med. Imaging* **20** 1084-92

Cal-González J 2008 Mejora de la identificación del cristal de interacción en escáneres PET de alta resolución mediante simulaciones (Universidad Complutense de Madrid: Thesis, unpublished)

Casey M, Gadagkar H and Newport D F 1995 A component based method for normalisation in volume PET. In: *3rd International Meeting on Fully Three-Dimensional Image Reconstruction in Radiology and Nuclear Medicine,* (Aix-les-Bains, France p 67

Casey M E and Hoffman E J 1986 Quantitation in Positron Emission Computed Tomography: 7. A technique to reduce noise in accidental coincidence measurements and coincidence efficiency calibration *J. Comput. Assit. Tomogr.* **10** 845-50

Casey M E and Nutt R 1986 A Multicrystal Two Dimensional BGO Detector System for Positron Emission Tomography *IEEE Trans. Nuc. Sci.* **33** 460-3

Chatziioannou A F 2002a Molecular imaging of small animals with dedicated PET tomographs *J. Nucl. Med. Mol.* **29** 98-114

Chatziioannou A F 2002b PET scanners dedicated to molecular imaging of small animal models *Mol. Imaging Biol.* **4** 47-63

Chen C M 1998 An efficient four-connected parallel system for PET image reconstruction *Parallel Comput.* **24** 1499-522

Chen Y, Liu B, O'Connor M, Didier C S and Glick S J 2006 Comparison of Scatter/Primary Measurements with GATE Simulations for X-Ray Spectra in Cone Beam CT Mammography. In: *IEEE NSS-MIC*, (San Diego: USA) pp 3909-14

Cherry S R, Meikle S R and Hoffman E J 1993 Correction and Characterisation of Scattered Events in Three-Dimensional PET Using Scanners with Retractable Septa *J. Nucl. Med.* **34** 671-8

Cherry S R, Shao Y and Siegel S 1996 Optical fiber readout of scintillator array using a multi-channel PMT: a high resolution PET detector for animal imaging *IEEE Trans. Nucl. Sci.* **43** 1932-7

Cherry S R, Sorenson J A and Phelps M E 2003 *Physics in Nuclear Medicine* (Los Angeles: Saunders)

Chien-Min K, Xiaochuan P and Chin-Tu C 2000 Accurate image reconstruction using DOI information and its implications for the development of compact PET systems *IEEE Trans. Nuc. Sci.* **47** 1551-60

Colombino P, Fiscella B and Trossi L 1965 Study of positronium in water and ice from 22 to -144 ◦C by annihilation quanta measurements *Nuovo Cimento* **38** 707-23

Cooke B E, Evans A C, Fanthome E O, Alarie R and Sendyk A M 1984 Performance figure and images from the Therascan 3128 positron emission tomograph *IEEE Trans. Nuc. Sci.* **31** 640-4

Cooper R J, Turk G, Boston A J, Boston H C, Cresswell J R, Mather A R, Nolan P J, Hall C J, Lazarus I, Simpson J, Berry A, Beveridge T, Gillam J and Lewis R A 2007 Position sensitivity of the first SmartPET HPGe detector *Nucl. Inst. Meth. In Phy. Res. A* **573** 72-5

Daube-Witherspoon M E and Carson R E 1991 Unified deadtime correction model for PET *IEEE Trans. Med. Imag.* **10** 267-75

Daube-Witherspoon M E and G. M 1987 Treatment of axial data in three-dimensional PET *J. Nucl. Med.* **28** 1717-24

De Pierro A R and Yamagishi M E B 2001 Fast EM-like methods for maximum "a posteriori" estimates in emission tomography *IEEE Trans. Med. Imag.* **20** 280-8

DeBenedetti S, Cowan C E, Konneker W R and Primakoff H 1950 On the angular distribution of two-photon annihilation radiation *Physical Review* **77** 205-12

Defrise M 1991 FAVOR: a fast reconstruction algorithm for volume imaging in PET. In: *Med. Imag. Conf. IEEE*, (Santa Fe pp 1919-23

Defrise M, Kinahan P E, Townsend D W, Michel C, Sibomana M and Newport D F 1997 Exact and approximate rebinning algorithms for 3D PET data *IEEE Trans. Med. Imag.* **16** 145-58

Derenzo S 1979 measurement of annihilation point spread distribution for medically important positron emitters. In: *5th Int. Conf. of Positron Annihilation*, (Lake Yamanaka, Japan pp 819–23

Dongming H, Atkins B E, Lenox M W, Castleberry B and Siegel S B 2006 A Neural Network Based Algorithm for Building Crystal Look-up Table of PET Block Detector. In: *IEEE NSS-MIC*, pp 2458-61

Du Y, Frey E C, Wang W T, Tocharoenchai C, Baird W H and Tsui B M W 2002 Combination of MCNP and SimSET for Monte Carlo simulation of SPECT with medium- and high-energy photons *IEEE Trans. Nuc. Sci.* **49** 668-74

Erdman K L 1955 The Angular Correlation of Annihilation Radiation. In: *Physical Society*, pp 304-11

España S, Herraiz J L, Vaquero J J, Desco M and Udias J M 2006 PeneloPET: A MonteCarlo PET simulation tool based on PENELOPE. In: *IEEE NSS-MIC*, (San Diego: USA) pp 2597-601

España S, Herraiz J L, Vicente E, Herranz E, Vaquero J J, Desco M and Udias J M 2007a Improved image reconstruction in small animal PET using a priori estimates of single-pixel events. In: *IEEE NSS-MIC*, (Honolulu: USA) pp 3876-80

España S, Herraiz J L, Vicente E, Herranz E, Vaquero J J, Desco M and Udias J M 2007b Validation of PeneloPET against two small animal PET scanners. In: *IEEE NSS-MIC*, (Honolulu: USA) pp 3640-3

España S, Herraiz J L, Vicente E, Vaquero J J, Desco M and Udías J M 2009 PeneloPET, a Monte Carlo PET simulation tool based on PENELOPE: features and validation *Phys. Med. Biol.* **54** 1723-42

España S, Tapias G, Fraile L M, Herraiz J L, Vicente E, Udias J, Desco M and Vaquero J J 2008 Performance evaluation of SiPM detectors for PET imaging in the presence of magnetic fields. In: *IEEE NSS-MIC*, pp 3591-5

Frese T, Rouze N C, Bouman C A, Sauer K and Hutchins G D 2001 Quantitative comparison of FBP, EM, and Bayesian reconstruction algorithms, including the impact of accurate system modeling, for the IndyPET scanner. In: *IEEE NSS-MIC*, (Norfolk: USA) pp 1806-10

Germano G and Hoffman E J 1988 Investigation of count rate and deadtime characteristics of a high resolution PET system *J. Comput. Assit. Tomogr.* **12** 836-46

Germano G and Hoffman E J 1990 A study of data loss and mispositioning due to pileup in 2-D detectors in PET *IEEE Trans. Nuc. Sci.* **37** 671-5

Green M V, Seidel J, Vaquero J J, Jagoda E, Lee I and Eckelman W C 2001 High resolution PET, SPECT and projection imaging in small animals *Comput. Med. Imaging Graph.* **25** 79-86

Green P J 1990 Bayesian reconstructions from emission tomography data using a modified EM algorithm *IEEE Trans. Med. Imag.* **9** 84-93

Halpern O 1954 Magnetic Quenching of the Positronium Decay *Phys. Rev.* **94** 904-7

Harrison R L, Dhavala S, Kumar P N and Shao Y 2003 Acceleration of SimSET photon history generator module of a public domain simulation system for emission tomography. In: *IEEE NSS-MIC*, pp 1835-8

Harrison R L, Vannoy S D, Haynor D R, Gillispie S B, Kaplan M S and Lewellen T K 1993 Preliminary Experience With The Photon History Generator Module Of A Public-domain Simulation System For Emission Tomography. In: *IEEE NSS-MIC*, pp 1154-8

Heinrichs U, Pietrzyk U and Ziemons K 2003 Design Optimization of the PMT-ClearPET Prototypes Based on Simulation Studies With GEANT3 *IEEE Trans. Nuc. Sci.* **50** 1428-32

Henkin R E, Bova D, Dillehay G L and Karesh S M 2006 *Nuclear Medicine* (Philadelphia: Elsevier Health Sciences)

Herman G T 1980 *Image reconstruction from projections* (New York: Academic Press)

Herraiz J L, España S, Vaquero J J, Desco M and Udias J M 2006 FIRST: Fast Iterative Reconstruction Software for (PET) tomography *Phys. Med. Biol.* **51** 4547-65

Herraiz J L, España S, Vicente E, Vaquero J J, Desco M and Udias J M 2007 Noise and physical limits to maximum resolution of PET images *Nucl. Inst. Meth. In Phy. Res. A* **580** 934-7

Hoffman E J 1979 Quantitation in positron emission tomography: 1. Effect of object size *J. Comput. Assit. Tomogr.* **3** 299-308

Hoffman E J, Guerrero R M, Germano G, Digby W M and Dahlbom M 1989 PET system calibrations and corrections for quantitative and spatially accurate images *IEEE Trans. Nuc. Sci.* **36** 1108-12

Huang S-C, Hoffman C S, Phelps M E and Kuhl D E 1979 Quantitation in positron emission computed-tomography: 2. effects if inaccurate attenuation correction *J. Comput. Assit. Tomogr.* **3** 804-14

Hudson H M and Larkin R S 1994 Accelerated image reconstruction using ordered subsets of projection data *IEEE Trans. Med. Imag.* **13** 604-9

Humm J L, Rosenfeld A and Del Guerra A 2003 From PET detectors to PET scanners *Eur. J. Nucl. Med. Mol. Imaging* **4** 11-26

Jan De B, Steven S, Dirk K, Ludovic F, Yves D A, Ignace L and Fernando R R 2007 Cluster computing software for GATE simulations *Medical Physics* **34** 1926-33

Jan S, Santin G, Strul D, Staelens S, Assié K, Autret D and Avner S 2004 GATE: a simulation toolkit for PET and SPECT *Phys. Med. Biol.* **49** 4543-61

Jennifer R S and Simon R C 2005 High-resolution PET detector design: modelling components of intrinsic spatial resolution *Phys. Med. Biol.* 179

Johnson C A, Seidel J, Carson R E, Gandler W R, Sofer A, Green M V and Daube-Witherspoon M E 1997 Evaluation of 3D reconstruction algorithms for a small animal PET camera *IEEE Trans. Nuc. Sci.* **44** 1303-8

Johnson C A and Sofer A 1999 A data-parallel algorithm for iterative tomographic image reconstruction. In: *IEEE NSS-MIC*, pp 126-37

Johnson V E 1987 A note on stopping rules in EM-ML reconstructions of ECT images *IEEE Trans. Med. Imaging* **13** 569-71

Joung J, Miyaoka R S and Lewellen T K 2001 cMiCE:a high resolution animal PET using continuous LSO with a statistics based positioning scheme. In: *IEEE NSS-MIC*, pp 1137-41 vol.2

Kadrmas D J 2004 LOR-OSEM: statistical PET reconstruction from raw line-of-response histograms *Phys. Med. Biol.* **49** 4731-44

Kak A C and Slaney M 1988 *Principles of Computerized Tomographic Imaging* (New York: Society for Industrial Mathematics)

Kalos M H and Whitlock P A 1986 *Monte Carlo Methods, vol. 1* (New York: Wiley)

Kawrakow I and Bielajew A F 1998 On the condensed history technique for electron transport *Nucl. Inst. Meth. In Phy. Res. B* **142** 253-80

Kemp B J, Lenox M, Newport D F, Siegel S and Nutt R 2006 Performance Measurements of the Siemens Inveon Small Animal PET Scanner. In: *IEEE NSS-MIC*, (San Diego: USA) p unpublished

Kitamura K, Yamaya T, Yoshida E, Tsuda T, Inadama N and Murayama H 2004 Preliminary Design Studies of a High Sensitivity Small Animal DOI-PET Scanner: jPET-RD. In: *IEEE NSS-MIC*, pp 3896-900

Knoll G F 2000 *Radiation Detection and Measurements* (New York: Wiley)

Krane K S 1987 *Introductory Nuclear Physics* (New York: Wiley)

Kudrolli H, Worstell W and Zavarzin V 2002 SS3D-Fast fully 3D PET iterative reconstruction using stochastic sampling *IEEE Trans. Nuc. Sci.* **49** 124-30

L'Ecuyer P 1988 Efficient and portable combined random number generators. In: *ACM*, (New York: ACM) pp 742-51

Lage E, Vaquero J J, Sisniega A, España S, Tapias G, Udías A, García V, Rodríguez-Ruano A and Desco M 2008 VrPET/CT: Development of a Rotating Multimodality Scanner for Small-Animal Imaging. In: *IEEE NSS-MIC*, pp 4671 – 4

Larobina M, Brunetti A and Salvatore M 2006 Small Animal PET: A Review of Commercially Available Imaging Systems *Current Medical Imaging Reviews* **2** 187-92

Lazaro D, Buvat I, Loudos G, Strul D, Santin G, Giokaris N and Donnarieix D 2004 Validation of the GATE Monte Carlo simulation platform for modelling a CsI(Tl) scintillation camera dedicated to small-animal imaging *Phys. Med. Biol.* **49** 271-85

Lee J, Vaquero J J, Barbosa F J, Seidel J and Green M V 2000 High performance phoswich detector module for small animal PET *J. Nucl. Med.* **41** 75

Lee K, Kinahan P E, Fessler J A, Miyaoka R S, Janes M and Lewellen T K 2004 Pragmatic fully 3D image reconstruction for the MiCES mouse imaging PET scanner *Phys. Med. Biol.* **49** 4563-78

Leo W R 1994 *Techniques for Nuclear and Particle Physics Experiments: A How-to Approach* (Heidelberg: Springer-Verlag)

Levin C S, Dahlbom M and Hoffman E J 1995 A Monte Carlo correction for the effect of Compton scattering in3-D PET brain imaging *IEEE Trans. Nuc. Sci.* **42** 1181-85

Levin C S, Foudray A M K and Habte F 2006 Impact of high energy resolution detectors on the performance of a PET system dedicated to breast cancer imaging *Physica Medica* **21** 28-34

Levin C S and Hoffman E J 1999 Calculation of positron range and its effect on the fundamental limit of positron emission tomography system spatial resolution *Phys. Med. Biol.* **44** 781-99

Lewellen T K, Laymon C M, Miyaoka R S, Ki Sung L and Kinahan P E 2001 Design of a Firewire based data acquisition system for use in animal PET scanners. In: *IEEE NSS-MIC,* pp 1974-8

Lewis J S, Achilefu S, Garbow J R, Laforest R and Welch M J 2002 Small animal imaging: current technology and perspectives for oncological imaging *Eur. J. Cancer* **38**

Lewitt R M and Matej S 2003 Overview of methods for image reconstruction from projections in emission computed tomography. In: *IEEE NSS-MIC,* pp 1588-611

Lewittt R M, Muehllehner G and Karpt J S 1994 Three-dimensional image reconstruction for PET by multi-slice rebinning and axial image filtering *Phys. Med. Biol.* **39** 321-39

Liow J S and Strother S C 1991 Practical tradeoffs between noise, resolution and quantitation, and number of iterationsfor maximum likelihood reconstructions *IEEE Trans. Med. Imag.* **10** 563-71

Ljungberg M, Strand S-E and King M A 1998 *Monte Carlo Calculations in Nuclear Medicine* (London: IOP)

Mair B A, Carrol R B and Anderson J M M 1996 Filter banks and the EM algorithm In: *IEEE NSS-MIC,* pp 2-9

McFarland A R, Siegel S, Newport D F, Mintzer R, Atkins B and Lenox M 2007 Continuously Sampled Digital Pulse Processing for Inveon Small Animal PET Scanner. In: *IEEE NSS-MIC,* (Honolulu: USA) pp 4262-65

Melcher C L 2000 Scintillation crystals for PET *J. Nucl. Med.* **41** 1051-5

Michel C, Hamill J, Panin V, Conti M, Jones J, Kehren F, Casey M, Bendriem B, Byars L and Defrise M 2002 FORE(J)+OSEM2D versus OSEM3D reconstruction for large aperture rotating LSO panel detector PET prototype. In: *IEEE NSS-MIC,* (Norfolk: USA) pp 1231-5 vol.2

Moszynski M, Kapusta M, Nassalski A, Szczesniak T, Wolski D, Eriksson L and Melcher C L 2006 New Prospects for Time-of-Flight PET with LSO Scintillators *IEEE Trans. Nuc. Sci.* **53** 2484-8

Mullani N A, Ficke D C, Hartz R, Markham J and Wong G 1981 System design of a fast PET scanner utilizing time-of-flight *IEEE Trans. Nuc. Sci.* **NS-28** 104-7

Mumcuoglu E U, Leahy R and Cherry S R 1996 Bayesian reconstruction of PET images: Methodology and performance analysis *Phys. Med. Biol.* **41** 1777-807

Murayama H, Ishibashi H and Omura T 1998 Depth encoding multicrystal detectors for PET *IEEE Trans. Nucl. Sci.* **45** 1152-7

Murphy-O'Connor C 2006 Mejora de la determinación del cristal de interacción de tomógrafos de emisión de positrones (PET). (Universidad Complutense de Madrid: Thesis, unpublished)

Myers R and Hume S 2002 Small animal PET *Eur. Neuropsychopharmacol* **12** 545-55

NEMA N- 2001 Performance measurements of positron emission tomographs. (NEMA: National Electrical Manufacturers Association)

NEMA N- 2008 Performance Measurements for Small Animal Positron Emission Tomographs. (NEMA: National Electrical Manufacturers Association)

Nutt R 2002 The history of Positron Emission Tomography *Mol. Imaging Biol.* **4** 11-26

Oliver J F and Rafecas M 2008 Revisiting the singles rate method for modeling accidental coincidences in PET. In: *IEEE NSS-MIC,* pp 4288-91

Ortuño J E, Guerra-Gutierrez P, Rubio J L, Kontaxakis G and Santos A 2006 3D-OSEM iterative image reconstruction for high-resolution PET using precalculated system matrix *Nucl. Inst. Meth. In Phy. Res. A* **569** 440-4

Ortuño J E, Vaquero J J, Kontaxakis G, Desco M and Santos A 2003 Preliminary studies on the design and simulation of high resolution small animal PET scanners with octagonal geometry. In: *IEEE NSS-MIC,* (Portland: USA) pp 2053-7

Otte A N, Barral J, Dolgoshein B, Hose J, Klemin S, Lorenz E, Mirzoyan R, Popova E and Teshima M 2005 A test of Silicon Photomultipliers as readout for PET *Nucl. Inst. Meth. In Phy. Res. A* **545** 705-15

Panettieri V, Wennberg B, Gagliardi G, Duch M A, Ginjaume M and Lax I 2007 SBRT of lung tumours: Monte Carlo simulation with PENELOPE of dose distributions including respiratory motion and comparison with different treatment planning systems *Phys. Med. Biol.* **52** 4265-81

Papenfuss A T, O'Keefe G J and Scott A M 2000 Segmented attenuation correction in whole body PET using neighbourhood EM clustering. In: *IEEE NSS-MIC,* pp 78-81

Parra L and Barrett H H 1998 List-mode likelihood: EM algorithm and image quality estimation demonstrated on 2D PET *IEEE Trans. Med. Imag.* **17** 228-35

Patro A P and Sen P 1971 Parapositronium lifetime *J.Phys. A: Gen. Phys.* **4** 856-8

Pepin C M, Berard P and Lecomte R 2001 Comparison of LSO, LGSO and MLS scintillators. In: *IEEE NSS-MIC,* pp 124-28

Phelps M E 2004 *PET: Molecular Imaging and Its Biological Applications* (New York: Springer)

Pichler B, Lorenz E, Mirzoyan R, Pimp W, Roder F, Schwaiger M and Ziegler S I 1998 Performance Test of a LSO-APD PET Module in a 9.4 Tesla Magnet. In: *IEEE NSS-MIC,* pp 1237-9

Poon E and Verhaegen F 2005 Accuracy of the photon and electron physics in GEANT4 for radiotherapy applications *Medical Physics* **32** 1696-711

Powsner R and Powsner E 2006 *Essential Nuclear Medicine Physics* (Haryana: Blackwell Publishing)

Qi J, Leathy R M, Cherry S R, Chatzioannou A and Farquhar T H 1998 High-resolution 3d Bayesian image reconstruction using the micropet small-animal scanner *Phys. Med. Biol.* **46** 2597-605

Rafecas M, Mosler B, Dietz M, Pgl M, Stamatakis A, McElroy M P and Ziegler S I 2004 Use of a Monte Carlo based probability matrix for 3d iterative reconstruction of MADPET-II data *IEEE Trans. Nuc. Sci.* **51** 2597-605

Raheja A, Doniere T F and Dhawan A P 1999 Multiresolution expectation maximization reconstruction algorithm for positron emission tomography using wavelet processing *IEEE Trans. Nuc. Sci.* **46** 594-602

Raichle M E 1983 Positron Emission Tomography *Ann. Rev. Neurosci.* **6** 249-67

Richardson J R and Kurie F N D 1936 The Rediations Emitted from Artificially Produced Radioactive Substances. II. The Gamma-Rays from Several Elements *Phys. Rev.* **50** 999-1006

Rogers D W O 1984 Low energy electron transport with EGS *Nucl. Inst. Meth. In Phy. Res. A* **227** 535-48

Rousset O G, Ma Y and Evans A C 1998 Correction for partial volume effects in PET: principle and validation *J. Nucl. Med.* **39** 904-11

Salvat F, Fernández-Varea J M and Sempau J 2006 *PENELOPE-2006: A Code System for Monte Carlo Simulation of Electron and Photon Transport* (France: NEA)

Schafers K P 2003 Imaging small animals with positron emission tomograph *Nuklearmedizin* **42** 86-9

Schmitz R E, Gillispie S B, Harrison R L, MacDonald L R, Kinahan P E and Lewellen T K 2007 Expanding SimSET to include block detectors: performance with pseudo-blocks and a true block model. In: *IEEE NSS-MIC*, (Honolulu: USA) pp 4275-8

Seidel J, Vaquero J J, Siegel S, Gandler W R and Green M V 1999 Depth Identification Accuracy of a Three-Layer Phoswich PET Detector Module *IEEE Trans. Nuc. Sci.* **46** 485-90

Sempau J and Andreo P 2006 Configuration of the electron transport algorithm of PENELOPE to simulate ion chambers *Phys. Med. Biol.* **51** 3533-48

Sempau J, Fernández-Varea J M, Acosta E and Salvat F 2003 Experimental benchmarks of the Monte Carlo code PENELOPE *Nucl. Inst. Meth. In Phy. Res. B* **207** 107-23

Sempere Roldan P, Cañadas M, Dietzel O, Pautrot C, Sarasola I and Wagner A 2007 Performance Evaluation of raytest ClearPET, a PET Scanner for Small and Medium Size Animals. In: *IEEE NSS-MIC*, (Honolulu: USA) pp 2859-64

Shepp L A and Vardi Y 1982 Maximum-likelihood reconstruction for emission tomography *IEEE Trans. Nuc. Sci.* **MI-1** 113-21

Slijpen E T P and Beekman F J 1999 Comparison of post-filtering and filtering between iterations for SPECT reconstruction *IEEE Trans. Nuc. Sci.* **46** 2233-8

Smith L 2002 An investigation into limits of resolution in Positron Emission Tomography resulting from non-collinear positron annihilation. University of Melbourne) p unpublished

Snyder D L, Miller M I, L. J. Thomas J and Politte D G 1987 Noise and edge artifacts in maximum-likelihood reconstruction for emission tomography *IEEE Trans. Nuc. Sci.* **MI-6** 228-38

Strother S C, Casey M E and Hoffman E J 1990 Measuring PET scanner sensitivity: relating count rates to image signaltonoise ratios using noiseequivalent counts *IEEE Trans. Nucl. Sci.* **37** 783-8

Surti S, Karp J S, Freifelder R and Liu F 2000 Optimizing the performance of a PET detector using discrete GSO crystals on continuous lightguide *IEEE Trans. Nucl. Sci.* **47** 1030-6

Tai C Y, Chatziioannou A, Young Y F, Silverman R W, Meadors K, Siegel S, Newport D F, Stickel J and Cherry S R 2003 MicroPET II: design, development and initial

performance of an improved microPET scanner for small-animal imaging *Phys. Med. Biol.* **48** 1519-38

Thiam C O, Breton V, Donnarieix D, Habib B and Maigne L 2008 Validation of a dose deposited by low-energy photons using GATE/GEANT4 *Phys. Med. Biol.* **53** 3039-55

Thomson C J, Moreno-Cantu J and Picard Y 1992 PETSIM: Monte Carlo simulation of all sensitivity and resolution parameters of cylindrical positron imaging systems *Phys. Med. Biol.* **37** 731-49

Torres-Espallardo I, Rafecas M, Spanoudaki V, McElroy D E and Ziegler S I 2008 Effect of inter-crystal scatter on estimation methods for random coincidences and subsequent correction *Phys. Med. Biol.* **53** 2391--411

Townsend D W 2004 Physical principles and technology of clinical PET imaging *Ann. Acad. Med. Singapore* **33** 133-45

van Eijk C W 2002 Inorganic scintillators in medical imaging *Phys. Med. Biol.* **47** 85-106

Vaquero J J, Lage E, Ricón L, Abella M, Vicente E and M. D 2005 rPET Detectors Design and Data Processing. In: *IEEE NSS-MIC,* (Fajardo: USA) pp 2885-9

Vaquero J J, Pascau J, Molins A, Arco J M and Desco M 2004 Performance characteristics of the ARGUS-drT smmal animal PET scanner: preliminary results. In: *IEEE NSS-MIC,* (Rome: Italy) pp 1060-3

Vaska P, Bolotnikov A, Carini G, Cabarda G, Pratte H-F, Dilmanian F A, Park S-J and James R B 2005 Studies of CZT for PET Applications. In: *IEEE NSS-MIC,* pp 2799-802

Vilches M, García-Pareja S, Guerrero R, Anguiano M and Lallena A M 2007 Monte Carlo simulation of the electron transport through thin slabs: A comparative study of PENELOPE, GEANT3, GEANT4, EGSnrc and MCNPX *Nucl. Inst. Meth. In Phy. Res. B* **254** 219-30

Visser E P, Disselhorst J A, Brom M, Laverman P, Gotthardt M, Oyen W J G and Boerman O C 2009 Spatial Resolution and Sensitivity of the Inveon Small-Animal PET Scanner *J. Nucl. Med.* **50** 139-47

Wang Y, Seidel J, Tsui B M W, Vaquero J J and Pomper M G 2006 Performance Evaluation of the GE Healthcare eXplore VISTA Dual-Ring Small-Animal PET Scanner *J. Nucl. Med.* **47** 1891-900

Westbrook C I, Gidley D W, Conti R S and Rich A 1987 New Precision Measurement of the Orthopositronium Decay Rate: A Discrepancy with Theory *Phys. Rev. Lett.* **58** 1328-31

Wirth V 1989 Effective energy resolution and scatter rejection in nuclear medicine *Phys. Med. Biol.* **34** 85-90

Wyss M T, Honer M, Schubiger P A and Ametamey S M 2006 NanoPET imaging of [F-18]fluoromisonidazole uptake in experimental mouse tumours *European Journal of Nuclear Medicine and Molecular Imaging* **33** 311-8

Yamaga T and Murayama H 2002-2003 DOI-PET image reconstruction with accurate system modeling that reduces redundancy of the imaging system. Institute of Radiological Sciences)

Yao R, Seidel J, Liow J S and Green M V 2005 Attenuation correction for the NIH ATLAS small animal PET scanner *IEEE Trans. Nuc. Sci.* **52** 664-8

Yiping S, Cherry S R, Siegel S and Silverman R W 1996 A study of inter-crystal scatter in small scintillator arrays designed for high resolution PET imaging *IEEE Trans. Nuc. Sci.* **43** 1938-44

Zaidi H 2000 Comparative evaluation of scatter correction techniques in 3D positron emission tomography *Eur. J. Nucl. Med. Mol. Imaging* **27** 1813-26

Zaidi H, Labbé C and Morel C 1998 Implementation of an Environment for Monte Carlo Simulation of Fully 3-D Positron Tomography on a High-Performance Parallel Platform *Parallel Comput.* **24** 1523-6

Zaidi H and Scheurer C 1999 An object-oriented Monte Carlo simulator for 3D cylindrical positron tomographs *Comput. Methods Programs Biomed.* **58** 133-45

Zanzonico P 2004 Positron emission tomography: a review of basic principles, scanner design and performance, and current systems *Semin. Nucl. Med.* **34** 87-111

Ziegler S I, Pichler B J and Boening G 2001 A prototype high-resolution animal positron tomograph with avalanche photodiode arrays and LSO crystals *Eur. J. Nucl. Med.* **28** 136-43

Appendix A. Description of the phantoms

In what follows we roughly describe the phantoms employed in this work.

Derenzo-like phantom

This phantom consists of five sectors, each one containing radioactive rods with various diameters (1.2, 1.5, 2.0, 2.5, and 3.0 mm), the distance between sources being twice their diameter. The sources were distributed within a disk of diameter 36 mm. This phanton description must be considered as a reference, but many other variations have been used in this thesis.

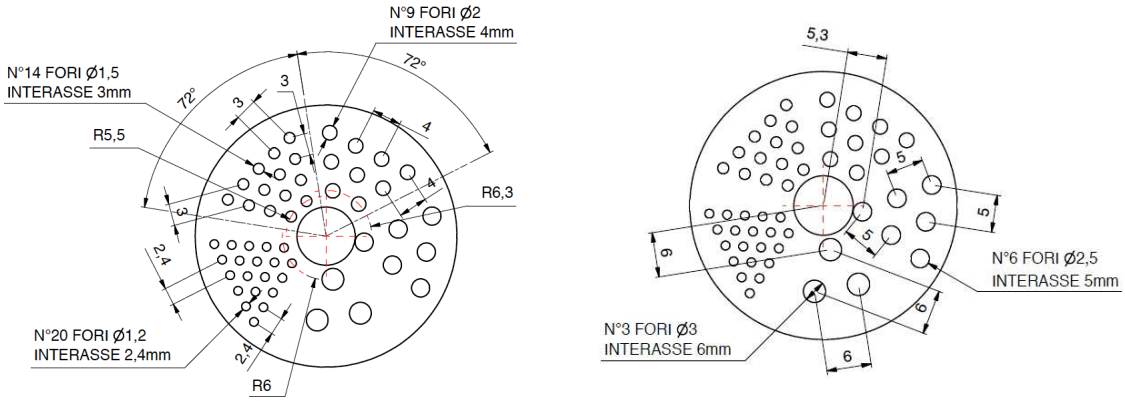

Image quality phantom

The main phantom body is composed of a fillable cylindrical chamber with 30 mm diameterand 30 mm length. The remaining 20 mm in length of the phantom body are solid with 5 fillable rods drilled through (at 7 mm from the center) with diameters of 1, 2, 3, 4, and 5 mm, respectively. This phantom is used to obtain the recovery coefficients for studying the resolution and noise properties of the images, and the spill over ratios, in order to study the efficiency of scatter correction methods.

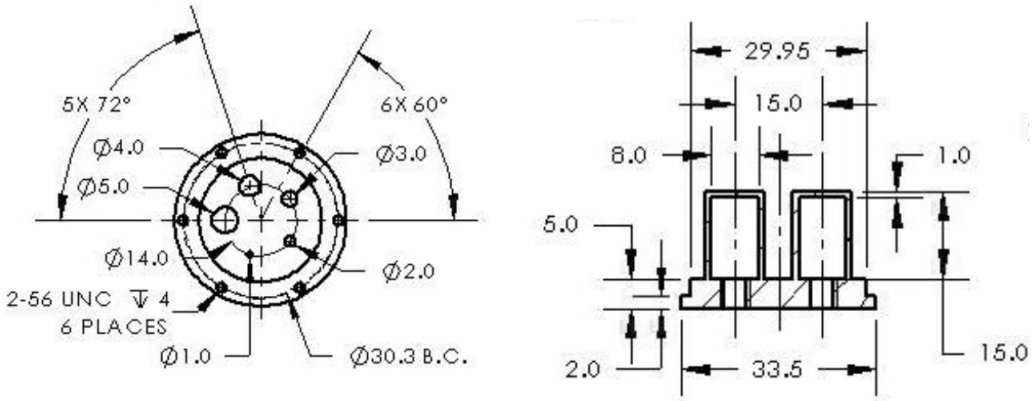

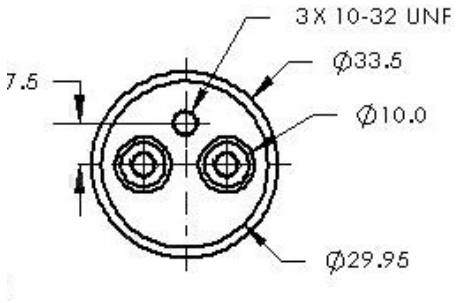

Micro-Defrise phantom

This phantom if formed by equidistant disks, axially distributed and with contains holes at different angular position. It is used for the evaluation of the uniformity of the slice profile, along the longitudinal axis of the scanner.

Specifications:

- Cylinder outer diameter: 5 cm
- Cylinder inside diameter: 4.5 cm
- Cylinder inner height: 6.3 cm
- Disk diameter: 4.3 cm
- Disk thickness: 4.3 mm
- Gap thickness: 4.3 mm

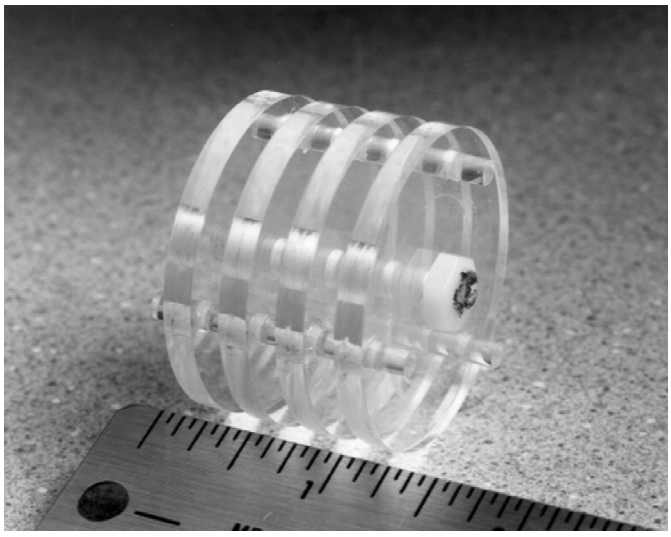

Appendix B. List of publications and conference presentations

Published Articles

- TITLE: “PeneloPET, a Monte Carlo PET simulation tool based on PENELOPE: features and validation”
  AUTHORS: S. España, J.L. Herraiz, E. Vicente, J.J. Vaquero, M. Desco, J.M. Udías
  PUBLICATION: Phys Med Biol, Vol 54 (2009) 1723-1742.

- TITLE: “Noise and physical limits to maximum resolution of PET images”
  AUTHORS: J.L. Herraiz, S. España, E. Vicente, J.J. Vaquero, M. Desco, J.M. Udías
  PUBLICATION: Nuclear Inst. and Methods in Physics Research, A, 580 (2007): 934-937

- TITLE: “FIRST: Fast Iterative Reconstruction Software for (PET) Tomography”
  AUTHORS: : J.L. Herraiz, S. España, J.J. Vaquero, M. Desco, J.M. Udías
  PUBLICATION: Phy Med Biol, Vol 51 (2006) 4547-4565

International Conferences

- CONFERENCE: Nuclear Science Symposium and Medical Imaging Conference IEEE 2008
  CENTER: Dresden (Germany)
  TITLE OF PRESENTATION: Performance Evaluation of SiPM Detectors for PET Imaging in the Presence of Magnetic Fields
  AUTHORS: S. España, G. Tapias, L. M. Fraile, J. L. Herraiz, E. Vicente, J. M. Udías, M. Desco, J. J. Vaquero
  TYPE OF PRESENTATION: Oral
  DATE: 20 October - 25October 2008

- CONFERENCE: Nuclear Science Symposium and Medical Imaging Conference IEEE 2008
  CENTER: Dresden (Germany)
  TITLE OF PRESENTATION: VrPET/CT: Development and Initial Results of a Rotating PET/CT Scanner for Rodents Imaging
  AUTHORS: E. Lage, J. J. Vaquero, A. Sisniega, S. España, G. Tapias, A. Udías, V. Garcia, A. Rodriguez-Ruano, M. Desco
  TYPE OF PRESENTATION: Poster
  DATE: 20 October - 25October 2008

- CONFERENCE: Nuclear Science Symposium and Medical Imaging Conference IEEE 2008
  CENTER: Dresden (Germany)
  TITLE OF PRESENTATION: Validation Effects of the Super Bialkali Photocathode on the Performance Characteristics of a Position-Sensitive Depth-of-Interaction PET Detector Module
  AUTHORS: J. J. Vaquero, J. M. Udías, S. España, M. Desco
  TYPE OF PRESENTATION: Poster
  DATE: 20 October - 25October 2008

- CONFERENCE: Nuclear Science Symposium and Medical Imaging Conference IEEE 2008
  CENTER: Dresden (Germany)
  TITLE OF PRESENTATION: Validation Nonlinear Effect of Pile-up in the Calibration Curve of a Small Animal PET Scanner
  AUTHORS: E. Vicente, S. España, J. L. Herraiz, E. Herranz, J. M. Udías, M. Desco, J. J. Vaquero
  TYPE OF PRESENTATION: Poster
  DATE: 20 October - 25October 2008

- CONFERENCE: Nuclear Science Symposium and Medical Imaging Conference IEEE 2008
  CENTER: Dresden (Germany)
  TITLE OF PRESENTATION: Frequency Selective Signal Extrapolation for Compensation of Missing Data in Sinograms
  AUTHORS: J. L. Herraiz, S. España, E. Vicente, E. Herranz, M. Desco, J. J. Vaquero, J. M. Udías
  TYPE OF PRESENTATION: Poster
  DATE: 20 October - 25October 2008

- CONFERENCE: Nuclear Science Symposium and Medical Imaging Conference IEEE 2007
  CENTER: Honolulu (USA)
  TITLE OF PRESENTATION: Validation of PeneloPET against two small animal PET scanners
  AUTHORS: S. España, J. L. Herraiz, E. Vicente, E. Herranz, J. J. Vaquero, M. Desco, J. M. Udías
  TYPE OF PRESENTATION: Poster
  DATE: 27 October - 3 November 2007

- CONFERENCE: Nuclear Science Symposium and Medical Imaging Conference IEEE 2007
  CENTER: Honolulu (USA)
  TITLE OF PRESENTATION: Improved image reconstruction in small animal PET

using a priori estimation of single-pixel events.
AUTHORS: S. España, J. L. Herraiz, E. Vicente, E. Herranz, J. J. Vaquero, M. Desco, J. M. Udías
TYPE OF PRESENTATION: Poster
DATE: 27 October - 3 November 2007

- CONFERENCE: Nuclear Science Symposium and Medical Imaging Conference IEEE 2007
  CENTER: Honolulu (USA)
  TITLE OF PRESENTATION: Revised Consistency Conditions for PET Data
  AUTHORS: J.L.Herraiz, S. España, E. Vicente, E. Herranz, J.J.Vaquero, M.Desco, J.M.Udías
  TYPE OF PRESENTATION: Poster
  DATE: 27 October - 3 November 2007

- CONFERENCE: Nuclear Science Symposium and Medical Imaging Conference IEEE 2007
  CENTER: Honolulu (USA)
  TITLE OF PRESENTATION: Influence of random and scatter corrections in the quantification properties of small animal PET scanners
  AUTHORS: E. Vicente, M. Soto-Montenegro, S. España, J. L. Herraiz, E. Herranz, J. J. Vaquero, M. Desco, J. M. Udías
  TYPE OF PRESENTATION: Poster
  DATE: 27 October - 3 November 2007

- CONFERENCE: Nuclear Science Symposium and Medical Imaging Conference IEEE 2006
  CENTER: San Diego (EEUU)
  TITLE OF PRESENTATION: PeneloPET, a Monte Carlo PET Simulation Tool Based on PENELOPE: Features and Validation
  AUTHORS: S. España, J.L.Herraiz , J.M.Udías, J.J.Vaquero, M.Desco
  TYPE OF PRESENTATION: Poster
  DATE: 29 October – 4 November 2006

- CONFERENCE: Nuclear Science Symposium and Medical Imaging Conference IEEE 2006
  CENTER: San Diego (EEUU)
  TITLE OF PRESENTATION: Normalization in 3D PET: Dependence on the Activity Distribution of the Source
  AUTHORS: E. Vicente, J.L. Herraiz, S. España, J.M. Udías, J.J. Vaquero, M. Desco
  TYPE OF PRESENTATION: Poster
  DATE: 29 October – 4 November 2006

- CONFERENCE: Nuclear Science Symposium and Medical Imaging Conference IEEE 2006
  CENTER: San Diego (EEUU)
  TITLE OF PRESENTATION: Optimal and Robust Filter for PET Data Based on the System Response Matrix
  AUTHORS: J.L.Herraiz, S. España, J.M.Udías, J.J.Vaquero, M.Desco
  TYPE OF PRESENTATION: Poster
  DATE: 29 October – 4 November 2006

- CONFERENCE: Imaging 2006
  CENTER: Stockholm (Sweden)
  TITLE OF PRESENTATION: Noise And Physical Limits To Resolution Of Pet Images Effects Involved In The Emission And Detection Of Pet Radiation
  AUTHORS: J.L.Herraiz, S. España, J.J.Vaquero, M.Desco,J.M.Udías
  TYPE OF PRESENTATION: Oral
  DATE: 27-30 June 2006

- CONFERENCE: Euromedim 2006
  CENTER: Marseille (France)
  TITLE OF PRESENTATION: PeneloPET, A Monte Carlo-based application for tomography based on PENELOPE
  AUTHORS: S. España, J.L.Herraiz, J.J.Vaquero, M.Desco,J.M.Udías
  TYPE OF PRESENTATION: Poster
  DATE: 9-12 May 2006

- CONFERENCE: Euromedim 2006
  CENTER: Marseille (France)
  TITLE OF PRESENTATION: Study of randoms-induced artifacts in several small animal PET scanners.
  AUTHORS: J.L.Herraiz, S. España, J.J.Vaquero, M.Desco,J.M.Udías
  TYPE OF PRESENTATION: Poster
  DATE: 9-12 May 2006

- CONFERENCE: Academy of Molecular Imaging. Annual Conference 2006
  CENTER: Orlando (USA)
  TITLE OF PRESENTATION: Resolution Improvement of small animal PET images using a step and shoot rotating scanner.
  AUTHORS: S. España, J.L.Herraiz, J.J.Vaquero, M.Desco,J.M.Udías
  TYPE OF PRESENTATION: Poster
  DATE: 25-29 March 2006

- CONFERENCE: Academy of Molecular Imaging. Annual Conference 2006
  CENTER: Orlando (USA)
  TITLE OF PRESENTATION: Small Animal PET Scanners Design Optimized for

Statistical Reconstruction Methods.
AUTHORS: J.L.Herraiz, S. España, , J.J.Vaquero, M.Desco,J.M.Udías
TYPE OF PRESENTATION: Poster
DATE: 25-29 March 2006

- CONFERENCE: Academy of Molecular Imaging. Annual Conference 2006
  CENTER: Orlando (USA)
  TITLE OF PRESENTATION: Iterative Vs Analytic Reconstruction Methods for PET's: Combining the best of both approaches.
  AUTHORS: J.L.Herraiz, S. España, J.J.Vaquero, M.Desco,J.M.Udías
  TYPE OF PRESENTATION: Poster
  DATE: 25-29 March 2006

- CONFERENCE: Nuclear Science Symposium and Medical Imaging Conference IEEE 2005
  CENTER: Fajardo (Puerto Rico)
  TITLE OF PRESENTATION: Statistical Reconstruction Methods in PET: Resolution Limit, Noise and Edge Artifacts.
  AUTHORS: J.L.Herraiz, S. España, J.M.Udías, J.J.Vaquero, M.Desco
  TYPE OF PRESENTATION: Poster
  DATE: 23-29 October 2005

- CONFERENCE: Nuclear Science Symposium and Medical Imaging Conference IEEE 2005
  CENTER: Fajardo (Puerto Rico)
  TITLE OF PRESENTATION: Quasi pseudo-inverse reconstruction for rotating PET scanners"
  AUTHORS: J. Sanchez-Gonzalez, S. España, M. Abella, J.J. Vaquero, E. Lage,J. Pascau,M. Desco
  TYPE OF PRESENTATION: Poster
  DATE: 23-29 October 2005

- CONFERENCE: Nuclear Science Symposium and Medical Imaging Conference IEEE 2004
  CENTER: Roma
  TITLE OF PRESENTATION: Full 3D-OSEM Reconstruction with Compressed Response of the System.
  AUTHORS: J.L.Herraiz, S. España, J.M.Udías, J.J.Vaquero, M.Desco
  TYPE OF PRESENTATION: Poster
  DATE: 16-23 October 2004

National Conferences

- CONFERENCE: XXXI Bienal de la Real Sociedad Española de Física
  CENTER: Facultad de Ciencias de Ourense
  TITLE OF PRESENTATION: PeneloPET: Un Entorno de Simulación Monte Carlo para la Tomografía por Emisión de Positrones
  AUTHORS: , S. España , J.L. Herraiz, J.M.Udías
  TYPE OF PRESENTATION: Oral Presentation
  DATE: 10-14 September 2007

- CONFERENCE: EFN 2006
  CENTER: Valencia (España)
  TITLE OF PRESENTATION: PeneloPET, una aplicación basada en métodos Monte Carlo para la tomografía de emisión de positrones
  AUTHORS: S. España ,J.L.Herraiz, J.M.Udías
  TYPE OF PRESENTATION: Oral Presentation
  DATE: 6-8 September 2006

- CONFERENCE: XXX Bienal de la Real Sociedad Española de Física
  CENTER: Facultad de Ciencias de Ourense
  TITLE OF PRESENTATION: Métodos Iterativos de Reconstrucción de Imagen Médica por Emisión de Positrones
  AUTHORS: J.L. Herraiz , S. España, J.M.Udías
  TYPE OF PRESENTATION: Oral Presentation
  DATE: 12-16 September 2005

Resumen en castellano

Introducción

Desde la aparición de los primeros escáneres PET en los años 70 del siglo pasado, el empleo de la tomografía por emisión de positrones se ha extendido de manera continuada en oncología, cardiología y neurología. La utilización de esta técnica en investigación preclínica ha supuesto un gran desafío durante la última década, durante la que se han desarrollado escáneres PET de muy alta resolución para animales de laboratorio como ratones y ratas. En la actualidad se consiguen imágenes PET con una resolución submilimétrica y algunos escáneres PET tienen una sensibilidad superior al 10%. Esto ha sido posible gracias al desarrollo tecnológico de los equipos de detección de fotones gamma y la electrónica de procesado. Así mismo, la aparición de ordenadores con gran capacidad de cálculo, unido al perfeccionamiento de los algoritmos de reconstrucción y al uso generalizado de los métodos de simulación Monte Carlo en todas las etapas del desarrollo de escáneres, han proporcionado un impulso muy importante en el desarrollo de la técnica PET.

La investigación en PET abarca varias áreas del conocimiento y requiere equipos multidisciplinares de biólogos, médicos, farmacéuticos, ingenieros, informáticos y también físicos, entre otros. Los principios básicos del PET están regidos por la Física Nuclear. Por ello, el Grupo de Física Nuclear (GFN) de la Universidad Complutense de Madrid ha resultado un lugar idóneo para el desarrollo del presente trabajo. El GFN ha aportado los conocimientos teóricos y experimentales de Física Nuclear necesarios para comprender la técnica PET en profundidad y poder así contribuir a su desarrollo. La colaboración con el Laboratorio de Imagen Médica del Hospital General Universitario Gregorio Marañón nos ha aportado su experiencia en imagen médica y nos ha dado acceso a los datos de varios escáneres PET.

La simulación realista de escáneres PET permite mejorar todas las fases de la producción de la imagen, desde el diseño del escáner y los detectores a el cálculo de la matriz de respuesta del sistema (MRS) empleada durante el proceso de reconstrucción, pasando por la adquisición, procesado y corrección de los datos. Como resultado se pueden obtener imágenes de mejor calidad. Es decir, imágenes con mejor resolución espacial y relación señal ruido y con unos resultados de cuantificación más precisos y reproducibles. La disponibilidad hoy en día de ordenadores con gran capacidad de cómputo y con programas de simulación Monte Carlo con resultados muy precisos, permiten incorporar en la simulación la física de emisión y detección y los procesos electrónicos de los escáneres PET.

En esta tesis doctoral se ha tratado de mejorar la calidad de las imágenes PET reconstruidas. Para ello se han utilizado de manera intensiva los métodos de simulación Monte Carlo para comprender a fondo los procesos que tienen lugar en la adquisición de datos PET. Hemos centrado este trabajo en los escáneres PET de alta resolución para animales pequeños. Estos escáneres requieren el uso de métodos de reconstrucción avanzados para conseguir una solución espacial de alrededor de 1 mm. De hecho, para conseguir esta resolución, la MRS utilizada en los métodos de reconstrucción estadísticos debe ser muy precisa (Herraiz et al., 2006).

Los objetivos de esta tesis pueden resumirse del siguiente modo:

- Desarrollo de una aplicación Monte Carlo (PeneloPET) para su uso en PET (capítulo 4).
- Validación de PeneloPET para demostrar la fiabilidad de sus resultados (capítulo 5).
- Usar PeneloPET para la mejora de la calidad de las imágenes obtenidas con escáneres existentes (capítulos 6 y 7).
- Estudiar el uso de PeneloPET para el diseño de nuevos escáneres PET de animales pequeños (capítulo 8).

La estructura de esta tesis puede resumirse del siguiente modo:

- Marco teórico
  - Capítulo 1. Introducción a los principios físicos de la técnica PET, el funcionamiento de los distintos componentes de un escáner PET y la descripción de los parámetros más relevantes de un escáner PET.
  - Capítulo 2. Introducción de los principios básicos de la reconstrucción de imagen.
  - Capítulo 3. Introducción a las técnicas de simulación Monte Carlo y a varios paquetes de simulación.
- Desarrollo de PeneloPET.
  - Capítulo 4. Descripción de PeneloPET, una herramienta Monte Carlo para las simulaciones PET.
  - Capítulo 5. Validación de PeneloPET. Comparación de adquisiciones simuladas con datos reales y con resultados de otros paquetes de simulación.
- Aplicaciones de PeneloPET.
  - Capítulo 6. Cálculo de la MRS utilizada en los métodos de reconstrucción 3D-OSEM.
  - Capítulo 7. Estimación a priori de la fiabilidad de los eventos detectados con el objetivo de mejorar la calidad de las imágenes reconstruidas.
  - Capítulo 8. Consideraciones a tener en cuenta durante el diseño de escáneres PET de animales pequeños.

A continuación se da una descripción más completa del trabajo presentado en esta tesis.

El primer objetivo de esta tesis ha sido el desarrollo de una herramienta Monte Carlo (PeneloPET (España et al., 2009)) capaz de realizar simulaciones realistas de escáneres PET. Existen varios códigos muy completos para la simulación de la interacción entre radiación y materia. Nosotros hemos partido de uno de ellos (PENELOPE (Baró et al., 1995)) como primera capa sobre la que hemos construido las herramientas necesarias para reproducir todos los aspectos específicos de la técnica PET. PeneloPET es descrito en el capítulo 4 y validado en el capítulo 5. Varios ejemplos del uso que se puede dar a una herramienta de simulación avanzada son mostrados en los restantes capítulos de esta tesis.

En el capítulo 6 se muestra cómo el disponer de una herramienta capaz de generar simulaciones realistas ha hecho posible obtener imágenes de mejor calidad, mediante el cálculo de la matriz de respuesta del sistema (MRS) del detector o escáner lo más cercana posible a la realidad para ser utilizada en métodos de reconstrucción estadístico-iterativos.

Además, al tener un conocimiento detallado de los procesos que ocurren en un escáner PET, es más simple el desarrollo y comprobación de nuevos métodos de eliminación coincidencias no deseadas, como son las de dispersión y aleatorias. Por ello, el segundo objetivo de este trabajo ha consistido en calcular de manera óptima, la matriz de respuesta del sistema, eliminando todas las redundancias y aprovechando simetrías y cuasi-simetrías, con el fin de obtener una MRS suficientemente pequeña como para caber en la memoria RAM de ordenadores personales. Este cálculo ha sido aplicado a la reconstrucción de imágenes de un escáner PET de animales pequeños mediante el método OSEM (Herraiz et al., 2006) en modo 3D.

Los dispositivos de detección introducen incertidumbre en los datos medidos. Esta incertidumbre puede reducirse con información a priori sobre la calidad de cada dato adquirido. Dicha información se obtiene de las simulaciones realistas. Se analiza la información obtenida durante la adquisición, tal como energía depositada en los detectores, tasa de llegada de los fotones, posición de interacción, etc. Al disponer de más información sobre cada evento, las imágenes obtenidas son de mejor calidad en términos generales. Como último objetivo de éste trabajo, En el capítulo 7 hemos tratado de introducir un complejo proceso de análisis de los eventos detectados que permita, como hemos dicho, diferenciar la calidad de los mismos y hemos adaptado el método de reconstrucción de imagen con el fin de introducir toda esta información en el proceso de reconstrucción.

El diseño de escáneres modernos pasa hoy en día por el desarrollo de herramientas de simulación Monte Carlo, las cuales desempeñarán un papel importante para la definición de la próxima generación de escáneres PET. En el capítulo 8 se muestran los resultados del uso intensivo de las simulaciones Monte Carlo para determinar los parámetros con mayor impacto en las prestaciones de los escáneres PET.

PeneloPET, una herramienta Monte Carlo para PET basada en PENELOPE

La tomografía por emisión de positrones (PET) es una técnica en constante crecimiento para su uso en imagen clínica y preclínica. Las simulaciones Monte Carlo desempeñan un papel muy importante en PET, tanto en la fase de investigación y desarrollo de nuevos escáneres (Braem et al 2004, Heinrichs et al 2003) como en las técnicas avanzadas de reconstrucción de imagen (Herraiz et al 2006). El empleo de códigos de simulación para PET se ha visto incrementado en los últimos años debido a la disponibilidad de potente ordenadores (Zaidi 2000, Ay and Zaidi 2006, Ortuño et al 2003, Ortuño et al 2006, Torres-Espallardo et al 2008).

Hemos desarrollado PeneloPET, una nueva herramienta de simulación para PET basada en PENELOPE (Baró et al 1995, Savat et al 2003). La aplicación has sido escrita en el lenguaje de programación FORTRAN 77. El objetivo para desarrollar un nuevo simulador PET fue la optimización del diseño de escáneres PET para animales pequeños. Este objetivo requiere una herramienta lo más rápida posible, con posibilidad de ejecutarse en paralelo en distintos ordenadores y que permita la simulación de distintas configuraciones de manera sencilla.

Los elementos que conforman una simulación en PeneloPET son la geometría y materiales de los detectores y otros materiales inertes (como maniquíes y blindajes), las fuentes de actividad y la electrónica de detección. Todos estos parámetros son definidos en una serie de ficheros de entrada escritos en texto plano. Los resultados pueden ser obtenidos tanto en sinogramas e histogramas de LOR como en ficheros en modo lista. Los ficheros en modo lista incluyen información detallada de las características del proceso de detección, llegando a especificar por ejemplo en el caso de las coincidencias, si se trata de coincidencias aleatorias, de dispersión, etc., la energía depositada, la diferencia de tiempos entre singles entre otros parámetros. Los ficheros en modo lista pueden ser obtenidos con tres niveles de procesado. En el nivel más básico se obtienen únicamente las coordenadas donde se producen las interacciones de cada partícula. En un segundo nivel se obtienen todos los eventos singles detectados y en el nivel más elaborado se obtienen directamente las coincidencias medidas.

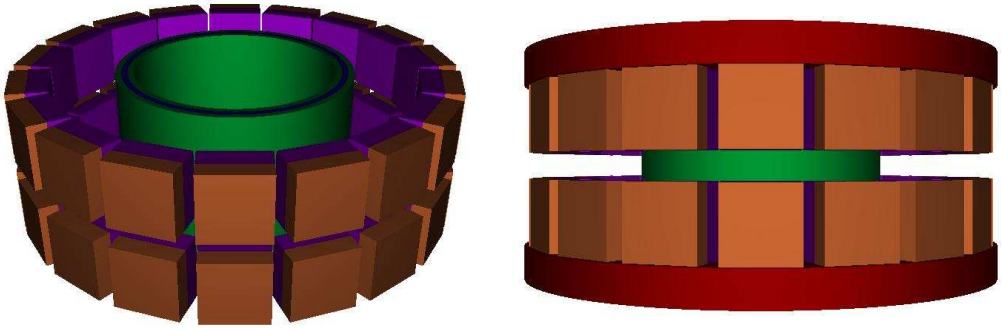

Figura 1. Visualización gráfica del escáner drT Argus con un maniquí de la normalización en el interior del FOV. La figura de la derecha incluye los materiales que constituyen el blindaje representados en color rojo. Estas figuras han sido obtenidas mediante la aplicación gview3d que se incluye dentro de PENELOPE.

El código de PeneloPET consite en dos módulos principales. El primero se encarga de la interacción con la rutinas de PENELOPE y el almacenamiento de toda la información resultante para su posterior procesado. Un segundo módulo se encarga del post-procesado de los datos de las interacciones. Este procesado tiene en cuenta por ejemplo, la lógica de Anger

para el posicionamiento de la interacción dentro de la matriz de cristales, apilamiento, resolución en energía y otros elementos de la electrónica como la ventana de coincidencias, el tiempo muerto, la resolución temporal y el tiempo de integración.

Se ha desarrollado un script de python que es capaz de dividir una simulación en tantos procesos paralelos como el usuario desee. El script divide la simulación completa en subconjuntos en los que se simula el mismo número de desintegraciones en cada uno. Para ello se ajustan la actividad inicial y el tiempo de adquisición de modo que se consiguen sub-simulaciones consecutivas y que conllevan el mismo tiempo de cómputo.

Para comenzar una simulación se deben definir unos pocos ficheros (ver Tabla 1). Un fichero (llamado main.inp) contiene algunas opciones para definir los parámetros generales de la simulación. Es posible simular la misma adquisición con distinto detalle de la física empleada y con distinto nivel de post-procesado. Por ejemplo, algunas opciones importantes son la que restringe la simulación únicamente a los fotones de aniquilación y la inclusión o no del rango del positron y la no-colineridad mediante la utilización de funciones predefinidas. Con esta segunda opción el tiempo de simulación es acortado drásticamente.

Otros ficheros contienen los parámetros que definen la configuración de la simulación. Las propiedades del escáner y otros objetos como el blindaje o los maniquíes son definidos de manera independiente en los ficheros scanner.inp y object.inp respectivamente. Es posible simular escáneres con varios anillos de detectores y con detectores con varias capas de cristal centelleador. Los principales materiales utilizados en PET están ya predefinidos dentro de PeneloPET, pero PENELOPE permite crear fácilmente otros nuevos materiales. PENELOPE incluye herramientas de visualización (gview2d, gview3d) que permiten visualizar las geometrías definidas. Estas herramientas están disponibles también con PeneloPET.

Las fuentes de actividad son definidas aparte en el fichero source.inp, indicando la geometría, actividad inicial e isótopo de cada una de ellas. Cuando se simulan únicamente fotones de aniquilación, la direcciones de emisión pueden ser restringidas para aumentar la eficiencia de la simulación siempre que las condiciones del estudio lo permitan. PeneloPET tiene en cuenta la variación temporal de la actividad durante la adquisición.

En la tabla 1 se muestran todos los ficheros de entrada necesarios para la simulación de una fuente puntual en el escáner rPET (Vaquero et al., 2005).

Tabla 1. Ficheros de entrada necesarios para la simulación de una fuente puntual en el escáner rPET usando PeneloPET. Una definición detallada de las opciones que pueden ser introducidas en estos ficheros se encuentra en el manual de usuario de PeneloPET (España et al., 2007a).

--- GENERAL PARAMETERS --- (main.inp)	
12345 54321	!Random number generator seeds
9000 1 F	!Acquisition time (sec); Number of Frames; Read Frame List File
1000	!Limit number of interactions for each particle
F T T	!Secondary Particles Simulation; Positron Range; Non-Collinearity
0 180 3000 40	!Init & Final angular posit (deg); Num. of Steps per cycle; time per cycle (sec)
0.	!Lower Level Energy Threshold (eV)
1000000.	!Upper Level Energy Threshold (eV)
5	!Coincidence Time Window (ns)
0.1	!Trigger's Dead Time (ns)
150	!Integration Time (ns)
1200	!Coincidence's Dead Time (ns)

```
F F T              !Hits LIST; Singles LIST; Coincidences LIST
F                  !Write LOR Histogram
T 117 190 4.49684    !Write Sinogram; radial bins; angular bins; maximum radio
F 99 99 55 4.48 4.2   !Write Emission Image; X Y Z voxels, Transaxial & Axial FOV (cm)
F                  !Hits checking
T                  !Verbose
F                  !Neglecting events if > 2 singles in coincidence
```

```
--- SCANNER PARAMETERS --- (scanner.inp)
4              !Number of Detectors per Ring
1              !Number of Detectors in Coincidence in the same Ring
1              !Number of Rings
0.             !Gap Between Rings (cm)
30             !Number of transaxial crystals per detector (columns)
30             !Number of axial crystals per detector (rows)
1              !Number of crystal layers per detector
1.2 13 0.26 1 40 0.01   !LAYER: Length (cm) ; Mat; Energy Resol.; Rise & Fall Time (ns) ; Timing Error (ns)
0.16 0.16      !Pitch: Distance between centre of adjacent crystals (cm)
8.             !Radius: Centre FOV - Centre Front of Detector (cm)
```

```
--- SOURCE PARAMETERS --- (source.inp)
P 1E6 F 1 0.5 1. 2. 0. 0. 0. 0. 0. 0. 0. 0. 180     ! Shape Act Units Isot X Y Z R1 R2 H PH TH TH1 TH2
```

```
--- BODY PARAMETERS --- (object.inp)
C  1  0.  0.  0.  0.  1.62  5.0  0.  0. !Shape Mat X Y Z R1 R2 HEIGHT (cm) PH TH (deg)
```

En éste capítulo hemos presentado PeneloPET, un paquete de simulaciones Monte Calor para PET. Es una herramienta fácil de utilizar, versátil, rápida y con resultados sencillos de analizar. PeneloPET es una herramienta útil para el diseño de escáneres, el cálculo de la respuesta del sistema y el desarrollo de métodos de corrección, entre otras aplicaciones.

Validación de PeneloPET

En este capítulo se presenta una comparación entre las simulaciones obtenidas con PeneloPET y datos medidos con escáneres reales y con otros paquetes de simulación.

La validación del código debe realizarse con el fin de evaluar la fiabilidad de la simulación para cada uno de los escáneres. La configuración de la simulación debe adecuarse para cada escáner hasta conseguir un buen acuerdo entre los datos reales y simulados. Una vez que el código ha sido validado para un escáner, puede ser utilizado con ese escáner para la investigación y desarrollo con el fin de mejorar su rendimiento.

Para comenzar con la validación, se ha realizado una comparación entre los resultados obtenidos con PeneloPET y con la herramienta GATE de simulación PET basada en GEANT4. Con este objetivo se ha utilizado una configuración sencilla basada en el escáner rPET (Vaquero et al 2005) para determinar el perfil de sensibilidad axial. Para continuar con la validación de PeneloPET, se ha realizado una comparación de los resultados de las simulaciones con las mediciones reales para cuatro escáneres PET comerciales. Los escáneres utilizados son el rPET (Vaquero et al 2005), ARGUS (Wang et al 2006), Raytest CLEARPET (Heinrichs et al 2003) y el Siemens INVEON (McFarland et al 2007), todos ellos dedicados a

estudios con los animales pequeños. Las mediciones de los tres últimos escáneres se han obtenido a partir de Wang et al (2006), Sempere Roldán et al (2007) y Blake et al (2006) respectivamente. Se ha intentado realizar simulaciones con la mayor precisión posible de la geometría y los materiales mencionados en las referencias.

En la Tabla 2 se muestran los resultados de velocidad de cómputo para los distintos escáneres simulados usando PeneloPET.

Tabla 2. La velocidad de simulación depende en gran medida de la geometría del escáner y el blindaje incluidos en la simulación. Se ha realizado la simulación de una adquisición de una fuente puntual de 18F situada en el centro del FOV para los distintos escáneres estudiados en este trabajo. Sólo se simulan los fotones de aniquilación. Esta tabla presenta los resultados obtenidos con un solo núcleo de un procesador Intel Xeon X5472 3,00 GHz quad-core.

Escáner	Tasa de simulación
rPET	75000 e^+/s
ARGUS	12000 e^+/s
CLEARPET	11000 e^+/s
INVEON	17000 e^+/s

Aunque una comparación detallada de GATE y PeneloPET no era el objetivo de este trabajo, hemos comparado PeneloPET frente a GATE en unos pocos casos con el propósito de la validación de esta nueva herramienta de simulación para PET, lo que demuestra que PeneloPET es más rápido que GATE, mientras que los resultados se desvían por debajo del 5% en las predicciones. También hemos comparado las simulaciones de PeneloPET con mediciones de cuatro escáneres PET de animales pequeños diferentes comparando las mediciones de la sensibilidad, perfiles de sinogramas, resolución espacial, perfil axial de cuentas, fracción de dispersión, tasas NEC. En general se ha conseguido un acuerdo bastante bueno entre simulación y datos reales.

Estimación de la matriz de respuesta del sistema

Los escáneres PET para pequeños animales requieren alta resolución espacial y una buena sensibilidad. Para reconstruir imágenes de alta resolución en 3D-PET, los métodos iterativos, como OSEM, son superiores a los algoritmos analíticos de reconstrucción, aunque su alto coste computacional sigue siendo un grave inconveniente. El mayor rendimiento de los ordenadores modernos podría hacer la reconstrucción iterativa lo suficientemente rápida como para manejar el gran número de coeficientes de probabilidad de la matriz de respuesta del sistema (MRS) en los escáneres PET de alta resolución. Teniendo en cuenta todas las posibles simetrías axiales y transaxiales, así como algunas cuasi-simetrías, hemos sido capaces de reducir los requisitos de memoria para almacenar la MRS en mucho menos de 1 GB, lo que nos permite mantener toda la MRS en la memoria RAM del sistema, de modo que el algoritmo de reconstrucción pueda alcanzar su máximo rendimiento. Los elementos de la MRS se almacenan como esplines cúbicos y son adaptados al tamaño del voxel durante la reconstrucción. De esta manera se combinan las ventajas del cálculo en tiempo real y de almacenar la MRS completa. El cálculo en tiempo real (adaptación de los perfiles precalculados a los vóxeles de la imagen) de la MRS ocupa entre un 10% y 30% del tiempo de reconstrucción, en función del número de voxeles elegido. Esta técnica ha sido probada

con datos reales de un escáner PET de animales pequeños comercial. Los resultados (calidad de imagen y tiempo de reconstrucción) muestran que la técnica propuesta es una solución viable.

Aparte de las tradicionales simetrías utilizadas para evitar almacenar datos redundantes de la MRS, proponemos el uso adicional de simetrías no exactas o cuasi-simetrías, con el fin de obtener una reducción adicional de la MRS. Los LORs cuya respuesta difiere relativamente poco son agrupados en conjuntos pertenecientes a una misma clase de cuasi-simetría. Las diferencias entre los elementos de la MRS para LORs pertenecientes a una determinada clase debería ser mucho menor que entre LORs de diferentes clases. Las clases de cuasi-simetría pueden obtenerse, por ejemplo, agrupando LORs de cristales con orientaciones LOR-cristal similares (ver Figura 2 y Figura 3). Las diferencias entre los elementos de la misma clase de cuasi-simetría son aproximadamente 5-10%, dependiendo de la cantidad de compresión (reducción de tamaño) que se desee aplicar.

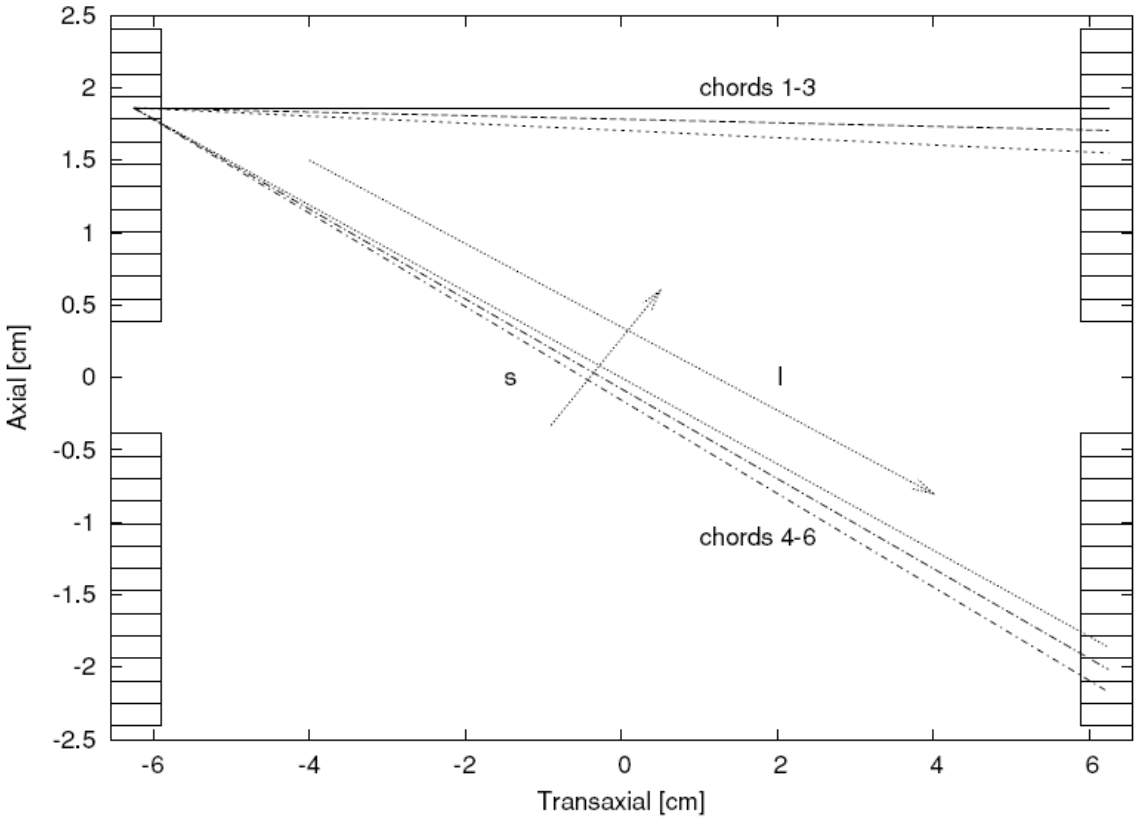

Figura 2. Representación esquemática de varias líneas de respuesta (LOR) consideradas para construir las clases de cuasi-simetría. Se representan tres LORS (1-3 numerados de arriba a abajo) con un ángulos relativos LOR-cristal pequeños y tres (los números 4-6, también de arriba a abajo) con ángulos relativos LOR-cristal grandes. L y S son las coordenadas a lo largo del LOR y la dirección transversal al mismo respectivamente.

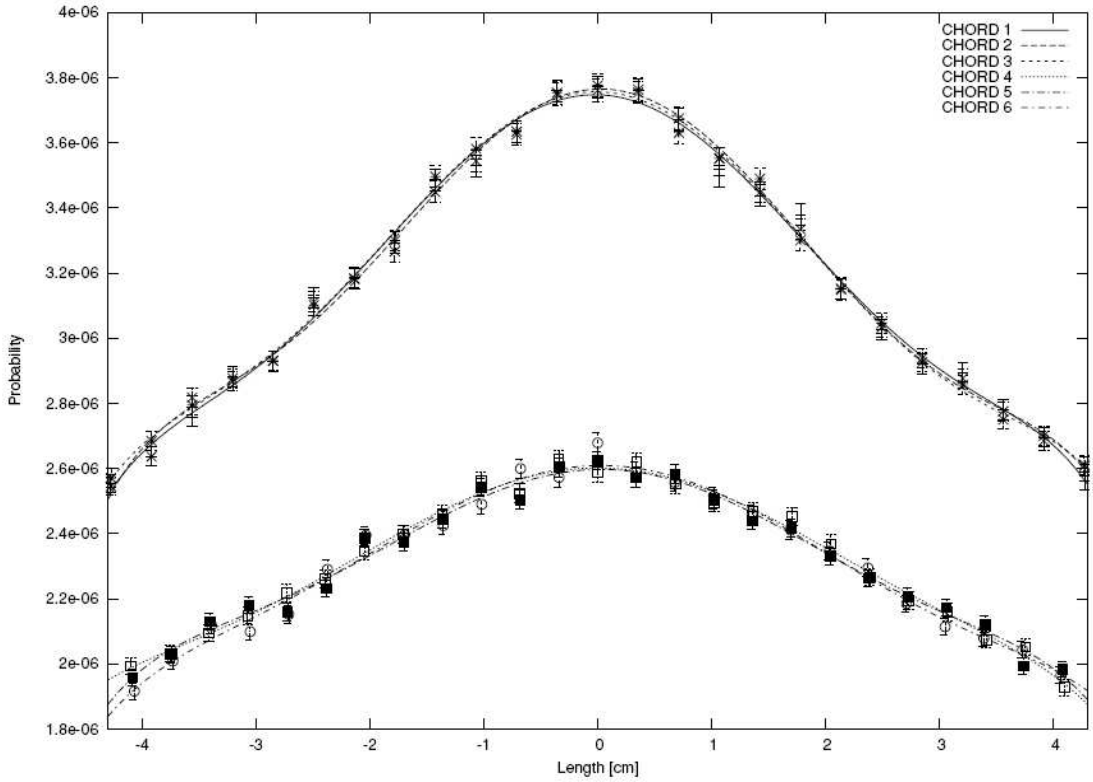

Figura 3. Perfil longitudinal de los elementos de probabilidad para los LORs que se muestran en la Figura 2. La probabilidad de detectar una coincidencia en los LORs 1-6 disminuye en función de la distancia al centro del mismo. Los puntos representan los resultados de la simulación MC y las barras de error la incertidumbre estadística. También se muestran los perfiles calculados por medio de esplines cúbicos. Los perfiles de los LORs con ángulo LOR-cristal pequeño (1-3) son muy similares entre ellos y diferentes de los LORs con ángulo LOR-cristal grande (4-6).

Nuestro software de reconstrucción ha sido probado con datos reales de ratones. Ratones a los que se les había inyectado 18F y FDG fueron adquiridos con un escáner PET explore Vista (GE) drT (Vaquero et al., 2004). La Figura 4 muestra las imágenes obtenidas utilizando el algoritmo de reconstrucción 3D-OSEM con 3 iteraciones de 25 + 25 + 50 subsets respectivamente. El número de voxels es de 175 × 175 × 168 (tres camas). El tamaño de voxel es 0,38 × 0,38 × 0,78 mm3. La adquisición con flúor muestra claramente los pequeños detalles, como las costillas y huesos de la columna vertebral, y los pequeños huesos en las patas delanteras. La adquisición con FDG muestra la acumulación habitual de la actividad del ratón en la vejiga urinaria, pero no se producen artefactos en sus alrededores.

La flexibilidad, la reducción de tiempo de reconstrucción, la exactitud y la resolución de las imágenes resultantes demuestran que las metodologías utilizadas para la reconstrucción pueden ser aplicadas a estudios reales de escáneres PET de animales pequeños de alta resolución. El uso de cuasi-simetrías para reducir (comprimir) el tamaño de la MRS parece ser una manera adecuada de tratar con el problema de almacenar la enorme MRS que requieren los escáneres PET de la alta resolución.

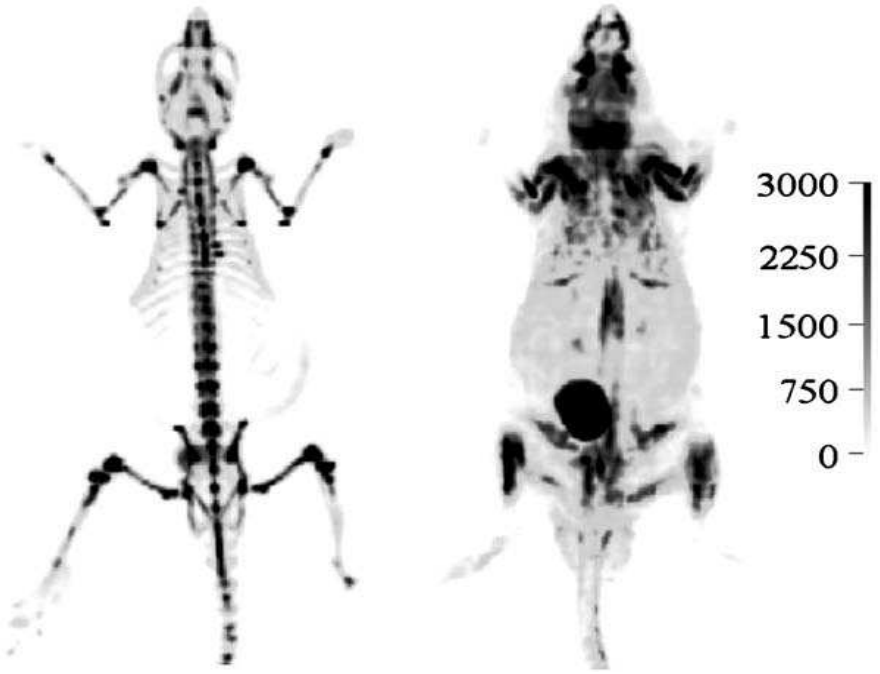

Figura 4. Imágenes reconstruidas adquisiciones de un ratón de 25 g. al que se le ha inyectado 250 µCi de (izquierda) 18F y (derecha) FDG realizadas con el escáner PET explore Vista (GE) drT. Cada estudio consta de 3 camas de 5 minutos de duración cada una. Se utilizaron 3 iteraciones 3D-OSEM de 25 + 25 + 50 subsets respectivamente para la reconstrucción de ambas imágenes.

Mejora de la calidad de imagen usando una estimación a priori de los eventos single-pixel

La mayoría de los escáneres PET de animales pequeños se basan en matrices de cristales centelleadores. Disponer de electrónica para leer de cada uno de los cristales es demasiado caro y, por tanto, la identificación de la interacción de cristal suele realizarse mediante el cálculo del centroide pesado por energía, como por ejemplo la lógica de Anger. Esto proporciona unas coordenadas XY que se emplean para el posicionamiento de la interacción de cada evento. A partir de estas coordenadas se construye una tabla de correspondencia que asigna un cristal a cada combinación de coordenadas (Dongming et al., 2006). En ocasiones el fotón interacciona en varios cristales o se producen dos interacciones de fotones distintos dentro del tiempo de integración. La información obtenida en estos casos de las coordenadas XY con los métodos tradicionales produce una identificación errónea del cristal de la primera interacción, y un deterioro de la calidad de imagen obtenida.

Hay varios factores que contribuyen a la degradación de la resolución espacial cuando se utilizan detectores pixelados. Por ejemplo, las cuentas procedentes de las líneas de respuesta oblicuas, presentan una mayor incertidumbre en el posicionamiento de fotones debido a los efectos de la penetración en el cristal. La situación ideal, donde la degradación de la resolución espacial debido a la dispersión en el detector es la menor posible, se corresponde con el caso de que un fotón interacciona sólo en un cristal, ya sea porque interactúa sólo una vez o porque todas las interacciones ocurren en la mismo píxel de la matriz. Nos referimos a esos eventos como single-crystal (España et al., 2007b). Cuando un fotón pasa por un cristal centellador, puede suceder una absorción fotoeléctrica o una interacción Compton. Si ocurre una absorción fotoeléctrica, toda la energía se deposita en el mismo cristal, pero la probabilidad de que esto ocurra es menor del 50% para los materiales centelleadores utilizados en PET (van Eijk, 2002). Si el fotón es dispersado por efecto Compton, su vuelo

continúa con menos energía y existen tres alternativas. El fotón puede escapar del detector con menos de 511 keV de energía, y por lo tanto, haber interaccionado en un sólo cristal. También puede sufrir otra interacción Compton o fotoeléctrica. En estos últimos casos, el fotón puede interactuar en el mismo cristal de la primera interacción o en uno diferente. Al interaccionar en un cristal diferente se contribuye a la degradación de la resolución espacial. Los múltiples puntos de interacción pueden dar lugar a errores en la asignación de cristal en el que ocurrió la primera interacción. Estos eventos podrían ser identificado, al menos parcialmente, a partir de un estudio detallado de imágenes de llenado de campo construidas a partir de los centroides de interacción (ver Figura 5). De hecho, los eventos cuyas coordenadas de interacción se encuentre en las regiones cercanas al pico máximo de cada cristal, se corresponden con mayor probabilidad con eventos single-crystal. Los eventos cuyes coordenadas de interacción se encuentran en los valles entre picos serían procedentes con mayor probabilidad de fotones que interaccionan en más de un cristal (multiple-crystal).

En la mayoría de los casos, los métodos de asignación de cristal son totalmente deterministas, en el sentido de que a cada evento se le atribuye a un sólo cristal con un 100% de certeza. Los criterios de aceptación de eventos pueden ser más estrictos y reducir más las contribuciones de eventos multiple-crystal, por ejemplo utilizando unas tablas de asignación (LUT, del inglés Look Up Table) más restrictivas, que no aceptan eventos que se encuentren fuera de un rango bastante estrecho en torno al pico de cada cristal. Estas LUT restringidas pueden producir imágenes con mejor resolución, pero a expensas de reducir la sensibilidad.

En este trabajo (España et al., 2007b) se propone un método alternativo, a fin de mejorar la calidad de las imágenes reconstruidas, que hace pleno uso de la información obtenida por el escáner para cada coincidencia, por lo general, las estimaciones de posición XY y energía depositada en el detector. Este método usa una especie de lógica borrosa, en el que cada coincidencia no es sólo aceptada o rechazada de acuerdo al cumplimiento de determinadas condiciones de energía y XY utilizando una lógica binaria, sino más bien, con la ayuda de comparaciones entre datos reales y simulados, se utiliza una combinación de ambos (energía y posición) para estimar la probabilidad de cada evento de ser single-crystal. Esta estimación de probabilidad es ajustada teniendo en cuenta la tasa de conteo, para lo cual se comparan mediciones reales con simulaciones (España et al., 2006, España et al., 2007a). A los eventos que son identificados con una alta probabilidad de ser single-crystal se les da una fiabilidad por encima de la media, mientras que otros son considerados como menos fiables. La asignación es por tanto, no sólo 0 ó 1, sino cualquier valor entre medias, en función de la probabilidad de ser un evento single-crystal. La hipótesis de este trabajo es que la calidad de imagen obtenida con escáneres PET de animales pequeños se puede mejorar utilizando una estimación a priori de los eventos single-crystal.

Una vez que se obtiene la estimación de la probabilidad de que un evento sea single-crystal, dos procedimientos para la mejora de la calidad de imagen han sido estudiados. En el primer método se calcula el sinograma antes de la reconstrucción de la imagen mediante la ponderación de cada coincidencia con la probabilidad de que los dos eventos que forman la coincidencia sean single-crystal. Por lo tanto, el sinograma contiene mayor contribución de eventos single-crystal y una reducción de la contribución de eventos multiple-crystal. El uso de este procedimiento proporciona imágenes con mejor resolución espacial, pero se produce también un aumento del ruido estadístico. Una ventaja de este procedimiento es que puede ser empleado por métodos de reconstrucción tanto analíticos como estadístico-iterativos. En este trabajo, sólo se muestran resultados obtenidos con el método iterativo 3D-OSEM.

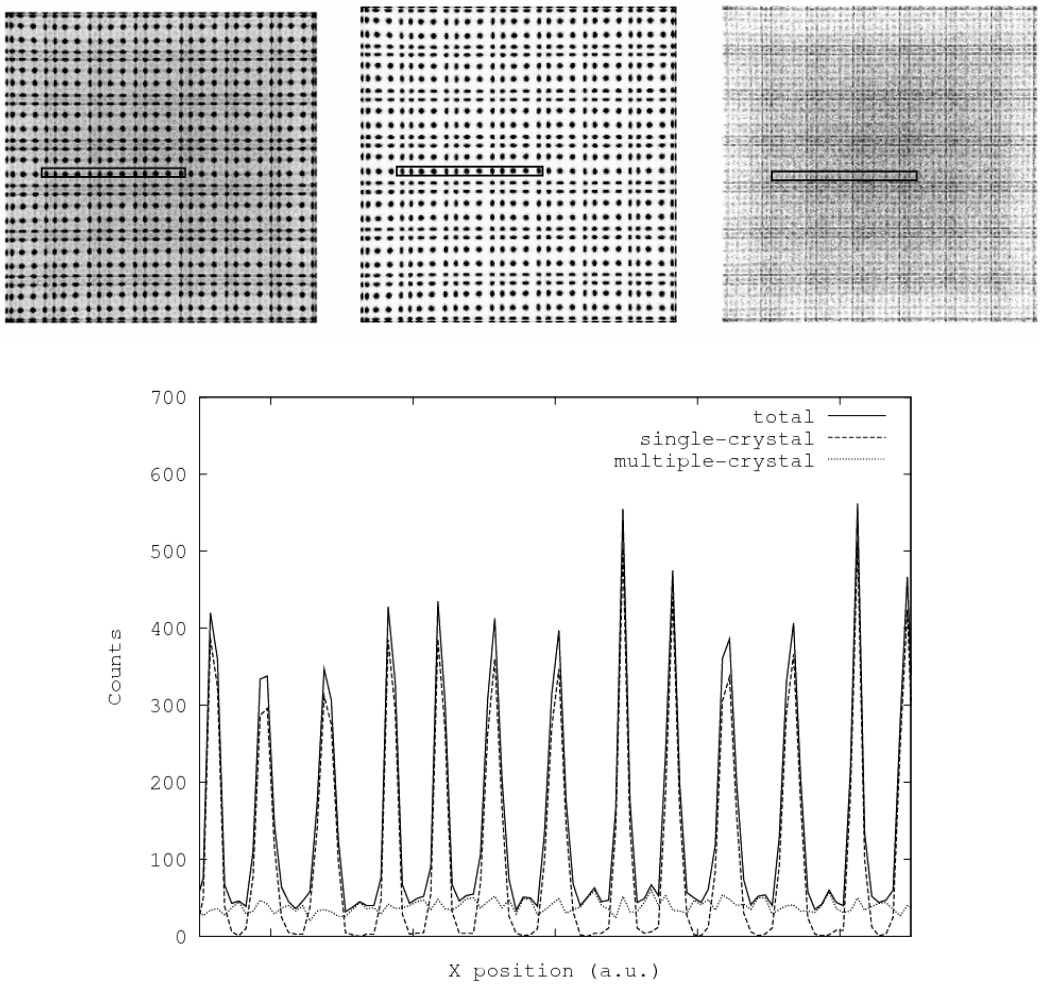

Figura 5. Imágenes de los llenados de campo obtenidos de simulaciones con PeneloPET para un detector formado por 30 × 30 cristales de LYSO con dimensiones de 1,5 x 1,5 x 12 mm3 acoplados a un fotomultiplicador Hamamatsu H8500. El bloque es iluminado de manera uniforme con una fuente de 18F de baja actividad. Arriba se muestran las imágenes de llenado de campo con los eventos totales (izquierda), single-crystal (centro) y multiple-crystal (derecha). En la figure inferior se muestran los perfiles de línea a través de la zona rectangular marcada arriba en las imágenes de llenado de campo. Como era de esperar, las regiones de los picos están en su mayor parte compuestas de eventos single-crystal, mientras que las regiones valle reciben una notable contribución de eventos multiple-crystal.

En el segundo procedimiento, la probabilidad de que el evento sea single-crystal se introduce dentro del procedimiento iterativo, de modo que todos los eventos son utilizados en la reconstrucción. A partir de cada adquisición se construyen cuatro sinogramas, cada uno formado a partir de las coincidencias con una combinación diferente de probabilidades single-crystal. Las cuatro combinaciones son las siguientes: a) Obtenidos a partir de la contribución de la probabilidad de que el primer y segundo eventos sean single-crystal (SC-SC), b) el primer evento sea single-crystal y el segundo sea multiple-crystal (SC-MC), c) el primer evento sea multiple-crystal y el segundo evento single-crystal (MC-SC) y d) el primer y segundo eventos sean multiple-crystal (MC-MC).

Se ha calculado una matriz de respuesta del sistema para cada tipo de sinograma. El mismo procedimiento de estimación de probabilidades para eventos single-crystal es utilizado para el cálculo de la matriz del sistema mediante simulaciones. En la Figura 6, se muestran las diferencias de los perfiles transversales de la matriz de respuesta para los diferentes tipos de sinogramas.

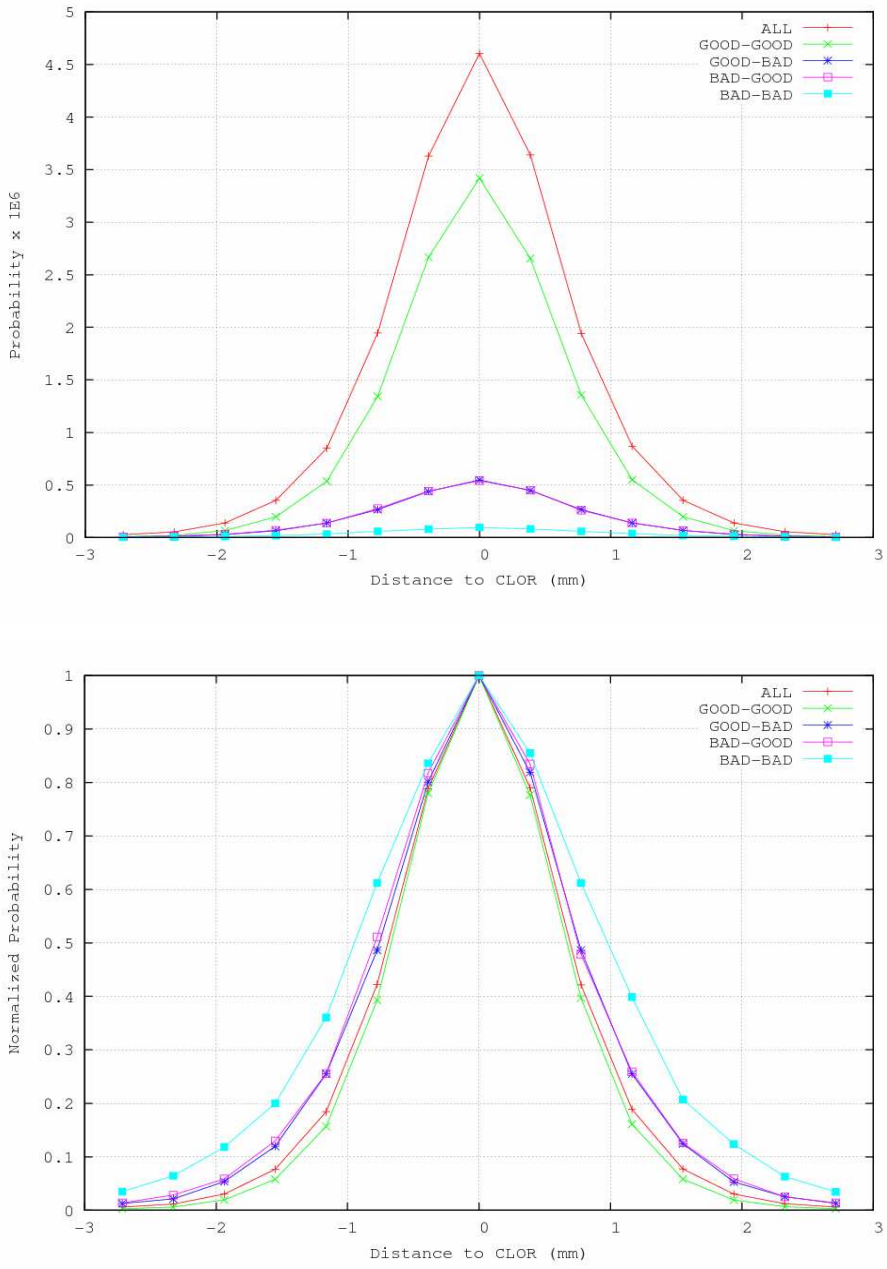

Figura 6. Perfil transversal de probabilidad a lo largo de un tubo de la respuesta de un LOR mostrando los distintos valores en el máximo (arriba) y las diferentes formas (abajo, donde todos los perfiles están reescalados al mismo valor del máximo) para las diferentes matrices de respuesta. También se muestra el perfil del procedimiento estándar de cálculo de la matriz de respuesta.

La evaluación de la mejora conseguida en la calidad de imagen ha sido realizada mediante la simulación de la adquisición, según el protocolo NEMA de animales pequeños (NEMA, 2008), para la obtención de los coeficientes de recuperación en la imagen. Dicha adquisición consiste en el empleo de un maniquí IQ que consta de una región con concentración de actividad uniforme y otra con capilares de distintos diámetros y la misma concentración de actividad que la zona uniforme. En la Figura 7 se muestran los resultados obtenidos midiendo los coeficientes de recuperación sobre el capilar de 1 mm de diámetro frente al ruido en la zona uniforme.

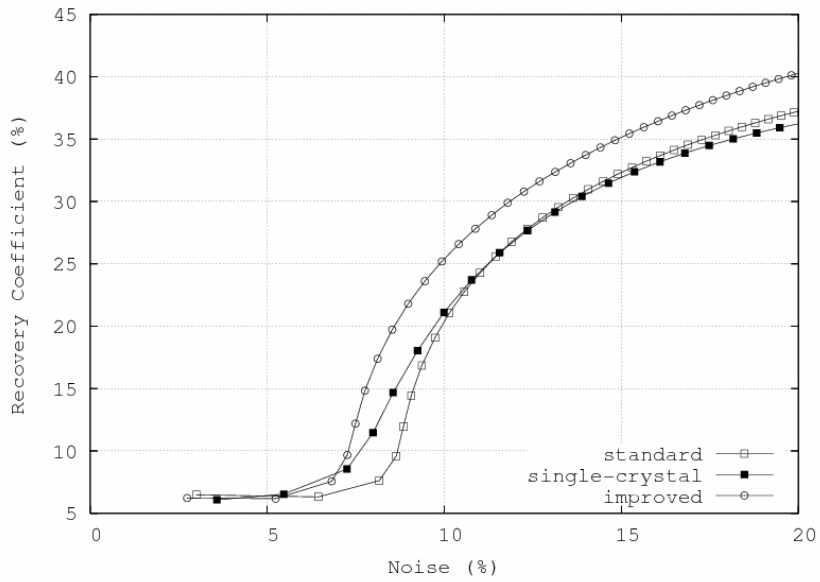

Figura 7. Coeficientes de recuperación frente al ruido para reconstrucción 3D-OSEM del capilar de 1 mm de una simulación de maniquí IQ adquirido con un escáner VrPET. Cada punto corresponde a cinco subiteraciones. Si fijamos un 8% como el límite aceptable de ruido se observa como el método propuesto (improved) consigue un coeficiente de recuperación del 20% en 40 subiteraciones mientras que los otros se quedan en un 15% (single-crystal) en 30 subiteraciones y 10% (standard) en 20 subiteraciones. Si observamos el ruido y las subiteraciones en las que los otros métodos consiguen un 20% de coeficiente de recuperación se obtiene 10% de ruido y 35 subiteraciones para el caso single-crystal y 10% de rudio y 45 subiteraciones para el caso standard.

Consideraciones para el diseño de un escáner PET de animales pequeños

Los escáneres PET de animales pequeños se encuentran en continuo desarrollo. Los nuevos dispositivos disponen de mayor sensibilidad, resolución espacial, y capacidad de conteo (Wang et al., 2006, McFarland et al., 2007). El diseño de un nuevo escáner PET es un proceso muy complicado que exige la toma de decisiones de varios tipos. Las simulaciones de Monte Carlo se han convertido en una herramienta de valor incalculable en este proceso, permitiendo estudios exhaustivos de todos los componentes que forman el escáner (Heinrichs et al., 2003). El propósito de este capítulo es el estudio, por medio de simulaciones de Monte Carlo, de la influencia que tiene la configuración de los parámetros típicos de escáneres PET de animales pequeños en sus prestaciones.

En la actualidad, los escáneres PET se componen de bloques detectores (Wang et al., 2006), formados por fotomultiplicadores sensibles a la posición (PS-PMT) acoplados a una matriz de cristales de centelleo. Los bloques detectores están dispuestos en anillos paralelos para lograr una mejor resolución transaxial. Diferentes configuraciones han sido evaluadas. Parámetros tales como el diámetro del anillo, tamaño de los detectores, tamaño de pixel, material centelleador y la electrónica han sido exhaustivamente probados a fin de evaluar cómo se ven modificadas las prestaciones del escáner.

Como punto de partida, se han establecido los objetivos de configuración que debe cumplir el escáner. La sensibilidad en el centro del FOV para una ventana de energía de 250 keV a 700 keV debe ser alrededor del 10%. La resolución espacial en el centro de la FOV debe ser mejor que 1,7 mm. Por último, tanto el FOV axial como el transaxial deben ser alrededor de 10 cm. El escáner debe tener también una alta capacidad de conteo.

Hay cuatro características de funcionamiento de los escáneres PET considerados aquí: la resolución espacial, la sensibilidad, tamaño del FOV y la tasa en el pico de la curva NEC. La resolución espacial, el tamaño del FOV y la sensibilidad dependen de la geometría y del material centelleador empleado, pero no de la electrónica. Por otro lado, la obtención de buenos valores para el pico de la curva NEC depende de la geometría y, más esencialmente, de la electrónica y de la respuesta temporal del centelleador. Por ejemplo, utilizando escáneres con la misma geometría y materiales, pero diferente configuración de la electrónica, se obtienen capacidades de conteo muy diferentes.

Algunas conclusiones extraídas de los resultados presentados en este capítulo se resumen a continuación. La resolución espacial depende más de la longitud del cristal que de su sección para escáneres de alta resolución. La mejor resolución se lograría con cristales más cortos y mayor diámetro del escáner, pero esto disminuirá la sensibilidad e incrementaría el número módulos detectores requeridos.

Suponiendo una electrónica ideal, los factores limitantes de la tasa en el pico de la curva NEC son el apilamiento de pulsos en el detector y las coincidencias aleatorias que entran dentro de la ventana de coincidencia. Éstos problemas sólo puede ser resueltos mediante la utilización de materiales centelleadores más rápidos que permitan reducir el tiempo de integración y estrechar la ventana de coincidencias y/o la lectura de menor volumen de cristal por cada elemento detector (PMT, ADC, SiPM), de manera que se reduce el número de eventos que llegan a cada uno de ellos.

Por otro lado, el elevado coste de los elementos de detección que componen los escáneres PET ha llevado al diseño de escáneres con menor número de detectores, a expensas de una reducción de la sensibilidad (Vaquero et al., 2005). El muestreo angular se logra mediante la rotación de los detectores alrededor del campo de visión. El uso generalizado de métodos de reconstrucción estadístico iterativos, junto con el hecho de que estos métodos iterativos de reconstrucción son más tolerantes a un muestreo angular incompleto, permite explorar la posibilidad de utilizar diferentes esquemas de rotación (es decir, rotación continua y adquisición en parada) de los detectores en para obtener la mejor resolución de imagen con el mínimo tiempo de adquisición y reconstrucción.

Tabla 3. Resolución espacial medida en imágenes reconstruidas de adquisiciones simuladas de un maniquí Derenzo adquiridas tanto en modo de rotación continua como de adquisición en parada con distinto número de pasos.

Radial - **Tangencial** (mm)	5 pasos	6 pasos	7 pasos	Rotación Continua
3 Iterations 50 Subsets	0.90 - **1.02**	0.73 - **0.85**	0.79 - **0.83**	1.06 - **1.27**
2 Iterations 75 Subsets	1.04 - **1.12**	0.75 - **0.87**	0.82 - **0.88**	1.07 - **1.30**
1 Iterations 150 Subsets	1.06 - **1.15**	0.92 - **1.00**	0.94 - **1.13**	1.09 - **1.32**

Se puede concluir que las adquisiciones de rotación con paradas son una ventajosa alternativa a la rotación continua para los escáneres PET con un muestreo angular incompleto. El cálculo de una matriz de respuesta del sistema más exacto para el caso de adquisiciones con paradas, permite obtener una mejora en la resolución de la imagen de hasta un 30%.

Conclusiones

En esta tesis doctoral se han utilizado las técnicas de simulación Monte Carlo en la mejora de la técnica PET. De este modo se han aprovechado al máximo los conocimientos en Física Nuclear tanto en la mejora de la calidad de imagen de escáneres existentes como en el diseño de nuevos prototipos. A continuación se resumen las principales aportaciones del trabajo realizado y las conclusiones obtenidas:

- Se ha desarrollado una herramienta de simulación Monte Carlo adaptada a la técnica PET (PeneloPET) que permite realizar de manera sencilla simulaciones que incorporan toda la física y la electrónica necesaria para conseguir resultados realistas. La herramienta ha sido desarrollada para realizar simulaciones complejas con el mínimo esfuerzo del usuario y poder ejecutarlas en un tiempo óptimo. Al reducir el tiempo de preparación y el de simulación, el usuario puede incluir mayor realismo en las simulaciones a la vez que realizar estudios en mayor profundidad con la misma dedicación. La posibilidad de obtener los resultados en diversos formatos, ya sea en forma de histogramas o sinogramas como ficheros en modo lista, reduce también el tiempo de análisis de los mismos. Un sencillo script escrito en lenguaje python permite ejecutar las simulaciones en clusters de ordenadores o procesadores con múltiples núcleos con el mínimo esfuerzo.

- Se ha realizado una validación exhaustiva del código de simulación desarrollado, comparándolo con otros simuladores y con resultados obtenidos de datos reales de diferentes escáneres PET comerciales de animales pequeños. La similitud encontrada entre los datos reales y los simulados garantiza el buen funcionamiento de la herramienta desarrollada y la convierten en idónea para la mejora de la técnica PET.

- Se ha calculado la matriz de respuesta del sistema mediante simulaciones Monte Carlo para varios escáneres comerciales. Esta matriz de respuesta incluye una descripción realista de los procesos físicos de emisión y detección, permitiendo la obtención de imágenes PET de alta calidad y resolución mediante el uso de técnicas de reconstrucción estadístico iterativas. Además, las estrategias de compresión utilizadas para almacenar dicha matriz, han permitido optimizar el proceso de reconstrucción, consiguiendo aprovechar al máximo los recursos informáticos con el fin de obtener imágenes en el menor tiempo posible.

- Se ha desarrollado un método de mejora de la calidad de imagen basado en el conocimiento a priori de la probabilidad de que un evento detectado provenga de la interacción de un fotón en un único cristal de la matriz del detector. La incorporación de este conocimiento a priori en el proceso de reconstrucción (obtenido de la comparación de simulaciones y datos reales), permite obtener imágenes con mejor relación señal-ruido y con un ritmo de convergencia superior al de los métodos tradicionales. El método mejorado permite obtener valores más altos de los coeficientes de recuperación para niveles de ruido razonables. La evaluación de los métodos propuestos sobre estudios realizados con escáneres reales no ha mostrado el el método single-crystal permite reducir el fondo de ruido que se produce en escáneres con una alta contribución de eventos con pile-up. Podemos concluir que, mediante uso de PeneloPET para obtener información a priori de los datos adquiridos, es posible mejorar la calidad de las imágenes reconstruidas.

- Se ha realizado un estudio sobre los principales parámetros de configuración que intervienen en el diseño de un escáner PET de pequeños animales. Como resultado de este estudio se han determinado los parámetros de configuración óptimos que deben ser tenidos en cuenta a la hora de diseñar un escáner PET con las máximas prestaciones de resolución espacial, sensibilidad y tasa de conteo. PeneloPET permite estimar perfiles de

resolución frente a sensibilidad para distintos valores de uno o más parámetros. El tamaño del cristal y el materia puede ser elegidos después de un uso intensivo de las simulaciones de PeneloPET. PeneloPET puede simular escáneres PET con distintos tamaños de detector, respuesta temporal y resolución temporal con el objetivo de establecer la configuración con la que se obtiene una tasa de conteo óptima para el escáner. Hemos utilizado también PeneloPET para comparar los protocolos de adquisición con rotación con paradas y con rotación continua, obteniendo una resolución espacial un 30% superior para el caso de rotación con paradas. Podemos concluir que PeneloPET es una herramienta potente para el diseño de nuevos escáneres PET de animales pequeños.